

Optical gain and laser properties of semiconductor quantum-dot systems

by Michael Lorke

University of Bremen 2008

Optical gain and laser properties of semiconductor quantum-dot systems

Dissertation
zur Erlangung des akademischen Grades
Doktor der Naturwissenschaften
(Dr. rer. nat.)
am Fachbereich Physik/Elektrotechnik
der Universität Bremen

vorgelegt von

Dipl. Phys.
Michael Lorke

Bremen, 17. Dezember 2008

Vom Fachbereich Physik/Elekrotechnik der Universität Bremen
genehmigte Dissertation

1. Gutachter Prof. Dr. Frank Jahnke, Universität Bremen
2. Gutachter Prof. Dr. Andreas Knorr, Technische Universität Berlin

Eingereicht 17.12.2008

Kolloquium 11.02.2009

Ne dubita, cum magna petes,
impendere parva

Cato maior

Abstract

For practical applications of quantum dots in light emitters as well as for fundamental studies of their emission properties, the understanding of many-body processes plays a central role. We employ a microscopic theory to study the optical properties of semiconductor quantum dots. The excitation-induced polarization dephasing due to carrier-phonon and carrier-carrier Coulomb interaction as well as the corresponding lineshifts of the optical interband transitions are determined on the basis of a quantum-kinetic treatment of correlation processes. Our theoretical model includes non-Markovian effects as well as renormalized single-particle states. Thus we achieve an accurate description of the partial compensation between different dephasing contributions and are able to systematically study their temperature and density dependencies. Applications of this theoretical model include optical gain spectra for quantum-dot systems that reveal a novel effect, not present in other gain materials. For large carrier densities, the maximum gain can decrease with increasing carrier density. This behavior arises from a delicate balancing of state filling and dephasing, and implies the necessity of an accurate treatment of the carrier-density dependence of correlations.

Measurements of the coherence properties of the light emitted from semiconductor quantum-dot lasers have raised considerable attention in recent years. We study the correlations between individual emission events on the basis of a microscopic semiconductor laser theory. This allows for a study of effects like Pauli blocking, modifications to the source term of spontaneous emission, and the absence of complete inversion, that strongly influence the emission characteristics of quantum dot based devices.

A new and challenging material system for applications in the visible spectral range are nitride semiconductors. As crystal symmetry and bandmixing effects strongly influence the optical selection rules, the single particle properties of quantum dot and wetting layer states are determined on an atomistic level from tight-binding calculations. The resulting tight-binding wave functions are used to calculate dipole transition matrix elements and Coulomb interaction matrix elements. As an example for the combination of microscopic single-particle calculations and many-body theory, optical spectra of quantum-dot wetting-layer systems including multiple subbands and the influence of the atomic structure and strong bandmixing effects are presented.

Contents

I	Introduction	1
1	Prologue	3
2	Semiconductor Quantum Dots	9
2.1	Quantum dot growth	10
II	Many-Body Theory for semiconductor nanostructures	13
3	Many-body Theory	15
3.1	Hamiltonian and Heisenberg's equations of motion	16
3.2	Single-particle density matrix	18
4	Theory of non-equilibrium Green's functions	21
4.1	Expectation values and time ordering	21
4.2	The Keldysh Contour	23
4.3	Green's functions in non-equilibrium	25
4.4	Dynamics of the non-equilibrium Green's function	28
4.4.1	Functional derivative technique and Dyson equation	29
4.4.2	Screened Coulomb interaction and vertex function	31
4.4.3	Fundamental system of equations	32
4.5	Kadanoff-Baym equations	34
4.5.1	Langreth-Wilkins theorems	34
4.5.2	Kadanoff-Baym equations	35
4.6	Martin-Schwinger hierarchy	35
4.7	Reduction to single-time propagators (generalized Kadanoff-Baym ansatz)	36
5	Cluster expansion method	39
5.1	Factorization scheme	39
5.2	Cluster expansion truncation scheme	40
6	Alternative methods	43

III Optical properties and dephasing mechanisms in Quantum Dots	45
7 Single-particle states and interaction matrix elements	51
7.1 Eigenfunction expansion	53
7.1.1 Dipole Hamiltonian	53
7.1.2 Coulomb Hamiltonian	55
8 Optical properties of quantum dot systems	57
8.1 Theoretical description of optical response	57
8.2 Evaluation of the Kadanoff-Baym equations	59
9 Coulomb interaction	61
9.1 Hartree-Fock approximation	61
9.2 Second Born approximation	65
9.2.1 Screening	66
9.3 Correlation contribution in the time-domain	69
9.4 Connection between memory effects and frequency dependence in the scattering integrals	71
9.5 Self-consistent single-particle energy renormalizations	74
9.6 Results	77
9.6.1 Importance of different dephasing processes	77
9.6.2 Renormalization of single-particle states	80
9.7 Conclusion	82
10 Carrier-phonon interaction	83
10.1 Hamiltonian for the carrier-phonon interaction	83
10.2 RPA selfenergy	85
10.3 Polarons in semiconductor quantum dots	86
10.4 Dephasing contributions	89
10.5 Optical spectra	90
11 Dephasing due to carrier-phonon and Coulomb interaction	93
11.1 Selfconsistent inclusion of both interaction mechanisms	94
11.2 A shortcoming of our theoretical model	100
12 Applications to quantum-dot gain media	103
12.1 Density dependence of the linewidth	104
12.2 Reduction of the peak gain in QD based active media	107
12.3 Linewidth enhancement factor (α -factor)	112
12.4 Conclusion	114

IV Laser Theory for semiconductor Quantum Dots	117
13 Laser model	121
13.1 Equations of motion	124
13.2 Laser equations	126
13.3 Rate equation limit	129
14 From thermal to Poissonian photon statistics: the laser threshold	133
14.1 Extended laser equations	133
14.2 Results	136
14.3 Verification of the treatment of correlations	137
14.4 Analytical results for $g^{(2)}(0)$	142
14.5 Conclusion	144
V Optical properties of nitride Quantum Dots	145
15 Tight-binding calculations for wurtzite crystals	149
15.1 The wurtzite crystal structure	149
15.2 Tight-binding wave-function model	151
15.2.1 The QD model	152
15.2.2 The WL model	154
15.3 Coulomb matrix elements	156
15.4 Dipole matrix elements	160
16 Optical properties	161
16.1 Kinetic equations	161
16.1.1 Coulomb interaction	163
16.1.2 Screened-exchange and Coulomb-hole approximation	165
16.2 Optical spectra	166
16.3 Comparison between different approaches for the Coulomb interaction	168
16.4 Carrier-phonon interaction	169
16.5 Dephasing due to carrier-phonon interaction	173
16.6 Conclusion	175
VI Summary and Outlook	177
VII Appendix	181

A Eigenfunctions in envelope function approximation and Coulomb matrix elements	183
B Derivation of the Lindhard formula	189
C Interplay of time constants for the laser model	193
D Material parameters and numerical methods	195
D.1 Material parameters	195
D.2 Numerical methods	196
D.3 Lifting of the Coulomb singularity	196
E Dipole matrix elements using tight-binding coefficients	199
List of Publications	a
Bibliography	e

Part I

Introduction

1 Prologue

The last century has seen a remarkable progress in miniaturization. Since the invention of the transistor by William B. Shockley, John Bardeen and Walter Brattain, electronic devices have become ever smaller, and a giant leap has been made from the first computer by Konrad Zuse to today's micro-processors. Comparable progress has been achieved in the field of photonic devices: From the first ideas of the maser¹ [1], and the first gas and atom lasers² [2], orders of magnitude in size and performance have been spanned to today's semiconductor devices. The common aspect of both, electronic and photonic devices, is the heavy use of semiconductor materials. No CD player would be feasible without the use of semiconductor laser diodes and the discoverers of other semiconductor effects like the giant magnetoresistance that is used in every computers harddisk have been awarded with Nobel prizes recently. Furthermore, progress made both in fabrication and understanding of light emitting devices has opened up the possibility to directly use the quantum nature of light for applications. Possible candidates for quantum computers have been discussed and first successes using quantum entanglement for secure data transport have been achieved in the field of quantum cryptography, see e.g. Refs. [3, 4].

Over the last decades, the field of semiconductor physics has shifted its focus to systems, where the effective dimensionality of the electron system is reduced to two dimension in quantum wells, one dimension in quantum wires, and even zero dimensions in quantum dots. While quantum well structures were extensively studied in the past, quantum dots have been predicted to be the basic building blocks for next generation optical devices, as due to the three-dimensional carrier confinement, they should behave like "artificial atoms" without the caveats of atomic systems, namely being tied to the periodic table and having the need to be confined in atom traps. Quantum dots therefore offer a great application potential and optoelectronic devices like LEDs, lasers, or amplifiers [5, 6, 7, 8, 9] have been realized. In the emerging field of quantum information technology, QDs have been successfully used to demonstrate the generation of single photons or correlated photon pairs [10, 11, 12, 13, 14, 15, 16, 17, 18, 19]. Furthermore, the strong coupling regime for QD emitters in optical microcavities has been demonstrated [20, 21].

¹Acronym: microwave amplification by stimulated emission of radiation

²Acronym: light amplification by stimulated emission of radiation

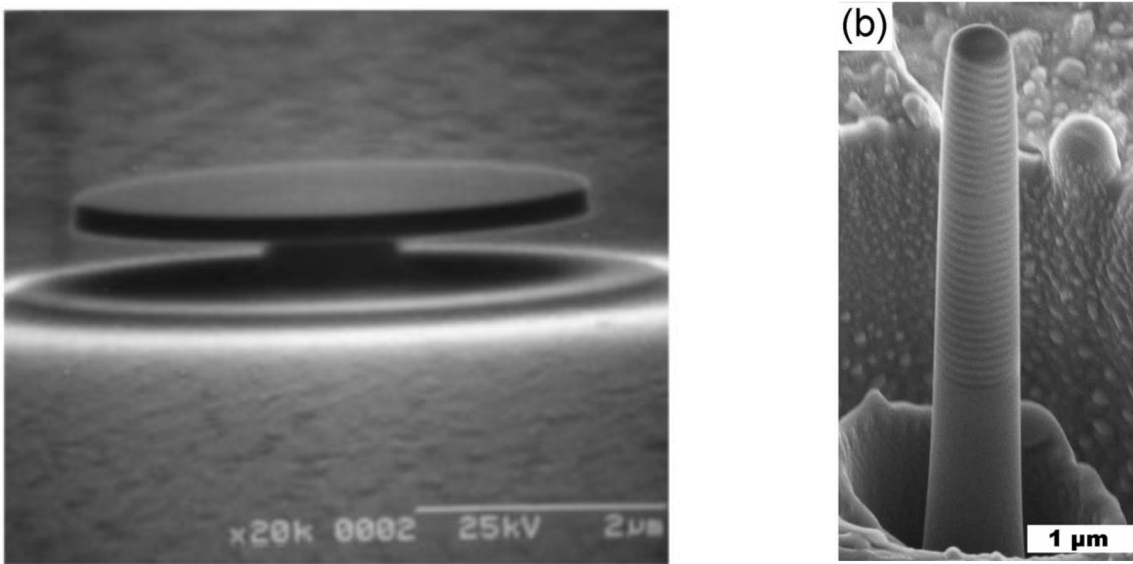


Figure 1.1: Microdisk (left) and Micropillar (right) resonators, taken from Refs. [10] and [24], respectively.

While quantum dots are most predominantly fabricated using the InGaAs/GaAs material system suited for optical applications in the infrared to red spectral region, the need for light emitters in the green and blue spectral regions has been the driving force for research towards alternative material systems in recent years. After the realization of the first GaN-based LED and laser diode by Shuji Nakamura [22, 23], the nitride material system has been regarded as one candidate to fulfill this need, as the bandgaps of nitride material systems range from the UV to the infrared spectral regions.

Further advances have been made in the fabrication of better optical resonators, providing confinement of the light field for laser applications or basic research on cavity quantum electrodynamics. The reduced dimensionality of the photonic system can be achieved by providing an effective confinement. Typically this is realized by total internal reflection or by Bragg reflection.

Figure 1.1 shows two examples of microresonators. In the case of the microdisk (left panel) and also in microspheres [25, 26] the confinement is achieved by total internal reflection only, realized by means of so-called “whispering gallery modes”. An example of such modes is shown in the right panel of Figure 1.2 together with an aerial view of St. Paul’s cathedral, after whose dome the modes are named. Also combinations of total internal reflection and Bragg reflection have been achieved in the VCSEL³ that can be realized via a micropillar resonator. Such a structure is shown in the right

³Acronym: vertical cavity surface emitting laser

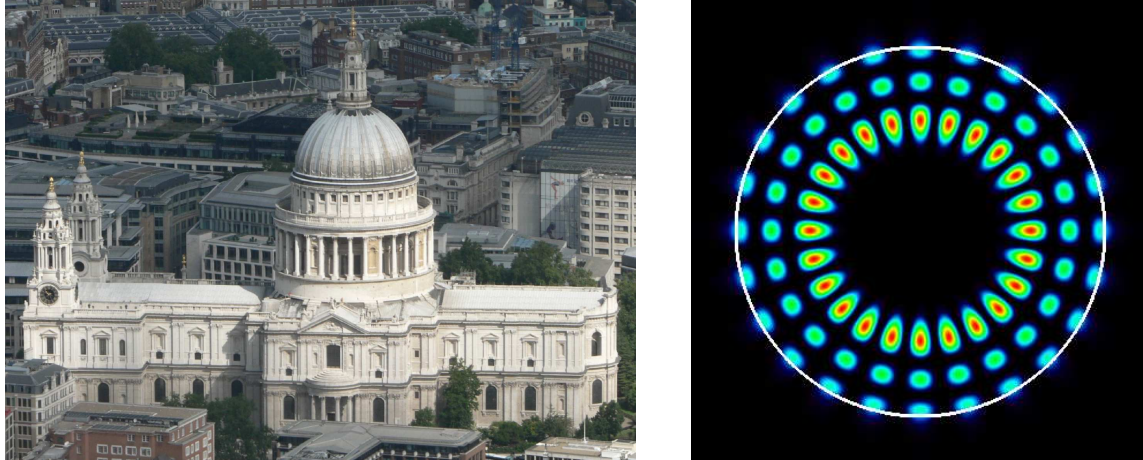


Figure 1.2: St. Paul’s cathedral (left panel, picture taken from Ref. [27]) and whispering gallery mode (right panel, picture courtesy of Prof. Dr. Jan Wiersig, Univ. Magdeburg).

panel of Figure 1.1. In that case, confinement of light is achieved by total internal reflection at the sidewalls, whereas the alternating layers in vertical direction act as distributed Bragg reflectors. The determination of the optical modes in micro-resonators is a fascinating and vivid field of research on its own and remarkable insight into possibilities to tailor also the emission and directionality properties of such resonators has been gained [24, 28, 29].

LED and laser devices need an active material, where the energy put into the system is converted into light. In quantum-dot based devices, the quantum dots typically act as the active medium. An important difference to quantum-well based devices stems from the aforementioned “artificial atom” picture, that also motivated the development of quantum dots historically. By choosing the material and growth parameters correctly, the emission properties can be tailored to a large degree. If we focus on the modelling of LED and laser structures, we need a description of the active medium. This typically starts from a calculation of single-particle states and continues to many-body questions like how carriers, that are generated by means of optical excitation or current injection, reach the optically active transitions. Moreover, to tailor the emission properties of semiconductor quantum-dot devices a detailed understanding not only of the active material but also of the optical modes of the cavity and their interaction with the active material is needed. Furthermore, in nearly all of the aforementioned applications or fundamental research questions, dephasing and many-body renormalization processes play a key role. They control the homogeneous lifetime of resonances in optical spectra and therefore e.g. limit coherence times for applications in quantum information technology as well as the maximum achievable optical gain for laser applications.

The aim of this thesis is twofold. First we will give a microscopic description of dephasing processes and study its influence on the optical gain of semiconductor quantum-dot systems. Consequently, we present a theoretical analysis of the fundamental carrier-carrier interaction and carrier-phonon interaction in self-assembled quantum dots, as the gain spectrum of this active medium is substantially governed by dephasing and many-body renormalizations due to scattering processes. To address the question of light-matter interaction in quantum-dot based laser structures, we will study quantum-dot laser emission and the impact of carrier-photon correlations on the coherence properties of the emitted light. Additionally, we will analyze the optical gain of nitride based quantum-dot structures. Here it turns out that, due to strong band-mixing effects, a microscopic model of the single-particle states is needed.

Collaborations

This thesis is concerned with the description of dephasing in quantum-dot systems and studies of the corresponding optical properties. As one of the first investigations of quantum-dot systems in our group, carrier scattering due to Coulomb interaction was investigated by Torben Nielsen [30]. This thesis is devoted to the extention of these investigations by a detailed consideration of the dephasing that is caused by the respective Coulomb scattering processes. For this purpose also a consistent treatment of the single-particle renormalizations turns out to be of particular importance. However, links are established with the ongoing work in our group as well as with the topics of two DFG research groups. This means that we will include the effects of the carrier-phonon interaction, which is the subject of the thesis of Jan Seebeck [31] into the dephasing calculations. As this requires a self-consistency scheme for the single-particle renormalizations due to Coulomb and carrier-phonon interaction we realized such a scheme in close collaboration with Jan Seebeck. However, it should be noted, that the focus here is on the dephasing and on the corresponding optical properties rather than on the carrier-phonon scattering. Likewise, the inclusion of semiconductor effects into laser models has been a collaboration with Christopher Gies. This resulted in a joint publication, Ref. [32], that was the basis for Part IV of the present thesis. As the nitride material system requires a microscopic description of the single-particle states, tight-binding results were provided by S. Schulz from the group of G. Czycholl in Bremen. As these single-particle properties influence both the carrier-carrier and the carrier-phonon interaction, the implementation was done together with Jan Seebeck.

Organization of this thesis

This thesis is organized into seven parts. In this first part we introduced our topic, followed by a short summary about self-assembled quantum dots in the next chapter. In the second part we will review the many-body hierarchy problem and discuss possible solution schemes, mainly the nonequilibrium Green's functions and the cluster expansion method. The third part will be devoted to the discussion of the relevant interaction mechanisms and the development of a theoretical model for the dephasing in quantum-dot system, followed by various applications of this model to study the optical properties of InGaAs quantum dots. In part four, we will apply the cluster expansion method to describe lasing properties of quantum-dot systems and to classify the emitted light by means of its statistical properties. As over the last decade nitride materials have achieved considerable research interest, we focus on this new and challenging material system in part five, introducing a tight-binding model for the single-particle states and studying the associated optical properties. The last parts of this thesis contain a conclusion and an outlook, along with other material appropriate for appendices.

2 Semiconductor Quantum Dots

All semiconductor systems with dimensional reduction share the same basic idea. One embeds a low bandgap material, e.g. InGaAs, into a material with a higher bandgap, e.g. GaAs, thus achieving carrier confinement in one to three dimensions. The confinement and the resulting free density of states (fDOS) is shown schematically in Figure 2.1.

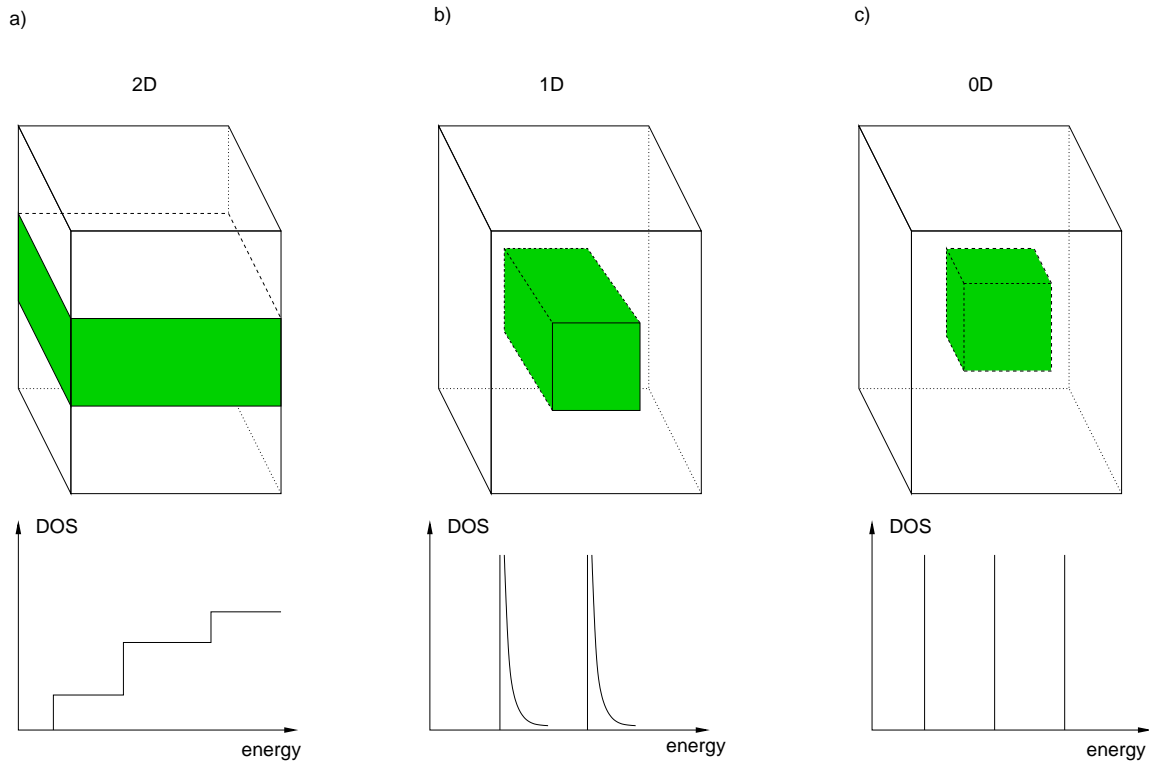


Figure 2.1: Dimensional reduction of a nanostructure and the corresponding free-particle density of states, (a) quantum well, (b) quantum wire and (c) quantum dot.

While for higher dimensional systems we find continuous parts in the fDOS, for quantum dots (QDs) it purely consists of δ -like peaks, allegedly leading to superior optical properties like, e.g. high optical gain and small linewidth-enhancement factor. This discrete structure is also what lead to the concept of “artificial atoms” as QDs are

often referred to in literature. However, in reality QDs consist of thousands of atoms of semiconductor material and furthermore they are embedded in a semiconductor matrix. This will lead to drastic deviations from the “artificial atom” picture as we will see throughout the thesis. However, QDs allow to a large degree the tailoring of their optical properties, as the confinement is heavily dependent on the QD size, as one can easily see from a simple particle-in-a-box model. Furthermore, the confinement can also be controlled by the material compositions, opening another degree of freedom for controlling QD properties.

2.1 Quantum dot growth

Whereas lots of techniques have been demonstrated to achieve three dimensional carrier confinement including nanocrystal QDs [33], confinement by metallic gate electrodes, and definition of QDs by means of lithography and etching [34], we focus in this thesis on self-assembled quantum dots (QDs) grown in the Stranski-Krastanow growth mode. Such QDs are typically fabricated by molecular beam epitaxy (MBE) or metal organic vapor phase epitaxy (MOVPE). While we will not give an extensive introduction into QD growth, a few comments on the basic physical mechanism of Stranski-Krastanow QD growth are appropriate.

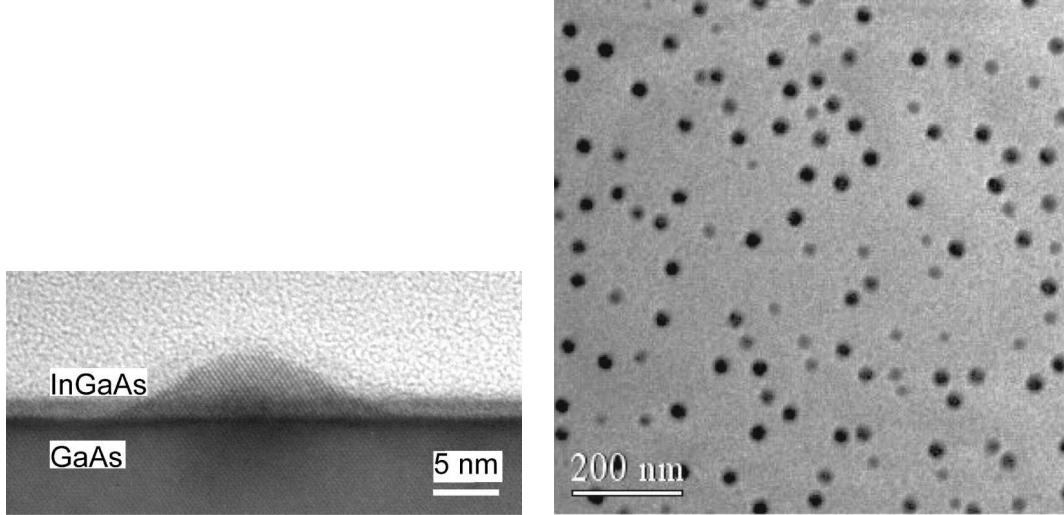


Figure 2.2: Transmission electron microscopic images of single InGaAs/GaAs QD and of an ensemble of self-assembled QDs, taken from Ref. [35]

The typical Stranski-Krastanow scheme can be described according to Refs. [36] and [37] as follows. On the substrate of the high bandgap material one starts to grow the low bandgap material. As the low bandgap material typically has a larger lattice

constant than the high bandgap material, the first few monolayers grow compressively strained, but homogeneous. However, after a few monolayers it is energetically favorable for the material not to further grow homogeneously but to relax parts of its elastic energy by means of island formation. While these islands form the actual QDs a thin quasi-two-dimensional layer, named wetting layer (WL), that resembles the remnant of the former homogeneous growth remains present underneath the islands.

Using these growth mechanism a variety of QD geometries has been achieved, ranging from flat lens-shaped QDs over spherical dots to ellipsoidal and even pyramidal structures. The exact geometry depends on various growth parameters as e.g. growth temperature, lattice mismatch of the materials, crystallographic orientation of the substrate and many others.

A common aspect of all these QD geometries is, that the QDs are randomly distributed on the WL due to the self-organization process. Furthermore, fluctuations in composition and size lead to inhomogeneous ensembles of QDs. This can be important for the determination of optical properties, because as already discussed, the energetic position of the bound QD states depends on both size and composition of the QDs. Thus an inhomogeneously ensemble of QDs will also have an inhomogeneous ensemble of transition energies leading e.g. to a broadening of optical spectra. Even though QDs possess localized states that heavily depend on QD size and geometry, their properties are also strongly influenced by the properties of the related bulk materials like symmetry and crystallographic structure.

Part II

Many-Body Theory for semiconductor nanostructures

3 Many-body Theory

A fundamental difficulty that is shared by all branches of theoretical solid-state physics is the large number of atoms in a crystal, typically on the order of 10^{23} interacting atoms and electrons. As this makes a direct solution of the many-particle Schrödinger equation impossible for all practical purposes, we rely on more sophisticated methods to tackle complicated many-particle systems, such as highly excited semiconductors. It is for this very reason, that quantum field theoretical (QFT) methods, that originally have been developed in high energy physics for the theory of quantum electrodynamics (QED) [38, 39, 40] and quantum chromodynamics (QCD), have successfully been used in semiconductor physics for several decades. As we learn in a basic course on statistical mechanics, the central quantity from which all physical quantities of interest may be determined is the statistical operator. However, it turns out that we can avoid the explicit knowledge of the statistical operator by using QFT methods. Not only would the statistical operator for a system of 10^{23} particles be impossible to tackle numerically, but moreover it contains much more information than what is needed to calculate the relevant observables. Therefore a basic goal in the theory should be the elimination of unnecessary information. Whereas the many-particle Schrödinger equation is in principle exact, we will see in the following section that by using QFT methods, we always have to deal with approximate schemes, as the many-particle interaction will lead to the so called “hierarchy problem”. We will briefly review the foundations of many-body theory, such as is the hierarchy problem, and discuss various methods that have been used to address semiconductor many-body problems, some of which allow to handle arbitrary non-equilibrium conditions that e.g. are typical for optical excited semiconductors.

This part is organized as follows: First the Hamiltonian is defined and the hierarchy problem is introduced. In Chapter 4 the non-equilibrium Green's function (NGF) technique is described. We will introduce the diagrammatic representation of NGFs and the equations of motion for the single-particle NGFs, that are the Kadanoff-Baym equations. This theoretical framework will be used to calculated optical gain spectra for semiconductor QD systems and their properties in Part III. In Chapter 5, we will discuss the cluster expansion scheme as an alternative method to treat the many-body problem, that has seen a tremendous amount of applications over the past years and that will be used in Part IV to describe laser properties and photon statistics of QD laser devices. In the last chapter of this part we will introduce

alternative methods that are not directly used in this thesis but are briefly discussed for completeness and to give an overview on the broad spectrum of methods that is used to deal with many-body problems in semiconductors.

3.1 Hamiltonian and Heisenberg's equations of motion

In this section we will briefly review the basics of many-body theory, introduce the hierarchy problem, and use the opportunity to define our notations. As we are interested in optical properties of semiconductors, that are governed by the transitions between electronic states, we restrict our analysis to the system of electrons. The ions of the crystal lattice will be considered only so far that they determine the single-particle states and give rise to the carrier-phonon interaction.

To describe the dynamics of the electronic system we employ Heisenberg's equations of motion for Heisenberg picture field operators $\hat{\psi}_s(\mathbf{r}, t)$ in second quantization [41]

$$i\hbar \frac{d}{dt_1} \hat{\psi}_{s_1}(\mathbf{r}_1, t_1) = [\hat{H}, \hat{\psi}_{s_1}(\mathbf{r}_1, t_1)] . \quad (3.1)$$

Here $\hat{\psi}_{s_1}(\mathbf{r}_1, t_1)$ denotes the annihilation operator for an electron at position \mathbf{r}_1 and time t_1 with spin s_1 . To specify our system and the the interaction processes that we will take into account, we need to define the Hamiltonian that generates the time evolution of the field operators via (3.1).

As we set out to describe optically excited semiconductors we will consider the following Hamiltonian

$$\hat{H} = \hat{H}_0 + \hat{H}_D + \hat{H}_{\text{Coul}} \quad (3.2)$$

with

$$\hat{H}_0 = \sum_{s_1} \int d\mathbf{r}_1 \hat{\psi}^\dagger(1) h_0(1) \hat{\psi}(1) \quad (3.3)$$

$$\hat{H}_D = \sum_{s_1} \int d\mathbf{r}_1 \hat{\psi}^\dagger(1) \mathbf{dE}(1) \hat{\psi}(1) \quad (3.4)$$

$$\hat{H}_{\text{Coul}} = \frac{1}{2} \sum_{s_1} \sum_{s_2} \int d\mathbf{r}_1 \int d\mathbf{r}_2 \int dt_2 \hat{\psi}^\dagger(1) \hat{\psi}^\dagger(2) V(1, 2) \hat{\psi}(2) \hat{\psi}(1) . \quad (3.5)$$

It consists of the free carrier part \hat{H}_0 , the dipole interaction of carriers with a classical electromagnetic field \hat{H}_D , and of the Coulomb interaction among carriers \hat{H}_{Coul} . In

Eq. (3.2) we have introduced a compact notation for space coordinate, time, and spin

$$1 = \{\mathbf{r}_1, t_1, s_1\} \quad \int d1 = \sum_{s_1} \int d^3 r_1 \int dt_1 ,$$

and defined

$$V(1, 2) = V(|\mathbf{r}_1 - \mathbf{r}_2|) \delta(t_1 - t_2) \quad (3.6)$$

with

$$V(|\mathbf{r}_1 - \mathbf{r}_2|) = \frac{e^2}{4\pi\varepsilon_0\varepsilon_b |\mathbf{r}_1 - \mathbf{r}_2|} , \quad (3.7)$$

as well as

$$h_0(1) = -\frac{\hbar^2}{2m} \Delta + U(\mathbf{r}) . \quad (3.8)$$

The single-particle potential $U(\mathbf{r})$ describes the interaction of the electrons with the ion lattice. While in most parts of this thesis we will make simplifying assumption about the single-particle states, one should not forget that the microscopic determination of single-particle states is a field of research in its own. Of this we will make explicit use in Part V, where we will use single-particle states stemming from a microscopic theory. Furthermore, we approximated the interaction with a classical electromagnetic field according to Ref. [42] as $\mathbf{dE}(1)$ with $\mathbf{d} = e\mathbf{r}$.

At some points of the discussion it might be advantageous to transform the equations into a eigenfunction basis of the single-particle Hamiltonian h_0 ,

$$h_0 \phi_\nu(\mathbf{r}) = e_\nu \phi_\nu(\mathbf{r}) . \quad (3.9)$$

In such a basis the Hamiltonian reads

$$\hat{H} = \hat{H}_0 + \hat{H}_D + \hat{H}_{\text{Coul}} \quad (3.10)$$

with

$$\hat{H}_0 = \sum_\nu e_\nu \hat{a}_\nu^\dagger(t_1) \hat{a}_\nu(t_1) \quad (3.11)$$

$$\hat{H}_D = \sum_{\nu_1 \nu_2} \hat{a}_{\nu_1}^\dagger(t_1) [dE(t_1)]_{\nu_1 \nu_2} \hat{a}_{\nu_2}(t_1) \quad (3.12)$$

$$\hat{H}_{\text{Coul}} = \frac{1}{2} \sum_{\nu_1 \nu_2 \nu_3 \nu_4} \int dt_2 \hat{a}_{\nu_1}^\dagger(t_1) \hat{a}_{\nu_2}^\dagger(t_1) V_{\nu_1 \nu_2 \nu_3 \nu_4} \hat{a}_{\nu_3}(t_1) \hat{a}_{\nu_4}(t_1) . \quad (3.13)$$

The explicit form of the basis and the discussion of the matrix elements $[dE(t_1)]_{\nu_1 \nu_2}$ and $V_{\nu_1 \nu_2 \nu_3 \nu_4}$ will be given when discussing a specific model, so far we leave it completely general.

Though we will formulate most parts of the theory using the Coulomb interaction as an exemplary interaction process, this will not pose a problem when widening

our analysis to other important interaction mechanisms in semiconductors as e.g. the carrier-phonon interaction. The general principles discussed will also hold in these cases, as e.g. the Fröhlich interaction with LO-phonons can be cast into an effective (Coulomb-like) carrier-carrier interaction [43].

From the equations of motion (3.1) and the Hamilton operator (3.2) we can deduce the equations of motion (EOM) for the field operators

$$i\hbar \frac{\partial}{\partial t_1} \hat{\psi}(1) = [h_0(1) + \mathbf{d}\mathbf{E}(1)] \hat{\psi}(1) + \int d2 V(1,2) \hat{\psi}^\dagger(2) \hat{\psi}(2) \hat{\psi}(1) \quad (3.14)$$

$$-i\hbar \frac{\partial}{\partial t_1} \hat{\psi}^\dagger(1) = [h_0(1) + \mathbf{d}\mathbf{E}(1)] \hat{\psi}^\dagger(1) + \int d2 V(1,2) \hat{\psi}^\dagger(1) \hat{\psi}^\dagger(2) \hat{\psi}(2), \quad (3.15)$$

that will be used in the following to determine the dynamics of physical observables such as the single-particle density matrix.

3.2 Single-particle density matrix

Physical observables can be calculated upon knowledge of the statistical operator by tracing out the corresponding hermitian operator \hat{A} with the statistical operator $\hat{\rho}$,

$$\langle \hat{A} \rangle = \text{Tr}(\hat{\rho} \hat{A}). \quad (3.16)$$

For a study of the optical properties of semiconductors typically we are interested in carrier density and the polarization

$$n = \sum_{\alpha,\lambda} \langle \hat{a}_\alpha^{\lambda\dagger} \hat{a}_\alpha^\lambda \rangle \quad (3.17)$$

$$\mathbf{P} = \sum_{\lambda,\lambda'} \sum_{\alpha,\beta} \mathbf{d}_{\alpha\beta}^{\lambda,\lambda'} \langle \hat{a}_\alpha^{\lambda\dagger} \hat{a}_\beta^{\lambda'} \rangle. \quad (3.18)$$

Here we moved for convenience into a eigenfunction basis for a two-band semiconductor $|\lambda, \alpha\rangle$. In this notation the operators \hat{c}_α^λ carry a band index λ and an index that differentiate between states in the same band α . For examples in a translation invariant bulk-semiconductor α could be a quasi-momentum state \mathbf{k} .

For a calculation of such single-particle quantities, we can restrict the analysis to the reduced single particle density matrix (spdm) $\rho_{ij} = \langle \hat{a}_i^\dagger \hat{b}_j \rangle$, that is obtained from the full density operator by tracing out all other degrees of freedom. However, in later parts of the thesis we will also focus on many-particle correlation functions where we will have to reconsider this statement and its consequences.

If we can furthermore restrict our analysis to population functions and to polarization functions that are diagonal in α , we can write the spdm as

$$\rho_\alpha(t) = \begin{pmatrix} \langle \hat{c}_\alpha^\dagger \hat{c}_\alpha \rangle & \langle \hat{c}_\alpha^\dagger \hat{v}_\alpha \rangle \\ \langle \hat{v}_\alpha^\dagger \hat{c}_\alpha \rangle & \langle \hat{v}_\alpha^\dagger \hat{v}_\alpha \rangle \end{pmatrix} \equiv \begin{pmatrix} f_\alpha^c & \psi_\alpha \\ \psi_\alpha^* & f_\alpha^v \end{pmatrix}. \quad (3.19)$$

However, even though we have narrowed down the necessary information considerably from the full statistical operator to the spdm, a calculation of the elements of the spdm is far from trivial. As we can infer from the EOM for the field operators (3.14) the calculation of the EOM for the elements of the single particle density matrix leads to expectation values of higher order, e.g. the EOM for the two-operator expectation value which gives the population function f_α couples via the Coulomb interaction to four-operator expectation values and so forth. This poses an apparent difficulty and a variety of methods has been developed for the treatment of this so-called *hierarchy problem* that is inherently coupled to the appearance of many-particle parts in the Hamiltonian.

In the next chapter we will tackle the hierarchy problem using the nonequilibrium Green's functions method, while in Chapter 5 the cluster expansion method is introduced.

4 Theory of non-equilibrium Green's functions

From time ordering problems to the Kadanoff-Baym equations

In this chapter we will discuss the nonequilibrium Green's function (NGF) technique that has been developed as an generalization of the by then well known ground state Green's function (GF) theory by ground-breaking works of Schwinger, Martin, Kadanoff, Baym, Abrikosov, Keldysh and others, see Refs. [44, 45, 46, 47, 48]. We will start from the problem of time ordering in a general non-equilibrium situation, and show how a uniform time ordering may be achieved by means of the Keldysh time contour. Afterwards, we will derive a closed system of equations for the single-particle GF, that will be our starting point in Part III and in Part V to describe optical properties of semiconductor QD systems.

As we can only give a brief overview of the basic principles and ideas of this vast subject in the shortness of a thesis, we refer the interested reader to the review articles by Kadanoff and Baym [49], DuBois [50], Danielewicz [51], Korenman [52], Binder and Koch [53], Henneberger et al. [54, 55, 56, 57] and Rammer [58] and to the textbooks by Schäfer [59], Haug and Jauho [60], Landau [61] and Kremp et al. [62] as these are the sources from which most of the information found in this chapter are gathered.

4.1 Expectation values and time ordering

As we have shown in Chapter 3.2 any physical observable can be calculated as expectation values of the statistical operator [63]. Here one uses the relation

$$\langle \hat{A} \rangle = \text{tr} (\rho_S(t) \hat{A}_S) = \text{tr} (\rho_H \hat{A}_H(t)) , \quad (4.1)$$

where $\rho_{S,H}$ is the statistical operator either in the Schrödinger or in the Heisenberg representation [41]. One of the basic problems for practical applications is that

the statistical operator is only known for certain special cases that are mostly of little interest for practical purposes, like ideal quantum gases in thermal equilibrium. Nevertheless these case studies provide valuable insight in the basic mechanisms of quantum mechanics. The QFT description that we will give in the following chapters has the advantage that an explicit knowledge of the statistical operator is not needed.

For the following discussion, we introduce an additional time-dependent external source $\hat{H}_{\text{ext}}(t)$ to the Hamiltonian (3.2).

$$\hat{H}_{\text{full}} = \hat{H} + \hat{H}_{\text{ext}}(t) . \quad (4.2)$$

This external source serves a twofold purpose. One one hand it can represent external controlled charged, that generate the non-equilibrium situation in the many-body system. On the other hand, if no such external sources are present, we can use it as a mathematical trick to generate correlation functions, via functional derivative methods, meaning that we probe the reaction of the system to a small perturbation.

In the following we use an interaction representation [41, 64] that is defined according to the convention of Dubois [50]. The time evolution of the Operators will be given by \hat{H} whereas the states $|\phi(t)\rangle$ will evolve in time according to $\hat{H}_{\text{ext}}(t)$. The statistical operator is then given by $\rho(t) = |\phi(t)\rangle \langle \phi(t)|$

In the interaction representation the time evolution of an initial state can be described by the time evolution operator $S(t, t_0)$

$$|\phi(t)\rangle = S(t, t_0) |\phi(t_0)\rangle \quad \text{with} \quad S(t, t_0) = T e^{-\frac{i}{\hbar} \int_{t_0}^t \hat{H}_{\text{ext}}(\tilde{t}) d\tilde{t}} , \quad (4.3)$$

In this equation the exponential of the operator $\hat{H}_{\text{ext}}(t)$ is defined in the usual way by its power series. The time-ordering symbol T will arrange the operators in Eq. (4.3) with deceasing times from left to right (“late goes left”). As the field operators are of fermionic nature each commutation of two field operators will lead to a change of sign.

The time dependence of the operators is given by

$$\hat{A}_D(t) = U^\dagger(t, t_0) \hat{A}_S U(t, t_0) \quad \text{with} \quad U(t, t_0) = e^{-\frac{i}{\hbar} (\hat{H}_0 + \hat{H}_{\text{WW}})(t-t_0)} . \quad (4.4)$$

The time evolution operators $U(t, t_0)$ and $S(t, t_0)$ share two important properties: For both time evolution operators the semi-group property

$$U(t_1, t_2)U(t_2, t_3) = U(t_1, t_3) \quad S(t_1, t_2)S(t_2, t_3) = S(t_1, t_3), \quad (4.5)$$

holds. Furthermore we find

$$U(t_1, t_2) = U^\dagger(t_2, t_1) \quad S(t_1, t_2) = S^\dagger(t_2, t_1), \quad (4.6)$$

which states that the adjoint of the time evolution operators gives the propagation backwards in time.

With these properties of the time evolution operators in mind, we are able to formulate an equation for a general single particle expectation value with Eqs. (4.3) and (4.4) in the interaction representation. We find

$$\langle \hat{A}(t) \rangle = \text{Sp} \left\{ \rho_D S(t_0, \infty) T[S(\infty, t_0) \hat{A}_D(t)] \right\}, \quad (4.7)$$

where we also use the statistical operator ρ_D in the interaction representation. The expectation value (4.7) is composed of two parts. In the time-ordered part, the time ordering symbol T will break the S -operators according to the semi-group property and order them around \hat{A}_D . On the contrary the left part is anti time-ordered. Even though our use of QFT methods do not rely crucially on a uniform time ordering, we would like to achieve this, as otherwise the bookkeeping of time-ordered and anti time-ordered expectations values will be to cumbersome for practical purposes. Also a systematic approach in terms of a diagrammatic expansion as in the ground state theory [39], would be complicated otherwise.

For a system in its ground state at $T=0K$, this problem can be overcome by applying the theorem of Gell-Mann & Low [65], that enables us to rewrite the anti time-ordered part into a time-ordered part, as at $T=0K$ the anti time-ordered part of Eq. (4.7) can be shown only to give a phase-factor [66]. Also for elevated temperatures it is possible to achieve a uniform time ordering by means of the Matsubara technique [67, 66]. However, this technique relies on thermal equilibrium that is an rather unlikely situation for optically excited semiconductors that we intend to investigate.

4.2 The Keldysh Contour

Unlike in thermal equilibrium we can not establish a uniform time-ordering in the general non-equilibrium case. However, one should note, that the operators in Eq. (4.7) are time-ordered as shown in Figure 4.1. With this in mind we can solve the problem by artificially distinguishing between times t_+ and t_- on the upper and lower branch of the thereby introduced *Keldysh contour* \mathcal{C} . Now we can view the expectation value (4.7) as being time ordered, however not with respect to physical times but with respect to the times on the contour \mathcal{C} . This "trick" was introduced by Schwinger [68] and Keldysh [48] to be able to give a generalized time ordering under non-equilibrium conditions. To achieve this differentiation formally, we need to distinguish the external perturbation on the upper $\hat{H}_{ext}^+(t_+)$ and lower $\hat{H}_{ext}^-(t_-)$ branch of the contour \mathcal{C} .

On the Keldysh contour the expectation value (4.7) is time-ordered, provided that

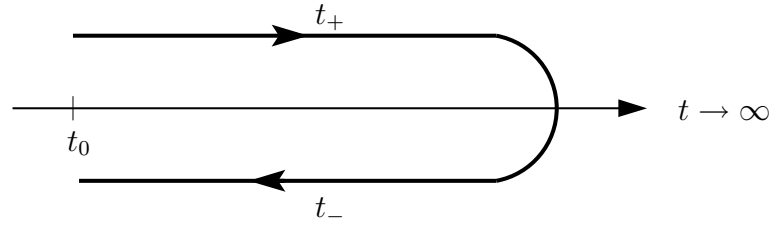


Figure 4.1: Keldysh time contour \mathcal{C} for the temporal evolution from the initial time t_0 to $t = \infty$ and back to t_0 . Translated into real times the upper branch t_+ is ordered chronologically while the lower branch t_- is ordered anti-chronologically.

we define times on the lower branch to be oppositely ordered and always later than times on the upper branch, even though they might correspond to the same *physical* time t .

A consequence of this formal differentiation is , that at the end of each calculation we have perform the "physical limit" and set $\hat{H}_{ext}^+(t_+) = \hat{H}_{ext}^-(t_-)$.

Taking this into account, we can specify the expectation value (4.1) analogous to (4.7) on the upper

$$\langle \hat{A}(t_+) \rangle = \frac{\text{Sp} \left\{ \rho_D S_-(t_0, \infty) T[S_+(\infty, t_0) \hat{A}_D(t_+)] \right\}}{\text{Sp} \{ \rho_D S_-(t_0, \infty) S_+(\infty, t_0) \}} \quad (4.8)$$

and lower

$$\langle \hat{A}(t_-) \rangle = \frac{\text{Sp} \left\{ \rho_D \tilde{T}[S_-(\infty, t_0) \hat{A}_D(t_-)] S_+(\infty, t_0) \right\}}{\text{Sp} \{ \rho_D S_-(t_0, \infty) S_+(\infty, t_0) \}} , \quad (4.9)$$

contour branch, respectively.

In this expression we also defined the S -operators on the Keldysh contour \mathcal{C}

$$\begin{aligned} S_{\pm}(\infty, t_0) &= T \exp \left(-\frac{i}{\hbar} \int_{t_0}^{\infty} d\tau_{\pm} \hat{H}_{ext}(\tau_{\pm}) \right) \\ S_{\pm}(t_0, \infty) &= \tilde{T} \exp \left(\frac{i}{\hbar} \int_{t_0}^{\infty} d\tau_{\pm} \hat{H}_{ext}(\tau_{\pm}) \right) = S_{\pm}^\dagger(\infty, t_0) . \end{aligned} \quad (4.10)$$

Here \tilde{T} is the anti-time ordering symbol that arranges later time arguments to the right. In the physical limit we recover

$$\text{Sp} \{ \rho_D S_-(t_0, \infty) S_+(\infty, t_0) \} = \text{Sp} \{ \rho_D \} = 1 , \quad (4.11)$$

so that the desired expectation values are generated.

To introduce a more compact notation, let us introduce time arguments on the Keldysh contour as $\underline{t} \in \mathcal{C}$. Furthermore we introduce a time ordering symbol $T_{\mathcal{C}}$ on the contour, that is equal to T on the upper and to \tilde{T} on the lower branch. In analogy to Eq. (4.3), we define S -operators on the contour

$$S_{\mathcal{C}} = T_{\mathcal{C}} \exp \left(-\frac{i}{\hbar} \int_{\mathcal{C}} d\underline{\tau} \hat{H}_{ext}(\underline{\tau}) \right), \quad (4.12)$$

where the integration over the contour is defined as

$$\int_{\mathcal{C}} = \eta_+ \int_+ + \eta_- \int_- = \int_+ - \int_- \quad (4.13)$$

with the contour indices η that are equal to $+1$ (-1) on the upper (lower) contour branch.

Using these definitions we can write the expectation value (4.1) as

$$\langle A(\underline{t}) \rangle_{\mathcal{C}} = \frac{\text{Sp} \left\{ \rho_D T_{\mathcal{C}} [S_{\mathcal{C}} \hat{A}_D(\underline{t})] \right\}}{\text{Sp} \{ \rho_D S_{\mathcal{C}} \}}. \quad (4.14)$$

The hereby achieved time ordering allows us to implement QFT methods like diagrammatic techniques for the general non-equilibrium case. We will further elaborate on that in what follows. However, we would like to point out, that the introduction of the contour is by no means necessary. One could alternatively directly work with the expectation values (4.8) and (4.9) and introduce different time orderings in these factors. In fact in Ref. [61] the theory is introduced precisely in that way. Nevertheless, we will use the contour in our argumentation as, to quote L.V. Keldysh directly on this matter "The contour, however, seems more spectacular" [69].

4.3 Green's functions in non-equilibrium

The concept of GFs, that one typically learns about in a course on electrodynamics [70], has been successfully carried over to QFT. In ground state theory [66], the definition of GFs is advantageous, as they allow for a easy calculation of single-particle expectation values, the determination of the total energy $\langle H \rangle$, and of the excitation spectrum of a many-body system [66, 67].

In complete analogy to the definition of the ground state GF, let us define a NGF on the Keldysh contour \mathcal{C} as

$$G(\underline{1}, \underline{2}) = -\frac{i}{\hbar} \left\langle \hat{\psi}(\underline{1}) \hat{\psi}^\dagger(\underline{2}) \right\rangle_c . \quad (4.15)$$

Here we have further compactified our notation by introducing $\underline{1} = \{\mathbf{r}_1, s_1, \underline{t}_1\}$ for space coordinate, spin and Keldysh time \underline{t} . Regarding the contour indices t_\pm the Keldysh-NGF (4.15) is a two-by-two matrix

$$G(\underline{1}, \underline{2}) = \begin{pmatrix} G(1_+, 2_+) & G(1_+, 2_-) \\ G(1_-, 2_+) & G(1_-, 2_-) \end{pmatrix} \xrightarrow{\text{phys. limit}} \begin{pmatrix} G(1, 2) & G^<(1, 2) \\ G^>(1, 2) & \tilde{G}(1, 2) \end{pmatrix} . \quad (4.16)$$

On the diagonal on the Keldysh matrix we find in the physical limit the time-ordered

$$G(1_+, 2_+) = -\frac{i}{\hbar} \langle T[\hat{\psi}(1_+) \hat{\psi}^\dagger(2_+)] \rangle \xrightarrow{\text{phys. limit}} G(1, 2) \quad (4.17)$$

and anti time-ordered

$$G(1_-, 2_-) = -\frac{i}{\hbar} \langle \tilde{T}[\hat{\psi}(1_-) \hat{\psi}^\dagger(2_-)] \rangle \xrightarrow{\text{phys. limit}} \tilde{G}(1, 2) \quad (4.18)$$

NGFs, respectively. In the non-diagonal elements

$$G(1_+, 2_-) = +\frac{i}{\hbar} \langle \hat{\psi}^\dagger(2_-) \hat{\psi}(1_+) \rangle \xrightarrow{\text{phys. limit}} G^<(1, 2) \quad (4.19)$$

$$G(1_-, 2_+) = -\frac{i}{\hbar} \langle \hat{\psi}(1_-) \hat{\psi}^\dagger(2_+) \rangle \xrightarrow{\text{phys. limit}} G^>(1, 2) , \quad (4.20)$$

one field operator has a time argument on the upper and one on the lower branch of the contour. We identify these quantities as the propagators of the system, that will play a key role in our description of dynamical processes.

To give an interpretation of the propagators let us note, that $G^>(1, 2)$ describes the probabilities that an electron is found at (\mathbf{r}_1, t_1, s_1) if an electron is brought into the system at (\mathbf{r}_2, t_2, s_2) . In that way $G^>$ can be thought of describing the electron propagation from 2 to 1. More importantly for our purposes however, $G^<$, taken at equal times, is proportional to the spdm of the system, hence kinetic properties such as population functions can be deduced [71]. Conversely, this also means, that we can interpret the propagators $G \gtrless$ as generalizations of the spdm, that also include temporal correlations.

From the propagators we can define additional NGFs that directly give important information about the physical system in question. The retarded and advanced GF, whose names are chosen according to their causality properties, are defined by

$$\begin{aligned} G^R(1, 2) &= +\Theta(t_1 - t_2) [G^>(1, 2) - G^<(1, 2)] \\ G^A(1, 2) &= -\Theta(t_2 - t_1) [G^>(1, 2) - G^<(1, 2)] , \end{aligned} \quad (4.21)$$

with the Heaviside step function $\Theta(t_1 - t_2)$. These GFs contain information about the excitation spectrum of the many-particle system. This can be most easily be

seen for the free retarded GF, that reads in a appropriate single-particle basis ϕ_ν (cf. Eq. (3.9))

$$G_\nu^r(t_1 - t_2) = -\frac{i}{\hbar} \Theta(t_1 - t_2) e^{-\frac{i}{\hbar} e_\nu(t_1 - t_2)} . \quad (4.22)$$

Its Fourier transform with respect to the relative time $t_1 - t_2$ can be written as [66]

$$G_\nu^r(\omega) = \frac{1}{\hbar\omega - e_\nu + i\delta} \quad \text{with} \quad \delta > 0 . \quad (4.23)$$

It shows a pole at the free single-particle energy e_ν . Alternatively we can look at the spectral function

$$\widehat{G}_\nu(\omega) = -2i\text{Im}G_\nu^R(\omega) \quad (4.24)$$

that has delta peaks at the free single-particle energies. In the interacting system we get

$$G_\nu^R(\omega) = \frac{1}{\hbar\omega + i\delta - e_\nu - \Sigma_\nu^R(\omega)} , \quad (4.25)$$

so that the selfenergy that we will define in Chapter 4.4 leads in the simplest case to energy renormalizations and to a broadening of the peaks in the spectral function. If the spectral function possesses a clear peak structure also in the interacting case, we can associate these peaks to so called quasi-particles. These are excitations of the interacting many-body system that behave like particles, but have a limited lifetime that is reflected by the broadening of the peaks in the spectral function.

Furthermore from the definition (4.21) we see, that retarded and advanced functions are directly related to the expectation value of the anti-commutator of the field operators.

After having defined several GFs, the question remains whether these GFs are independent from another. It turns out, that while in thermal equilibrium or in the ground state case one GF contains all relevant information, we need two independent GFs in the general non-equilibrium case. As we will need some of the relations between the elements of the NGF $G(1, 2)$ in what follows, we will summarize them here. By taking the hermitian adjoint of the field operators in G we find

$$\begin{aligned} [G^{\geqslant}(1, 2)]^* &= -G^{\leqslant}(2, 1) \\ [G^R(1, 2)]^* &= G^A(2, 1) , \end{aligned} \quad (4.26)$$

whereas

$$\begin{aligned} G(1, 2) &= G^R(1, 2) + G^<(1, 2) = G^A(1, 2) + G^>(1, 2) \\ \tilde{G}(1, 2) &= G^R(1, 2) + G^>(1, 2) = G^A(1, 2) + G^<(1, 2) \end{aligned} \quad (4.27)$$

can be shown simply by comparison of the definitions.

In what follows we will focus on G^R and $G^<$ that contain the excitation spectrum and the spdm, respectively. It is important to notice, that due to the matrix structure of the Keldysh GF a coupling between spectral and kinetic properties is directly evident.

4.4 Dynamics of the non-equilibrium Green's function

In this section we will derive the dynamics of the Keldysh matrix, and show how functional derivative techniques can be used to formally break the hierarchy. This procedure will lead to a closed set of equations for the elements of the Keldysh matrix.

For the following discussion it is advantageous to combine the influences of the single-particle Hamiltonians H_0 and H_D and to redefine

$$\begin{aligned} \hat{H} &= \hat{H}_{\text{SP}} + \hat{H}_{\text{Coul}} \\ \hat{H}_{\text{SP}} &= \sum_{s_1, \eta_1} \int dr_1 \hat{\psi}^\dagger(\underline{1}) h_0(\underline{1}) \hat{\psi}(\underline{1}) \\ \hat{H}_{\text{Coul}} &= \frac{1}{2} \sum_{s_1, s_2} \sum_{\eta_1, \eta_2} \int dr_1 \int dr_2 \int dt_2 \hat{\psi}^\dagger(\underline{1}) \hat{\psi}^\dagger(\underline{2}) V(\underline{1}, \underline{2}) \hat{\psi}(\underline{2}) \hat{\psi}(\underline{1}), \end{aligned} \quad (4.28)$$

as well as

$$V(\underline{1}, \underline{2}) = V(|\mathbf{r}_1 - \mathbf{r}_2|) \delta(t_1 - t_2) \delta_{\eta_1, \eta_2} \quad (4.29)$$

and

$$h_0(\underline{1}) = -\frac{\hbar^2}{2m} \Delta + U(\mathbf{r}) + \mathbf{d}\mathbf{E}(1). \quad (4.30)$$

Using (4.28) and (3.1) we can give Heisenberg's EOM for the field operators on the contour

$$i\hbar \frac{\partial}{\partial t_1} \hat{\psi}(\underline{1}) = h(\underline{1}) \hat{\psi}(\underline{1}) + \int d\underline{2} V(\underline{1}, \underline{2}) \hat{\psi}^\dagger(\underline{2}) \hat{\psi}(\underline{2}) \hat{\psi}(\underline{1}) \quad (4.31)$$

$$-i\hbar \frac{\partial}{\partial \underline{t}_1} \hat{\psi}^\dagger(\underline{1}) = h(\underline{1}) \hat{\psi}^\dagger(\underline{1}) + \int d\underline{2} V(\underline{1}, \underline{2}) \hat{\psi}^\dagger(\underline{1}) \hat{\psi}^\dagger(\underline{2}) \hat{\psi}(\underline{2}), \quad (4.32)$$

in complete analogy to Eq. (3.14).

As an external source we can allow for a general spatially and temporal non-local potential $U_{\text{ext}}(\underline{1}, \underline{2})$. However, that in most cases we will consider the limit $\underline{1} = \underline{2}$. Then we will identify it with a potential caused by an external charge density $\rho_{\text{ext}}(t)$,

$$\phi_{\text{ext}}(\mathbf{r}, \underline{t}) = \int d^3 r' \frac{e}{4\pi\varepsilon_0 |\mathbf{r} - \mathbf{r}'|} \rho_{\text{ext}}(\mathbf{r}, t), \quad (4.33)$$

that corresponds to the Hamiltonian

$$\begin{aligned}\hat{H}_{\text{ext}}(\underline{t}) &= \int d^3r \rho_{\text{ext}}(\mathbf{r}, t) \hat{\phi}(\mathbf{r}, \underline{t}) \\ \hat{\phi}(\underline{1}) &= \int d\underline{2} V(\underline{1}, \underline{2}) \hat{\psi}^\dagger(\underline{2}^+) \hat{\psi}(\underline{2}) ,\end{aligned}\tag{4.34}$$

The abbreviation $\underline{2}^+$, that is defined as

$$\underline{2}^+ = \{\mathbf{r}_2, s_2, \underline{t}_2 + \eta\delta\} \quad \text{with} \quad \delta > 0 ,\tag{4.35}$$

assures the correct time ordering, as it orders by definition the time \underline{t}_2^+ infinitesimal later on the contour.

Using Eqs. (4.15) and (4.31) we find for the EOM of the NGF

$$\begin{aligned}\left[i\hbar \frac{\partial}{\partial \underline{t}_1} - h(\underline{1}) + e\phi_{\text{ext}}(\underline{1}) \right] G(\underline{1}, \underline{2}) &= \delta(\underline{1} - \underline{2}) - \frac{i}{\hbar} e \left\langle \hat{\phi}(\underline{1}) \hat{\psi}(\underline{1}) \hat{\psi}^\dagger(\underline{2}) \right\rangle_c \\ &= \delta(\underline{1} - \underline{2}) - i\hbar \int d\underline{3} V(\underline{1}, \underline{3}) G_2(\underline{1}, \underline{3}; \underline{2}, \underline{3}^+) ,\end{aligned}\tag{4.36}$$

where

$$\delta(\underline{1} - \underline{2}) = \delta(1_{\eta_1}, 2_{\eta_2}) = \eta_1 \delta_{\eta_1, \eta_2} \delta(1, 2)\tag{4.37}$$

is a generalized delta function with the contour indices $\eta_{1,2}$. In the second line of Eq.(4.36) we introduced the two-particle GF

$$G_2(\underline{1}, \underline{2}; \underline{3}, \underline{4}) = \left(-\frac{i}{\hbar} \right)^2 \left\langle T_c \left[\hat{\psi}(\underline{1}) \hat{\psi}(\underline{2}) \hat{\psi}^\dagger(\underline{4}) \hat{\psi}^\dagger(\underline{3}) \right] \right\rangle .\tag{4.38}$$

At this point we explicitly see the hierarchy of EOMs. the single-particle GF couples to a two-particle GF G_2 , whose EOM will couple to a three-particle GF and so on. When formulated in terms of higher order GFs this is called the Martin-Schwinger hierarchy [62]. A systematic way to decouple the hierarchy is the functional derivative technique, introduced by Schwinger and others [44, 45, 49], that allows to generate a Dyson equation for the NGF and therefore to retain diagrammatic techniques known from ground-state theory.

4.4.1 Functional derivative technique and Dyson equation

The functional derivative technique allows to generate the answer of a given physical system to an external perturbation. Furthermore, it is possible to eliminate the two-particle GF from the EOM of the single-particle GF in Eq. (4.36) formally, and hence

overcome the hierarchy problem. However, we will only sketch the derivations here, referring the interested reader to Refs. [59, 53, 72, 62] for details.

Using the functional derivative of the NGF (4.15),

$$\begin{aligned} i\hbar e \frac{\delta G(\underline{1}, \underline{2})}{\delta \rho_{\text{ext}}(\underline{3})} &= -\frac{i}{\hbar} e \left\langle \hat{\phi}(3) \hat{\psi}(1) \hat{\psi}^\dagger(2) \right\rangle_c - e \left\langle \hat{\phi}(3) \right\rangle_c G(\underline{1}, \underline{2}) \\ &= -i\hbar \int d\underline{4} V(\underline{3}, \underline{4}) G_2(\underline{1}, \underline{4}; \underline{2}, \underline{4}^+) - e \left\langle \hat{\phi}(3) \right\rangle_c G(\underline{1}, \underline{2}), \end{aligned} \quad (4.39)$$

we can cast the EOM in the form

$$\left[i\hbar \frac{\partial}{\partial t_1} - h(\underline{1}) - e\hat{\phi}_{\text{eff}}(\underline{1}) \right] G(\underline{1}, \underline{2}) = \delta(\underline{1} - \underline{2}) + i\hbar e \frac{\delta G(\underline{1}, \underline{2})}{\delta \rho_{\text{ext}}(\underline{1})}. \quad (4.40)$$

Here we additionally defined an effective potential

$$\hat{\phi}_{\text{eff}}(\underline{1}) = \phi_{\text{ext}}(\underline{1}) + \left\langle \hat{\phi}(\underline{1}) \right\rangle_c, \quad (4.41)$$

that consists of the external potential and of the Hartree-potential

$$\left\langle \hat{\phi}(\underline{1}) \right\rangle_c = -i\hbar \int d\underline{3} V(\underline{1}, \underline{3}) \hat{\psi}^\dagger(\underline{3}^+) \hat{\psi}(\underline{3}) = -i\hbar \int d\underline{3} V(\underline{1}, \underline{3}) G(\underline{3}, \underline{3}^+). \quad (4.42)$$

The latter corresponds to the electrostatic mean-field interaction of a carrier with all other carriers. We will elaborate further on the Hartree-interaction in Section 9.1.

At this point, we can formally introduce the selfenergy via

$$i\hbar e \frac{\delta G(\underline{1}, \underline{2})}{\delta \rho_{\text{ext}}(\underline{1})} = \int d\underline{3} \Sigma(\underline{1}, \underline{3}) G(\underline{3}, \underline{2}). \quad (4.43)$$

For the further discussion it is advantageous to define an inverse GF that fulfills

$$\int d\underline{3} G^{-1}(\underline{1}, \underline{3}) G(\underline{3}, \underline{2}) = \int d\underline{3} G(\underline{1}, \underline{3}) G^{-1}(\underline{3}, \underline{2}) = \delta(\underline{1} - \underline{2}). \quad (4.44)$$

In the absence of interaction we can directly specify the free inverse GF

$$G_0^{-1}(\underline{1}, \underline{2}) = \left[i\hbar \frac{\partial}{\partial t_1} - h(\underline{1}) - e\hat{\phi}_{\text{eff}}(\underline{1}) \right], \quad (4.45)$$

that fullfills the EOM

$$\left[i\hbar \frac{\partial}{\partial t_1} - h(\underline{1}) - e\hat{\phi}_{\text{eff}}(\underline{1}) \right] G_0(\underline{1}, \underline{2}) = \delta(\underline{1} - \underline{2}). \quad (4.46)$$

These definitions can be used to cast the EOM (4.40), into the form

$$G(\underline{1}, \underline{2}) = G_0(\underline{1}, \underline{2}) + \int d\underline{3} \int d\underline{4} G_0(\underline{1}, \underline{3}) \Sigma(\underline{3}, \underline{4}) G(\underline{4}, \underline{2}), \quad (4.47)$$

that resembles the Dyson equation, known from ground state theory. However, we have to remember that all times are defined on the Keldysh contour.

4.4.2 Screened Coulomb interaction and vertex function

Following similar steps as in the last section, we can give an expressions for the self-energy by means of repeated applications of the chain rule. For the further discussion it is useful to define the vertex function

$$\Gamma(\underline{1}, \underline{2}, \underline{3}) = -i\hbar e \frac{\delta G^{-1}(\underline{1}, \underline{2})}{\delta \hat{\phi}_{\text{eff}}(\underline{3})} \quad (4.48)$$

and the GF of the screened Coulomb interaction

$$\begin{aligned} W(\underline{1}, \underline{2}) &= \int d\underline{3} V(\underline{1}, \underline{3}) \varepsilon^{-1}(\underline{2}, \underline{3}) \quad \text{with} \quad \varepsilon^{-1}(\underline{2}, \underline{3}) = \frac{\delta \hat{\phi}_{\text{eff}}(\underline{2})}{\delta \phi_{\text{ext}}(\underline{3})} \\ &= \frac{\delta \hat{\phi}_{\text{eff}}(\underline{1})}{\delta \rho_{\text{ext}}(\underline{2})}. \end{aligned} \quad (4.49)$$

The latter has an immediate physical interpretation. As we can infer from the last line of Eq. (4.49), it describes a change of the effective potential as a reaction of a change in the external source. Using these definitions we find for the selfenergy

$$\Sigma(\underline{1}, \underline{2}) = \int d\underline{3} \int d\underline{4} G(\underline{1}, \underline{3}) \Gamma(\underline{3}, \underline{2}, \underline{4}) W(\underline{4}, \underline{1}). \quad (4.50)$$

Following an analogous derivation that lead to the Dyson equation for the carrier GF in the last section, we find a Dyson equation for the screened interaction

$$W(\underline{1}, \underline{2}) = V(\underline{1}, \underline{2}) + \int d\underline{3} \int d\underline{4} V(\underline{1}, \underline{3}) P(\underline{3}, \underline{4}) W(\underline{4}, \underline{2}). \quad (4.51)$$

Here the role of the selfenergy is played by the polarization function

$$P(\underline{1}, \underline{2}) = -i\hbar \frac{\delta G(\underline{1}, \underline{1}^+)}{\delta \hat{\phi}_{\text{eff}}(\underline{2})}, \quad (4.52)$$

that via the chain rule we can express as

$$P(\underline{1}, \underline{2}) = \int d\underline{3} \int d\underline{4} G(\underline{1}, \underline{3}) \Gamma(\underline{3}, \underline{4}, \underline{2}) G(\underline{4}, \underline{1}). \quad (4.53)$$

Analogous to the screened potential itself we can give a direct physical interpretation of the polarization function, as it describes the change of the average charge density¹ via an effective potential.

Further application of the chain rule leads to an equation for the vertex function

$$\begin{aligned} \Gamma(\underline{1}, \underline{2}, \underline{3}) &= i\hbar e^2 \delta(\underline{1} - \underline{2}) \delta(\underline{1} - \underline{3}) \\ &+ \int d\underline{4} \int d\underline{5} \int d\underline{6} \int d\underline{7} \frac{\delta \Sigma(\underline{1}, \underline{2})}{\delta G(\underline{4}, \underline{5})} G(\underline{4}, \underline{6}) \Gamma(\underline{6}, \underline{7}, \underline{3}) G(\underline{7}, \underline{5}). \end{aligned} \quad (4.54)$$

¹proportional to $G(\underline{1}, \underline{1}^+)$

4.4.3 Fundamental system of equations

The equations from the preceding two sections form the fundamental system of equations:

Dyson equations

$$G(\underline{1}, \underline{2}) = G_0(\underline{1}, \underline{2}) + \int d\underline{3} \int d\underline{4} G_0(\underline{1}, \underline{3}) \Sigma(\underline{3}, \underline{4}) G(\underline{4}, \underline{2}), \quad (4.55)$$

$$W(\underline{1}, \underline{2}) = V(\underline{1}, \underline{2}) + \int d\underline{3} \int d\underline{4} V(\underline{1}, \underline{3}) P(\underline{3}, \underline{4}) W(\underline{4}, \underline{2}); \quad (4.56)$$

Selfenergy and polarization function

$$\Sigma(\underline{1}, \underline{2}) = \int d\underline{3} \int d\underline{4} G(\underline{1}, \underline{3}) \Gamma(\underline{3}, \underline{2}, \underline{4}) W(\underline{4}, \underline{1}), \quad (4.57)$$

$$P(\underline{1}, \underline{2}) = \int d\underline{3} \int d\underline{4} G(\underline{1}, \underline{3}) \Gamma(\underline{3}, \underline{4}, \underline{2}) G(\underline{4}, \underline{1}); \quad (4.58)$$

Vertex function

$$\begin{aligned} \Gamma(\underline{1}, \underline{2}, \underline{3}) &= i\hbar\delta(\underline{1} - \underline{2})\delta(\underline{1} - \underline{3}) \\ &+ \int d\underline{4} \int d\underline{5} \int d\underline{6} \int d\underline{7} \frac{\delta\Sigma(\underline{1}, \underline{2})}{\delta G(\underline{4}, \underline{5})} G(\underline{4}, \underline{6}) \Gamma(\underline{6}, \underline{7}, \underline{3}) G(\underline{7}, \underline{5}). \end{aligned} \quad (4.59)$$

The fundamental system of equations (4.55)-(4.59) is known from diagram technique [66], only that all time arguments are defined on the Keldysh contour. If we translate this system of equations via the Feynman rules [67] into an diagrammatic technique on the Keldysh contour, we get the diagrammatic system of equations that is shown in Figure 4.2.

Eqs.(4.55)-(4.59) are formally a closed system of equations for the GFs G and W , the selfenergies Σ and P and for the vertex function Γ . Whereas in these equations there is no apparent hierarchy problem, we instead rely on adequate approximate solutions for the selfenergies or for the vertex function. However, we have the advantage that systematic approximate schemes are available from ground state diagram technique.

In principle two approaches are possible. Using the simplest expression for the vertex function, $\frac{\delta\Sigma(\underline{1}, \underline{2})}{\delta G(\underline{4}, \underline{5})} = 0$, we could iterate the system of equations (4.55)-(4.59). Thereby we generate a perturbation series that needs to be truncated at a certain order.

However, this method has several pitfalls. Non-perturbative phenomena like bound states, can not be described by such an approach.

Alternatively, one can provide an expression for the vertex function (or approximate equation (4.59)) and solve the system of equations selfconsistently. This has the advantage, that all interaction processes that are described by the selfenergy of choice are included in the calculation non-perturbatively up to infinite order. However,

$$1 \xrightarrow{\quad} 2 = 1 \xrightarrow{\quad} 2 + 1 \xrightarrow{\quad} \underset{\Sigma}{\circlearrowleft} \xrightarrow{\quad} 2 \quad \text{a) (4.55)',}$$

$$1 \rightsquigarrow 2 = 1 \rightsquigarrow 2 + 1 \rightsquigarrow \underset{P}{\square} \xrightarrow{\quad} 2 \quad \text{b) (4.56)',}$$

$$\underset{\Sigma}{\circlearrowleft} \cdot \underset{P}{\square} \cdot = \underset{\Sigma}{\circlearrowleft} \underset{P}{\square} \cdot \quad \text{c) (4.57)',}$$

$$\underset{P}{\square} \cdot = \underset{P}{\square} \underset{\Sigma}{\circlearrowleft} \cdot \quad \text{d) (4.58)',}$$

$$\underset{\Gamma}{\triangleright} \cdot = \underset{\Gamma}{\bullet} + \underset{\delta G}{\boxed{\delta \Sigma}} \underset{\Gamma}{\triangleright} \cdot \quad \text{e) (4.59)',}$$

Figure 4.2: Diagrammatic representation of the fundamental system of equations

- (a) Dyson equation for carriers,
- (b) Dyson equation for the screened interaction,
- (c) Carrier selfenergy,
- (d) Polarization function,
- (e) Vertex function.

there might be processes that contribute in lower order but are not described by the chosen selfenergy. As those processes are disregarded completely, one relies on good approximation schemes. In principle the choices of P and Σ are not to be made independently. As it was shown in Ref. [73], the vertex function used in Eq. (4.58) for the polarization function needs to be computed from the selfenergy of choice. We will elaborate on those consistency problems in Section 9.2.1.

4.5 Kadanoff-Baym equations

In the preceding sections we developed the theory on the Keldysh contour \mathcal{C} . This was necessary to ensure the time ordering of operators. To return to equations for physical quantities we use the Langreth-Wilkins theorems [71], that allow to generate equations for the elements of the Keldysh matrix by choosing the contour indices in the Dyson equations (4.55)-(4.56) appropriately.

4.5.1 Langreth-Wilkins theorems

The integrations in the Dyson equations splits into integrations on the upper and lower contour branch via

$$\int_{\mathcal{C}} dt = \int_{-\infty}^{\infty} dt_+ - \int_{-\infty}^{\infty} dt_- . \quad (4.60)$$

To evaluate expressions of the kind

$$X(1,2) = \int d3 A(1,3) B(3,2) , \quad (4.61)$$

we can use the definitions of retarded and advanced GFs, and find after a short calculation (see Ref. [71])

$$\begin{aligned} X(1,2)^< &= \int d3 [A^R(1,3)B^<(3,2) + A^<(1,3)B^A(3,2)] \\ X(1,2)^> &= \int d3 [A^R(1,3)B^>(3,2) + A^>(1,3)B^A(3,2)] \\ X(1,2)^R &= \int d3 A^R(1,3) B^R(3,2) \\ X(1,2)^A &= \int d3 A^A(1,3) B^A(3,2) . \end{aligned} \quad (4.62)$$

These relations allow for a direct translation of the Dyson equations into equations for the retarded and advanced GF as well as for the propagators $G^<$ and $G^>$. However, we have to keep in mind that this translation via the Langreth-Wilkins theorems only works if we have a matrix structure as in Eq. (4.61). This will not be the case, e.g. for selfenergies that we will have to evaluate in Chapter 9 and more care has to be taken there.

4.5.2 Kadanoff-Baym equations

Via application of G_0^{-1} on (4.55) and using the Langreth-Wilkins theorems (4.62), we find the Kadanoff-Baym equations (KBE), that are coupled equations for spectral (G^r, G^a) and kinetic ($G^<, G^>$) properties of the system under investigation.

First Kadanoff-Baym equations:

$$\int d\mathbf{3} [G_0^{-1}(1, 3) - \Sigma^R(1, 3)] G^R(3, 2) = \delta(1, 2) \quad (4.63)$$

$$\int d\mathbf{3} \left\{ [G_0^{-1}(1, 3) - \Sigma^R(1, 3)] G^<(3, 2) - \Sigma^<(1, 3) G^A(3, 2) \right\} = 0 . \quad (4.64)$$

Second Kadanoff-Baym equations:

$$\int d\mathbf{3} G^A(1, 3) [G_0^{-1}(3, 2) - \Sigma^A(3, 2)] = \delta(1, 2) \quad (4.65)$$

$$\int d\mathbf{3} G^<(1, 3) \left\{ [G_0^{-1}(3, 2) - \Sigma^A(3, 2)] - G^R(1, 3) \Sigma^<(3, 2) \right\} = 0 . \quad (4.66)$$

In the second KBE the time derivative, contained in G_0^{-1} , has to be understood as acting to the left.

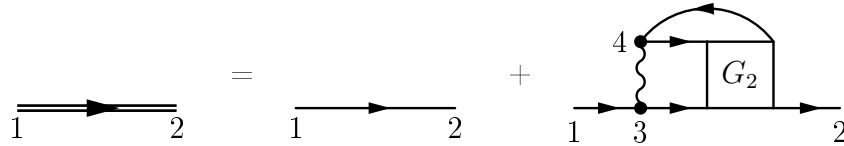
As shown in Chapter 4.3, the Keldysh matrix (4.16) contains only two independent elements. We will concentrate on the lesser and the retarded GFs as the lesser GF $G^<$ is connected to the spdm and the retarded GF G^R is connected to the quasi-particle spectrum, as discussed above.

4.6 Martin-Schwinger hierarchy

A different approach for calculating the single-particle GF is to directly solve Eq. (4.36). With the definition of the two-particle GF (4.38), we can write the Dyson equation as

$$G(\underline{1}, \underline{2}) = G_0(\underline{1}, \underline{2}) + \int d\underline{3} \int d\underline{4} G_0(\underline{1}, \underline{3}) V(\underline{3}, \underline{4}) G_2(\underline{3}, \underline{4}; \underline{2}, \underline{4}^+) , \quad (4.67)$$

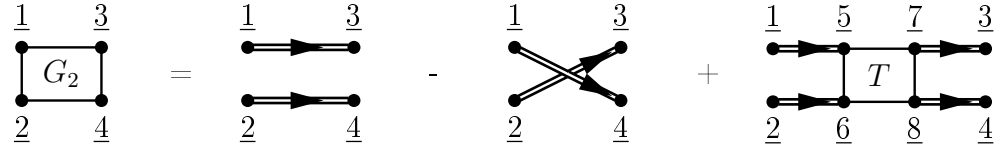
whose diagrammatic representation is shown in Figure 4.3. Here, the two-particle GF G_2 has to be calculated. This approach is followed in e.g. Ref. [74]. The advantage of this approach lies in the fact, that 2-particle correlations are directly included via G_2 . However, it faces the fundamental problem of the hierarchy that is given here in terms of GFs.


 Figure 4.3: G_2 Dyson equation; diagrammatic representation of (4.36)

To distinguish between effective single-particle renormalizations and true correlations, one can write the two-particle GF as

$$G_2(\underline{1}, \underline{2}; \underline{3}, \underline{4}) = G(\underline{1}, \underline{3}) G(\underline{2}, \underline{4}) - G(\underline{1}, \underline{4}) G(\underline{2}, \underline{3}) + G(\underline{1}, \underline{5}) G(\underline{2}, \underline{6}) T(\underline{5}, \underline{6}; \underline{7}, \underline{8}) G(\underline{7}, \underline{3}) G(\underline{8}, \underline{4}), \quad (4.68)$$

where we defined the T -matrix $T(\underline{5}, \underline{6}; \underline{7}, \underline{8})$. The diagrammatic representation of this equation is given in Figure 4.4.


 Figure 4.4: Diagrammatic representation of the connection between G_2 and the T -matrix .

4.7 Reduction to single-time propagators (generalized Kadanoff-Baym ansatz)

As two-time calculation are tremendously demanding numerically, the direct solution is only possible for short time intervals. For example in [75] the two-time quantum kinetics due to interaction with LO-phonons after pulse excitation has been studied up to times of about 1.5 picoseconds and in [76] Coulomb quantum-kinetics was studied up to several hundred femtoseconds. For larger times we therefore rely on approximate schemes that prevent the necessity of calculating the full two-time information.

As the spdm that describes the relevant observables of our system is contained on the time diagonal of the two-time propagators G^{\gtrless} , we would like to restrict our analysis to those propagators only. As it was shown in Ref. [77] by Lipavsky et al. and later re-derived by Tso et al. in Ref. [78], the propagators $G^{\gtrless}(t_1, t_2)$ can be reconstructed anywhere in the two time plane from their time diagonal elements $G^{\gtrless}(t, t)$ by an

iterative procedure using the exact identity

$$\begin{aligned}
 G^{\gtrless}(t_1, t_2) = & i\hbar \left[G^R(t_1, t_2) G^{\gtrless}(t_2, t_1) - G^{\gtrless}(t_1, t_1) G^A(t_1, t_2) \right] \\
 & + \Theta(t_1 - t_2) \int_{t_2}^{t_1} dt_3 \int_{-\infty}^{t_2} dt_4 \\
 & \times G^R(t_1, t_3) [\Sigma^R(t_3, t_4) G^{\gtrless}(t_4, t_2) + \Sigma^{\gtrless}(t_3, t_4) G^A(t_4, t_3)] \\
 & + \Theta(t_2 - t_1) \int_{t_1}^{t_2} dt_3 \int_{-\infty}^{t_1} dt_4 \\
 & \times [G^{\gtrless}(t_1, t_4) \Sigma^A(t_4, t_3) + G^R(t_1, t_4) \Sigma^{\gtrless}(t_4, t_3)] G^A(t_3, t_2) .
 \end{aligned} \tag{4.69}$$

The generalized Kadanoff-Baym ansatz (GKBA) corresponds to using only the zeroth order term,

$$G^{\gtrless}(t_1, t_2) = i\hbar [G^R(t_1, t_2) G^{\gtrless}(t_2, t_1) - G^{\gtrless}(t_1, t_1) G^A(t_1, t_2)] , \tag{4.70}$$

that is exact in the non-interacting case. This means that the assumption of the GKBA corresponds to the assumption of a weak interaction, that results in a dominant contribution of the elements from the time diagonal. For a detailed discussion of the different timescales involved, we refer the reader to Refs. [79, 80, 81, 82]. It should be noted that this approximation does not prevent a calculation of the two-time retarded and advanced GFs. However, here simplifying approximations are possible, some of which we will discuss in Part III.

The mapping in Eq. (4.70) is by no means unambiguous, as pointed out in Ref. [59]. The particular choice in Eq. (4.70) is guided by the causality properties of the retarded and advanced GFs, and the idea of obtaining a maximum of retardation and correlation effects. Alternatively, we could interchange G^R and G^A to obtain an ansatz that yields a minimum of retardation effects, an ansatz that actually results in the Markov approximation.

Physically, the ansatz (4.70) means that the quasi-particles will be described by a single population function, how extended in frequency space the quasi-particles might be. This can lead to a failure of the GKBA under certain conditions. For example it was shown in Ref. [75], that for the interaction with LO-phonons, the GKBA fails to provide a proper thermalization for material systems with intermediate polar coupling strength (cf. Chapter 10). Here one cannot circumvent a full two-time solution of the KBE with an appropriate choice of the selfenergy.

5 Cluster expansion method

From Heisenberg's equations of motion to a systematic truncation of the hierarchy

In this chapter we will treat an alternative method to the NGF approach to tackle the hierarchy problem. This method has seen a lot of applications in semiconductor physics during the past ten years, mostly in conjunction with problems concerning a quantized light field [83, 84, 85, 86, 87, 88]. The cluster expansion scheme was developed by J. Fricke in Refs. [89, 90] and a review concerning semiconductor optics can be found in Ref. [91].

Let us start by noting that the simplest way of truncating the hierarchy at a certain order is to factorize an expectation value containing $2N$ carrier into all possible combinations of two-operator expectation values. This resembles the result of Wick's theorem [92], that holds at zero temperature. On the four-operator level this corresponds to the Hartree-Fock like factorization

$$\langle \hat{a}_1^\dagger \hat{a}_2^\dagger \hat{a}_3 \hat{a}_4 \rangle = \langle \hat{a}_1^\dagger \hat{a}_3 \rangle \langle \hat{a}_2^\dagger \hat{a}_4 \rangle - \langle \hat{a}_1^\dagger \hat{a}_4 \rangle \langle \hat{a}_2^\dagger \hat{a}_3 \rangle . \quad (5.1)$$

However, such a scheme is not treating correlations between particles in a systematic way and hence we rely on a better factorization scheme that we will discuss below.

5.1 Factorization scheme

Using Heisenberg's equations of motion together with the Hamiltonian of the interacting system, we obtain the time evolution of the carrier and photon operators. From this coupled equations for operator averages, like the spdm, are derived. As each operator average contains a certain number of operators, that corresponds to a certain number of particles involved, we can classify occurring operator averages into singlets, doublets, triplets, quadruplets, etc., according to the number of particles they involve. Note, that for an application of the cluster expansion method to the carrier-phonon or the carrier-photon interaction, one has to take into account that photon or phonon operators correspond to two carrier operators (for their classification in the hierarchy), as we can infer by means of adiabatic elimination, see

e.g. [93, 88, 94]. This fact is used to classify mixed expectation values with photon and carrier operators. For example, the electron population $f_\nu^e = \langle c_\nu^\dagger c_\nu \rangle$ is a singlet contribution, while operator averages like $\langle c_\alpha^\dagger v_\alpha v_\nu^\dagger c_\nu \rangle$ and $\langle b_q^\dagger v_\nu^\dagger c_\nu \rangle$ are doublet terms.

In the following, N -particle averages, schematically denoted as $\langle N \rangle$ and containing $2N$ carrier operators or an equivalent replacement of photon or phonon operators, are factorized into all possible combinations of averages involving one up to $N-1$ particle averages. For the difference between the full operator average and this factorization, we introduce a correlation function of order N , denoted as $\delta\langle N \rangle$. Schematically the factorization of singlets, doublets, triplets, and quadruplets is given by

$$\langle 1 \rangle = \delta\langle 1 \rangle , \quad (5.2a)$$

$$\langle 2 \rangle = \langle 1 \rangle \langle 1 \rangle + \delta\langle 2 \rangle , \quad (5.2b)$$

$$\langle 3 \rangle = \langle 1 \rangle \langle 1 \rangle \langle 1 \rangle + \langle 1 \rangle \delta\langle 2 \rangle + \delta\langle 3 \rangle , \quad (5.2c)$$

$$\begin{aligned} \langle 4 \rangle = & \langle 1 \rangle \langle 1 \rangle \langle 1 \rangle \langle 1 \rangle + \langle 1 \rangle \langle 1 \rangle \delta\langle 2 \rangle \\ & + \langle 1 \rangle \delta\langle 3 \rangle + \delta\langle 2 \rangle \delta\langle 2 \rangle + \delta\langle 4 \rangle . \end{aligned} \quad (5.2d)$$

In the last equation, the first four terms on the right hand side represent all possible combinations of singlets, singlets and doublets, singlets and triplets, and doublets, respectively. The last term is the remaining quadruplet correlation function. Continuing the series (5.2a)–(5.2d) leads to quintuplet terms and so on. Note that singlets cannot be factorized any further.

5.2 Cluster expansion truncation scheme

From Heisenberg's equations of motion an infinite hierarchy arises due to the two-particle parts of the Hamiltonian, here the Coulomb and the light-matter interaction. The essential idea of what has become known as the *cluster expansion method* [89, 90] is to replace all occurring operator expectation values $\langle N \rangle$ according to Eqs. (5.2). Hereby equations of motion for the correlation functions $\delta\langle N \rangle$ rather than for the operator averages themselves are obtained. Then if a truncation is performed, this leads to a truncation of the hierarchy of correlation functions rather than the hierarchy of expectation values. In contrast to the EOM technique this approach consistently includes all collision terms as well as energy renormalizations of higher correlation functions up to N th order. Alternatively, also a diagram technique is available [89, 90]. This truncation procedure has been used to describe the luminescence dynamics of quantum wells [83, 85] and QDs [95, 88, 87]. If the hierarchy is truncated at the level of two-particle correlation functions, the so-called semiconductor luminescence equations (SLE) for the coupled carrier and photon populations emerge, which consistently include correlations up to the doublet level.

However, as all approximate schemes also this one reveals some caveats. At the last level of the hierarchy that is taken into account, renormalization effects like dephasing, energy shifts, and screening are not included consistently, as the corresponding contributions would stem from one level higher in the hierarchy.

In the following section we will discuss alternative methods, that are used in the literature to deal with optical properties of semiconductor systems, but that are not used directly in this thesis.

6 Alternative methods

Alternatively to the NGF method and the cluster expansion scheme, two prominent methods exist in literature to describe optical properties of semiconductors. For the situation where one is interested in coherent effects only, Axt et al. [96, 97] developed the dynamics-controlled truncation scheme (DCT) which consistently takes into account all coherent correlations up to N -th order in the optical field. Here effects are classified into $\chi^{(n)}$ regimes, i.e. into effects where the optical light field contributes in n -th order. Then, the truncation is performed at a certain $\chi^{(n)}$, whereas effects of the Coulomb interaction are fully taken into account without any truncation. However, one should note, that this method only works in the coherent regime. As soon as incoherent population effects come into play the DCT formalism breaks down. This scheme was successfully applied to describe the coherent dynamics, e.g. in four-wave-mixing (FWM) experiments [98, 99, 100]. However, including consistently incoherent effects like carrier scattering is difficult. The DCT equations can also be recovered from a NGF technique as a limiting case [101, 100], even though a different approximation scheme not relying on self-energies and a dyson equation is used there [100].

A further approach is given by the *cumulant expansion* method or *linked cluster expansion* scheme [102]. This approach has been used to calculate optical spectra of QD systems and dephasing due to interaction with acoustic phonons in the low temperature regime [103, 104, 105, 106, 107]. The basic idea consists of performing a series expansion for $\ln G$ instead of the GF G itself, which means that by taking the exponent to recover G , diagrams that can be factorized are automatically taken into account. The idea of this approach is adopted from basic statistical mechanics, where it turns out to be advantageous to perform calculation using the grandcanonical potential $\Omega(T, V, \mu) = -kT \ln Z(T, V, \mu)$ instead of the partition function Z .

With these short remarks about alternative methods we would like to conclude our survey of many-body methods in semiconductor physics. It goes without saying, that we could only give those results and derivations that are directly relevant to the work in this thesis, as a complete description of possible treatments of many-body interactions would clearly be beyond the scope of even a normal sized textbook. Nevertheless, we hope that we could convey the basic ideas and principles that the various methods share as well as those in which they differ. The remaining parts of this thesis will be devoted to the application of the schemes presented in this part to

optical properties of semiconductor QD systems.

Part III

Optical properties and dephasing mechanisms in Quantum Dots

A common aspect both in fundamental studies and practical applications of QDs is the critical role of dephasing processes. They determine the homogeneous linewidth of the QD resonances, limit the coherence properties of QD lasers as well as their ultrafast emission dynamics, and have a strong influence on coherent optical nonlinearities. Moreover, dephasing processes are intimately linked to lineshifts of the QD resonances. As it presently is the standard material system for QD research, we will focus in this part of the thesis on QDs in the InGaAs material system.

For the interaction of QD carriers with LA-phonons, extensive work has been devoted to studies of the low temperature regime of dephasing [103, 108, 104, 105, 106, 107], and its influence in Rabi-oscillations [109, 110] in QDs. Also QD molecules, i.e. QDs vertically or horizontally stacked, have been investigated in the low temperature regime [111, 112]. It is generally acknowledged that acoustic phonons dominate the dephasing at low temperatures. However, in Refs. [113, 114, 115, 116] it was suggested that for temperatures above 100K the dephasing due to carrier-LO-phonon interaction is of growing importance. The interaction of QD carriers with LO phonons is strongly influenced by hybridization effects [117], which require the application of the polaron picture. A quantum-kinetic description of carrier-phonon scattering based on polarons has been used in our group to explain ultrafast carrier capture and relaxation processes in QDs [118]. At elevated temperature and carrier densities, being relevant for application in QD laser devices, we can restrict our analysis to dephasing due to carrier-carrier Coulomb and carrier-LO-phonon interaction.

Theoretical studies of absorption and gain in QDs at elevated temperatures and carrier densities have been performed on the basis of multilevel optical Bloch equations [119], stochastic equations [120], or semiconductor Bloch equations with screened exchange and Coulomb hole contributions [121]. However, a serious weakness of both atom-like and screened Hartree-Fock treatments is the phenomenological description of scattering effects with an effective relaxation time approximation. Not only is the predictive capability severely compromised by assuming the dephasing rate as a phenomenological parameter via a T_2 -time, but experimental spectral shapes are not accurately reproduced. Furthermore, unlike the bulk and QW cases, there is indication that the QD dephasing rate is strongly dependent on carrier density and possible electronic transitions. Consequently, the implementation of the effective relaxation rate description is not straightforward. To ensure accurate results, a microscopic gain theory with a rigorous treatment of carrier scattering processes should be used.

In Ref. [122] the dephasing due to Coulomb interaction has been calculated using semiconductor Bloch equations with correlation contributions, where scattering integrals have been evaluated in terms of free-carrier energies. In [123] a similar approach has been used to describe four-wave mixing experiments with QDs, where also effects of dynamical screening have been incorporated. A more elaborate analysis of dephasing due to Coulomb interaction in quantum wells (QWs), including non-Markovian

scattering integrals based on renormalized energies revealed quantitative modifications of the results [124].

We will show that for QD systems the situation is different due to the appearance of localized states with a discrete spectrum. The calculation of scattering integrals in terms of free-carrier energies breaks down for processes due to Coulomb interaction which involve only localized states. It turns out that these are among the dominant processes for QDs containing more than one confined shell. For other processes involving localized states, their energy renormalization is also of enhanced importance.

In the first chapters of this part we present the single-particle model used to calculate matrix elements of the interaction Hamiltonians. After a discussion of the general scheme that is used to describe optical properties of QD systems, we present a non-Markovian treatment of dephasing due to Coulomb and carrier-LO-phonon interaction, taking the correct polaronic renormalizations for the carrier-phonon interaction, as well as the corresponding energy renormalizations due to Coulomb interaction into account. We assume the carriers to be generated long enough *before* the linear optical probing either by optical or electrical excitation. This means that they have equilibrated in the respective bands by carrier-carrier and carrier-phonon scattering [125, 118]. As the optical absorption or gain coefficient is defined as the linear response to a weak probe beam, we can analyze the combined influence of Coulomb interaction and carrier-phonon interaction on optical absorption and gain spectra for quasi-equilibrium excitation conditions.

Moreover, at elevated temperatures and carrier densities, where screening of the Coulomb interaction becomes important, sufficiently long after the excitation carriers predominantly do not exist in the form of bound excitons, but as an incoherent electron-hole plasma. This is in contrast to the treatment of the interaction with acoustic phonons, where the carriers are assumed to exist as excitons only [103, 106]. Also the configuration interaction scheme [126, 127], that has been successfully used to describe optical properties of QD systems in the low temperature and low density regime, allows for an inclusion of higher excitonic complexes and their respective Coulomb interactions. However, these methods can only account for a finite number of states, making the inclusion of the WL states impossible.

Our investigations show that the efficiency of dephasing processes depends strongly on the carrier density in the system. For low carrier densities and room temperature, we find that the electron-LO-phonon interaction is the dominant mechanism, leading to the appearance of additional side-peaks in the optical spectra due to polaronic hybridization effects. Even though for high carrier densities the Coulomb interaction becomes the dominant mechanism, we will show that the electron-LO-phonon interaction remains important.

This part is organized as follows. In Chapter 7 we introduce the single-particle states,

that we use to describe the QD system. Chapter 8 is devoted to the theoretical description of the equations used to determine optical properties of semiconductor QDs, where we use the non-equilibrium Green's function method described in Chapter 4. In Chapter 9 we discuss the dephasing due to carrier-carrier Coulomb interaction that dominates the dephasing at elevated carrier-densities. In the results of that chapter a detailed investigation of the importance of various scattering channels is given. Chapter 10 is devoted to a study of dephasing due to carrier-LO-phonon interaction, which is not only important at low carrier-densities, but, as we will see, continues to contribute significantly to the dephasing at higher carrier densities. Chapter 11 deals with the self-consistent treatment of Coulomb and carrier-LO-phonon interaction, that leads to a self-consistency problem for the renormalized single-particle energies. This chapter comprises our main results, but also place some emphasis on shortcomings of the presented model that might lead to future studies. Chapter 12 entirely devoted to applications of the presented QD model. We investigate the carrier-density dependence of both QD linewidth and QD gain, present a new phenomenon that silhouettes semiconductor QD gain materials from other known gain media, and study the linewidth enhancement factor that is of enormous importance for practical applications of QD laser systems.

7 Single-particle states and interaction matrix elements

To describe the combined QD-WL system we need to know its free energy spectrum. It is given by the solutions to the single-particle problem

$$h_0\phi_\nu(\mathbf{r}) = e_\nu\phi_\nu(\mathbf{r}) \quad (7.1)$$

with the single-particle Hamilton operator defined in Eq. (3.8). The spectrum of h_0 typically consists of discrete energy levels belonging to localized QD states and a quasi-continuum belonging to delocalized WL states, as we have depicted it schematically in Figure 7.1. For the WL continuum we consider only one conduction and one valence band, as the topmost valence band gives the dominant contributions to the optical absorption near the fundamental band-edge of the InGaAs system.

The explicit calculation of single-particle states in semiconductor QD systems can be performed using various degrees of sophistication. From effective mass approaches the variety of methods spans over continuum $\mathbf{k} \cdot \mathbf{p}$ calculations including bandmixing effects [128] all the way to tight-binding models taking into account the full atomistic structure of the QDs [129]. However, in most of these methods an inclusion of the delocalized WL states is not easy as periodic boundary conditions, that are typically used, lead to an artificial ordering of QDs unusual for the Stranski-Krastanow method. This leaves us with the problem to find suitable states for the WL continuum.

For typical InGaAs QDs, phenomena like bandmixing only play a minor role and as we are predominantly focussing on many-body effects in this part of the thesis, we employ an envelope wavefunction approach in effective mass approximation

$$\phi_\nu(\mathbf{r}) = \phi_\alpha^\lambda(\mathbf{r}) = \xi_\alpha^\lambda(z) \varphi_\alpha^\lambda(\boldsymbol{\rho}) u_{\mathbf{k}\approx 0}^\lambda(\mathbf{r}) . \quad (7.2)$$

Furthermore, we assume that we can decompose the envelope wavefunction for the state α in the band λ , that can be either a QD or WL state, into a product of two functions depending on growth direction and in-plane coordinates, z and $\boldsymbol{\rho}$, respectively. The Bloch function $u_{\mathbf{k}\approx 0}^\lambda(\mathbf{r})$ contains the information about the underlying atomistic structure. As we are interested in the vicinity of the band-edge only we use its $k = 0$ value, that is fully rotational invariant. The spin will be assumed to

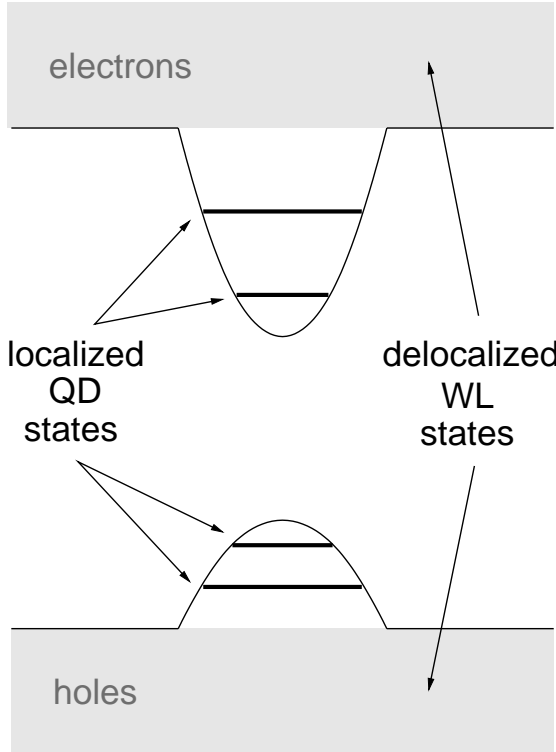


Figure 7.1: Energy spectrum of self-assembled semiconductor QDs, grown on a WL.

be hidden in the state index α , unless it is necessary to specify it explicitly. For the eigenfunction of the confinement in growth direction $\xi(z)$ the problem reduces to that of an one-dimensional potential well. Details about our treatment of this problem can be found in Appendix A.

Assuming flat, lens-shaped QDs, we can describe the in-plane parts of the eigenfunctions $\varphi_\alpha^\lambda(\rho)$ for the bound QD states in very good approximation by the eigenstates of a two-dimensional harmonic oscillator as shown in Refs. [130, 131]. For our calculations in this part of the thesis we will consider up to two confined shells both for electrons and holes, that due to their angular momentum properties we will denote as s-shell and p-shell for the ground and first excited state, respectively.

For the in-plane part of the WL states the most simple approximation consists of two-dimensional plane-wave states. However, this leads to a serious problem: Originating from two independent calculations (the oscillator states from the calculation of the QD states, the plane wave states from a treatment of the WL without QDs), while the two subspaces form orthonormal sets among themselves, the WL states are not orthonormal on the QD states. This leads to drastic overestimations of the resulting matrix elements, as has been shown in Refs. [125, 30]. A simple solution to this

problem is to orthonormalize the WL states to the bound QD states by means of the orthogonalized plane wave (OPW) method [132, 125, 30] and to use a simple parabolic dispersion for both conduction and valence band. Furthermore, as it turns out to be a reasonable approximation for InGaAs systems, we will typically assume equal electron and hole envelope wavefunctions. Details about the wavefunctions, the overlaps and on the OPW method can be found in Appendix A.

However, we would like to point out that nearly all of the approximations discussed above depend heavily on the negligibility of bandmixing effects and the fact that we are describing rather flat QDs. If one or more of these criteria are not met anymore, we have to use single-particle states obtained from more sophisticated models. For example, in nitride-based system some of these approximation do not hold, and in Part V we base our calculations of the relevant matrix elements on states that are obtained from a semi-empirical tight-binding model.

7.1 Eigenfunction expansion

For our calculations for InGaAs QDs we expand field operators as well as GFs and Selfenergies into the eigenbasis of the single-particle problem given above:

$$\hat{\psi}(\mathbf{r}, t) = \sum_{\nu} \hat{a}_{\nu}(t) \phi_{\nu}(\mathbf{r}) , \quad (7.3)$$

$$G(1, 2) = G(\mathbf{r}_1 t_1, \mathbf{r}_2 t_2) = \sum_{\nu_1 \nu_2} \phi_{\nu_1}(\mathbf{r}_1) G_{\nu_1 \nu_2}(t_1, t_2) \phi_{\nu_2}^*(\mathbf{r}_2) . \quad (7.4)$$

In the following we will specify the matrix elements of the dipole and Coulomb Hamiltonians as used in Eq. (3.10).

7.1.1 Dipole Hamiltonian

For the dipole Hamiltonian used for describing the interaction with a classical electromagnetic field, the matrix elements are

$$[dE(t)]_{\nu_1 \nu_2} = \int d^3 r \phi_{\nu_1}^*(\mathbf{r}) \mathbf{dE}(\mathbf{r}, t) \phi_{\nu_2}(\mathbf{r}) .$$

For those readers more familiar with the language of Feynman diagrams, the corresponding interaction vertex is given in Figure 7.2. Using the explicit form of the eigenfunctions (7.2) we find

$$[dE(t)]_{\nu_1 \nu_2} = \int d^3 r \left(\xi_{\alpha_1}^{\lambda_1}(z) \varphi_{\alpha_1}^{\lambda_1}(\boldsymbol{\rho}) u_{\mathbf{k} \approx 0}^{\lambda_1}(\mathbf{r}) \right)^* \mathbf{dE}(\mathbf{r}, t) \xi_{\alpha_2}^{\lambda_2}(z) \varphi_{\alpha_2}^{\lambda_2}(\boldsymbol{\rho}) u_{\mathbf{k} \approx 0}^{\lambda_2}(\mathbf{r}) . \quad (7.5)$$

$$\nu_1 \xrightarrow{\quad X \quad} \nu_2$$

Figure 7.2: Basic interaction vertex for the light-matter interaction with the classical electromagnetic field.

Splitting the integral over the whole volume in a sum over integrals over individual unit cells, we can exploit the fact that the envelope wavefunctions and the electric field amplitude vary only slightly over the spread of a unit cell, and thus take their corresponding values at the center \mathbf{R}_j of the unit cell j

$$\begin{aligned} [dE(t)]_{\nu_1 \nu_2} &= \sum_j \left(\xi_{\alpha_1}^{\lambda_1}(z_j) \varphi_{\alpha_1}^{\lambda_1}(\boldsymbol{\rho}_j) \right)^* \xi_{\alpha_2}^{\lambda_2}(z_j) \varphi_{\alpha_2}^{\lambda_2}(\boldsymbol{\rho}_j) \mathbf{E}(\mathbf{R}_j, t) \\ &\quad \times \underbrace{\int_{V_j} d^3r \left(u_{\mathbf{k} \approx 0}^{\lambda_1}(\mathbf{r}) \right)^* e(\mathbf{r} + \mathbf{R}_j) u_{\mathbf{k} \approx 0}^{\lambda_2}(\mathbf{r})}_{\mathbf{d}_{\lambda_1, \lambda_2}} . \end{aligned}$$

The dipole matrix elements $\mathbf{d}_{\lambda_1, \lambda_2}$ can be readily evaluated using the symmetry properties of the Bloch functions

$$\mathbf{d}_{\lambda_1, \lambda_2} = \mathbf{p}_d \begin{pmatrix} d_{cc} & d_{cv} \\ d_{vc} & d_{vv} \end{pmatrix} = \mathbf{p}_d \begin{pmatrix} 0 & d_{cv} \\ d_{vc} & 0 \end{pmatrix}, \quad (7.6)$$

with the polarization vector \mathbf{p}_d . Note that in general the matrix d_{λ_1, λ_2} can depend on the direction of \mathbf{p}_d . However, as we will only consider normal incidence and thus only one possible choice of \mathbf{p}_d we use Eq. (7.6) in what follows. With the Fourier transform of the electric field

$$\mathbf{E}_q(t) = \sum_{\mathbf{R}_j} e^{-i\mathbf{q}\mathbf{R}_j} \mathbf{E}(\mathbf{R}_j, t)$$

we find in the continuum limit with respect to \mathbf{R}_j

$$[dE(t)]_{\nu_1 \nu_2} = \sum_{\mathbf{q}} \langle \xi_{\alpha_1}^{\lambda_1} \varphi_{\alpha_1}^{\lambda_1} | e^{i\mathbf{q}\mathbf{r}} | \xi_{\alpha_2}^{\lambda_2} \varphi_{\alpha_2}^{\lambda_2} \rangle \mathbf{d}_{\lambda_1, \lambda_2} \mathbf{E}_q(t). \quad (7.7)$$

Restricting our analysis to small momentum transfers \mathbf{q} , which is consistent with the dipole approximation itself, and to equal electron and hole envelope wavefunctions, the matrix elements of the dipole Hamiltonian are given by

$$[dE(t)]_{\nu_1 \nu_2} = \mathbf{d}_{\lambda_1, \lambda_2} \mathbf{E}(t) \delta_{\alpha_1, \alpha_2}, \quad (7.8)$$

meaning that only optical transitions between valence and conduction band exist, which conserve the in-plane quantum number α . Eq. (7.8) is the result that will be used in the following chapters for InGaAs systems.

If we have to loosen the assumptions on the wave-function model we also have to reconsider the possible optical transitions in the system. This becomes necessary in Part V when focusing on QDs in the nitride material system.

7.1.2 Coulomb Hamiltonian

The matrix elements of the Coulomb Hamiltonian (3.10) read

$$V_{\nu_1\nu_2\nu_3\nu_4} = \int d^3r d^3r' \phi_{\nu_1}^*(\mathbf{r}) \phi_{\nu_2}^*(\mathbf{r}') V(\mathbf{r} - \mathbf{r}') \phi_{\nu_3}(\mathbf{r}') \phi_{\nu_4}(\mathbf{r}). \quad (7.9)$$

With the ansatz (7.2) for the single-particle wavefunctions and the Fourier transform of the Coulomb potential

$$V_{\mathbf{q}} = \sum_{\mathbf{r}} e^{-i\mathbf{qr}} V(\mathbf{r}) \quad (7.10)$$

we find for the Coulomb matrix elements (7.9) in a Fourier basis

$$V_{\nu_1\nu_2\nu_3\nu_4} = \sum_{\mathbf{q}} V_{\mathbf{q}} \langle \phi_{\alpha_1}^{\lambda_1} | e^{i\mathbf{qr}} | \phi_{\alpha_4}^{\lambda_4} \rangle \langle \phi_{\alpha_2}^{\lambda_2} | e^{-i\mathbf{qr}} | \phi_{\alpha_3}^{\lambda_3} \rangle \quad (7.11)$$

$$\begin{aligned} &= \sum_{\mathbf{q}} V_{\mathbf{q}} \langle \xi_{\alpha_1}^{\lambda_1} \varphi_{\alpha_1}^{\lambda_1} | e^{i\mathbf{qr}} | \xi_{\alpha_4}^{\lambda_1} \varphi_{\alpha_4}^{\lambda_1} \rangle \\ &\quad \langle \xi_{\alpha_2}^{\lambda_2} \varphi_{\alpha_2}^{\lambda_2} | e^{-i\mathbf{qr}} | \xi_{\alpha_3}^{\lambda_2} \varphi_{\alpha_3}^{\lambda_2} \rangle \delta_{\lambda_1,\lambda_4} \delta_{\lambda_2,\lambda_3}, \end{aligned} \quad (7.12)$$

where (7.10) explicitly yields

$$V_{\mathbf{q}} = \frac{e^2}{\varepsilon_0 \varepsilon_b} \frac{1}{\mathbf{q}^2}. \quad (7.13)$$

The orthonormality in the band index stems from the orthonormality of the Bloch functions, leading to a limited number of band index combinations for the matrix elements, excluding e.g. interband exchange effects in envelope function approximation. For the wavefunction model (7.2) a further simplification is possible, as the product ansatz in the envelope wavefunctions leads to a decomposition in the overlap functions $\langle \phi | e^{i\mathbf{qr}} | \phi \rangle$. However, as this also is a rather technical point, we will swap the discussion to Appendix A. These matrix elements will be used in the following to describe dephasing due to carrier-carrier Coulomb as well as carrier-LO-phonon scattering. Having discussed the eigenfunctions and matrix elements in this chapter, we will focus on the theoretical description of optical properties of semiconductor QDs in the next chapter.

8 Optical properties of quantum dot systems

In this chapter we will discuss the theoretical model used to describe linear optical properties of QDs in the presence of a excited electron-hole plasma. Even though we derive the theory in a rather general fashion, at some points it is inevitable to use the assumption of a weak probe field belonging to a *linear* absorption experiment explicitly. We will identify those points when appropriate. In this chapter we will derive the equations of motion for the relevant GFs, after discussing the foundations for the description of optical response.

8.1 Theoretical description of optical response

The electro-magnetic field that is emitted from the sample originates from the macroscopic polarization inside the sample and is given by the propagation equation

$$\left(\frac{1}{c^2} \frac{\partial^2}{\partial t^2} - \Delta \right) \mathbf{E}(\mathbf{r}, t) = -\mu_0 \frac{\partial^2}{\partial t^2} \mathcal{P}(\mathbf{r}, t) . \quad (8.1)$$

The optical polarization $\mathcal{P}(t)$ that enters Maxwell's equations [70] is connected to an external optical filed via

$$\mathcal{P}(t) = \int dt' \underline{\underline{\chi}}(t, t') \mathbf{E}(t') , \quad (8.2)$$

where only the time arguments are given for notational simplicity. As we will only consider one possible direction of incident and a material without birefringence effects, we can neglect the tensorial character and calculate χ as

$$\chi(t, t') = \frac{\delta \mathcal{P}(t)}{\delta E(t')} \quad (8.3)$$

$$\propto \sum_{\alpha\beta,\gamma\delta} d_{\alpha\beta} d_{\mu\nu} G_{\alpha\beta\mu\nu}^R(tt, t't') . \quad (8.4)$$

Equation (8.4) shows, that the linear response is connected with a retarded two-particle GF in an appropriate eigenbasis (cf. Section 7.1). Details on the derivation of this relation can be found in [74].

To calculate the linear response function, different strategies are possible. One method that is used, e.g. in Refs. [133, 74] is to calculate the 2-particle GF by means of a T -matrix (cf. Eq. (4.68)) and to evaluate Eq. (8.4). Alternatively, for the reaction to a weak probe field that we would like to investigate, we can exploit the fact, that χ only depends on the difference time and Fourier transform both the optical polarization $\mathcal{P}(t)$ and the optical field $E(t)$ to calculate directly the linear optical susceptibility via

$$\chi(\omega) = \frac{\mathcal{P}(\omega)}{E(\omega)}. \quad (8.5)$$

Remarkably, we can trace back the (two-particle) optical response to the (single-particle) optical polarization. Furthermore, as we will only consider electronic but no excitonic populations, we can fully restrict our analysis to single-particle quantities, and use the Kadanoff-Baym equations (4.63). The knowledge of the transition amplitudes $\psi_{\nu_1\nu_2}(t)$ allows for a direct calculation of the optical polarization

$$\mathcal{P}(t) = \sum_{\nu_1\nu_2} d_{\nu_1\nu_2}^* \psi_{\nu_1\nu_2}(t), \quad (8.6)$$

and, hence, of the susceptibility $\chi(\omega)$. However, it should be emphasized that Eq. (8.5) only holds in the linear regime.

For the thin layer of a QD-WL system and for normal incidence of the electromagnetic probe field, the susceptibility is directly linked to the linear absorption coefficient via

$$\alpha(\omega) = \frac{\omega}{\varepsilon_0 n c L} \text{ Im } \chi(\omega), \quad (8.7)$$

with the speed of light in vacuum c , the background refractive index n , and the thickness of the layer L , thus allowing for a direct determination of optical spectra.

8.2 Evaluation of the Kadanoff-Baym equations

Using the eigenfunction expansion (7.4) for the GF and for the selfenergy in the Kadanoff-Baym equations (4.63), we find for the QD-WL system

$$\begin{aligned} \sum_{\nu_3} \int dt_3 & \left\{ \left[G_{0,\nu_1\nu_3}^{-1}(t_1, t_3) - \Sigma_{\nu_1\nu_3}^R(t_1, t_3) \right] G_{\nu_3\nu_2}^<(t_3, t_2) \right. \\ & \left. - \Sigma_{\nu_1\nu_3}^<(t_1, t_3) G_{\nu_3\nu_2}^A(t_3, t_2) \right\} = 0 , \\ \sum_{\nu_3} \int dt_3 & \left\{ G_{\nu_1\nu_3}^<(t_1, t_3) \left[\left(G_{0,\nu_3\nu_2}^{-1}(t_3, t_2) \right) - \Sigma_{\nu_3\nu_2}^A(t_3, t_2) \right] \right. \\ & \left. - G_{\nu_1\nu_3}^R(t_1, t_3) \Sigma_{\nu_3\nu_2}^<(t_3, t_2) \right\} = 0 . \end{aligned} \quad (8.8)$$

Originally, the free inverse GF is defined by (4.45). As the dipole Hamiltonian is also a single-particle operator we will combine the influences of h_0 and of the dipole Hamiltonian in the free inverse GF leading to

$$G_{0,\nu_1\nu_2}^{-1}(t_1, t_2) = \left(i\hbar \frac{\partial}{\partial t_1} - e_{\nu_1} \right) \delta(t_1 - t_2) \delta_{\nu_1, \nu_2} + dE(t_1)_{\nu_1\nu_2} \delta(t_1 - t_2) . \quad (8.9)$$

Here we employed the notation of Eq. (7.5) for the matrix elements of the dipole Hamiltonian.

Using (8.9) and forming the difference of the equations (8.8) we find

$$\begin{aligned} & \left[i\hbar \left(\frac{\partial}{\partial t_1} + \frac{\partial}{\partial t_2} \right) - (e_{\nu_1} - e_{\nu_2}) \right] G_{\nu_1\nu_2}^<(t_1, t_2) \\ & + \sum_{\nu_3} [dE(t_1)]_{\nu_1\nu_3} G_{\nu_3\nu_2}^<(t_1, t_2) - \sum_{\nu_3} G_{\nu_1\nu_3}^<(t_1, t_2) [dE(t_2)]_{\nu_3\nu_2} \\ & = \hat{S}_{\nu_1\nu_2}(t_1, t_2) , \end{aligned} \quad (8.10)$$

with the correlation contribution

$$\begin{aligned} \hat{S}_{\nu_1\nu_2}(t_1, t_2) &= \sum_{\nu_3} \int dt_3 \left[\Sigma_{\nu_1\nu_3}^R(t_1, t_3) G_{\nu_3\nu_2}^<(t_3, t_2) + \Sigma_{\nu_1\nu_3}^<(t_1, t_3) G_{\nu_3\nu_2}^A(t_3, t_2) \right. \\ & \left. - G_{\nu_1\nu_3}^R(t_1, t_3) \Sigma_{\nu_3\nu_2}^<(t_3, t_2) - G_{\nu_1\nu_3}^<(t_1, t_3) \Sigma_{\nu_3\nu_2}^A(t_3, t_2) \right] . \end{aligned} \quad (8.11)$$

Focusing our analysis to the time diagonal ($t_1 = t_2 = t$) we end up with

$$\begin{aligned} & \left[i\hbar \frac{\partial}{\partial t} - (e_{\nu_1} - e_{\nu_2}) \right] G_{\nu_1\nu_2}^<(t) \\ & + \sum_{\nu_3} [dE(t)]_{\nu_1\nu_3} G_{\nu_3\nu_2}^<(t) - \sum_{\nu_3} G_{\nu_1\nu_3}^<(t) [dE(t)]_{\nu_3\nu_2} \\ & = \hat{S}_{\nu_1\nu_2}(t, t) \end{aligned} \quad (8.12)$$

The restriction to the time diagonal physically means that instead of calculating the full two-time information contained in the propagator $G^<$, we try to restrict our analysis to the calculation of elements of the reduced single-particle density matrix that live on the time diagonal of the two-time propagator. At first glance this does not make the calculation of the full two-time GF information unnecessary, as they enter in the correlation contribution. Indeed, this is only the case in combination with a further approximation, namely the generalized Kadanoff-Baym ansatz, that we discussed in Section 4.7, and that allows to trace back all propagators $G^<$ to the time diagonal. We will come back to this point when discussing specific interaction mechanisms. Physically, as explained in detail in Ref. [53], by evaluating the *difference* of the equations (8.8), we focus our attention on the *macroscopic* reaction of the system to an external perturbation, which is exactly the situation at hand for an optical experiment.

Taking into account explicitly the relation between the propagators $G^<$ for equal times and the single-particle density matrix (cf. Eq. (3.19)),

$$\begin{aligned}\psi_{\nu_1\nu_2}(t) &= -i\hbar G_{\nu_1\nu_2}^<(t,t) \\ f_{\nu_1}(t) &= -i\hbar G_{\nu_1\nu_1}^<(t,t)\end{aligned}\quad (8.13)$$

we can give the interpretation of Eq. (8.12) straight away: The equations describe generalizations of the optical Bloch equation to the semiconductor case, where the actual many-body interaction is hidden in the selfenergy that we need to specify in chapters to follow.

For the wave-function model discussed in Chapter 7 we can restrict ourselves to propagators $G^<$ that are diagonal in the state index α throughout. This is the case as both the transition amplitudes that are optically active (have non-vanishing dipole matrix elements) and the population functions, that describe the presence of an excited electron-hole-plasma, are diagonal in that index. Using Eq. (8.13), we can translate Eq. (8.12) into a set of equations for the elements of the single-particle density matrix

$$\begin{aligned}\left[i\hbar\frac{\partial}{\partial t} - e_\alpha^c(t) + e_\alpha^v(t)\right]\psi_\alpha^{cv}(t) + [f_\alpha^c(t) - f_\alpha^v(t)][dE(t)]_{\alpha\alpha}^{cv}(t) &= -i\hbar\hat{S}_{\nu_1\nu_2}^{cv}(t) \\ i\hbar\frac{\partial}{\partial t}f_\alpha^\lambda(t) + [dE(t)]_{\alpha\alpha}^{cv}(t)[\psi_\alpha^{cv}(t)]^* - \psi_\alpha^{cv}(t)[[dE(t)]_{\alpha\alpha}^{cv}(t)]^* &= -i\hbar\hat{S}_{\alpha\alpha}^{\lambda\lambda}(t)\end{aligned}\quad (8.14)$$

with the correlation contributions, still defined in terms of GFs, given by (8.11). Having developed the theory up to this point in a rather general fashion, only using the particularities of the dipole transitions in the system under investigation, we now have to specify the interaction mechanisms that we take into account and define the appropriate selfenergies, starting with the Coulomb interaction in the following chapter.

9 Coulomb interaction

One could argue that the Coulomb interaction is the most important interaction mechanism for the optical response of semiconductors. It gives rise to the excitonic and bi-excitonic resonances in QW and bulk systems as well as to complicated multi-excitonic complexes in the low density low temperature spectra of semiconductor QDs. Furthermore, it dominates the dephasing of a coherent optical polarization at elevated carrier densities. In quantum-optical applications that employ the bi-exciton exciton cascade the interband electron-hole exchange interaction plays a crucial role, as it controls the degree of entanglement that can be achieved in those experiments [134]. In this chapter we will focus on the role of the Coulomb interaction as a dephasing mechanism. First of all, we discuss the Hartree-Fock approximation to the Coulomb interaction as it gives rise to important many-body effects, like the renormalization of the optical Rabi-energy that, in turn, is responsible for the appearance of the excitonic resonance in linear optical spectra of QWs and bulk materials. However, as we will see, the Hartree-Fock approximation does not lead to carrier scattering or dephasing. Thus it is necessary to treat the Coulomb interaction beyond the Hartree-Fock approximation. This is done in Section 9.2–9.5, utilizing the second-order Born approximation. On that level, we need to discuss the screening of the Coulomb interaction and the renormalizations of the single-particle energies.

9.1 Hartree-Fock approximation

A peculiarity of the Coulomb interaction is the existence of an instantaneous contribution to the selfenergy due to the instantaneous nature of the bare Coulomb potential. As a consequence the retarded and advanced components of the selfenergy can be cast into the form

$$\begin{aligned}\Sigma^R(1, 2) &= \Sigma^{HF}(1, 2) + \Theta(t_1 - t_2) [\Sigma^>(1, 2) - \Sigma^<(1, 2)] \\ \Sigma^A(1, 2) &= \Sigma^{HF}(1, 2) - \Theta(t_2 - t_1) [\Sigma^>(1, 2) - \Sigma^<(1, 2)] ,\end{aligned}\tag{9.1}$$

where the instantaneous or *Hartree-Fock* (HF) part

$$\Sigma^{HF}(1, 2) = \Sigma^{HF}(1, 2)\delta(t_1 - t_2)\tag{9.2}$$

can be defined diagrammatically as

$$\frac{1}{\Sigma} \cdot (\sum) \cdot \frac{2}{\Sigma} = \text{Diagram 1} + \text{Diagram 2} . \quad (9.3)$$

Due to its instantaneous nature, the HF selfenergy only adds to the retarded and advanced components of the selfenergy as. This result is also immediately obvious when formally unfolding the Keldysh contour for (9.3).

With the Feynman rules we can write (9.3) as

$$\begin{aligned} \Sigma^{\text{HF}}(1, 2) &= \Sigma^{\text{H}} + \Sigma^{\text{F}} \\ \text{with} \\ \Sigma^{\text{H}}(1, 2) &= -i\hbar\delta(1-2) \int d3V(1-3)G(3, 3^+) , \\ \Sigma^{\text{F}}(1, 2) &= i\hbar G(1, 2)V(2-1) . \end{aligned} \quad (9.4)$$

The first term is the Hartree contribution, that describes the mean-field interaction of a carrier with all others. The Fock term is the corresponding quantum mechanical exchange contribution. Note that in our general derivation of the GF theory in Chapter 4, the Hartree diagram arises from setting up the LHS of the equation of motion, (4.40), specifically from the $\hat{\phi}_{\text{eff}}(1)$ contribution. In the fundamental set of equations, (4.55)–(4.59), it is included in G_0 , rather than in the selfenergy. However, as this is purely a matter of definition, we can also take it as part of the selfenergy, as long as we are consistent in our description.

The simplest and most intuitive way to understand the physical content of the Hartree-Fock selfenergy is given by a derivation based on the alternative formulation of the Dyson equation in terms of the two-particle GF in Eq. (4.67). If we approximate

$$G_2(\underline{1}, \underline{2}; \underline{3}, \underline{4}) = G(\underline{1}, \underline{3}) G(\underline{2}, \underline{4}) - G(\underline{1}, \underline{4}) G(\underline{2}, \underline{3}) \quad (9.5)$$

$$\text{Diagram } G_2 = \text{Diagram 1} - \text{Diagram 2}$$

Figure 9.1: Hartree-Fock factorization of the two-particle GF into uncorrelated single-particle GFs.

in Eq. (4.67), we directly find Eq. (9.3). This shows that the HF approximation is the best effective single-particle approximation, as the two-particle GF is described by a product of *full* single-particle GFs. However, as it is evident from the fact that Figure 9.1 corresponds to a neglection of the T -matrix in Figure 4.4, correlations between two particles are neglected. This also points directly to one of the major flaws of the HF approximation: Even though Coulomb effects are taken into account, on HF level we will not find dephasing or particle scattering, which is *caused* by correlations between the carriers in the two-particle GF. Nevertheless, as the HF contributions to the selfenergy lead to important many-particle corrections in the optical properties, we evaluate them for the QD system under investigation in the remainder of this chapter.

To evaluate the HF selfenergies we use once more the eigenfunction expansion (7.4). We find for the Hartree selfenergy

$$\Sigma_{\nu_1,\nu_2}(t_1,t_2)\Big|_{\text{H}} = -i\hbar\delta(t_1-t_2) \sum_{\nu_3,\nu_4} G_{\nu_3,\nu_4}(t_1,t_1^+) V_{\nu_1\nu_4\nu_3\nu_2}, \quad (9.6)$$

and for the Fock selfenergy

$$\Sigma_{\nu_1,\nu_2}(t_1,t_2)\Big|_{\text{F}} = i\hbar\delta(t_1-t_2) \sum_{\nu_3,\nu_4} G_{\nu_3,\nu_4}(t_1,t_1^+) V_{\nu_1\nu_4\nu_2\nu_3}, \quad (9.7)$$

with the Coulomb matrix elements as defined in Eq. (7.12). As $G(t,t^+) = G^<(t,t)$ we can use the relations (8.13) and get

$$\begin{aligned} \Sigma_{\alpha}^{cc}(t)\Big|_{\text{H}} &= \sum_{\beta} [V_{\alpha\beta\beta\alpha}^{\text{cccc}} f_{\beta}^c(t) + V_{\alpha\beta\beta\alpha}^{\text{cvvc}} (f_{\beta}^v(t) - 1)] \\ \Sigma_{\alpha}^{vv}(t)\Big|_{\text{H}} &= \sum_{\beta} [V_{\alpha\beta\beta\alpha}^{\text{vvvv}} (f_{\beta}^v(t) - 1) + V_{\alpha\beta\beta\alpha}^{\text{vccv}} f_{\beta}^c(t)] \\ \Sigma_{\alpha}^{cv}(t)\Big|_{\text{H}} &= \Sigma_{\alpha}^{vc}\Big|_{\text{H}} = 0 \end{aligned} \quad (9.8)$$

as well as

$$\begin{aligned} \Sigma_{\alpha}^{cc}(t)\Big|_{\text{F}} &= - \sum_{\beta} [V_{\alpha\beta\alpha\beta}^{\text{cccc}} f_{\beta}^c(t)] \delta_{s_{\alpha},s_{\beta}} \\ \Sigma_{\alpha}^{vv}(t)\Big|_{\text{F}} &= - \sum_{\beta} [V_{\alpha\beta\alpha\beta}^{\text{vvvv}} (f_{\beta}^v(t) - 1)] \delta_{s_{\alpha},s_{\beta}} \\ \Sigma_{\alpha}^{cv}(t)\Big|_{\text{F}} &= - \sum_{\beta} [V_{\alpha\beta\alpha\beta}^{\text{cvvc}} \psi_{\beta}^{cv}(t)] \delta_{s_{\alpha},s_{\beta}}, \end{aligned} \quad (9.9)$$

where $\delta_{s_{\alpha},s_{\beta}}$ assures that the exchange term couples only particles with identical spin. The attentive reader might notice at this point, that e.g. in the selfenergy $\Sigma_{\alpha}^{vv}(t)\Big|_{\text{F}}$ we

have added $\sum_{\beta} V_{\alpha\beta\alpha\beta}^{\text{vvvv}} \delta_{s_{\alpha}, s_{\beta}}$. This seemingly arbitrary procedure assures, that the HF renormalizations vanish in the zero density limit, as the renormalization due to the presence of the full valence band are already included in the calculation of the single-particle states. A further inclusion at this point would lead to a double-counting of those contributions.

Using the results for the HF selfenergy and Eq. (9.1) in Eq. (8.14), we find the well-known semiconductor Bloch equations (SBE)

$$\begin{aligned} \left[i\hbar \frac{\partial}{\partial t} - \varepsilon_{\alpha}^{c,\text{HF}}(t) + \varepsilon_{\alpha}^{v,\text{HF}}(t) \right] \psi_{\alpha}^{\text{cv}}(t) + [f_{\alpha}^v(t) - f_{\alpha}^c(t)] \Omega_{\alpha}^{\text{cv,HF}}(t) &= -i\hbar S_{\alpha\alpha}^{\text{cv}}(t) \\ i\hbar \frac{\partial}{\partial t} f_{\alpha}^c(t) + \Omega_{\alpha}^{\text{cv,HF}}(t) [\psi_{\alpha}^{\text{cv}}(t)]^* - \psi_{\alpha}^{\text{cv}}(t) [\Omega_{\alpha}^{\text{cv,HF}}(t)]^* &= -i\hbar S_{\alpha\alpha}^{\text{cc}}(t) \end{aligned} \quad (9.10)$$

with the HF renormalizations of the single-particle energies and of the Rabi energy

$$\begin{aligned} \varepsilon_{\alpha}^{c,\text{HF}}(t) &= e_{\alpha}^c(t) - \sum_{\beta} [V_{\alpha\beta\alpha\beta}^{\text{cccc}} f_{\beta}^c(t)] \delta_{s_{\alpha}, s_{\beta}} + [\Sigma_{\alpha}^{\text{cc}}(t)]_{\text{H}} \\ \varepsilon_{\alpha}^{v,\text{HF}}(t) &= e_{\alpha}^v(t) - \sum_{\beta} [V_{\alpha\beta\alpha\beta}^{\text{vvvv}} (f_{\beta}^v(t) - 1)] \delta_{s_{\alpha}, s_{\beta}} + [\Sigma_{\alpha}^{\text{vv}}(t)]_{\text{H}} \\ \Omega_{\alpha}^{\text{cv,HF}}(t) &= [dE(t)]_{\alpha\alpha}^{\text{cv}}(t) + \sum_{\beta} [V_{\alpha\beta\alpha\beta}^{\text{cvvc}} \psi_{\beta}^{\text{cv}}(t)] \delta_{s_{\alpha}, s_{\beta}}, \end{aligned} \quad (9.11)$$

and correlation contributions beyond the HF approximation

$$S_{\alpha_1\alpha_2}^{\lambda_1\lambda_2}(t) = \sum_{\alpha_3\lambda_3} \int_{-\infty}^t dt_3 \left[\begin{aligned} &\Sigma_{\alpha_1\alpha_3}^{\lambda_1\lambda_3,>}(t, t_3) G_{\alpha_3\alpha_2}^{\lambda_3\lambda_2,<}(t_3, t) \\ &- \Sigma_{\alpha_1\alpha_3}^{\lambda_1\lambda_3,<}(t, t_3) G_{\alpha_3\alpha_2}^{\lambda_3\lambda_2,>}(t_3, t) \\ &+ G_{\alpha_1\alpha_3}^{\lambda_1\lambda_3,<}(t, t_3) \Sigma_{\alpha_3\alpha_2}^{\lambda_3\lambda_2,>}(t_3, t) \\ &- G_{\alpha_1\alpha_3}^{\lambda_1\lambda_3,>}(t, t_3) \Sigma_{\alpha_3\alpha_2}^{\lambda_3\lambda_2,<}(t_3, t) \end{aligned} \right].$$

Over the past decades, the SBE have been used as a starting point for the analysis of optically excited semiconductors and therefore are discussed extensively in literature, see e.g. Refs. [59, 128, 71, 53, 132].

If we assume that the populations have been generated long enough before the optical experiment, that they have equilibrated by means of carrier-carrier [125] or carrier-phonon [118] interaction, the population functions are time independent. As one can infer from Eqs. (9.10) the time changes of the populations due to the optical field are in higher order in the field, as ψ and Ω enter linearly in the field, and thus can be neglected for linear excitation conditions.

For the Hartree terms, we find that due to momentum conservation only the $\mathbf{q} = 0$ term contributes from the WL, when classifying the inner indices into QD and WL contributions. For the QDs, averaging over randomly distributed QDs leads to an inter-dot contribution where the momentum conservation $\mathbf{q} = 0$ is restored on average as well as an intra-dot term. Due to global charge neutrality, the $\mathbf{q} = 0$ contributions cancel out and only the intra-dot term

$$\Sigma_{mm}^{\lambda\lambda}(t) = -i\hbar \sum_{\lambda'} \sum_{m_2} V_{mm'm'm'}^{\lambda\lambda'} G_{m'm'}^{<,\lambda'\lambda'}(t). \quad (9.12)$$

has to be considered. Furthermore, due to the presence of carriers in the WL, the Coulomb interaction within the intra-dot Hartree contributions becomes effectively screened. For details see Refs. [135, 30].

9.2 Second Born approximation

As pointed out before, a treatment of dephasing requires the inclusion of Coulomb effects beyond the HF level. This necessitates a detailed evaluation of the correlation contributions in Eq. (9.12), that we will perform in this section for the Coulomb interaction and in Chapter 10 for the interaction of carriers with LO-phonons.

To describe dephasing caused by carrier-carrier Coulomb interaction we use the second-order Born approximation (SBA), that can be defined diagrammatically by choosing the selfenergy as

$$\begin{aligned} \frac{1}{i} \cdot (\Sigma) \cdot \frac{2}{i} &= \text{Diagram 1} + \text{Diagram 2} \\ &= \text{Diagram 1} + \text{Diagram 3} \end{aligned} \quad (9.13)$$

or

$$\begin{aligned} \Sigma(\underline{1}, \underline{2}) &= i\hbar G(\underline{1}, \underline{2})W(\underline{2}, \underline{1}) \\ &+ (i\hbar)^2 \int d3 \int d4 G(\underline{1}, \underline{4})G(\underline{4}, \underline{3})G(\underline{3}, \underline{2})W(\underline{2}, \underline{4})W(\underline{3}, \underline{1}). \end{aligned} \quad (9.14)$$

The first term on the RHS corresponds to the random-phase approximation (RPA), that is defined by evaluating the definition of the selfenergy (4.57) with a point-like vertex function. The second term is the first self-consistent vertex correction, that gives contributions in the same order in the screened potential W^R as the RPA term.

To evaluate the correlation contribution (9.12), we need to break the Keldysh-contour \mathcal{C} , and extract the greater and lesser components of the selfenergy Σ^{\gtrless} . Choosing the exterior indices appropriately, the sums over the inner contour indices lead to a magnitude of terms. However, as are restricting the analysis to contributions in second order in the screened potential, we can neglect most of those terms. To see this we take into account the general connection between the propagators and the retarded components of the plasmon-GF W , which is also known as the *optical theorem* [59]

$$W^{\gtrless}(2, 1) = - \int d3 \int d4 W^R(2, 3) P^{\gtrless}(3, 4) W^A(4, 1). \quad (9.15)$$

This shows that W^{\gtrless} itself is second order in the screened potential $W^{R,A}$, so that we can identify contributions as $W^{\gtrless}W^{R,A}$ as being *third* order in the screened potential and hence can be neglected. If we use this approximation as well as the optical theorem (9.15) and anticipate the RPA polarization function (9.18) from the next section, we find

$$\begin{aligned} \Sigma^{\gtrless}(1, 2) &= i\hbar G^{\gtrless}(1, 2) W^{\leqslant}(2, 1) \\ &\quad + (i\hbar)^2 \int d3 \int d4 G^{\gtrless}(1, 4) G^{\leqslant}(4, 3) G^{\gtrless}(3, 2) W^R(2, 4) W^A(3, 1) \\ &= \hbar^2 \int d3 \int d4 [G^{\gtrless}(1, 2) W^R(2, 3) G^{\leqslant}(3, 4) G^{\gtrless}(4, 3) W^A(4, 1) \\ &\quad - G^{\gtrless}(1, 4) G^{\leqslant}(4, 3) G^{\gtrless}(3, 2) W^R(2, 4) W^A(3, 1)]. \end{aligned} \quad (9.16)$$

In this expression the correlation contributions are defined completely by means of screened potentials $W^{R,A}$ and carrier propagators G^{\gtrless} . In the next section we will discuss the screened Coulomb interaction $W(\underline{1}, \underline{2})$ that enters the SBA selfenergy and describes further many-body effects.

9.2.1 Screening

Two important many-body effects in semiconductor systems have their origin in the Coulomb interaction between the carriers: On one hand we have the screening of the Coulomb interaction, which leads to a shortening of the interaction range (e.g. from a bare Coulomb-like to a Debye- (Yukawa-) like potential). On the other hand there is the phenomenon of collective plasma oscillations, that can be described by a new quasi-particle, the *plasmon* [102]. Both effects are described by the GF of the screened interaction that we formally introduced in Eq. (4.49), and that has a Dyson equation of its own, which is (4.56). The corresponding selfenergy for this Dyson equation is given by the polarization function P of Eqs. (4.56) and (4.58). We would

like to stress at this point, that the polarization P and the *optical* polarization \mathcal{P} are different quantities, though they have a common origin. This can be understood when taking into account that the former is given as the reaction of the system to the longitudinal component of the electromagnetic field (the Coulomb field), while the latter is given by the response to a transversal electromagnetic field (the optical field).

For our calculations we use the polarization function P in self-consistent RPA

$$\frac{1}{2} \cdot \boxed{P} \cdot \frac{2}{2} = \underline{1} \circlearrowleft \underline{2}, \quad (9.17)$$

or

$$P(\underline{1}, \underline{2}) = i\hbar G(\underline{1}, \underline{2})G(\underline{2}, \underline{1}). \quad (9.18)$$

In the following we assume that the screened potential, like the bare one, retains its instantaneous nature

$$W^{\text{R,A}}(1, 2) = W^{\text{R,A}}(\mathbf{r}_1 - \mathbf{r}_2, t_1)\delta(t_1 - t_2). \quad (9.19)$$

For practical calculations we can assume that screening only comes from carriers in the WL, which is reasonable for higher carrier densities and low to intermediate densities of QDs on the WL. The inclusion of the QD carriers is not possible in a straightforward way, as the assumption of translation invariance, that is used in the derivation of Eq. (9.20) in Appendix B does not hold for carriers confined to QDs. Then the retarded polarization function can be derived in the eigenbasis of Eq. (7.2) as

$$P_{\mathbf{q}}^{\text{R}} = \sum_{\alpha\beta,\lambda} |\langle \alpha | e^{i\mathbf{qr}} | \beta \rangle|^2 \frac{f_{\alpha}^{\lambda} - f_{\beta}^{\lambda}}{e_{\alpha}^{\lambda} - e_{\beta}^{\lambda}}, \quad (9.20)$$

which resembles the static limit of the well known Lindhard formula. The corresponding screened Coulomb matrix elements follow from

$$W_{\alpha\beta\gamma\delta}^{\text{R}} = \sum_{\mathbf{q}} W_{\mathbf{q}}^{\text{R}} \langle \alpha | e^{-i\mathbf{qr}} | \delta \rangle \langle \beta | e^{+i\mathbf{qr}} | \gamma \rangle, \quad (9.21)$$

with

$$W_{\mathbf{q}}^{\text{R}} = \frac{V_{\mathbf{q}}}{1 - V_{\mathbf{q}} P_{\mathbf{q}}^{\text{R}}}. \quad (9.22)$$

Details of these derivations are given in Appendix B.

The assumption of a static screening has two physical consequences. We neglect both the buildup of screening and the collective excitations of the plasma (the plasmons).

In general, the screening of the Coulomb interaction does not follow the generation of carriers instantaneously, but is a complicated quantum-kinetic problem of its own, that has been studied extensively over the last decades. For an overview see the books by Kremp *et al.* [62] and by Haug and Jauho [136]. However, as we are dealing with a situation where the carriers have been generated and equilibrated already, and are investigating the reaction of the system to a weak probe pulse that does not generate further carriers, the assumption (9.19) is reasonable.

Even though these approximations have been used extensively for research in semiconductor systems, e.g. in QWs [137, 138, 139], the combination of the SBA for the carrier selfenergy and the RPA approximation for the polarization function is problematic from a fundamental viewpoint. As Gartner *et al.* have shown in Ref. [73], the polarization function has to follow from the functional derivative of the selfenergy in combination with the equations from the fundamental system of equations, Eqs. (4.59) and (4.58). If this is not the case, at least a full two-time calculation of the carrier propagators $G^<(t_1, t_2)$ is hopeless, as singularities appear in the theory. However, even for the choice of the RPA selfenergy for the carrier system, that only consists of the first term in Eq. (9.13), one would need to compute the screening in a ladder approximation, which is an extremely demanding task. This is further complicated by the choice of the SBA selfenergy for the carrier system. As an appetizer for a future generation of PhD students, we will, utilizing the scheme outlined in Ref. [73], give the consistent treatment of screening belonging to the SBA selfenergy:

$$\begin{array}{c}
 \text{Diagram 1:} \\
 \begin{array}{ccc}
 \begin{array}{c} \text{1} \\ \text{2} \end{array} & \xrightarrow{\Gamma} & \begin{array}{c} \text{3} \end{array} \\
 & = & \\
 \begin{array}{c} \bullet \\ \text{1}=\text{2}=\text{3} \end{array} & + &
 \end{array}
 \end{array}
 + \begin{array}{c}
 \text{Diagram 2:} \\
 \begin{array}{cc}
 \begin{array}{c} \text{1} \quad \text{4} \\ \text{2} \quad \text{5} \end{array} & \xrightarrow{\Gamma} \begin{array}{c} \text{3} \end{array} \\
 + & \\
 \begin{array}{c} \text{1} \quad \text{7} \quad \text{4} \\ \text{2} \quad \text{6} \quad \text{5} \end{array} & \xrightarrow{\Gamma} \begin{array}{c} \text{3} \end{array}
 \end{array}
 \end{array}
 + \begin{array}{c}
 \text{Diagram 3:} \\
 \begin{array}{cc}
 \begin{array}{c} \text{1} \quad \text{4} \\ \text{2} \quad \text{7} \end{array} & \xrightarrow{\Gamma} \begin{array}{c} \text{3} \end{array} \\
 + & \\
 \begin{array}{c} \text{1} \quad \text{7} \quad \text{4} \\ \text{2} \quad \text{6} \quad \text{5} \end{array} & \xrightarrow{\Gamma} \begin{array}{c} \text{3} \end{array}
 \end{array}
 \end{array} . \tag{9.23}$$

Using this vertex function the polarization function and the screened potential are to be determined from Eqs. (4.58)' and (4.56)'. Such a treatment of the screening would allow for a solution of the full two-time problem for the carrier propagators.

At this point the reader might ask: If there are singularities in the theory why has it been used for a long time and is used even in the present thesis? The answer to this lies in the point that we restrict our analysis to the time evolution of the propagators

$G^<$ on the time diagonal by performing a one-time calculation. For $t_1 = t_2$, we are in the fortunate situation that the leading singularities cancel out and we are left with integrable singularities only. From this perspective it is advantageous that we restrict ourselves to a one-time calculation. Not only would a two-time calculation be tremendously demanding numerically, but it would also be fundamentally impossible on the level of approximation that we have presented here.

After discussing the screened Coulomb interaction, we will evaluate the correlation contributions due to Coulomb interaction in the next section.

9.3 Correlation contribution in the time-domain

As the derivation of the dephasing rates is rather lengthy, we give here only the ingredients for the derivation and discuss the physical contents. After expanding into the eigenbasis (7.2), we employ the GKBA that was discussed in Section 4.7 and that reads in the eigenbasis of Eq.(7.2) as follows

$$\begin{aligned} G_{\nu_1 \nu_2}^{\gtrless}(t, t_3) &= i\hbar G_{\nu_1}^R(t, t_3) G_{\nu_1 \nu_2}^{\gtrless}(t_3, t_3) \\ G_{\nu_1 \nu_2}^{\gtrless}(t_3, t) &= -i\hbar G_{\nu_1 \nu_2}^{\gtrless}(t_3, t_3) G_{\nu_2}^A(t_3, t) . \end{aligned} \quad (9.24)$$

As can be seen from Eq. (9.12), $t_3 \leq t$ always holds, and thus we only have to consider one term of the GKBA in Eq. (4.70). Additionally, we have assumed that the retarded and advanced GFs are diagonal in both state and band index. This means that we are focusing on retarded and advanced GFs that are direct generalizations of free retarded GFs (cf. Eq. (4.22)). Off-diagonal retarded GFs would only be induced by the interaction and are disregarded here. Restricting ourselves to terms linear in the transition amplitudes ψ , which corresponds to linear optical properties, we find after rearranging and transforming into the electron-hole picture [140]

$$S_{\alpha\alpha}^{eh}(t)\Big|_{\text{Coul}} = - S_{\alpha}^{eh,\text{DD}}(t)\Big|_{\text{Coul}} + S_{\alpha}^{eh,\text{OD}}(t)\Big|_{\text{Coul}}, \quad (9.25)$$

with the *diagonal* and *off-diagonal* dephasing contributions, $S_{\alpha}^{eh,DD}(t)\Big|_{\text{Coul}}$ and $S_{\alpha}^{eh,OD}(t)\Big|_{\text{Coul}}$, given by

$$\begin{aligned} S_{\alpha}^{eh,DD}(t)\Big|_{\text{Coul}} &= \int_{-\infty}^t dt_3 \hbar^2 \sum_{\beta\gamma\delta} \sum_{\substack{a,b=e,h \\ b \neq a}} \left\{ \right. \\ &\quad + \left[W_{\alpha\beta\gamma\delta}^{aaaa}(t) W_{\alpha\beta\gamma\delta}^{aaaa}(t_3)^* - W_{\alpha\beta\gamma\delta}^{aaaa}(t) W_{\alpha\beta\delta\gamma}^{aaaa}(t_3)^* \right] \\ &\quad G_{\delta}^{a,\text{R}}(t, t_3) [G_{\beta}^{a,\text{R}}(t, t_3)]^* G_{\gamma}^{a,\text{R}}(t, t_3) G_{\alpha}^{b,\text{R}}(t, t_3) \\ &\quad \psi_{\alpha}(t_3) \left[(1 - f_{\delta}^a(t_3)) f_{\beta}^a(t_3) (1 - f_{\gamma}^a(t_3)) + f_{\delta}^a(t_3) (1 - f_{\beta}^a(t_3)) f_{\gamma}^a(t_3) \right] \\ &\quad + W_{\alpha\beta\gamma\delta}^{abba}(t) W_{\alpha\beta\gamma\delta}^{abba}(t_3)^* \\ &\quad G_{\delta}^{a,\text{R}}(t, t_3) G_{\beta}^{b,\text{R}}(t, t_3) [G_{\gamma}^{b,\text{R}}(t, t_3)]^* G_{\alpha}^{b,\text{R}}(t, t_3) \\ &\quad \psi_{\alpha}(t_3) \left[(1 - f_{\delta}^a(t_3)) (1 - f_{\beta}^b(t_3)) f_{\gamma}^b(t_3) + f_{\delta}^a(t_3) f_{\beta}^b(t_3) (1 - f_{\gamma}^b(t_3)) \right], \end{aligned} \quad (9.26)$$

and

$$\begin{aligned} S_{\alpha}^{eh,OD}(t)\Big|_{\text{Coul}} &= \int_{-\infty}^t dt_3 \hbar^2 \sum_{\beta\gamma\delta} \sum_{\substack{a,b=e,h \\ b \neq a}} \left\{ \right. \\ &\quad + \left[W_{\alpha\beta\gamma\delta}^{baab}(t)^* W_{\alpha\beta\gamma\delta}^{aaaa}(t_3) - W_{\alpha\beta\gamma\delta}^{baab}(t)^* W_{\alpha\beta\delta\gamma}^{aaaa}(t_3) \right] \\ &\quad G_{\alpha}^{a,\text{R}}(t, t_3) G_{\delta}^{b,\text{R}}(t, t_3) G_{\beta}^{a,\text{R}}(t, t_3) [G_{\gamma}^{a,\text{R}}(t, t_3)]^* \\ &\quad \psi_{\delta}(t_3) \left[f_{\alpha}^a(t_3) f_{\beta}^a(t_3) (1 - f_{\gamma}^a(t_3)) + (1 - f_{\alpha}^a(t_3)) (1 - f_{\beta}^a(t_3)) f_{\gamma}^a(t_3) \right] \\ &\quad + W_{\alpha\beta\gamma\delta}^{aaaa}(t) W_{\alpha\beta\gamma\delta}^{baab}(t_3)^* \\ &\quad G_{\delta}^{a,\text{R}}(t, t_3) [G_{\beta}^{a,\text{R}}(t, t_3)]^* G_{\gamma}^{a,\text{R}}(t, t_3) G_{\alpha}^{b,\text{R}}(t, t_3) \\ &\quad \psi_{\delta}(t_3) \left[f_{\beta}^a(t_3) (1 - f_{\gamma}^a(t_3)) (1 - f_{\alpha}^b(t_3)) + (1 - f_{\beta}^a(t_3)) f_{\gamma}^a(t_3) f_{\alpha}^b(t_3) \right], \end{aligned} \quad (9.27)$$

respectively. As for the particle scattering [125], we can identify direct and exchange contributions which are proportional to $2|W_{\alpha\beta\gamma\delta}|^2$ and $W_{\alpha\beta\gamma\delta} W_{\alpha\beta\delta\gamma}^*$, respectively. The population factors describe the availability of initial and final states. As already discussed, the population functions and thus via the Lindhard formula (9.20) also the screened Coulomb matrix are time independent. The non-Markovian character of the correlation contributions, or, in other words, the inclusion of memory effects, is directly evident via the time integrals in $S_{\alpha}^{eh,DD}(t)\Big|_{\text{Coul}}$ and $S_{\alpha}^{eh,OD}(t)\Big|_{\text{Coul}}$, as the change of ψ_{α} at a given time t depends explicitly on the whole past of the system. The origin of the memory effects lies in the quantum-mechanical correlations and

quantum-coherence phenomena that enter via the retarded GFs. It should be noticed, that even though we are interested in stationary spectroscopy, the short-time regime can play a crucial role. Another example of this importance of the short-time regime in the theory of linear spectroscopy is the description of the Urbach tail [141, 142] below the bandgap of a semiconductor, where the correct lineshape also can only be given by a non-Markovian treatment including memory-effects.

9.4 Connection between memory effects and frequency dependence in the scattering integrals

As we are investigating linear optical spectra, it is advantageous to transform the whole set of equations (9.10), (9.11) and (9.25) into Fourier space and directly write down and evaluate a set of equations for $\psi_\alpha(\omega)$. In this section we show how non-Markovian scattering integrals lead to frequency dependent dephasing terms. Conversely the use of the Markov approximation, that consists of neglecting memory effects, will lead to frequency independent dephasing rates. The time-domain formulation of the SBE with correlation contributions due to Coulomb interaction is given by Eqs. (9.10), (9.11) and (9.25). In the following we only explicitly consider the direct e-e and h-h interaction contributions of the diagonal dephasing,

$$S_\alpha^{\text{DD}}(t) \Big|_{\text{Coul}} = \hbar^2 \int_{-\infty}^t dt' \sum_{\substack{a,b=e,h \\ b \neq a}} \sum_{\delta\beta\gamma} 2W_{\alpha\beta\gamma\delta} W_{\alpha\beta\gamma\delta}^* \\ \times G_\alpha^{b,\text{R}}(t, t') \left[G_\beta^{a,\text{R}}(t, t') \right]^* G_\gamma^{a,\text{R}}(t, t') G_\delta^{a,\text{R}}(t, t') \psi_\alpha(t') F_{\beta\gamma\delta}^a , \quad (9.28)$$

as all other terms can be treated in complete analogy. Here we have defined

$$F_{\beta\gamma\delta}^a = (1 - f_\beta^a) f_\gamma^a f_\delta^a + f_\beta^a (1 - f_\gamma^a) (1 - f_\delta^a) .$$

As discussed above both populations f and screened Coulomb matrix elements W are time independent. With the ansatz

$$G_\alpha^{a,\text{R}}(t, t') = -\frac{i}{\hbar} \Theta(t - t') e^{-\frac{i}{\hbar} \tilde{\varepsilon}_\alpha^a(t-t')} , \quad (9.29)$$

which corresponds exactly to the form of the free retarded GF (cf. Eq (4.22)) only that instead of the free single-particle energy e_α^a , being granted with the gift of foresight, we allow for an effective single-particle energy. The explicit choice of this

effective single-particle energy is the subject of Section 9.5. Using the ansatz (9.29) we obtain for

$$\begin{aligned} S_{\alpha}^{\text{DD}}(t)\Big|_{\text{Coul}} &= \frac{1}{\hbar^2} \sum_{\substack{a,b=e,h \\ b \neq a}} \sum_{\delta\beta\gamma} 2W_{\alpha\beta\gamma\delta} W_{\alpha\beta\gamma\delta}^* F_{\beta\gamma\delta} \\ &\times \int_{-\infty}^t dt' e^{-\frac{i}{\hbar}(\tilde{\varepsilon}_{\alpha}^b + \tilde{\varepsilon}_{\delta}^a - (\tilde{\varepsilon}_{\beta}^a)^* + \tilde{\varepsilon}_{\gamma}^a)(t-t')} \psi_{\alpha}(t') . \end{aligned}$$

With the Fourier transform

$$\psi_{\alpha}(t) = \int \frac{d\omega}{2\pi} e^{-i\omega t} \psi_{\alpha}(\omega) \quad (9.30)$$

and using the integral relation

$$\int_{-\infty}^t dt' e^{\frac{i}{\hbar}\Delta(t-t')} = \frac{i\hbar}{\Delta}, \quad \text{Im } \Delta > 0 \quad (9.31)$$

we find for the SBE of Eq. (9.10)

$$\begin{aligned} (\hbar\omega - \varepsilon_{\alpha}^{e,\text{HF}} - \varepsilon_{\alpha}^{h,\text{HF}}) \psi_{\alpha}^{\text{eh}}(\hbar\omega) + [1 - f_{\alpha}^e - f_{\alpha}^h] \Omega_{\alpha}^{eh,\text{HF}}(\hbar\omega) \\ = S_{\alpha}^{\text{eh}}(\hbar\omega) . \end{aligned} \quad (9.32)$$

The Coulomb part $S_{\alpha}^{\text{eh}}\Big|_{\text{Coul}}$ of the correlation contributions S_{α}^{eh} is given by

$$S_{\alpha}^{\text{eh}}(\hbar\omega) \Big|_{\text{Coul}} = -\Gamma_{\alpha}^{\text{DD}}(\hbar\omega)\Big|_{\text{Coul}} \psi_{\alpha}^{\text{eh}}(\hbar\omega) + \Gamma_{\alpha\delta}^{\text{OD}}(\hbar\omega)\Big|_{\text{Coul}} \psi_{\delta}^{\text{eh}}(\hbar\omega) , \quad (9.33)$$

with

$$\begin{aligned} \Gamma_{\alpha}^{\text{DD}}(\hbar\omega)\Big|_{\text{Coul}} &= i \sum_{\substack{a,b=e,h \\ b \neq a}} \sum_{\delta\beta\gamma} \left\{ W_{\alpha\beta\gamma\delta} [2W_{\alpha\beta\gamma\delta}^* - W_{\alpha\beta\delta\gamma}^*] \right. \\ &\quad g(\hbar\omega - \tilde{\varepsilon}_{\alpha}^b - \tilde{\varepsilon}_{\delta}^a + (\tilde{\varepsilon}_{\beta}^a)^* - \tilde{\varepsilon}_{\gamma}^a) \\ &\quad \left[(1 - f_{\beta}^a) f_{\gamma}^a f_{\delta}^a + f_{\beta}^a (1 - f_{\gamma}^a) (1 - f_{\delta}^a) \right] \\ &\quad + 2W_{\alpha\beta\gamma\delta}^* W_{\alpha\beta\gamma\delta} \\ &\quad g(\hbar\omega - \tilde{\varepsilon}_{\alpha}^b - \tilde{\varepsilon}_{\delta}^a - \tilde{\varepsilon}_{\beta}^b + (\tilde{\varepsilon}_{\gamma}^b)^*) \\ &\quad \left. \left[f_{\beta}^b (1 - f_{\gamma}^b) f_{\delta}^a + (1 - f_{\beta}^b) f_{\gamma}^b (1 - f_{\delta}^a) \right] \right\} , \end{aligned} \quad (9.34)$$

and

$$\begin{aligned} \Gamma_{\alpha\delta}^{\text{OD}}(\hbar\omega) \Big|_{\text{Coul}} &= i \sum_{\substack{a,b=e,h \\ b \neq a}} \sum_{\beta\gamma} \left\{ W_{\alpha\beta\gamma\delta} [2W_{\alpha\beta\gamma\delta}^* - W_{\alpha\beta\delta\gamma}^*] \right. \\ &\quad g(\hbar\omega - \tilde{\varepsilon}_\alpha^a - \tilde{\varepsilon}_\delta^b - \tilde{\varepsilon}_\beta^a + (\tilde{\varepsilon}_\gamma^a)^*) \\ &\quad \left[(1 - f_\gamma^a) f_\beta^a f_\alpha^a + f_\gamma^a (1 - f_\beta^a) (1 - f_\alpha^a) \right] \\ &\quad + 2W_{\alpha\beta\gamma\delta} W_{\alpha\beta\gamma\delta}^* \\ &\quad g(\hbar\omega - \tilde{\varepsilon}_\alpha^a - \tilde{\varepsilon}_\delta^b + (\tilde{\varepsilon}_\beta^b)^* - \tilde{\varepsilon}_\gamma^b) \\ &\quad \left. \left[f_\gamma^b (1 - f_\beta^b) f_\alpha^a + (1 - f_\gamma^b) f_\beta^b (1 - f_\alpha^a) \right] \right\}. \end{aligned} \quad (9.35)$$

Here we have defined

$$g(\Delta) = \frac{i}{\Delta}. \quad (9.36)$$

As we easily see from these manipulations, the frequency dependence of Γ^{DD} and Γ^{OD} in Eqs. (9.34) and (9.35) directly reflects the non-Markovian treatment of the dephasing processes.

For the Markov approximation, that consists of a neglection of memory effects, we separate a rapidly oscillating phase factor from the transition amplitude via the ansatz

$$\psi_\alpha(t) = e^{\frac{i}{\hbar}(\tilde{\varepsilon}_\alpha^e + \tilde{\varepsilon}_\alpha^h)t} \tilde{\psi}_\alpha(t). \quad (9.37)$$

Now we assume that a weakly time dependent $\tilde{\psi}_\alpha(t')$ can be replaced by the transition amplitude at the actual time t , $\tilde{\psi}_\alpha(t)$, thus neglecting the memory effects of $\tilde{\psi}_\alpha$. Using the integral relation (9.31) again, we arrive at a expression similar to Eq. (9.34) but e.g. with

$$g(\hbar\omega - \tilde{\varepsilon}_\alpha^b - \tilde{\varepsilon}_\delta^a + (\tilde{\varepsilon}_\beta^a)^* - \tilde{\varepsilon}_\gamma^a)$$

replaced by

$$g(\tilde{\varepsilon}_\alpha^a - \tilde{\varepsilon}_\delta^a + (\tilde{\varepsilon}_\beta^a)^* - \tilde{\varepsilon}_\gamma^a),$$

as the fast component $e^{\frac{i}{\hbar}(\tilde{\varepsilon}_\alpha^a + \tilde{\varepsilon}_\alpha^b)t}$ ($a \neq b$) fixes the frequency value at $\omega = \omega_\alpha = \frac{1}{\hbar}(\tilde{\varepsilon}_\alpha^e + \tilde{\varepsilon}_\alpha^h)$ for Γ^{DD} and at $\omega = \omega_\delta$ for Γ^{OD} , so that in this limit both dephasing contributions become frequency independent.

If we combine the Markov approximation with the use of free-carrier energies in the scattering contributions, the diagonal dephasing is given by the sum of in- and out-scattering rates, $\text{Im}(\Gamma_\alpha^{\text{DD}}) = S_\alpha^{\text{in}} + S_\alpha^{\text{out}}$. Here $S_\alpha^{\text{in,out}}$ are the rates in the Markovian kinetic equation for the carrier population, as defined e.g. in Ref. [125]. Results of these equations for optical spectra have been studied in detail for QW systems. Restricting the analysis to diagonal dephasing contributions Γ^{DD} and neglecting off-diagonal dephasing terms Γ^{OD} , damping of the excitonic resonances is strongly overestimated,

as shown in Ref. [143]. Non-Markovian calculations further reduce the interaction-induced broadening and line-shift of the excitonic resonances in QW systems [124]. It has been shown in Ref. [122] that the non-Markovian treatment is more crucial in QD systems compared to QWs, since the discrete part of the spectrum with large energy separation emphasizes the frequency-dependence of the dephasing rates.

As it simplifies the numerical evaluation of the theory considerably, we perform all numerical calculations in this part of the thesis in the frequency domain, solving Eqs. (9.32)–(9.35).

9.5 Self-consistent single-particle energy renormalizations

At this point, we are still left with the task to define the effective single-particle energies $\tilde{\varepsilon}_\alpha^a$ that determine via (9.29) the retarded and advanced GFs and enter in the dephasing contributions. As an approximation, that has been used successfully for QW structures [143], let us first consider free single-particle energies, namely

$$\tilde{\varepsilon}_\alpha^a = e_\alpha^a \quad (9.38)$$

leading to the free retarded GF in Fourier space

$$G_{0,\alpha}^{a,R}(\hbar\omega) = \frac{1}{\hbar\omega - e_\alpha^a + i\delta}. \quad (9.39)$$

For the use of these free-carrier energies in the dephasing contributions, the limit $\delta \rightarrow 0^+$ leads in the dephasing rates to $g(\Delta) = \pi\delta(\Delta) + iP\frac{1}{\Delta}$ where P denotes the principal value integral. This approximation implies serious difficulties in a QD system when processes are taken into account which involve only discrete states. In these cases the δ -functions are not integrated out and thus the results are not well defined. Note that this is not a artifact of the Markov approximation but also applies to the non-Markovian calculation. Even if we would introduce a finite broadening of the δ -function, e.g., due to interaction of carriers with acoustic phonons, the non-Markovian calculation still yields unphysical results. This is because the spectrum predicted by Eq. (9.32) has peaks at the energies of the LHS renormalized by the correlation contributions on the RHS and, hence, $\hbar\omega$ samples renormalized interband transitions. If they are mixed with free-carrier energies in the correlation contributions, Eqs. (9.34) and (9.35), via $g(\hbar\omega - \Delta)$, then also free carrier transitions and hybridization effects between all these energies can appear in the optical spectra, which are absent when self-consistently renormalized energies are used. Exemplarily, we show these artifacts in a calculation with free single-particle energies in the

scattering integrals (dashed line) in comparison to the result with self-consistently renormalized energies (solid line), that we will discuss below, in Figure 9.2.

The calculation with free carrier energies exhibits a multitude of peaks, stemming from the resonance denominator of $g(\Delta)$ in (9.34) and (9.35). The mixing of renormalized and free energies leads to a splitting of the interband transition lines. Furthermore, as discussed above, lines corresponding to the free s-shell and p-shell transition appear. In contrast, the calculation with self-consistently renormalized energies shows clearly the s-shell and p-shell transitions at about -130 meV and -80 meV, respectively.

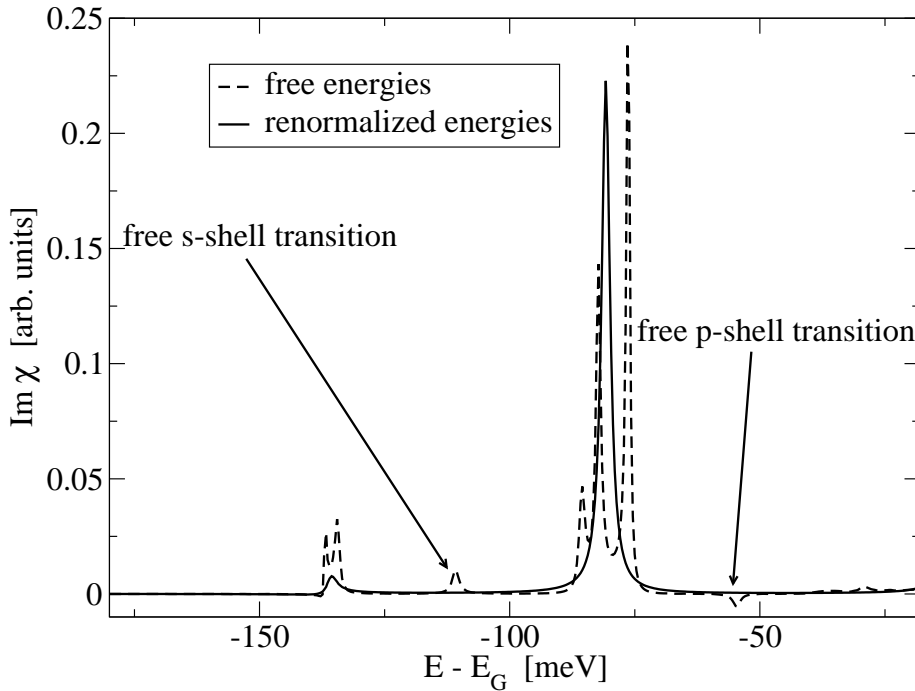


Figure 9.2: Imaginary part of the optical susceptibility for the QD resonances and a carrier density of $1 \times 10^{10} \text{ cm}^{-2}$ with (dashed line) and without (solid line) self-consistently renormalized single-particle energies in the scattering integrals ($T=77\text{K}$). For illustrative purposes only the intra-dot scattering processes (cf. Section 9.6.1) causing the artifacts are included.

The renormalizations of the single-particle energies, which enter in the dephasing rates, originate from the same interaction processes that determine the dephasing itself. Technically speaking, they can be traced back to the retarded and advanced instead of the greater and lesser components of the same many-body Keldysh self-energy. At elevated carries densities, it is a reasonable approximation, that the main effect of the Coulomb interaction is a shift of the single-particle energy and the addi-

tion of a quasi-particle broadening such that the single-pole structure of the retarded GF remains valid. This picture corresponds to the Landau theory of a Fermi liquid and leads to the retarded GF of the interacting system

$$G_{a,\alpha}^R(\hbar\omega) = \frac{1}{\hbar\omega - \tilde{\varepsilon}_\alpha^a} = \frac{1}{\hbar\omega - \varepsilon_\alpha^a + i\gamma_\alpha^a} . \quad (9.40)$$

With this ansatz, we define complex effective single-particle energies

$$\tilde{\varepsilon}_\alpha^a = \varepsilon_\alpha^a - i\gamma_\alpha^a = e_\alpha^a + \Delta_\alpha^a - i\gamma_\alpha^a , \quad (9.41)$$

consisting of the renormalized energies ε_α^a and the corresponding quasi-particle broadenings γ_α^a , that enter in the dephasing rates of (9.34) and (9.35). In the pole approximation, the self-consistency requirement leads to

$$\tilde{\varepsilon}_\alpha^a = e_\alpha^a + \Sigma_\alpha^{a,\text{HF}} + \Sigma_\alpha^{a,R}(\tilde{\varepsilon}_\alpha^a) \quad (9.42)$$

with the correlation part of the retarded selfenergy that can be evaluated from the greater and lesser components via the second term in Eq. (9.1), leading to

$$\begin{aligned} \Sigma_\alpha^{a,R}(\hbar\omega) = & -i \sum_{\substack{b=e,h \\ b \neq a}} \sum_{\delta\beta\gamma} \left\{ W_{\alpha\beta\gamma\delta}^* [2W_{\alpha\beta\gamma\delta}^* - W_{\alpha\beta\delta\gamma}^*] \right. \\ & g (\hbar\omega - \tilde{\varepsilon}_\delta^a + (\tilde{\varepsilon}_\beta^a)^* - \tilde{\varepsilon}_\gamma^a) \\ & \left[(1 - f_\beta^a) f_\gamma^a f_\delta^a + f_\beta^a (1 - f_\gamma^a) (1 - f_\delta^a) \right] \\ & + 2W_{\alpha\beta\gamma\delta}^* W_{\alpha\beta\gamma\delta} \\ & g (\hbar\omega - \tilde{\varepsilon}_\delta^a - \tilde{\varepsilon}_\beta^b + (\tilde{\varepsilon}_\gamma^b)^*) \\ & \left. \left[f_\beta^b (1 - f_\gamma^b) f_\delta^a + (1 - f_\beta^b) f_\gamma^b (1 - f_\delta^a) \right] \right\} . \end{aligned} \quad (9.43)$$

The close connection between the dephasing rates (Σ^{\gtrless}) and the retarded selfenergy $\Sigma_\alpha^{a,R}$ can be expressed as

$$\Gamma_\alpha^{\text{DD}}(\hbar\omega) = \sum_{\substack{a,b=e,h \\ b \neq a}} \Sigma_\alpha^{a,R}(\hbar\omega - \tilde{\varepsilon}_\alpha^b) . \quad (9.44)$$

Using these self-consistently renormalized energies, we get the optical spectrum shown in Figure 9.2 with the solid line. As expected, the lines corresponding to free carrier transitions as well as hybridization effects are no longer present in the optical spectrum, as the energies in the dephasing rates are consistent with the energies that effectively appear in the LHS of Eq.(9.32).

In the next section we discuss optical spectra calculated within the theoretical framework established so far for the dephasing due to Coulomb interaction.

9.6 Results

Throughout this chapter, results are presented for a carrier and lattice temperature of 300K and a density of QDs on the WL of $n_{\text{QD}} = 10^{10} \text{ cm}^{-2}$. Further details and parameters of the QD model are given in Appendices A and D.

In Fig. 9.3 we show optical absorption spectra for the combined QD-WL system and various carrier densities. Excitation-induced dephasing and energy renormalizations due to Coulomb interaction have been included according to Eqs. (9.34), (9.35) and (9.42), (9.43). Identifiable are the excitonic resonance of the WL at around -15meV as well as the p-shell and s-shell resonances at about -90meV and -150meV, respectively. We observe a strong damping of these resonances with increasing carrier density which is accompanied by a pronounced red shift of the QD lines. The transition from absorption to gain takes place at a density $\sim 1 \times 10^{11} \text{ cm}^{-2}$ ($\sim 5 \times 10^{11} \text{ cm}^{-2}$) for the s-shell (p-shell). An important point for practical applications is the saturation of the optical gain for the s-shell accompanied by the increasing red-shift. This is due to a combination of state filling effects and a saturation of the dephasing at the s-shell resonance. In contrast, the gain at the p-shell resonance increases further and shows no saturation for the densities investigated here.

9.6.1 Importance of different dephasing processes

The Coulomb matrix elements allow to distinguish between different dephasing processes in complete analogy to the carrier scattering processes discussed in Ref. [125]. If all four indices of the screened Coulomb matrix elements $W_{\alpha\beta\gamma\delta}$ are WL states, we refer to the corresponding processes as WL relaxation. They describe dephasing and energy shifts of the WL states in the optical spectra. Apart from the fact that we have to include OPW corrections to the interaction matrix elements for a proper description of the coupled QD-WL system, this resembles the case of a QW system.

If one and only one of the four indices of $W_{\alpha\beta\gamma\delta}$ corresponds to a QD state, we consider the dephasing mechanism as WL-assisted carrier-capture, because in the corresponding scattering process an electron or a hole is captured from the WL to the QD [125]. Likewise we refer to processes with two QD state indices as WL-assisted relaxation and to processes with three QD state indices as dot-assisted processes. Intra-dot processes are described when all four indices of $W_{\alpha\beta\gamma\delta}$ correspond to QD states. These scattering events are not important in the carrier dynamics, because we only consider two confined shells for electrons and holes and, therefore, such scattering processes cannot redistribute carriers. However, they clearly provide additional dephasing of the coherent optical polarization. Note that the intra-dot processes are not the only events which produce dephasing without redistribution of carriers. Such processes,

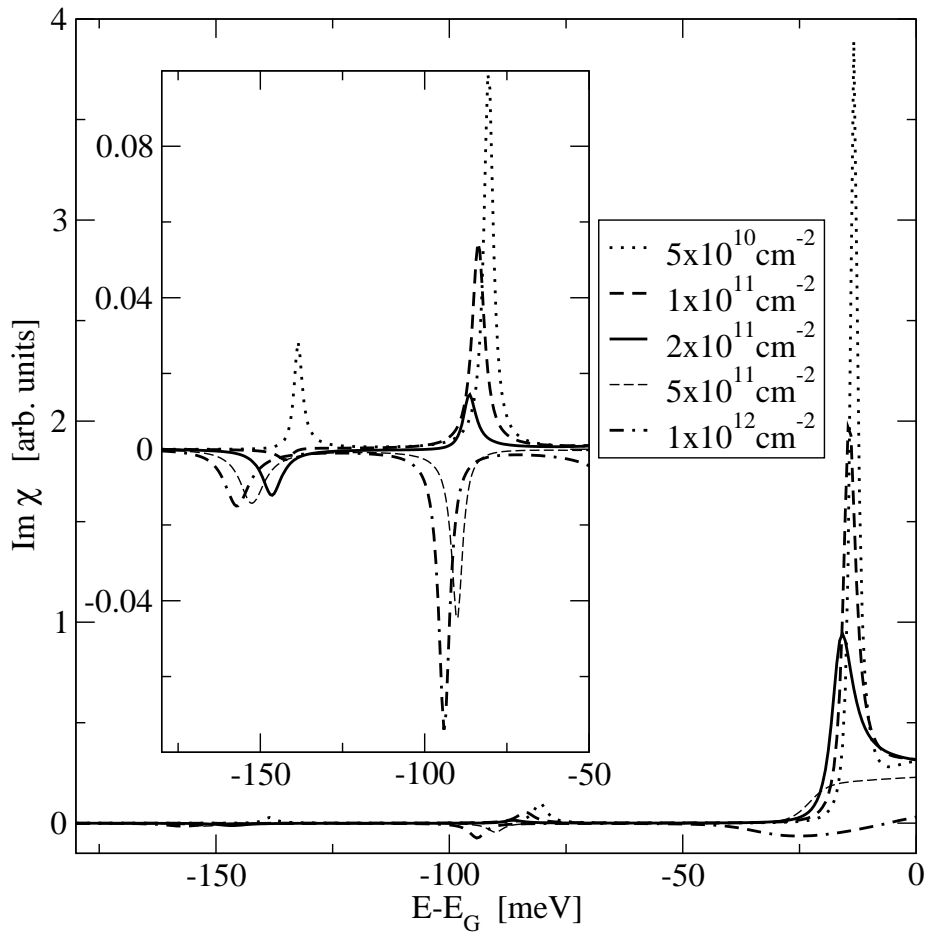


Figure 9.3: Imaginary part of the optical susceptibility for the combined QD-WL system including interaction-induced dephasing and line shifts due to Coulomb interaction for various total carrier densities. The inset shows a scale up of the QD resonances.

in which two carriers merely switch their states, also appear in the WL assisted relaxation and in the WL relaxation.

Figure 9.4 shows that WL assisted relaxation (dash-dotted line) and intra-dot scattering (thin solid line), which include the processes leading to dephasing without redistribution of carriers, are the most important contributions, while WL assisted capture (dotted line) and dot-assisted (dashed line) processes cause a rather small dephasing. However, since this picture can change with carrier density, it is important to test the influence of all dephasing channels individually.

In Figure 9.5 we compare the optical susceptibility from the full calculation (solid line)

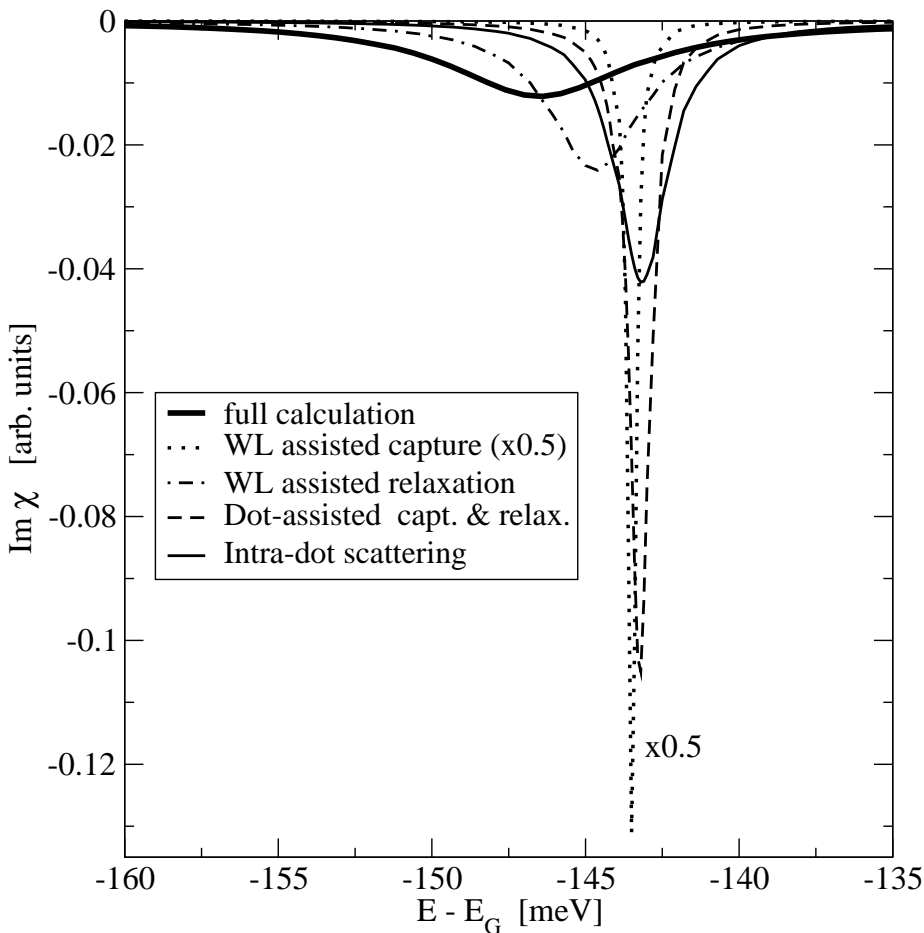


Figure 9.4: Imaginary part of the optical susceptibility for the s-shell resonances at a carrier density of $2 \times 10^{11} \text{ cm}^{-2}$. The result including all considered Coulomb scattering processes (thick solid line) is compared to calculations where only certain classes of processes are evaluated.

with a result where only the diagonal dephasing contributions were taken into account (dotted lines). For the excitonic resonance of the WL, the absence of the off-diagonal dephasing leads to an overestimation of the linewidth by roughly a factor of two under the considered excitation conditions. Using only the diagonal dephasing contributions turns out to be a reasonable approximation for the lowest QD resonances, while for the excited QD transition the lineshape is not fully reproduced. Off-diagonal dephasing contributions are less important for the QD resonances due to the rather large spectral separation between the QD states and the WL states. For the same reason off-diagonal contributions are stronger for the p-shell than for the s-shell.

Note that the foregoing discussion applies to the non-Markovian treatment. If we

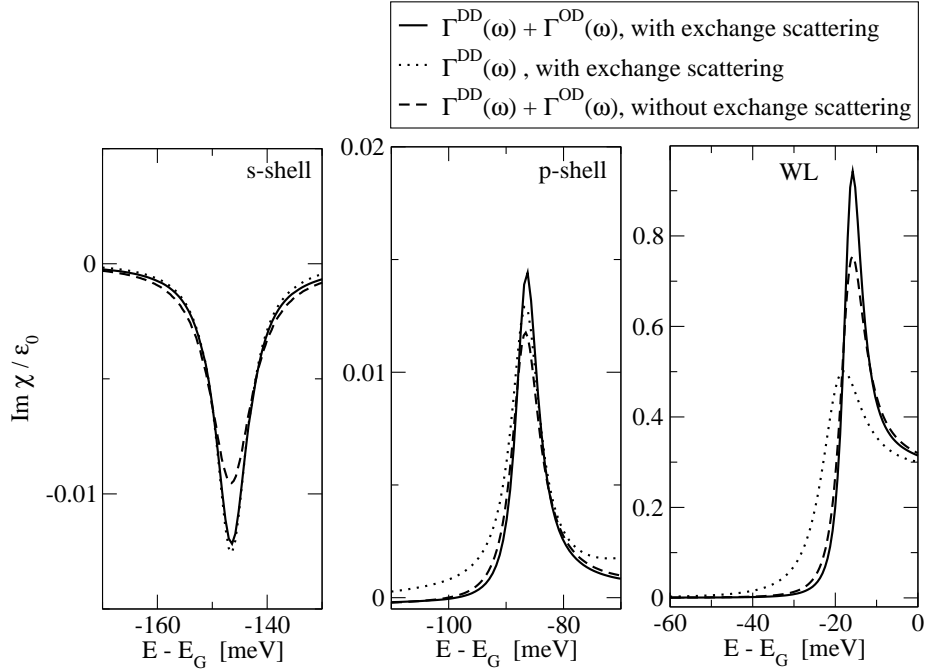


Figure 9.5: Imaginary part of the optical susceptibility for a carrier density of $2 \times 10^{11} \text{ cm}^{-2}$ with full dephasing contributions (solid lines), with diagonal dephasing contributions only (dotted lines), and with diagonal and off-diagonal dephasing but without the exchange scattering in both terms (dashed lines).

neglect the off-diagonal dephasing and uses the Markov approximation, again the dephasing is strongly overestimated when all relevant scattering processes are included. For the discussed QD model, the QD transitions itself would be completely damped out by influences of the WL.

The influence of the exchange term in the dephasing rates, which is often disregarded, is also investigated in Fig. 9.5. Neglecting the exchange scattering in the dephasing contributions clearly overestimates the homogeneous linewidth by about 30 %, thus pointing out that the exchange terms should be included in the calculation.

9.6.2 Renormalization of single-particle states

As discussed in Section 9.5, the single particle renormalizations are of critical importance for the proper determination of the dephasing rates. In Fig. 9.6a the single particle renormalizations due to Coulomb interaction are shown. The Fock and correlation contributions lead to a decrease of the single-particle energies with increasing carrier density. The Hartree terms increase the energies for electrons and decrease

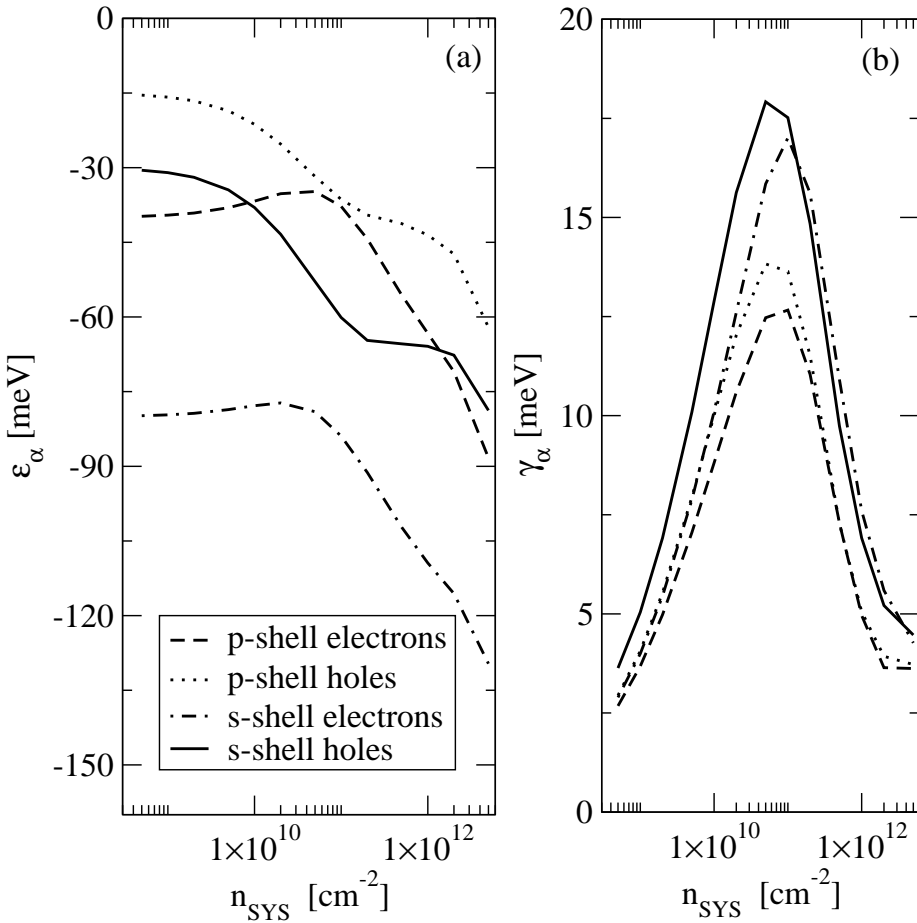


Figure 9.6: Renormalized single-particle energies of the QD states for electrons and holes as a function of the total carrier density in the system (a) and corresponding single-particle broadening(b).

the energies for holes (for a detailed discussion see e.g. Ref. [135]). This leads to slightly increasing (decreasing) single-particle energies for the electrons (holes) from low to intermediate carrier densities. For higher carrier densities, both electron and hole energies strongly decrease.

With increasing carrier densities the single-particle broadening (Fig. 9.6b) strongly grows up to intermediate carrier densities due to the larger number of available scattering partners. For higher carrier densities, the strong single-particle energy shifts lead to a reduction of the scattering efficiency. Additionally at very high carrier densities the intra-dot processes are suppressed due to Pauli-blocking. These effects result in a strong decrease of the single-particle broadening.

9.7 Conclusion

In this chapter we discussed the effects of Coulomb interaction on linear optical spectra of semiconductor QD systems. After a discussion of the relevant assumptions and approximations (and some of their shortcomings) we turned to the calculation of optical spectra with dephasing due to Coulomb interaction. In those spectra, we observe a broad variety of effects. Both the excitation dependence of the dephasing as well as the excitation dependence of the renormalized single particle states can only be described properly by means of a quantum-kinetic theory. We have studied the influence of diagonal and off-diagonal dephasing contributions as well as the influence of different scattering channels. It turns out, that the most important scattering channels are those which include processes that do not cause population changes but only switch two carriers in their states. This is in a way analogous to the pure dephasing mechanisms that dominate the short-time dynamics of dephasing due to acoustic phonons [106]. In the next chapter we will be concerned with the carrier-LO-phonon interaction, that also significantly contributes to dephasing at elevated temperatures.

10 Carrier-phonon interaction

Apart from the Coulomb interaction, one of the main sources of dephasing in QD systems is at elevated temperatures given by the interaction of carrier with LO phonons. Although the carrier phonon interaction was believed for a long time to be inefficient in QDs due to the mismatch between the flat phonon dispersion and the level spacing of the QDs, recent theoretical studies point out that the perturbative approach that underlies this line of reasoning is not valid in QDs and a description of the carrier-LO-phonon interaction in QDs has to use the polaron picture [117, 118]. This quantum-kinetic treatment of the quasi-particle associated with the carrier phonon interaction also calls for an appropriate treatment of dephasing due to carrier-LO-phonon scattering. This theoretical modeling will be the subject of the present chapter. However, as the effects of the carrier-LO-phonon interaction in QDs is described in great detail in Ref. [31] we will try to give only an overview of the basic ingredients of carrier-phonon physics, concentrating our analysis of the dephasing contributions. As mentioned in Chapter 1, the results of this chapter have been obtained in close collaboration with Jan Seebbeck.

10.1 Hamiltonian for the carrier-phonon interaction

The carrier-phonon interaction stems from the interaction of the carriers with the ions of the crystal lattice. If we expand the motion of the ions around their equilibrium positions into a set of eigenmodes $u(\mathbf{q})$ [132, 59], we find the free Hamiltonian of the phonon system in harmonic approximation to be given by

$$\hat{H} = \sum_j \sum_{\mathbf{q}} \hbar \omega_j(\mathbf{q}) \left(\hat{b}_{\mathbf{q},j}^\dagger \hat{b}_{\mathbf{q},j} + \frac{1}{2} \right) , \quad (10.1)$$

where the operators $\hat{b}_{\mathbf{q},j}(\hat{b}_{\mathbf{q},j}^\dagger)$ annihilate (create) a phonon in the eigenmode \mathbf{q} and have a simple harmonic time dependence

$$\hat{b}_{\mathbf{q},j}(t) = \hat{b}_{\mathbf{q},j} e^{-i\omega_j(\mathbf{q}) t} .$$

The index j specifies the phonon branch (LO, LA, TO, TA). In the harmonic approximation, the Hamiltonian is given by a sum over independent harmonic oscillators.

While the harmonic approximation might be good for the understanding of scattering and dephasing, it lacks certain basic phenomena in solids that are associated with phonons. One particularly popular example is the thermal expansion of a solid, that can only be described by taking into account anharmonic effects. However, as we are only interested in the effects of scattering and dephasing, the harmonic approximation is justified. It should be noted, that we will only consider optical phonons, that provide the dominant scattering channel at elevated temperatures, whereas acoustic phonons play the dominant role at low temperatures. Furthermore, TO phonons are neglected as they couple only inefficiently to the carrier system [132].

Using the Hamiltonian (10.1), we can define in complete analogy to the carrier system a Keldysh-GF for the branch j of the phonon dispersion,

$$i\hbar d_j(\mathbf{q}, \underline{t}_1, \underline{t}_2) = \left\langle \hat{b}_{\mathbf{q},j}(\underline{t}_1) \hat{b}_{\mathbf{q},j}^\dagger(\underline{t}_2) + \hat{b}_{\mathbf{q},j}^\dagger(\underline{t}_1) \hat{b}_{\mathbf{q},j}(\underline{t}_2) \right\rangle , \quad (10.2)$$

that describes the correlation of lattice displacements.

The coupling between carriers and LO phonons is described by the Fröhlich coupling [144, 102]. According to Refs. [59, 43], the effective interaction is given by

$$M_{\nu_1\nu_2}^{\text{LO}}(\mathbf{q}) = \frac{M_{\text{LO}}}{\sqrt{V}} \frac{1}{|\mathbf{q}|} \left\langle \nu_1 \left| e^{i\mathbf{q}\mathbf{r}} \right| \nu_2 \right\rangle , \quad (10.3)$$

$$M_{\text{LO}} = \sqrt{\alpha \frac{4\pi\hbar}{\sqrt{2}\mu} (\hbar\omega_{\text{LO}})^{3/2}} . \quad (10.4)$$

It includes the reduced mass μ and the dimensionless polar coupling constant

$$\alpha = \frac{e^2}{8\pi\varepsilon_0} \frac{1}{\hbar\omega_{\text{LO}}} \sqrt{\frac{2\mu\omega_{\text{LO}}}{\hbar}} \left(\frac{1}{\varepsilon_\infty} - \frac{1}{\varepsilon_b} \right) , \quad (10.5)$$

that contains information about the coupling strength and can reach from values of $\alpha = 0.06$ for GaAs systems that are considered here, over value of $\alpha \approx 0.5$ for II-VI or nitride semiconductors to values of well over $\alpha = 2$, e.g. for alkali halides [145].

For the interaction of carriers with LO phonons we are typically interested in self-energy diagrams, in which the external lines are carrier GFs, as other diagrams would describe the back-interaction to the phonon system. The basic building block that exhibits this structure,

$$D_{\alpha\beta\gamma\delta}(\underline{t}_1, \underline{t}_2) = \sum_{\mathbf{q}} M_{\alpha\delta}(\mathbf{q}) d(\underline{t}_1, \underline{t}_2) M_{\gamma\beta}(-\mathbf{q}) , \quad (10.6)$$

contains two basic carrier-phonon interaction vertices M connected by a phonon GF d . As shown in Ref. [43] and inferable from Eq. (10.6), the carrier-phonon interaction

acts on the carrier system as an effective Coulomb interaction, only that (like the screened Coulomb interaction) it is not instantaneous. This also means that the techniques that we have developed for the screened Coulomb interaction can be directly transferred to the carrier-LO-phonon interaction [43].

As we do not consider the back action of the carrier system onto the phonon system or the relaxation of the phonon system itself, which are two whole fields of research on their own, it is a natural and convenient choice to treat the phonon system as a thermal bath. This leads to the free phonon propagator [102, 59]

$$i\hbar d^{\gtrless}(t_1, t_2) = N_{\text{LO}} e^{\pm i\omega_{\text{LO}}(t_1 - t_2)} + (N_{\text{LO}} + 1) e^{\mp i\omega_{\text{LO}}(t_1 - t_2)}. \quad (10.7)$$

As phonons are of bosonic character, the equilibrium phonon population at the lattice temperature T is given by a Bose distribution function.

$$N_{\text{LO}} = \frac{1}{e^{\frac{\hbar\omega_{\text{LO}}}{k_B T}} - 1}. \quad (10.8)$$

In Figure 10.1 both the basic interaction vertex as well as the effective Coulomb-like interaction are shown.

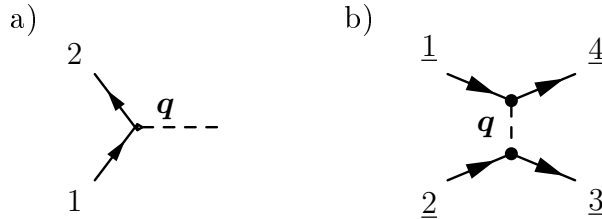


Figure 10.1: (a) Basic interaction vertex for the carrier-phonon interaction (b) basic building block of the effective Coulomb-like interaction between carriers by means of the carrier-phonon interaction.

10.2 RPA selfenergy

The first order selfenergy diagram for the carrier-phonon interaction is shown in Figure 10.2. On the Keldysh contour, it can be written as

$$\Sigma^{\text{RPA}}(\underline{1}, \underline{2}) = -i\hbar G(\underline{1}, \underline{2}) D(\underline{2}, \underline{1}). \quad (10.9)$$

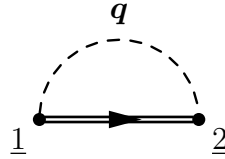


Figure 10.2: RPA selfenergy for the carrier-phonon interaction.

Unfolding the Keldysh contour we find for the greater, lesser, and retarded components

$$\Sigma^{\text{RPA},\gtrless}(1, 2) = -i\hbar G^{\gtrless}(1, 2) D^{\lessgtr}(2, 1) , \quad (10.10)$$

$$\Sigma^{\text{RPA},\text{R}}(1, 2) = -i\hbar [D^>(1, 2) G^{\text{R}}(1, 2) - D^{\text{R}}(1, 2) G^<(1, 2)] . \quad (10.11)$$

Expanding into the single-particle basis (7.2), using the phonon propagator (10.7) and the interaction matrix element (10.3), the selfenergy can be cast into the form

$$\Sigma_{\alpha\beta}^{\text{RPA},\gtrless}(t_1, t_2) = -i\hbar \sum_{\gamma\delta} \sum_{\mathbf{q}} M_{\alpha\gamma}(\mathbf{q}) M_{\delta\beta}(-\mathbf{q}) G_{\gamma\delta}^{\gtrless}(t_1, t_2) d_{\mathbf{q}}^{\gtrless}(t_1, t_2) \quad (10.12)$$

$$\begin{aligned} \Sigma_{\alpha\beta}^{\text{RPA},\text{R}}(t_1, t_2) = & -i\hbar \sum_{\gamma\delta} \sum_{\mathbf{q}} M_{\alpha\gamma}(\mathbf{q}) M_{\delta\beta}(-\mathbf{q}) \\ & \times [d_{\mathbf{q}}^>(t_1, t_2) G_{\gamma\delta}^{\text{R}}(t_1, t_2) - G_{\gamma\delta}^<(t_1, t_2) d_{\mathbf{q}}^{\text{R}}(t_1, t_2)] . \end{aligned} \quad (10.13)$$

To recline the notation for the phonon propagators to that for the Coulomb interaction, we will merge interaction matrix elements and phonon propagator according to an effective propagator, defined as

$$D_{\alpha\beta\gamma\delta}^{\gtrless}(t_1, t_2) = \sum_{\mathbf{q}} M_{\alpha\delta}(\mathbf{q}) M_{\gamma\beta}(-\mathbf{q}) d^{\gtrless}(t_1, t_2) . \quad (10.14)$$

10.3 Polaron in semiconductor quantum dots

One of the most important influences of the carrier-phonon interaction is the formation of a new quasi-particle. The quasi-particle obtained by dressing the carriers with the carrier-phonon interaction – the polaron – describes the lattice distortion accompanying the electron in its motion. In the framework of GFs polarons are described using the retarded GF Kadanoff-Baym equation (4.63) in the eigenfunction expansion (7.2)

$$\begin{aligned} \left[i\hbar \frac{\partial}{\partial \tau} - e_\alpha^a \right] G_\alpha^{a,R}(\tau) &= \delta(\tau) \\ &+ \int d\tau' \Sigma_\alpha^{a,\text{ret}}(\tau - \tau') G_\alpha^{a,\text{ret}}(\tau') , \end{aligned} \quad (10.15)$$

where we have used the explicit form of G_0^{-1} from Eq. (8.9). As for the Coulomb interaction we restrict our analysis to retarded GFs that are diagonal in both state and band index, as the inclusion of off-diagonal contributions has only a minor influence on the results [146]. The corresponding retarded selfenergy in RPA is given by

$$\Sigma_\alpha^{a,R}(\tau) = i\hbar \sum_\beta G_\beta^{a,R}(\tau) D_{\beta\alpha\beta\alpha}^<(-\tau). \quad (10.16)$$

We assume for the calculations restricted to electron-phonon interaction that the polaronic retarded GF is not influenced by population effects, thus neglecting the second term in Eq. (10.13), which describes the influences of carrier populations (cf. the connection between $G^<$ and the elements of the density matrix, Eq. (8.13)). This has been verified for a bulk system in Ref. [147].

Using the results from the previous section, we can rewrite the effective phonon propagator as

$$\begin{aligned} i\hbar D_{\beta\alpha\beta\alpha}^<(\tau) &= \frac{M_{LO}^2}{e^2/\varepsilon_0\varepsilon_b} V_{\beta\alpha\beta\alpha} \\ &\times \left[N_{LO} e^{-i\omega_{LO}\tau} + (1 + N_{LO}) e^{i\omega_{LO}\tau} \right] , \end{aligned} \quad (10.17)$$

with the bare Coulomb matrix element $V_{\beta\alpha\beta\alpha}$ defined in Eq. (7.12). For the eigenmodes of the phonon system, we restrict ourselves to LO-phonons that posses a nearly constant dispersion around $\mathbf{q} = 0$ and that hence are treated as monochromatic with the frequency ω_{LO} .

The result of the calculation for the spectral functions of the electrons, that is the imaginary part of the retarded GF (cf. Eq.(4.24)), is shown in Figure 10.3. We find a complex structure, exhibiting a polaron shift to lower energies as well as a broadening of the main peak. Additionally we observe phonon replicas spaced approximately one LO phonon energy apart. Moreover, a closer examination reveals a hybridization of individual peaks, as e.g. phonon replicas of the p-shell come close to the main peak of the s-shell spectral function. This shows, that even though the coupling parameter for the GaAs material system $\alpha = 0.06$ is fairly small, due to the influences of the confinement we are already in the strong coupling regime. This makes a description of the carrier-phonon interaction in QDs by means of perturbative methods faulty. An relatively straightforward approach to the understanding of the

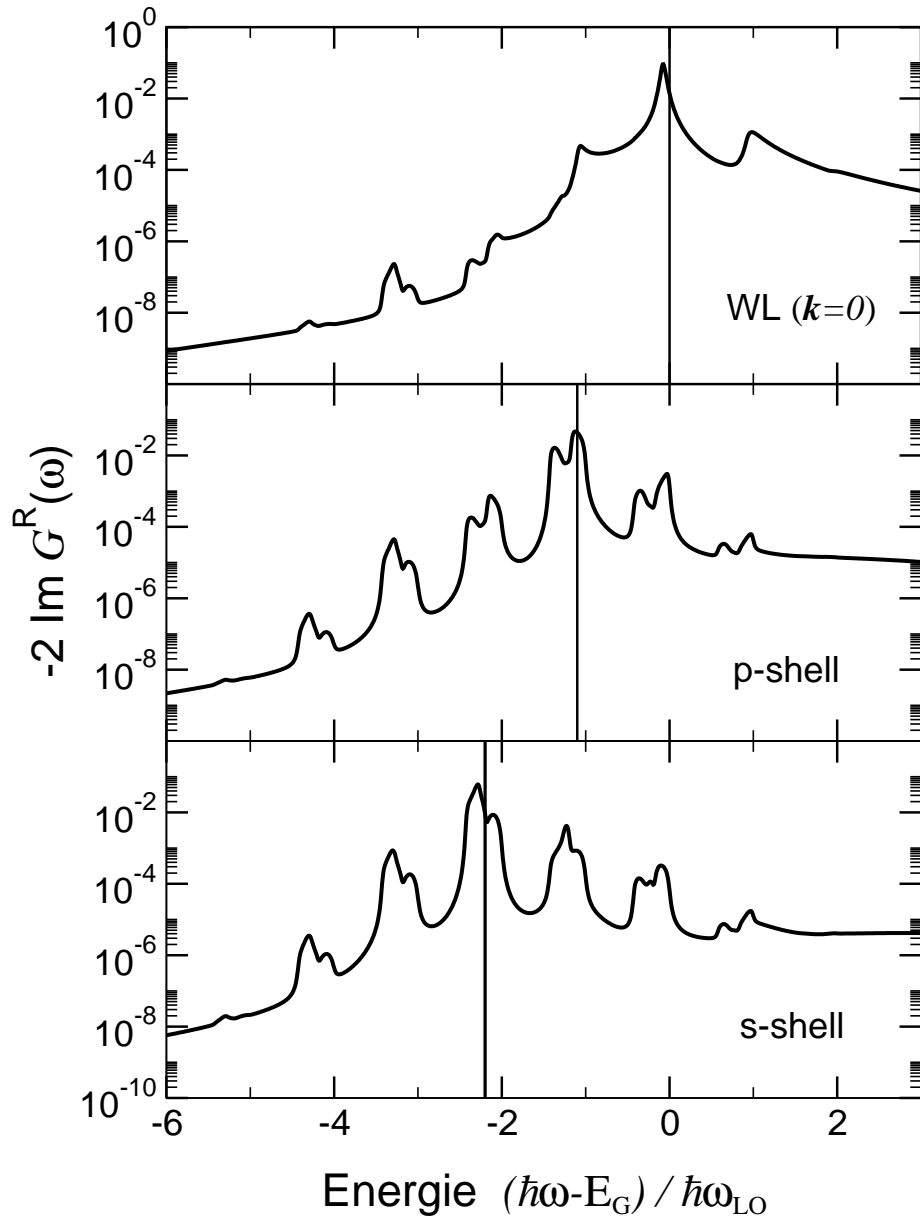


Figure 10.3: Polaronic spectral function in a logarithmic representation for
 (a) WL $\mathbf{k} = 0$ state
 (b) QD p-shell
 (c) QD s-shell .

Picture courtesy of Jan Seebeck.

basic mechanisms of the polaron problem in semiconductor QDs is given by the independent boson model that describes the interaction of a single electronic level with a bath of phonons [102] and by the Jaynes-Cummings model [148] that describes the coupling between different electronic shells via a single-mode of the phonon field. While the former model predicts the structure of phonon satellites spaced one phonon energy apart, the latter describes the hybridization of individual satellites in the spectral function by means of the phonon field. With the combination of these two models we can understand the structure of the QD spectral function, even though the interaction with the WL leads to some modifications. For details we refer to the detailed discussion of this subject in Ref. [31].

After having studied the polaron itself we now focus on the correlation contributions caused by the carrier-LO-phonon interaction. Using the same calculation scheme as for the Coulomb interaction, we can derive the correlation contributions due to electron-LO-phonons interaction.

10.4 Dephasing contributions

In Ref. [118], quasi-particle renormalizations described by a polaronic retarded GFs have been used within a quantum-kinetic theory to evaluate scattering processes and populations changes. In this chapter we show the corresponding treatment of the polarization dynamics to analyze the corresponding dephasing and interband-energy renormalizations. Following the same scheme as for the Coulomb interaction, we can evaluate the dephasing contributions for the carrier-LO-phonon interaction in the frequency domain, leading to

$$S_\alpha^{\text{eh}}(\hbar\omega) \Big|_{\text{Phon}} = - \Gamma_\alpha^{\text{DD}}(\hbar\omega) \Big|_{\text{Phon}} \psi_\alpha^{\text{eh}}(\hbar\omega) + \Gamma_{\alpha\delta}^{\text{OD}}(\hbar\omega) \Big|_{\text{Phon}} \psi_\delta^{\text{eh}}(\hbar\omega), \quad (10.18)$$

with

$$\begin{aligned} \Gamma_\alpha^{\text{DD}}(\hbar\omega) \Big|_{\text{Phon}} &= i \sum_{\substack{a,b=e,h \\ b \neq a}} \sum_\beta \frac{M_{LO}^2}{e^2/\varepsilon_0\varepsilon_b} V_{\alpha\beta\alpha\beta} \\ &\quad \left\{ (1 - f_\beta^a) [(1 + N_{\text{LO}}) G_{\beta,\alpha}^{a,b}(\hbar\omega - \hbar\omega_{\text{LO}}) \right. \\ &\quad \quad \quad \left. + N_{\text{LO}} G_{\beta,\alpha}^{a,b}(\hbar\omega + \hbar\omega_{\text{LO}})] \right. \\ &\quad + f_\beta^a [(1 + N_{\text{LO}}) G_{\beta,\alpha}^{a,b}(\hbar\omega + \hbar\omega_{\text{LO}}) \\ &\quad \quad \quad \left. + N_{\text{LO}} G_{\beta,\alpha}^{a,b}(\hbar\omega - \hbar\omega_{\text{LO}})] \right\} \end{aligned} \quad (10.19)$$

and

$$\Gamma_{\alpha\beta}^{\text{OD}}(\hbar\omega) \Big|_{\text{Phon}} = i \sum_{\substack{a,b=e,h \\ b \neq a}} \frac{M_{LO}^2}{e^2/\varepsilon_0\varepsilon_b} V_{\alpha\beta\alpha\beta} \\ \left\{ (1 - f_\alpha^a) \left[(1 + N_{\text{LO}}) G_{\beta,\alpha}^{b,a}(\hbar\omega - \hbar\omega_{\text{LO}}) \right. \right. \\ \left. \left. + N_{\text{LO}} G_{\beta,\alpha}^{b,a}(\hbar\omega + \hbar\omega_{\text{LO}}) \right] \right. \\ \left. + f_\alpha^a \left[(1 + N_{\text{LO}}) G_{\beta,\alpha}^{b,a}(\hbar\omega + \hbar\omega_{\text{LO}}) \right. \right. \\ \left. \left. + N_{\text{LO}} G_{\beta,\alpha}^{b,a}(\hbar\omega - \hbar\omega_{\text{LO}}) \right] \right\}. \quad (10.20)$$

In these equations we have introduced the abbreviation

$$G_{\beta,\alpha}^{a,b}(\omega) = \int d\tau e^{i\omega\tau} G_{\beta}^{a,R}(\tau) G_{\alpha}^{b,R}(\tau), \quad (10.21)$$

for the Fourier transform of a product of two retarded polaronic GFs. Through these functions polaronic renormalization effects such as phonon replicas and hybridization between the localized states (cf. Figure 10.3) are included in Eqs. (10.19) and (10.20).

10.5 Optical spectra

The optical spectra with dephasing due to Coulomb interaction exhibit only three resonances, namely s-shell, p-shell and the excitonic resonance of the WL. Absorption spectra with dephasing contributions due to interaction of carriers with LO phonons are shown in Fig. 10.4. Polaronic renormalizations of the single-particle states lead to a more complicated resonance structure for the interband transitions displayed in the inset of Fig. 10.4. We can identify phonon replicas and results of the hybridization of the single-particle states. For example, the s-shell resonances has a shoulder on the lower energetic side due to hybridization of the corresponding electron state. Energetically above the resonances of the s-shell and the p-shell several peaks due to phonon replicas and their hybridizations can be observed. The non-Lorentzian character of the lineshapes is even more pronounced than for the spectra with dephasing due to Coulomb interaction. The damping of the resonances at higher carrier densities is rather weak, and a saturation of the s-shell gain is not found. This shows that at elevated carrier densities, the Coulomb interaction needs to be included. After our discussion of the Coulomb interaction in Chapter 9 and of the carrier-phonon interaction in this chapter, the subject of the next chapter is the calculation of optical spectra taking both dephasing mechanisms into account.

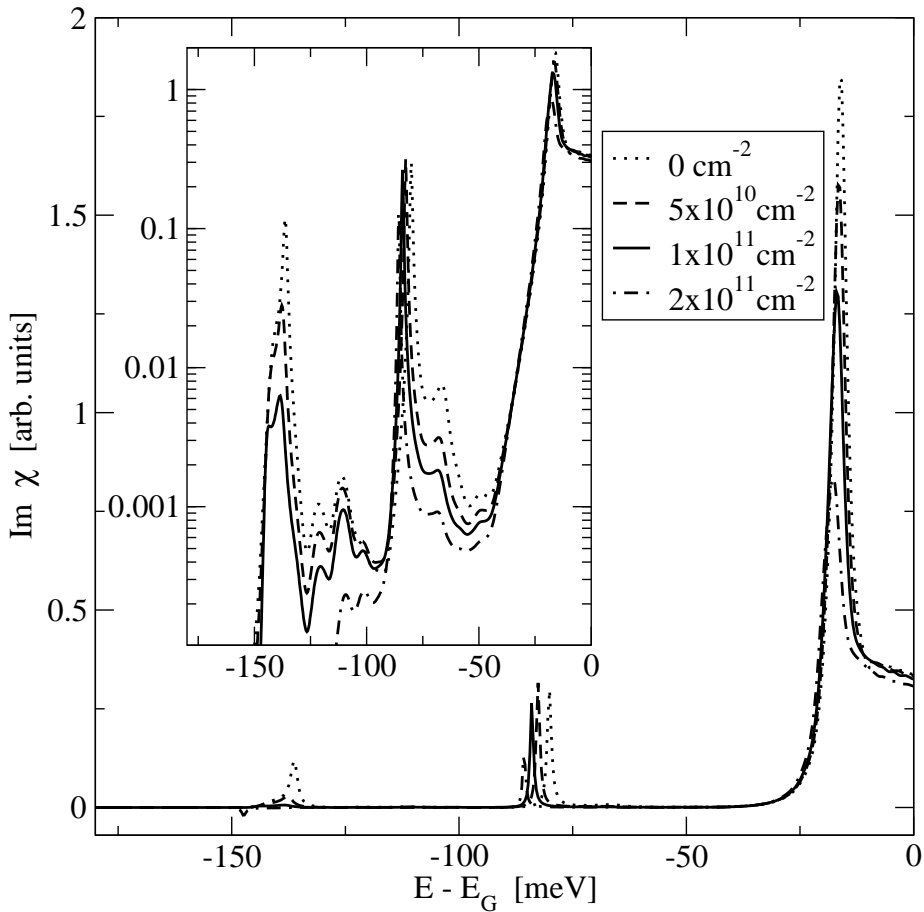


Figure 10.4: Imaginary part of the optical susceptibility for the combined QD-WL system including interaction-induced dephasing and line shifts due to carrier-phonon interaction for various total carrier densities. The inset is a logarithmic representation that reveals the more complicated structure of the spectra.

11 Dephasing due to carrier-phonon and Coulomb interaction

After studying the dephasing due to Coulomb interaction and due to carrier-phonon interaction separately in the last two chapters, we now would like to study the inclusion of both interaction mechanisms into the calculation of optical spectra.

The easiest and also rather intuitive way of evaluating the combined influence of Coulomb and carrier-phonon interaction is to add the dephasing contributions due to both mechanisms

$$S_{\alpha}^{\text{eh}}(\hbar\omega) = S_{\alpha}^{\text{eh}}(\hbar\omega)\Big|_{\text{Coul}} + S_{\alpha}^{\text{eh}}(\hbar\omega)\Big|_{\text{Phon}}. \quad (11.1)$$

In Fig. 11.1 the resulting absorption spectra are shown. In contrast to our results for the dephasing due to Coulomb interaction only in Figure 9.3, the optical spectra including also dephasing due to carrier-phonon interaction display a more complicated structure, since various kinds of polaronic features are revealed. As in the case of dephasing only due to Coulomb interaction (Figure 9.3), we find the bleaching and red-shift of the resonances and also the saturation of the s-shell gain. We observe that the Coulomb interaction is clearly the dominant dephasing mechanism for high carrier densities, although even in the gain regime some of the polaronic features remain present. For example, the high energetic side of the p-shell resonance shows a second peak at low densities (arrow 1), which becomes completely damped out with increasing carrier density. On the other hand, the peak on the low energetic side of the p-shell resonance (arrow 2) is almost not visible at low densities but becomes more pronounced in the gain regime.

It is expected that these polaronic features vanish at high densities as the polaronic features in the spectral function should be damped out by Coulomb effects. This requires a self-consistent treatment of the spectral properties with inclusion of both Coulomb and polaronic effects. The basic shortcoming of the combined treatment presented here, lies in the fact, that from a principle viewpoint not the dephasing contributions but the *selfenergies* (or equivalently the Hamiltonians) of the Coulomb and carrier-phonon interaction are additive. Via the interaction, the two mecha-

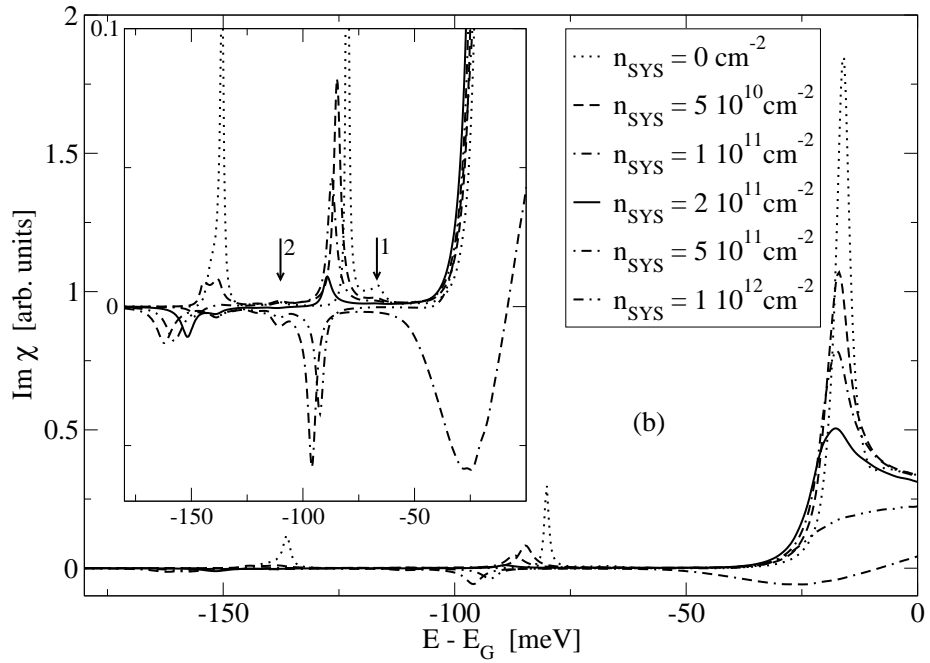


Figure 11.1: Imaginary part of the optical susceptibility for the combined QD-WL system and various carrier densities with dephasing due to Coulomb and carrier-phonon interaction.

The inset shows a magnification of the QD resonances ($T=300\text{K}$).

nisms influence each other and these influences are neglected when simply adding the dephasing contributions.

11.1 Selfconsistent inclusion of both interaction mechanisms

Having shown, that a naive approach for the inclusion of both interaction mechanisms gives results, that are qualitatively unsatisfactory, we now give a self-consistent model for the combined influence of the carrier-carrier Coulomb scattering and the interaction of carrier with LO phonons. Since our goal is a calculation of optical spectra for the QD-WL system under the influence of correlation effects at elevated carrier densities, we use for the description of polaronic single-particle properties a retarded GF obeying Eq. (10.15) with the free carrier energies e_α^a in the LHS replaced by renormalized energies $\tilde{\varepsilon}_\alpha^a = e_\alpha^a + \Delta_\alpha^a - i\gamma_\alpha^a$, which are determined from Eqs. (9.42) and (9.43)(cf. the definition in Eq. (9.41)). In other words the polaron is obtained by dressing with the phonon interaction not the free particles, but the quasi-particles

obtained by Coulomb renormalization. Rewriting the retarded GF as

$$G_{\alpha}^{\text{a,R}}(\tau) = \mathcal{G}_{\alpha}^a(\tau) e^{-\frac{i}{\hbar}(\Delta_{\alpha}^a - i\gamma_{\alpha}^a)\tau}, \quad (11.2)$$

we separate in $\mathcal{G}_{\alpha}^a(\tau)$ the phonon renormalization effects, which are influenced by the presence of the Coulomb interaction, as the equation obeyed by \mathcal{G} still contains Δ and γ . The finite lifetime of these quasi-particles produces in general sufficient damping to reduce the polaronic GF \mathcal{G}_{α}^a to a single-pole structure. This pole is used instead of e_{α}^a in Eq. (9.42). In this way the Coulombian and the polaronic problems become coupled and have to be solved self-consistently. The iterative solution to this problem converges rapidly. Results of the spectral function of QD and WL states are shown in Fig. 11.2. Even for low carrier densities, polaronic structures are strongly broadened as a result of the dominant role of damping due to Coulomb scattering. For low carrier densities the exponential decay $e^{-\frac{\gamma_{\alpha}^a}{\hbar}\tau}$ due to Coulomb interaction, which is superimposed to the polaronic function $\mathcal{G}_{\alpha}^a(\tau)$ in Eq. (11.2), might overestimate the damping of the polaronic resonances. Nevertheless at higher carrier densities we expect a strong broadening of the polaron satellites.

In Fig. 11.3 calculated absorption spectra are shown, which include correlations due to carrier-carrier scattering (Eqs. (9.34)–(9.35)), and interaction with LO-phonons, (Eqs. (10.19)–(10.20)), both evaluated with self-consistently renormalized single-particle energies. As for the result for dephasing due to Coulomb interaction, shown in Figure 9.3, we see the bleaching and red-shift of the resonances due to many-body interactions and also the saturation of the s-shell gain. Although we observe that the Coulomb interaction is the clearly dominant dephasing mechanism for high carrier densities, we also infer from a comparison of Figs. 11.3 and 9.3 that even in the gain regime the electron-phonon interaction gives rise to a clear increase in the dephasing. Nevertheless, polaronic features that we observed in Section 10.5 are absent in the spectra, since the complicated multi-peak structure of the spectral function is completely damped out due to Coulomb effects.

For intermediate carrier densities around $5 \times 10^{10} \text{ cm}^{-2}$, both types of interaction processes are equally important. Comparing the results in Figure 11.4 we can conclude for the situation investigated here, that taking only the Coulomb dephasing mechanism into account underestimates the dephasing of the ground state transition by roughly a factor of two, while the damping of the WL is even dominated by carrier-phonon interaction. For higher carrier densities, however, this picture changes, as can be seen in Figure 11.5. Using a carrier density of $2 \times 10^{11} \text{ cm}^{-2}$, the Coulomb interaction is clearly the dominant mechanism for the QD resonances. For the excitonic resonance of the WL, the two mechanisms are equally important even at this rather high carrier density, where we are already in the gain regime for the s-shell transition.

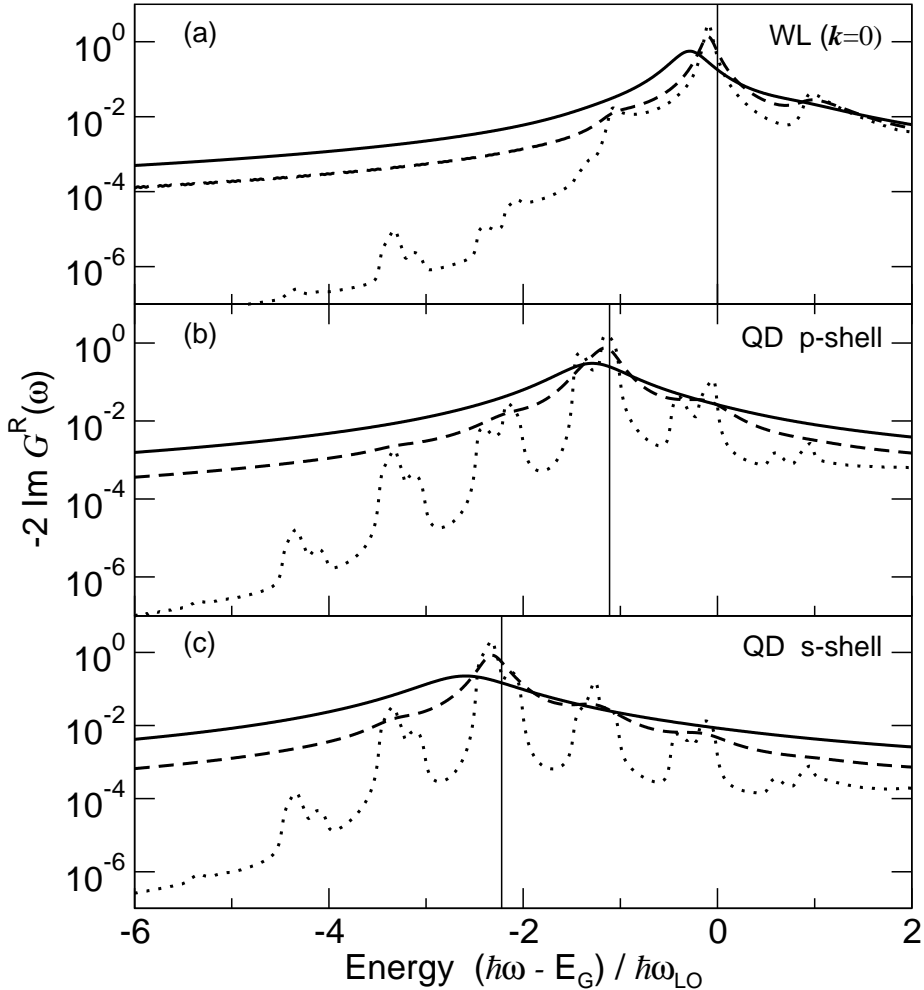


Figure 11.2: Spectral function of the $k = 0$ WL state and the QD p- and s-shell states including the interaction with LO phonons and Coulomb interaction of carriers. The zero density case (dotted line) is compared to total carrier densities of $5 \times 10^8 \text{ cm}^{-2}$ (dashed line) and $2 \times 10^{11} \text{ cm}^{-2}$ (solid line). Vertical lines indicate the free carrier energies.

Comparison with experimental observations

In Refs. [149] and [150] photoluminescence (PL) spectroscopy measurements revealed homogeneous linewidths of several meV at room temperature. Comparable results have also been found by four-wave mixing experiments [113]. Our microscopic calculations can reproduce these experimental findings qualitatively. A direct quantitative comparison, which is not our purpose here, would require better knowledge of the

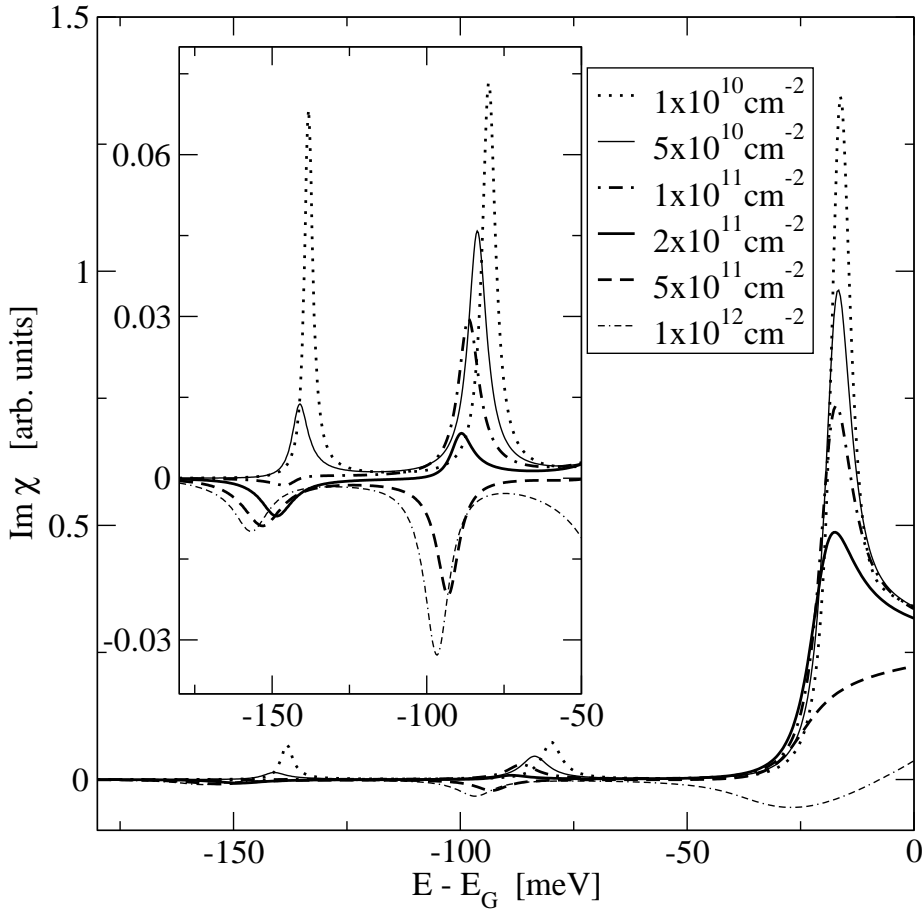


Figure 11.3: Imaginary part of the optical susceptibility for the combined QD-WL system including interaction-induced dephasing and line shifts due to Coulomb interaction and carrier-phonon interaction for various total carrier densities. The inset shows a magnification of the QD resonances.

specific QD parameters such as energy levels, material composition and so on.

In most experiments, the emission from an ensemble of QDs is studied such that the additional inhomogeneous broadening of the QD resonances due to size and composition fluctuations contributes. However, recent experiments [149, 150] have been performed at room temperature on single QDs to eliminate inhomogeneous effects. Those experiments revealed homogeneous linewidths of several meV at room temperature. Comparable results have also been found by four-wave mixing experiments [113].

In Figure 1(a) of Ref. [150] optical spectra are displayed for different pulse excitation

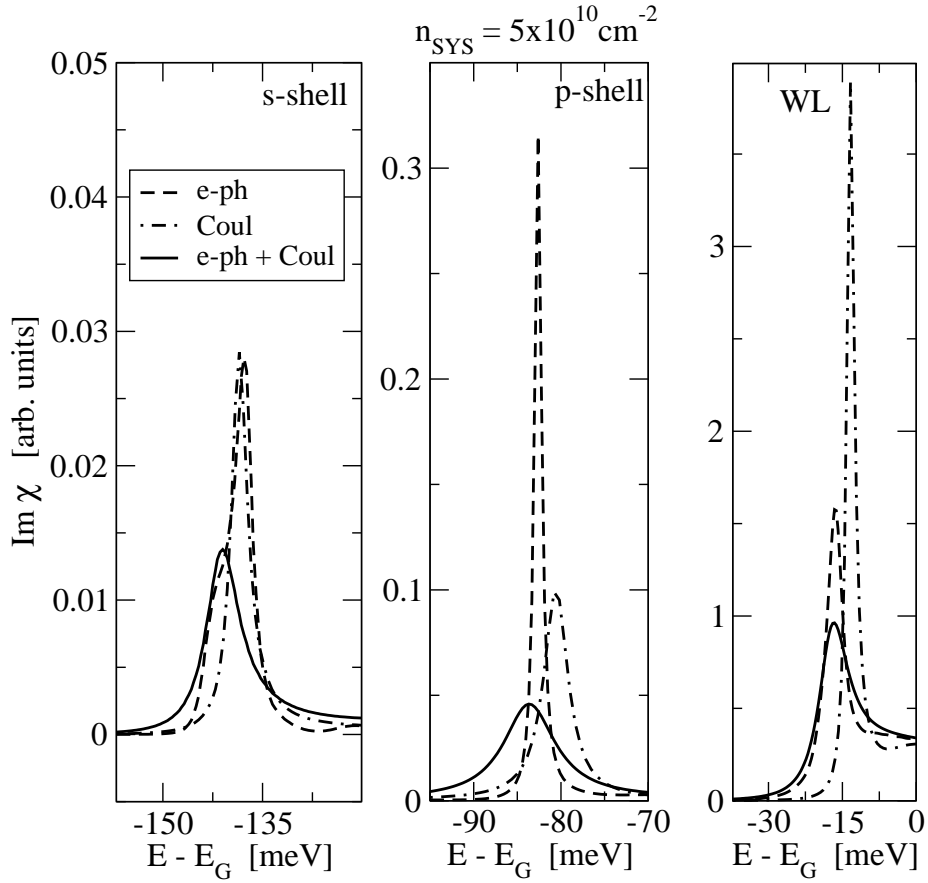


Figure 11.4: Comparison of spectra with different dephasing mechanisms for a carrier density of $5 \times 10^{10} \text{ cm}^{-2}$.

intensities. Although a direct comparison of the excitation dependence is not possible, due to uncertainties in the carrier densities generated in the experiment, the general features of the spectra are identical. A clear distinction between the QD transitions and the excitonic resonance of the WL can be observed. The QD resonances show a density dependent bleaching and a pronounced red shift due to many-body correlations while the spectral position of the WL is almost unchanged. This implies that the red-shift of the QD resonances cannot be attributed to band-gap shrinkage effects of the WL, but are rather purely correlation induced. The observed homogeneous linewidth in Ref. [150] is 8–13 meV depending on the excitation intensity. Whereas this is larger than our findings, we have to take into account that the QD investigated in Ref. [150], has three confined electronic shells, which results in more dephasing channels. A better comparison is possible with the results of Ref. [149] because in that paper a QD is investigated that has two confined electronic shells

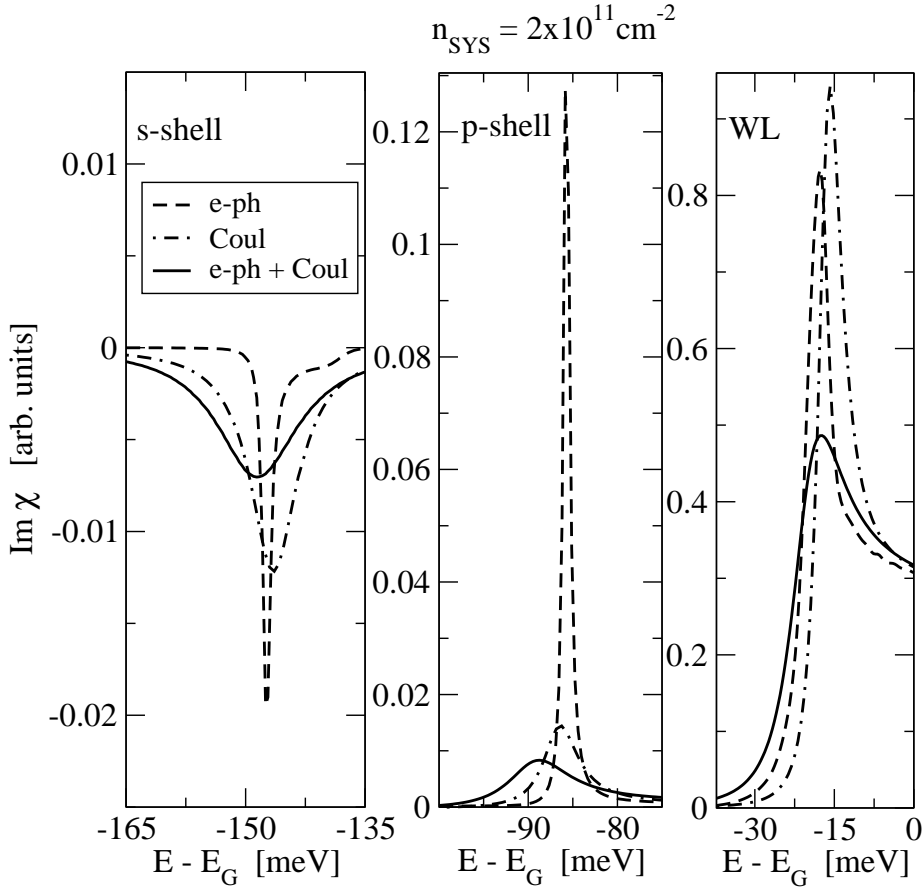


Figure 11.5: Comparison of spectra with different dephasing mechanisms for a carrier density of $2 \times 10^{11} \text{ cm}^{-2}$.

and therefore closely resembles our model system. Regarding the s-shell resonance, we can infer from Figure 3 of Ref. [149] that the observed homogeneous linewidth is slightly above 3 meV at room temperature which is even quantitatively comparable the results we obtain for a wide range of carrier densities.

For a better comparison with experiments, we have also calculated the temperature dependence of the homogeneous linewidth in a temperature range in which the influence of LA-phonons remains small. As shown in Figure 11.6, for low carrier densities (where carrier-carrier scattering is sufficiently weak) we obtain the expected reduction of dephasing with decreasing temperature, as observed in Ref. [149]. For the case of a higher excitation density of 10^{10} cm^{-2} , the linebroadening is almost temperature independent due to a balancing of different scattering channels. The dephasing due to LO-phonons decreases with temperature as in the low-density case. However,

the Coulomb interaction is no longer negligible for this carrier density. With decreasing temperature, the WL states are less populated while the occupation of QD states increases. This enhances intra-dot relaxation processes and provides stronger dephasing due to Coulomb interaction.

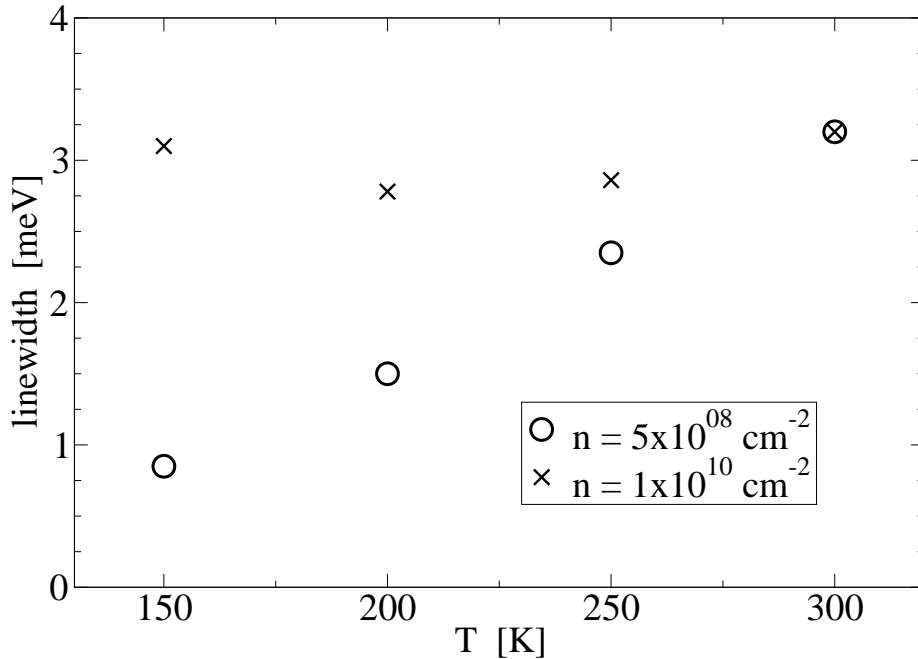


Figure 11.6: Temperature dependence of the linewidth (full half-width) for the QD ground state resonance and different carrier densities.

Concluding this section, we can infer that our theoretical model can reproduce recent experimental findings, if inhomogeneous effects were ruled out in those experiments either by performing experiments on single QDs or by experimental techniques like four-wave mixing that are not sensitive to inhomogeneous effects. Our microscopic approach is able to reproduce the strong red-shift of the QD resonances that was observed in Ref. [150], as well as values for the homogeneous linewidth, that are in good agreement with the experimental findings of Ref. [149].

11.2 A shortcoming of our theoretical model

Even though we have highlighted the importance of using renormalized energies in the dephasing rates, a closer examination of the frequency dependence still reveals a shortcoming of the presented model. This is highlighted in Figure 11.7, where the

frequency dependence of the diagonal dephasing is investigated together with the absorption spectrum. The positions of the peaks of the diagonal dephasing rate do

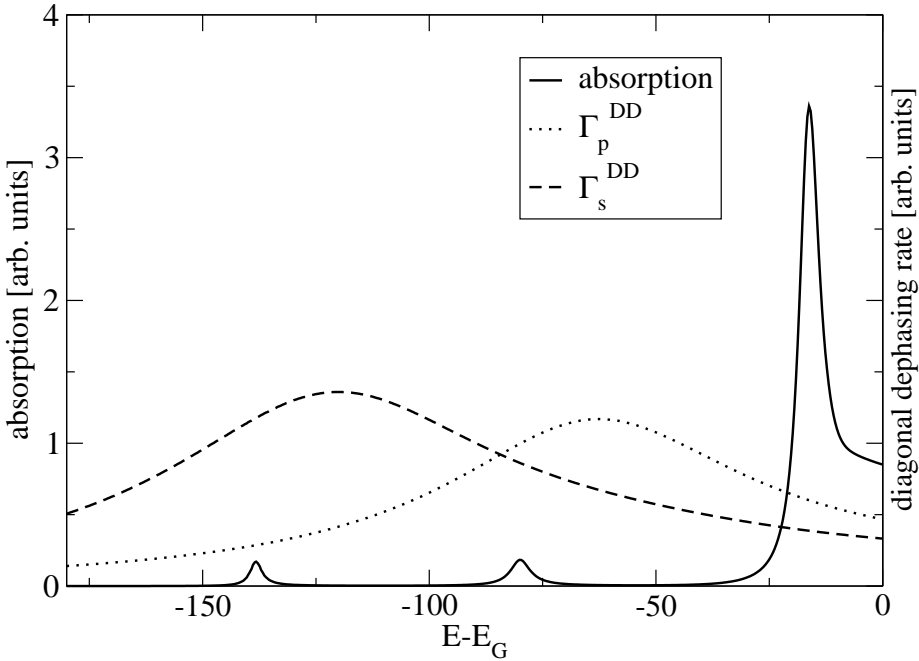


Figure 11.7: Frequency dependence of the diagonal dephasing contributions and of the absorption for a carrier density of $1 \times 10^{10} \text{ cm}^{-2}$

not coincide with the positions of the QD resonances in the absorption. This is due to the fact that in the equation for the energy renormalizations we do not have an analogue of the energy shift due to the renormalized Rabi energy. Indeed if one does artificially switch off the renormalized Rabi energy in the calculations, the positions of the peaks in absorption and dephasing rate coincide exactly. However, an inclusion of the analogous contributions in the energy renormalizations is not easily achievable, as it would call for a T-matrix description of the spectral functions. However, as we can infer from Figure 11.7 the deviations of the dephasing taken either at its maximum or at the position of the absorption peak are only about 10%, even for a rather low carrier density of $1 \times 10^{10} \text{ cm}^{-2}$. This means that for higher carrier densities, where the broadening of the peak in the dephasing is expected to be higher, this error decreases further. Moreover, the off-diagonal dephasing suffers from the same problem and the error in the total dephasing, that is governed by the compensation of both terms is likely to be even smaller. For this reason we will employ the theory presented so far for the calculation of device relevant QD quantities in the next chapter. However, this section points toward a possible improvement of our theoretical model that might

be the subject of further studies.

12 Applications to quantum-dot gain media

The advantages of semiconductor quantum-dot (QD) lasers are being intensively studied and discussed in literature. Low transparency carrier density, high differential gain and small carrier-induced refractive index change have been predicted [151]. For laser devices, these gain medium properties translate to low threshold currents, temperature-insensitive performance, suppression of filamentation and reduced sensitivity to optical feedback, all of which have been experimentally demonstrated [152, 153, 154, 155]. Furthermore, the damping of relaxation oscillations has been studied [156]. Some questions remain, e.g., the extend to which high-speed modulation characteristics can be better than in quantum-well (QW) lasers [157]. A first step towards answering this question is the knowledge of the excitation dependencies of the gain and the carrier-induced refractive index. The former helps to determine the modulation bandwidth, while the latter controls the noise characteristics from frequency chirp and laser linewidth.

The beneficial QD gain and refractive index properties are linked to the discrete nature of the energy spectrum associated with localized carrier states. Application of a simple atom-like (i.e., non-interacting two-level system) description predicts symmetric absorption and gain resonances, as well as the absence of carrier-induced refractive index changes at the resonance peaks. The atom-like description is an acceptable approximation in many situations, such as when inhomogeneous broadening, caused by size or composition fluctuations, dominates. However, recent studies show deviations that can become significant as sample quality improves or when laser behavior is examined in greater detail. These deviations originate from the carrier many-body interaction, involving the localized states, as well as the quasi-continuum of delocalized states, which reside in the wetting layer of self-assembled QD structures often used as laser gain media. In the screened Hartree-Fock approximation (see Part V and Ref. [158]), the many-body interaction between localized and delocalized states can lead to substantial energy shifts in the QD resonances and to nonvanishing carrier-induced refractive index changes [121]. These predictions have been either directly or indirectly verified in experiments [154, 150].

In the following sections we present applications of the theoretical model for QD gain calculations that we introduced in the last chapters. We will focus on two different

QD model systems that exhibit different confinement potentials. One structure corresponds to an $\text{In}_{0.3}\text{Ga}_{0.7}\text{As}$ QD embedded in a GaAs QW that has one confined shell for electrons and holes and that we denote as *shallow dot*. The other structure, that we will denote as *deep dot*, consists of InAs QDs in a GaAs matrix, allowing for two confined shells for electrons and holes with a larger level spacing as in the shallow dot case. Details on the electronic structure are given in Appendix D

We will study several quantities that are of direct application relevance for QD based laser devices. We start in Section 12.1 with an analysis of the density dependence of the linewidth of QD resonances. This quantity gives a direct measure of the dephasing and determines the maximum achievable gain. We will move on in Section 12.2 to a study of the carrier density dependence of the peak gain. This is directly relevant for laser applications and it will turn out, that we actually can predict a new phenomenon in QD gain media, that has to the best of our knowledge not been observed in any other gain material: We find a reduction of the peak gain with *increasing* carrier density. This behavior arises due to a delicate balancing between dephasing and Pauli blocking. In Section 12.3 the linewidth enhancement factor, that e.g. via the Shawlow-Townes formula determines the laser linewidth, and also controls filamentation anti-guiding properties of the material, is investigated. Throughout this chapter the carrier populations are fixed at their quasi-equilibrium values at a lattice temperatures of $T = 300K$.

12.1 Density dependence of the linewidth

A central quantity in all applications of QDs is the homogeneous linewidth of the QD resonances that is determined directly by the dephasing processes. In the past, the carrier-dependence of the optical dephasing has been compared between quantum wells (QWs) and bulk semiconductors. In early investigations it was found that the homogeneous linewidth γ of the excitonic resonance follows a power law $\gamma = an^b$ with the carrier density n . In first investigations on the subject the parameter b was connected to the dimensionality of the system with $b = 1/3$ for bulk and $b = 1/2$ for QWs [159]. However, in Ref. [160] it was shown that the excitation dependencies of the dephasing times in QWs and bulk are practically identical if the carrier densities are scaled appropriately. Corresponding calculations for QWs have been presented in Ref. [161]. We will perform the corresponding investigation for QDs and evaluate whether the excitation dependence of the homogeneous linewidth can be described by a power law for QD transitions.

Typical absorption spectra for the shallow dot, that we introduced above, and different carrier densities are given in Fig. 12.1. In these spectra we can clearly distinguish between the QD resonance at around -100meV relative to the WL bandgap and the

excitonic resonance of the WL at around -15meV . Like in our results of Chapter 11, we find a bleaching of the QD resonance and the transition from absorption to gain as well as the distinct *correlation induced* red-shift. The spectra for the deep dot show similar features (cf. Figure 12.4). In this chapter we focus on the density dependence

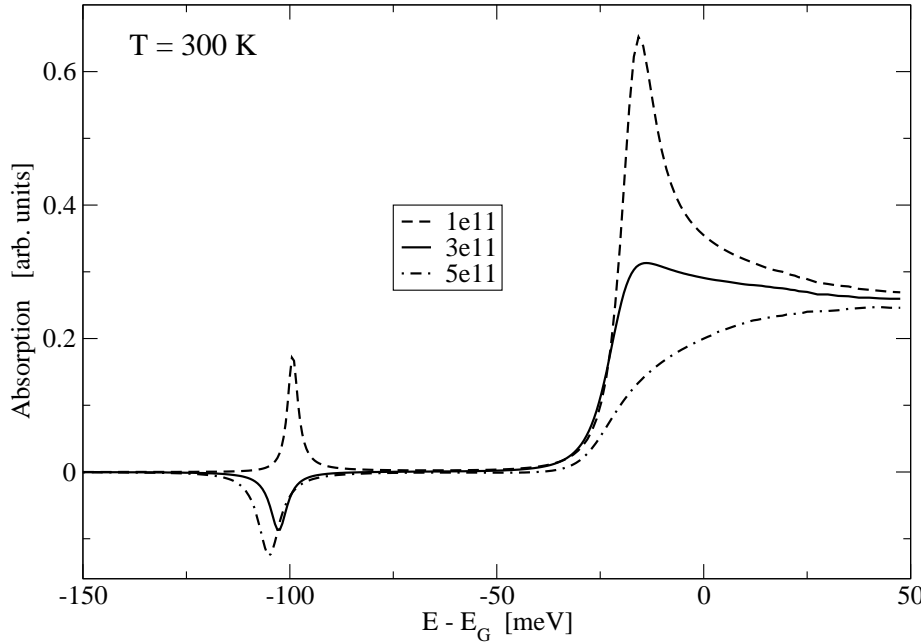


Figure 12.1: Optical absorption spectra for an ensemble of $\text{In}_{0.3}\text{Ga}_{0.7}\text{As}$ QDs embedded in a GaAs WL at a temperature of $T = 300\text{K}$ and for various carrier densities. The energy axis is given relatively to the QW bandgap energy.

of the homogeneous linewidth of the resonances. Comparison with a Lorentzian function with the same amplitude maximum and FWHM indicates a basically good fit except for the asymmetry in the actual resonance and deviations at the spectral tails.

The results are given in Fig. 12.2 in double logarithmic representation. Note that it is not possible to extract a “width” for the WL transition in a certain density regime close to transparency (cf. e.g. the dash-dotted line in Fig. 12.1).

In our results for the QD-WL system we find that the linewidth of the excitonic resonance of the WL as well as the QD ground state resonance can be described by a power law $\gamma = an^b$. For the WL we find $b \approx 0.45$, which is somewhat different from the experimental findings of Ref. [160]. However, we have to take into account that, as our system consist of both WL and QD states, the increase of the occupations with density is different from the QW case.

For the QD ground state transition we find $b \approx 0.56$ for the shallow dot model and $b \approx 0.63$ for the deep dot model. Interestingly the broadening of the s-shell resonance

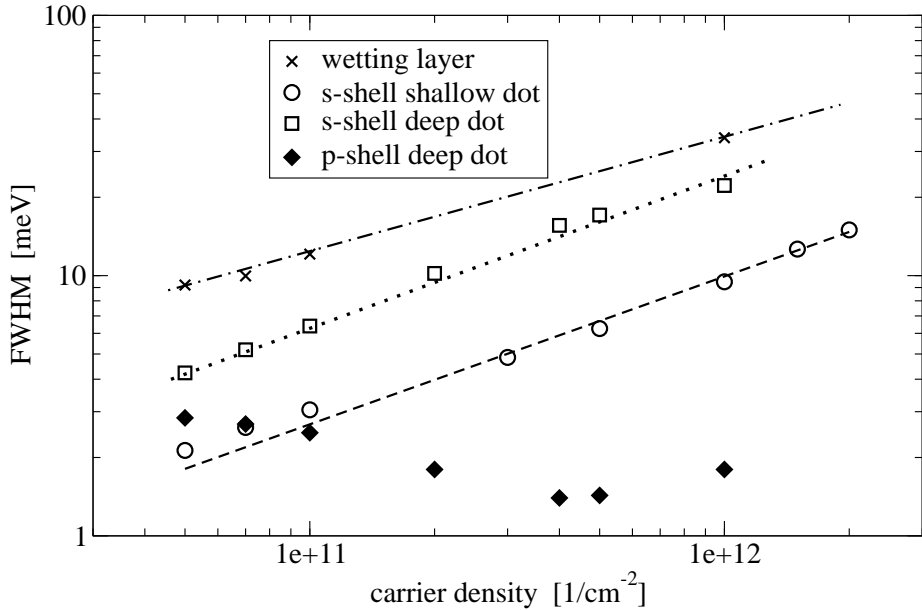


Figure 12.2: Excitation dependence of the FWHM of both WL and QD resonances. The straight lines are guide to the eyes.

of the deep dot model exceeds the broadening of the shallow dot resonance. This is quite an unexpected behavior as in the shallow dot structure we would expect stronger scattering due to the smaller energy spacing between s-shell and WL. However, the QD occupations are higher for the deep dot case because of the larger level spacing, leading to higher intra-dot scattering. Furthermore, due to the smaller level spacing, the compensation between diagonal and off-diagonal dephasing is stronger in the shallow dot case, which also contributes to the observed behavior. For the p-shell resonance of the deep dot model the picture is completely different. The change of the homogeneous linewidth with carrier density cannot be described by a power law. Surprisingly we observe a slight decrease of the FWHM at the transition from absorption to gain, and only at very high carrier densities the linewidth increases again. These finding stems from a complicated interplay of diagonal and off-diagonal dephasing contributions. The linewidth is reduced, since the off-diagonal contributions grow faster than the diagonal ones, leading to a net reduction of the linewidth. At the point where the p-shell is fully populated and only the WL populations increase with increasing carrier density, the diagonal dephasing contributions increase faster and so does the net linewidth.

Our investigations clearly show that for the ground state transition of the QDs investigated here, the density dependence can be described by a power law. There is no evidence, however, that the exponent in that power law is connected to the dimensionality of the system, as the parameters b extracted from our calculations are

comparable for WL (2d states) and QD (0d states) transitions. This is in agreement with the findings of Ref. [160], where no dependence on the dimensionality was found in a comparison between QWs (2d states) and bulk semiconductors (3d states). For the resonances of the excited QD state, the behavior is more complicated due to the interplay between diagonal and off-diagonal dephasing contributions. The complex dependencies shown in Figure 12.2 are describable only with a rigorous treatment of scattering effects.

12.2 Reduction of the peak gain in QD based active media

Having discussed the linewidth of QD resonances we now turn to a direct study of the peak gain, that is directly relevant for laser applications. Furthermore, we discuss in this section the influence of inhomogeneous broadening, which is present in practically all QD samples, grown in the Stranski-Krastanow growth mode. For the shallow dot that we discussed in the introduction to this chapter, gain spectra with and without inhomogeneous broadening are presented in Figure 12.3. As in the last section, the spectra are calculated from the solution of the SBE (9.32) with the correlation contributions of Eqs. (9.34),(9.35),(10.19), and (10.20). For the shallow dot structure, each spectrum shows a distinct s-shell resonance and a broad QW contribution. Figure 12.3(b) depicts the corresponding inhomogeneously broadened spectra. These results are obtained by performing a statistical average of the homogeneous spectra assuming an inhomogeneous width, σ_{inh} . Origins of inhomogeneous broadening arise from QD size or composition fluctuations in an ensemble of QDs. By assuming an inhomogeneous broadening of $\sigma_{inh} = 20\text{meV}$, the spectra in Figure 12.3(b) resemble closely those observed in recent experiments [162]. Comparison of the homogeneous to the inhomogeneous results reveals a significant masking of the intrinsic QD properties by inhomogeneous broadening. The homogeneously broadened result clearly shows the distinct red-shift that was discussed in Chapter 11. Moreover, we observe a strongly excitation dependent broadening of the QD resonances that is not observed in the inhomogeneously broadened case.

Closer examination of the spectra in Figure 12.3(a) reveals a novel behavior in the intrinsic QD gain. For carrier densities $N \geq 5 \times 10^{11} \text{ cm}^{-2}$, the s-shell QD peak gain actually decreases with increasing carrier density. This counterintuitive behavior is caused by two factors. One is the saturation of the state filling contribution to gain at high carrier densities. This saturation is significantly more pronounced in QD than in QW or bulk systems because of 0d versus 2d or 3d density of states differences. The second is the increase in dephasing with increasing carrier density. While increased dephasing always causes gain amplitude reduction, its effect usually lags that of state

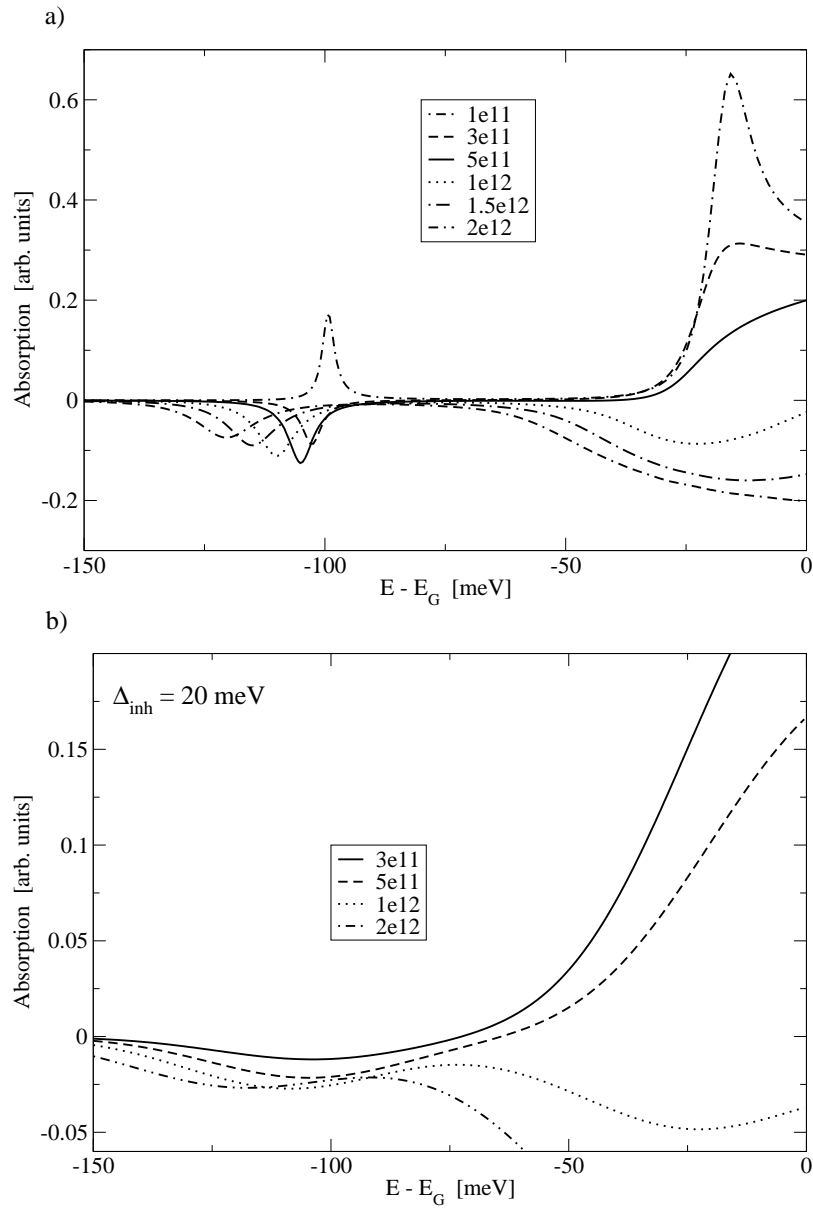


Figure 12.3: Optical absorption spectra for an ensemble of $\text{In}_{0.3}\text{Ga}_{0.7}\text{As}$ QDs embedded in a GaAs WL with (a) and without (b) inhomogeneous broadening at a temperature of $T = 300\text{K}$ and for various carrier densities. The energy axis is given relatively to the QW bandgap energy.

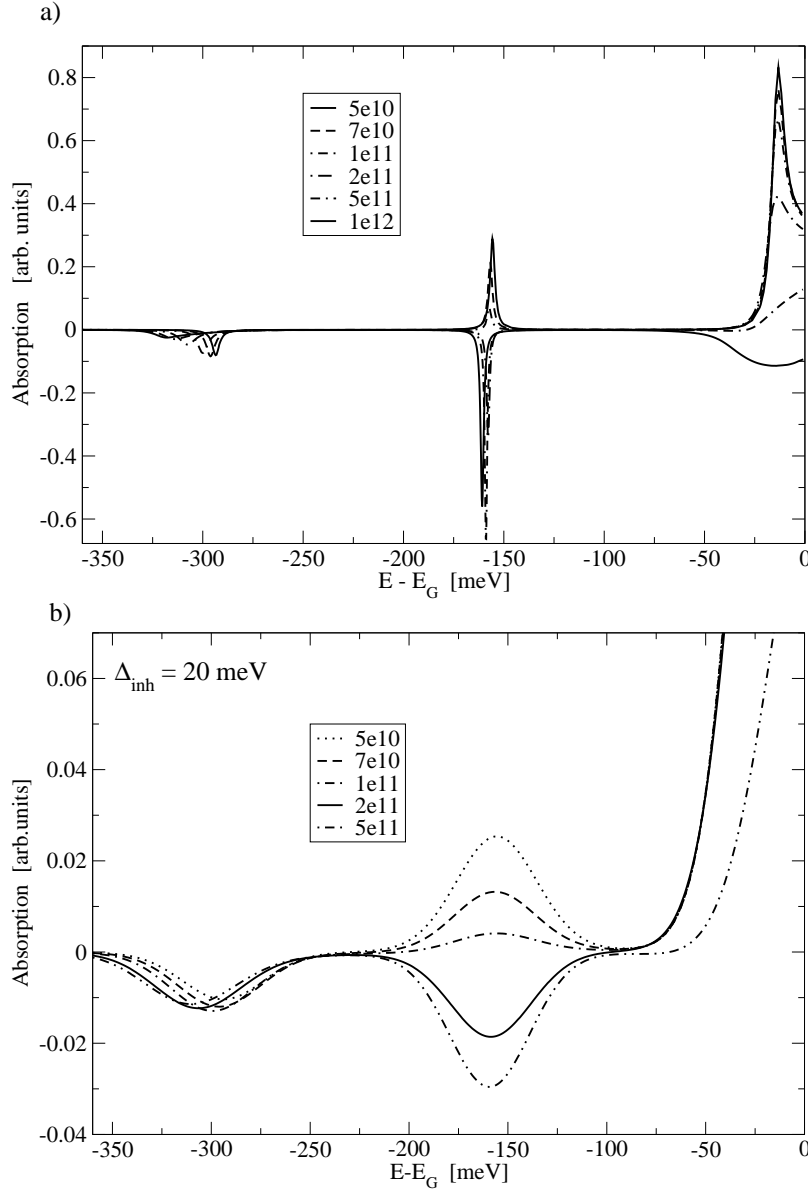


Figure 12.4: Optical absorption spectra for an ensemble of InAs QDs embedded in GaAs with (a) and without (b) inhomogeneous broadening at a temperature of $T = 300K$ and for various carrier densities. The energy axis is given relatively to the QW bandgap energy.

filling. Consequently, in all active media encountered until now, the peak gain always increases with increasing excitation. The difference in a QD-WL system is that in spite of the discussed saturation of state filling, an increase in the carrier density can further increase the dephasing, due to the QD-WL coupling. This in turn causes

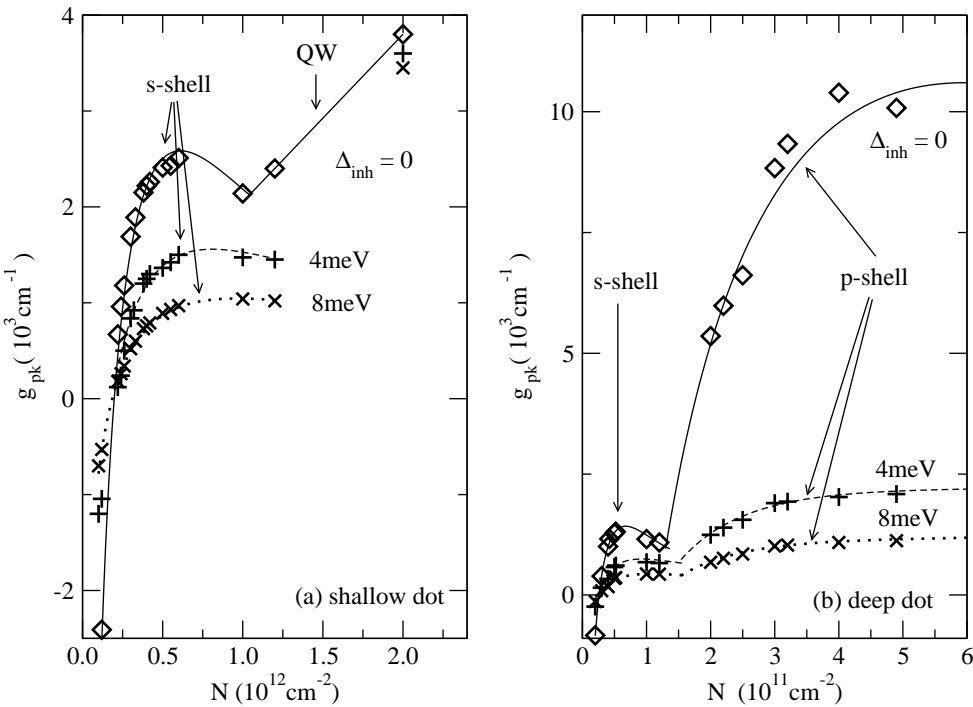


Figure 12.5: Peak gain versus carrier density for different inhomogeneous broadening. Symbols are data from the calculations, lines represent the fitting functions discussed in the text.

the gain to decrease throughout the spectral width of the QD resonance. However, this picture changes as inhomogeneous broadening is taken into account. As the inhomogeneously broadened spectra are more sensitive to the total area under the QD resonance than to the value of the peak gain itself, the gain reduction effect is strongly masked. The net result is a smoothing of the gain reduction features in Figure 12.3(b), and behavior reverts to what is expected for conventional active materials.

Figure 12.4(a) shows that the gain reduction behavior is more pronounced for the deep dot model system. The calculated gain spectra consists of s-shell and p-shell QD resonances, and a broad QW contribution. Consequently also the effect of inhomogeneous broadening is larger than for the shallow dot case, as also in the deep dot case the gain reduction effect vanishes almost completely in the presence of inhomogeneous broadening, as evident from Figure 12.4(b).

Many useful laser properties are determined by the excitation dependence of g at the resonance peaks. Moreover, gain saturation is of critical importance for laser applications, because it limits the useful range of excitation densities. To show the

anomaly found for QD systems explicitly, Figure 12.5 shows a plot of the overall peak gain, g_{pk} , as a function of carrier density N . The points are extracted from the computed spectra and the curves are the least squares fit using fitting functions that are discussed below. The overall (QD+QW) peak gain is chosen because it impacts laser performance in a conventional edge emitter more than a transition-specific peak gain.

In Figure 12.5(a) the solid curve, which describes the homogeneously broadened case for the shallow dot, clearly contains a carrier-density range where the slope, dg_{pk}/dN , is negative. For higher carrier densities dg_{pk}/dN remains negative until the gain from the QW transitions exceeds that from the QD resonance. The other curves in Figure 12.5(a) are for different inhomogeneous broadening. We note that inhomogeneous broadening always reduces the peak gain, with the decrease being inversely proportional to the width of the gain resonance. The g_{pk} versus N curve for the deep dot model in Figure 12.5(b) indicates two regions where dg_{pk}/dN is negative, corresponding to gain reduction for the s-shell and p-shell resonances. As discussed above, the deep dot structure exhibits a greater sensitivity to inhomogeneous broadening, as it is directly evident by comparing Figs. 12.5(a) and 12.5(b).

Nevertheless, for moderate inhomogeneous broadening a plateau in the peak gain versus carrier density curve remains clearly visible. This means that in high quality QD samples, with exhibit only moderate inhomogeneous broadening, one should be able to observe the gain reduction phenomenon directly.

As the dependency of g_{pk} on the carrier density is used extensively in semiconductor laser simulations. To facilitate the use of these results in laser models, we introduce the following fitting function for the QDs:

$$g_{pk}(N) = A \ln(N/N_0) + B \exp(-N/N_1) \quad (12.1)$$

with the parameters A , B , N_0 and N_1 . In (12.1) the first term is similar to the widely used QW gain fit function whereas we added the second term to account for the stronger gain saturation and possible gain reduction effects in QDs.

In this section we have discussed unique optical gain properties of QD active media. The most interesting is the decrease in peak gain with increasing excitation for certain carrier density ranges. This anomalous behavior depends on the delicate balancing of band-filling and dephasing contributions in a coupled QD-WL system. Even though this phenomenon can be masked by inhomogeneous broadening, it should be possible to observe it, either in samples with moderate inhomogeneous broadening or alternatively by means of single-dot spectroscopy.

12.3 Linewidth enhancement factor (α -factor)

While we restricted our discussion of QD based laser properties up to now to the analysis of absorption and gain, that are given by the imaginary part of the susceptibility, also the real part of the susceptibility, that gives rise to refractive index changes, influences the properties of QD based laser systems. The importance of the refractive index changes δn is that its excitation dependence, relative to that of the gain, characterizes important contributions of the active QD material to characteristics of the laser operation, like linewidth, frequency chirp and output beam quality. Specifically

$$\alpha = \frac{(d\text{Re}\chi(\omega)) / dN}{(d\text{Im}\chi(\omega)) / dN} \Big|_{\omega=\text{const}} \quad (12.2)$$

defines the linewidth enhancement factor α . A nonvanishing α -factor leads to a enhancement of the laser linewidth

$$\Delta = \Delta_{\text{ST}}(1 + |\alpha|^2) \quad (12.3)$$

in comparison to the Schawlow-Townes result Δ_{ST} [140], hence the name “linewidth enhancement factor”. Furthermore the α -factor leads to a modified damping of relaxation oscillations

$$\frac{1}{\tau'_r} = \frac{1}{\tau_r} + k\alpha \quad (12.4)$$

with the damping rate $\frac{1}{\tau'_r}$ and a device specific constant k , and it also influences chirp and filamentation [154].

On the basis of atomistic models, that are often employed for the description of QD systems, one would infer a vanishing (or at least a very small) α -factor, as the lorenzian resonances predicted by atomic model do not shift with carrier density. Hence, as we can easily see from the schematic picture of Figure 12.6, the change of the real part of the susceptibility with carrier density vanishes. As our microscopic theory allows for a calculation of the full complex susceptibility (both real and imaginary part) we can calculate the α -factor by calculating optical spectra for two adjoining carrier densities and performing the derivatives numerically.

The results of this procedure are given in Figure 12.7, that illustrates the dependence of α at the gain peak (where a laser typically operates) as a function of peak gain, both in the case of purely homogeneous broadening and under the assumption of additional inhomogeneous broadening. In the range of small peak gain our results show small values for the magnitude of α as expected for atomic-like systems. We find $|\alpha| \lesssim 1$ with and $|\alpha| \lesssim 2$ without inhomogeneous broadening. When gain saturation is approached (cf. Figure 12.5) the denominator in the definition of the α -factor, Eq. (12.2), approaches zero and, hence, the magnitude of the α -factor increases drastically. The sign of the α -factor is determined by the behavior of the index change

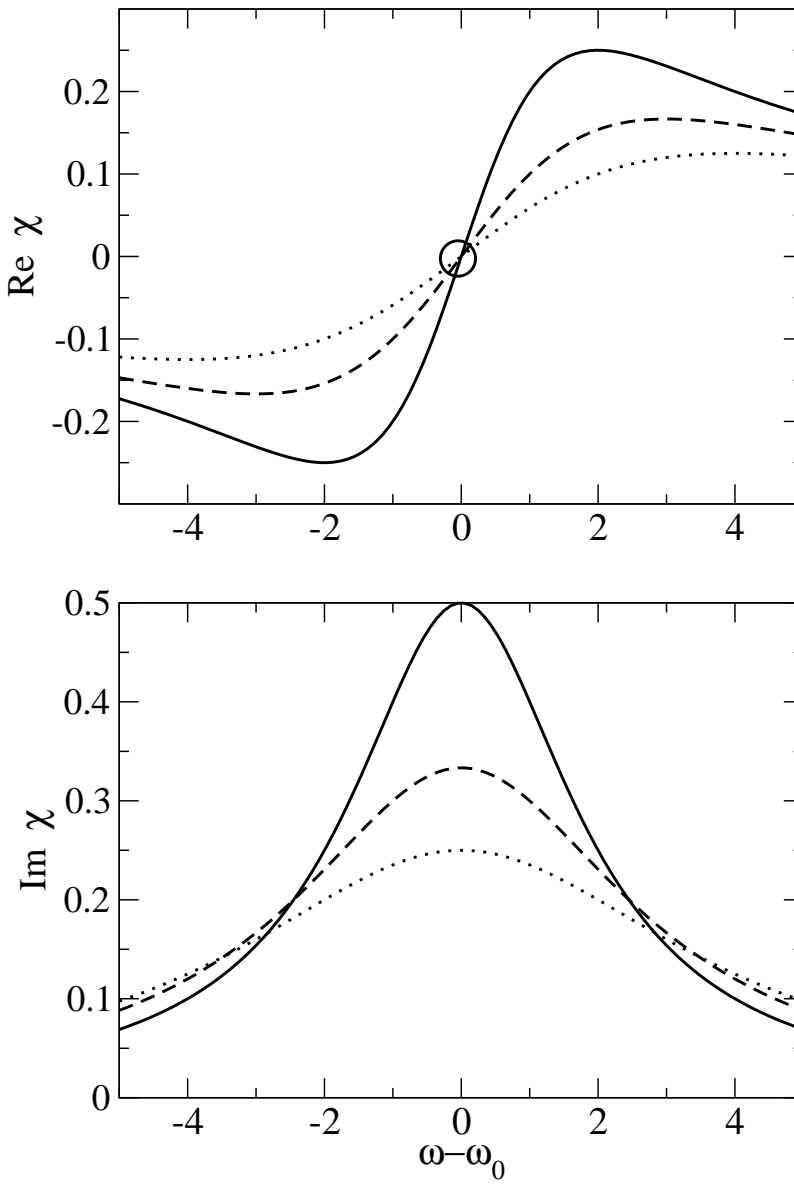


Figure 12.6: Schematic representation of real and imaginary part of the optical susceptibility for a atomic model of optical transitions in QDs

at constant energy, and this behavior changes due to the flattening of the index curves in the presence of inhomogeneous broadening. For the deep dot, the divergence of α may be delayed by operating with the p-shell transition, as indicated in Figure 12.7. The greater sensitivity of the deep QD system to inhomogeneous broadening is clearly evident by comparing Figure 12.7 (a) and (b). The latter shows that in the presence of inhomogeneous broadening α as well as the maximum obtainable gain are more

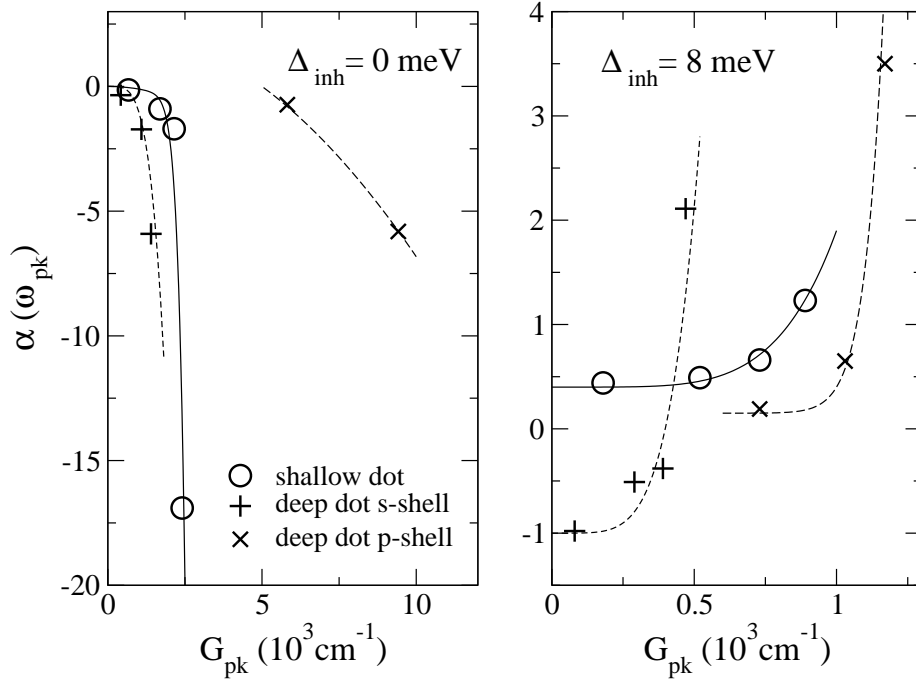


Figure 12.7: α -factor versus peak gain for deep and shallow dot and (a) without inhomogeneous broadening (b) with inhomogeneous broadening of 8 meV. The lines are guides to the eye.

similar in the deep and shallow QD structures. The large range of obtainable α_{pk} is consistent with recent experiments [163].

In this section we have explored the excitation dependencies of the linewidth enhancement factor in QD based active media. The behavior in the vicinity of the gain peak is important for the understanding of the laser threshold, as well as noise and modulation response characteristics. Furthermore it serves as an important input to QD laser models. The theory also uncovers the complicated influences of dephasing and lineshifts on gain and refractive index in QD system, which in turn lead to a complex behavior of the linewidth enhancement factor.

12.4 Conclusion

In this part of the thesis we have presented a theoretical model to calculate excitation-induced dephasing and lineshifts for an InGaAs QD-WL system on a microscopic basis. These results are used to obtain optical absorption and gain spectra. The influences of both Coulomb interaction and carrier-LO-phonon interaction have been

analyzed and compared and it is found that both Coulomb and LO-phonon contributions to the homogeneous linewidths are equally important for elevated carrier densities. For the theoretical description various pitfalls in the determination of the dephasing have been highlighted, and the importance of self-consistent single-particle energy renormalizations in the scattering integrals has been emphasized.

In Section 11.2 we haven given explicit reasons why the deviations from a fully self-consistent treatment of the single-particle energies are expected to be small in application related problems. Hence the presented theory was used to calculate various application relevant to QD laser structures.

We could show, that our theory predict a surprising new phenomenon in semiconductor QD structures. Due to the interplay of localized and de-localized states. The optical gain can decrease with increasing carrier density, leading to an optimum carrier density for laser applications. Moreover, the influence of inhomogeneous broadening on this phenomenon was investigated and we found a strong masking of the gain reduction effect by inhomogeneous broadening.

Furthermore, we determined the α -factor in QD systems, and found a strong dependency of the α -factor on the ratio of homogeneous and inhomogeneous broadening.

Part IV

Laser Theory for semiconductor Quantum Dots

Recently it became possible to combine optical microcavities that exhibit long-lived modes with QD emitters as the active material. These cavities are realized in form of microdisks [164, 165, 166], micropillars [13, 9] or photonic crystals [7, 8]. All of them have been used to demonstrate high Q -factors together with small mode volumes, resulting in highly selective emission into few cavity modes, or even a single mode. Correspondingly, large β -values, which describe the fraction of the spontaneous emission into the laser mode, are realized, leading to low threshold currents required to achieve lasing with such devices. In the limit of a β -factor of unity the so-termed “thresholdless” laser is obtained as the jump in the input/output curve vanishes [167, 168, 169, 170]. Thus, for the case that β approaches unity, information about the photon statistics of the outcoupled light is necessary to identify the transition from dominating spontaneous to dominating stimulated emission. Experimentally this is possible in a Hanbury-Brown and Twiss (HBT) coincidence measurement [171]. Depending on the measurement setup, a kink or a peak is visible in the measured intensity correlation function at the transition from spontaneous to stimulated emission. The list of recent efforts and publications where the threshold behavior of QD- or quantum-well-based laser devices is investigated, partly by using HBT-like setups, show the current strong topical interest not only in the quantum optics, but also the nanotechnology community [172, 173, 165, 13, 166, 7, 8, 9].

In the literature, semiconductor QD-based laser devices are commonly modeled by considering atomic two- or multi-level systems, resulting either in a set of rate equations [168, 169], or a master equation for the reduced density matrix [170, 174, 175]. To describe the statistical properties of the emission from the microcavity, such as the intensity correlation function, the latter approach has been used. Alternatively, for two-level systems the quantum regression theorem can be applied [148].

On the basis of underlying atomic models, it is, however, not possible to consider intrinsic semiconductor effects, such as a modified source term of spontaneous emission and Coulomb effects [88, 176]. Also, unlike conventional four-level gas lasers, QD-based microcavity lasers usually do not operate at full inversion, which leads to considerable differences in the input/output curve of these devices. Especially if characteristic values are derived from measured data, such as the β -factor, one must be aware of the differences between an atomic and a semiconductor laser model. Therefore, a semiconductor approach is desirable if QD-based devices are studied. A general semiconductor laser model based on a microscopic Hamiltonian has been previously used to study the influence of the carrier dynamics and many-body effects [137, 128], lasing without inversion [177], and noise spectra [178], but did not include correlations required to determine the photon statistics.

The purpose of this part is a study of the threshold behavior of semiconductor QD based laser devices by means of the cluster expansion technique, that we introduced in Chapter 5. By discriminating between the emission into lasing and non-lasing modes

and by explicitly considering the pump process, a laser theory can be formulated. This allows for an investigation of the influence of the correct semiconductor source term of spontaneous emission [88, 176] on the threshold properties and specifically on the “jump” in the input/output curve. An important motivation for this work is the observation that for large values of the spontaneous emission coupling β , typical for state-of-the-art microcavity systems, this “jump” broadens significantly, and can no longer be used to uniquely determine the onset of coherent light emission.

To get further insight into the threshold behavior, we also study the photon statistics. This becomes necessary for high β values, as for the limiting case of $\beta = 1$ the “jump” in the input/output curve disappears and therefore we rely on an alternative method to classify the statistical nature of the emitted light. We will present a scheme based on the cluster expansion, that allows for a calculation of the second order correlation function $g^{(2)}(\tau = 0)$, first introduced by Roy Glauber in Ref. [179]. This quantity, also known as intensity correlation function or autocorrelation function, is a measure of the probability to detect a second photon immediately after an initial photon detection. Hence, it contains valuable information about the statistical nature of the emitted light.

This part is structured as follows: In the next section we show how the equations of motion follow from the Hamiltonian for the coupled carrier-photon system and explain how operator averages are classified within the scheme of the cluster expansion technique. In Section 13.2 the laser equations are derived and the atomic rate equation limit is discussed. Section 14 is concerned with higher order correlations needed to obtain the photon statistics in terms of the autocorrelation function. First we present results from the coupled equations for laser dynamics and photon correlations in Section 14.2. A direct comparison of a reduced two-level version of our equations to the master equation is used to verify our approach in Section 14.3. Finally, analytic results for the autocorrelation function are considered in Section 14.4 and compared to the numerical solutions.

We would like to point out, that the results discussed in this part of the thesis have been achieved in a collaboration with Christopher Gies, and as outlined in Chapter 1 the results are taken from a joint publication, [32]. Therefore we will, where appropriate, confer to his excellent thesis on the subject at hand [94].

13 Laser model

To calculate the input/output characteristics, the inclusion of the quantized light field (in comparison to the quasi-classical approach we used in Part III) is mandatory, as below threshold the emission is dominated by spontaneous emission, that is a pure quantum process. Moreover, also the laser linewidth and the photon statistics are influenced by the spontaneous emission. Therefore we must replace the dipole Hamiltonian that we originally discussed in Section 3.1, with the Hamiltonian of the quantized light-matter interaction and take the free photon field into account. Starting from that Hamiltonian, we derive coupled equations of motion for the relevant expectation values that describe the carrier and photon population dynamics and – in an extended version – also the photon statistics.

The electronic part of the Hamiltonian contains, as discussed in Section 3.1, the single-particle contributions for conduction and valence band carriers with the energies $\varepsilon_\nu^{c,v}$ and the two-particle Coulomb interaction,

$$H_{\text{carr}}^0 = \sum_\nu \varepsilon_\nu^c c_\nu^\dagger c_\nu + \sum_\nu \varepsilon_\nu^v v_\nu^\dagger v_\nu , \quad (13.1)$$

$$\begin{aligned} H_{\text{Coul}} = & \frac{1}{2} \sum_{\alpha' \nu' \nu' \alpha} \left[V_{\alpha' \nu', \nu' \alpha}^{cc} c_{\alpha'}^\dagger c_{\nu'}^\dagger c_{\nu'} c_\alpha + V_{\alpha' \nu', \nu' \alpha}^{vv} v_{\alpha'}^\dagger v_{\nu'}^\dagger v_{\nu'} v_\alpha \right] \\ & + \sum_{\alpha' \nu' \nu' \alpha} V_{\alpha' \nu', \nu' \alpha}^{cv} c_{\alpha'}^\dagger v_{\nu'}^\dagger v_{\nu'} c_\alpha . \end{aligned} \quad (13.2)$$

It should be noted, that we give the Hamiltonian directly in an eigenbasis of the single-particle problem h_0 as defined in Eq. (3.10). In comparison to Part III we not only need the single-particle states of the QD system at hand, but also information about the eigenstates of the photonic system, the so-called *modes*, inside the microcavity. Such information can be obtained directly from experiment via transmission measurements. Alternatively, one can perform mode calculations that are in many respects equivalent to single-particle calculations for the carriers. Here the variety of methods span from transfer-matrix methods over vectorial transfer-matrix methods [180, 181] and finite difference time-domain formulations to Green's function methods¹.

¹Here we refer to the classical GF of Maxwell's equations rather than the quantum mechanical quantities that we discussed in Part II.

An example for a mode calculation is shown in Figure 13.1 for micropillars grown in the II-VI material system. The calculation in the right panel show the fundamental mode of the micropillar depicted in the left panel. The mode shows a clear field strength maximum at the position of the cavity that is formed by a $\lambda/2$ layer. From these calculations, we can infer the energetic position of the fundamental mode as well as its broadening, that is usually given in terms of the quality factor

$$Q = \frac{\omega}{\Delta\omega}, \quad (13.3)$$

such that a small energetic broadening corresponds to large values of the Q-factor.

With the results of such a mode calculation in mind, we can directly give the Hamiltonian for the free part of the electromagnetic field in an appropriate eigenbasis of the optical modes q in the microresonator

$$H_{\text{ph}} = \sum_q \hbar\omega_q \left(b_q^\dagger b_q + \frac{1}{2} \right), \quad (13.4)$$

where the Bose operators b_q (b_q^\dagger) annihilate (create) a photon in the mode q . Furthermore we will where appropriate differentiate between the fundamental cavity mode q_l with energy $\hbar\omega_{q_l}$, used for the laser emission, and other non-lasing modes with $q \neq q_l$.

The two-particle Hamiltonian for the light-matter interaction in dipole approximation is given by

$$H_D = -i \sum_{q, \alpha\nu} \left(g_{q\alpha\nu} c_\alpha^\dagger v_\nu b_q + g_{q\alpha\nu} v_\alpha^\dagger c_\nu b_q \right) + \text{h.c.} . \quad (13.5)$$

The light-matter coupling strength $g_{q\alpha\nu}$ is determined by the overlap of the mode function of the electromagnetic field with index q and the single-particle wave functions belonging to the states $|\alpha\rangle$ and $|\nu\rangle$, see Ref. [88]. We use the approximation of equal wave-function envelopes for conduction- and valence-band carriers, resulting in diagonal transitions between the corresponding conduction- and valence-band states, i. e. $g_{q\alpha\nu} = g_{q\nu}\delta_{\alpha\nu}$. The total Hamiltonian is the sum of all discussed contributions:

$$H = H_{\text{carr}}^0 + H_{\text{Coul}} + H_{\text{ph}} + H_D . \quad (13.6)$$

As we would like to calculate not only the input-/output characteristics but also the photon statistics, we will employ the cluster expansion method, that we introduced in Chapter 5. The use of NGFs would of course also be possible but as the photon statistics are given by a two-photon GF, we would need to employ the method of the Martin-Schwinger hierarchy (cf. Section 4.6), as the Kadanoff-Baym equations are only equations for single-particle GFs². For the application of the cluster expansion

²The Kadanoff-Baym equations can also be formulated including single *photon* GFs.

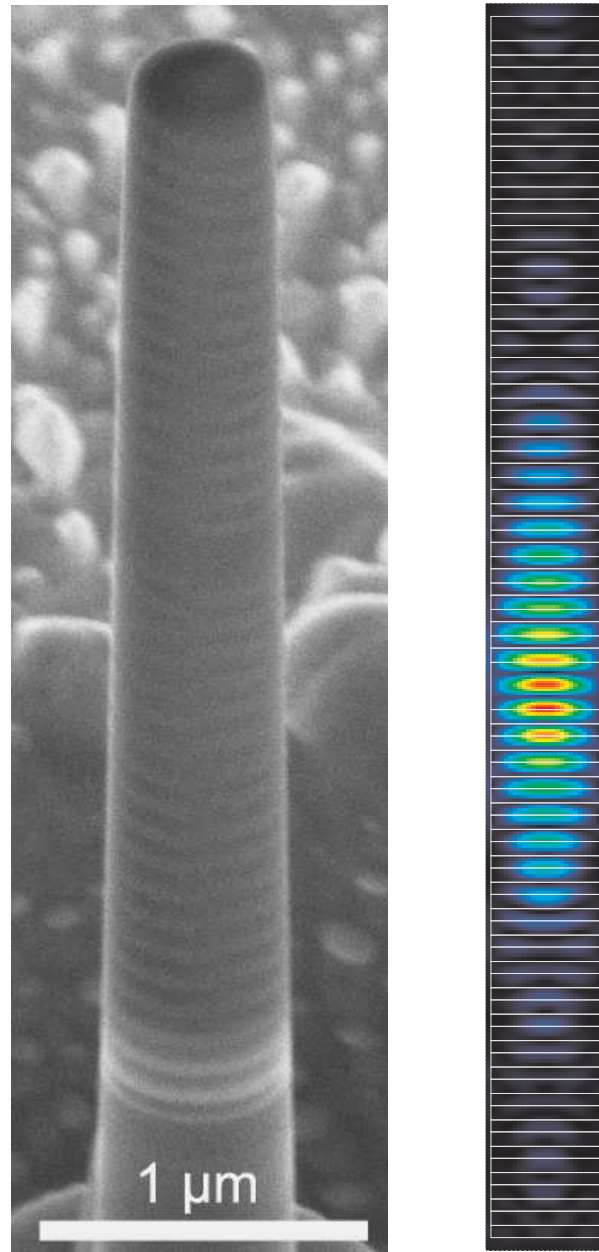


Figure 13.1: Left: SEM image of a micropillar structure with embedded II/VI QDs. The micropillar structures have been processed by focused ion beam lithography. Picture taken from Refs. [28, 182]. Right: Electromagnetic field strength for the fundamental mode in a micropillar structure, picture courtesy of Prof. Dr. Jan Wiersig, Univ. Magdeburg. The position of the cavity coincides with the field maximum.

method to a system containing carriers and photons, we want to point out that for the purpose of classification of clusters a photon operator is equivalent to two carrier operators, as we can infer from an adiabatic elimination procedure [94].

13.1 Equations of motion

For the temporal evolution of the photon number $\langle b_q^\dagger b_q \rangle$ in the mode q and the carrier populations $f_\nu^e = \langle c_\nu^\dagger c_\nu \rangle$, $f_\nu^h = 1 - \langle v_\nu^\dagger v_\nu \rangle$, the contribution of the light matter interaction H_D in the Heisenberg equations of motion leads to

$$\left(\hbar \frac{d}{dt} + 2\kappa_q \right) \langle b_q^\dagger b_q \rangle = 2 \operatorname{Re} \sum_{\nu'} |g_{q\nu'}|^2 \langle b_q^\dagger v_{\nu'}^\dagger c_{\nu'} \rangle , \quad (13.7)$$

$$\hbar \frac{d}{dt} f_\nu^{e,h} \Big|_{\text{opt}} = -2 \operatorname{Re} \sum_q |g_{q\nu}|^2 \langle b_q^\dagger v_\nu^\dagger c_\nu \rangle . \quad (13.8)$$

Note, that we have scaled $\langle b_q^\dagger v_\nu^\dagger c_\nu \rangle \rightarrow g_{q\nu} \langle b_q^\dagger v_\nu^\dagger c_\nu \rangle$ to have the modulus of the coupling matrix elements appear. This is purely for matters of convenience and has no direct physical meaning. In Eq. (13.7) we have introduced the cavity loss rate $2\kappa_q$. For the laser mode, this is directly connected to the Q -factor of the fundamental cavity mode, $Q = \hbar\omega/2\kappa$. The dynamics of the photon number in a given mode is determined by the photon-assisted polarization $\langle b_q^\dagger v_\nu^\dagger c_\nu \rangle$ that describes the expectation value for a correlated event, where a photon in the mode q is created in connection with an interband transition of an electron from the conduction to the valence band. The sum over ν involves all possible interband transitions from various QDs. The dynamics of the carrier population in Eq. (13.8) is governed by contributions of photon-assisted polarizations from all possible modes q . The influence of carrier-carrier interaction on the carrier dynamics is discussed below.

The dynamical equation for the photon-assisted polarization is given by

$$\begin{aligned} & \left(\hbar \frac{d}{dt} + \kappa_q + \Gamma + i(\tilde{\varepsilon}_\nu^e + \tilde{\varepsilon}_\nu^h - \hbar\omega_q) \right) \langle b_q^\dagger v_\nu^\dagger c_\nu \rangle = \\ & f_\nu^e f_\nu^h - (1 - f_\nu^e - f_\nu^h) \langle b_q^\dagger b_q \rangle \\ & + i(1 - f_\nu^e - f_\nu^h) \sum_\alpha V_{\nu\alpha\nu\alpha} \langle b_q^\dagger v_\alpha^\dagger c_\alpha \rangle + \frac{1}{g_{q\nu}} \sum_\alpha g_{q\alpha} C_{\alpha\nu\nu\alpha}^x \\ & + \delta \langle b_q^\dagger b_q c_\nu^\dagger c_\nu \rangle - \delta \langle b_q^\dagger b_q v_\nu^\dagger v_\nu \rangle . \end{aligned} \quad (13.9)$$

The free evolution of $\langle b_q^\dagger v_\nu^\dagger c_\nu \rangle$ is determined by the detuning of the QD transitions from the cavity resonances. In a semiconductor, the source term of spontaneous emission is described by an expectation value of four carrier operators $\langle c_\alpha^\dagger v_\alpha v_\nu^\dagger c_\nu \rangle$,

see Ref. [88]. For uncorrelated carriers, the Hartree-Fock factorization of this source term leads to $f_\nu^e f_\nu^h$, which appears as the first term on the right hand side of Eq. (13.9). Corrections to this factorization are provided by the Coulomb and light-matter interaction are included in $C_{\alpha\nu\nu'\alpha}^x = \delta\langle c_\alpha^\dagger v_\nu^\dagger c_\nu v_\alpha \rangle$.

A restriction of the source term of spontaneous emission to the factorization approximation is justified in certain situations, such as the laser applications considered here. As we discussed in Part III, high carrier densities efficiently screen the Coulomb interaction between the carriers and lead to strong dephasing that directly suppresses carrier-carrier correlations [88]. The feedback of the laser cavity can support strong carrier-photon correlations that dominate over carrier-carrier correlations. The calculation of carrier-carrier-correlation contributions C^x to the source term of spontaneous emission is a central issue of Ref. [88], and a discussion about the sensitivity of C^x to dephasing can be found there. Note that in atomic systems, the spontaneous emission is always linear in the excited-state population. This difference to semiconductor systems is the origin of interesting new effects in QDs, which are not present in atomic systems [95, 176].

The stimulated emission/absorption term in Eq. (13.9), which is proportional to the photon number $\langle b_q^\dagger b_q \rangle$ in the mode q , provides feedback due to the photon population in the cavity. Hartree-Fock (singlet) contributions of the Coulomb interaction lead to the appearance of renormalized energies $\tilde{\varepsilon}$ and to the interband exchange contribution in Eq. (13.9) that couples the photon-assisted polarizations from different states α . The last two terms in Eq. (13.9) are carrier-photon correlations that are discussed in Section 14. Carrier-carrier and carrier-phonon interaction lead to dephasing, which corresponds to a damping of the photon-assisted transition amplitude. While the used formalism allows for a microscopic evaluation of these effects [85], this is not the purpose of this part and dephasing is included via a phenomenological damping constant Γ . It should be emphasized, that this approximation neglects the complicated microscopic dependence of the dephasing on carrier density and electronic structure, that were the central issue of Part III of the present thesis. However, as the phenomena that we analyze in this part are influenced predominantly by carrier-photon correlations, the approximation is justified.

Furthermore, in the above equations we have used the fact that *in the incoherent regime*, that we are considering here, polarization-like averages of the form $\langle c_\nu^\dagger v_\nu \rangle$, that were the subject of Part III in connection with a classical external electromagnetic field, vanish [83].

13.2 Laser equations

To evaluate the laser theory for QDs in optical microcavities, we have to specify the electronic structure of the system as well as the mode structure of the resonator. The QD model under consideration is the one discussed in Section 11.1 and Appendix A. We consider the QDs to be embedded in a microcavity, which provides one (potentially degenerate) fundamental mode with a large Q -factor that is in resonance with the QD s -shell emission. Higher cavity modes are assumed to be energetically well-separated from the fundamental mode, and a continuum of leaky modes is used to define the spontaneous emission coupling β , i. e. only a fraction of the spontaneous emission at the laser transition energy involves the laser mode. This will be specified in details below.

In the following scheme, several assumptions are included, which are justified by possible experimental conditions and which lead to a convenient formulation of the theory. They provide no principle limitations and their use can be circumvented at the cost of more complicated analytical and numerical formulations.

1. We assume that optical processes involving the laser mode (stimulated and spontaneous emission as well as photon reabsorption) are exclusively connected to the s -shell transitions. In this case, higher shells and WL states contribute only to the carrier dynamics.
2. Ultrafast carrier scattering processes in QDs have been predicted in recent studies of carrier-carrier [125] and carrier-phonon [118] interaction. Based on these grounds, we assume that the carrier system is close to equilibrium, so that scattering processes can be described in relaxation-time approximation [125].
3. To include the simplest possible pump process, we consider carrier generation in the p -shell at a given rate P . This can be traced back either to resonant optical pumping in connection with rapid dephasing, or to carrier injection into the delocalized WL or bulk states and fast successive carrier capture and relaxation processes.
4. For the non-lasing modes, stimulated emission and reabsorption of photons is neglected, which corresponds to a situation where photons spontaneously emitted into non-lasing modes rapidly leave the cavity. In the case of strong dephasing (provided by efficient carrier scattering) it is then possible to analytically solve the equation for the corresponding photon-assisted polarization and to introduce a rate of spontaneous emission into the non-lasing modes.

5. It has been shown in Ref. [95] that the major emission into the fundamental mode is due to those QDs, which are on resonance, whereas slightly detuned dots contribute only inefficiently. Therefore, in the following we consider in a good approximation only those emitters in resonance with the fundamental mode, rather than using an inhomogeneously broadened sample of QDs. For a system of identical dots, which are on resonance with the non-degenerate fundamental mode of the cavity, the occurring energy differences with the laser mode, $\tilde{\varepsilon}_\nu^e + \tilde{\varepsilon}_\nu^h - \hbar\omega_{q_l}$, drop out in the equations of motion in the following.

So far we have derived the fundamental equations for the carrier and photon dynamics, which, on singlet-doublet level, are known as semiconductor luminescence equations. In order to describe a pumped laser system, we must incorporate carrier generation and the β -factor into the theory, and deal with the correlations appearing in Eq. (13.9).

Regarding the treatment of many-body Coulomb effects, we can distinguish between two limiting cases. In the high-carrier density and high-temperature regime, the WL states accommodate a substantial carrier density that screens the Coulomb interaction between the QD carriers. At the same time, the Coulomb interaction between QD and WL carriers leads to broadening and energy shifts of the QD transitions, that were the subject of Part III. In the low-temperature regime that was recently studied in several experiments [95, 9], the population of the WL states is expected to be marginal. The remaining Coulomb interaction between the QD carriers leads to intra- and interband interaction effects and will be summarized in an effective transition energy and oscillator strength for the coupling to the laser mode. Therefore in all calculations in this part of the thesis the WL is *not* included explicitly.

While the main focus of this part is on carrier-photon and photon-photon correlations in QD lasers, also the explicit inclusion of carrier-carrier Coulomb correlations, in terms of the cluster expansion or with alternative methods, is desirable.

While this is an ongoing research subject, our approximations should be valid for these investigations, as dominantly QDs with transitions in resonance with the high- Q laser mode contribute to the emission, so that possible line shifts are not explicitly included subsequently. Moreover, in calculations of the source term of spontaneous emission for QDs *in microcavities* [95] it turned out that the role of C^x is small, when typical material parameters and high Q -values are considered. In this case the strong feedback of the cavity dominates over the correlations and the singlet factorization $f_\nu^e f_\nu^h$ provides a good approximation for the source term. Thus, in the following calculations, C^x is not included.

Under the discussed conditions, the equation of motion for the photon-assisted po-

larization of the laser mode takes the form

$$\left(\hbar \frac{d}{dt} + \kappa + \Gamma \right) \langle b^\dagger v_s^\dagger c_s \rangle = f_s^e f_s^h - (1 - f_s^e - f_s^h) \langle b^\dagger b \rangle + \delta \langle b^\dagger b c_s^\dagger c_s \rangle - \delta \langle b^\dagger b v_s^\dagger v_s \rangle , \quad (13.10)$$

where, from now on, the index $q = q_l$ is omitted for the laser mode. In the equation of motion for the photon-assisted polarization of the non-lasing modes, the negligible photon population allows the omission of the feedback term and carrier-photon correlations,

$$\left(\hbar \frac{d}{dt} + \kappa_q + \Gamma + i(\tilde{\varepsilon}_s^e + \tilde{\varepsilon}_s^h - \hbar\omega_q) \right) \langle b_q^\dagger v_s^\dagger c_s \rangle \Big|_{q \neq q_l} = f_\nu^e f_\nu^h . \quad (13.11)$$

As a result, Eq. (13.11) can be solved in the adiabatic limit and the part $q \neq q_l$ of the sum in Eq. (13.8) can be evaluated, yielding a time constant τ_{nl} for the spontaneous emission into non-lasing modes according to the Weißkopf-Wigner theory [148],

$$\frac{2}{\hbar} \text{Re} \sum_{q \neq q_l} \frac{|g_{qs}|^2}{\kappa_q + \Gamma + i(\tilde{\varepsilon}_s^e + \tilde{\varepsilon}_s^h - \hbar\omega_q)} = \frac{1}{\tau_{nl}} . \quad (13.12)$$

In a laser theory, one typically distinguishes between the rate of spontaneous emission into lasing and non-lasing modes, $1/\tau_l$ and $1/\tau_{nl}$, respectively. Both rates add up to the total spontaneous emission rate $1/\tau_{sp}$. Then the spontaneous emission factor is given by

$$\beta = \frac{\frac{1}{\tau_l}}{\frac{1}{\tau_{sp}}} = \frac{\frac{1}{\tau_l}}{\frac{1}{\tau_l} + \frac{1}{\tau_{nl}}} \quad (13.13)$$

and the rate of spontaneous emission into non-lasing modes can be expressed according to

$$\frac{1}{\tau_{nl}} = \frac{1 - \beta}{\tau_{sp}} . \quad (13.14)$$

For a further discussion of the time constants, see Appendix C. From Eq. (13.8) we can now determine the population dynamics in the s -shell. For the spontaneous emission into non-lasing modes, the adiabatic solution of Eq. (13.11) is used according to Eqs. (13.12) and (13.14). Furthermore, we include the carrier scattering from p -to s -shell

$$R_{p \rightarrow s}^{e,h} = (1 - f_s^{e,h}) f_p^{e,h} / \tau_r^{e,h} \quad (13.15)$$

with a phenomenological scattering rate $1/\tau_r^{e,h}$, and $g \equiv g_{q_l,s}$ to obtain

$$\frac{d}{dt} f_s^{e,h} = -2 |g|^2 \text{Re} \langle b^\dagger v_s^\dagger c_s \rangle - (1 - \beta) \frac{f_s^e f_s^h}{\tau_{sp}} + R_{p \rightarrow s}^{e,h} . \quad (13.16)$$

Physically, the scattering is caused by the combined effect of carrier-carrier and carrier-phonon scattering, that are the subject of Refs. [30] and [31], respectively. The first term describes the carrier dynamics due to the interaction with the laser mode, while the second term represents the loss of carriers into non-lasing modes. The carrier dynamics for the p -shell can be written as

$$\frac{d}{dt} f_p^{e,h} = P(1 - f_p^e - f_p^h) - \frac{f_p^e f_p^h}{\tau_{sp}} - R_{p \rightarrow s}^{e,h}, \quad (13.17)$$

where a carrier generation rate P is included together with the Pauli-blocking factor $(1 - f_p^e - f_p^h)$. The second term describes spontaneous recombination of p -shell carriers and the third contribution is the above-discussed carrier relaxation.

The resulting set of equations (13.16) and (13.17), together with (13.7) and (13.10) allows us to calculate the coupled dynamics for the photon number and the carrier population. The results of the calculations are shown in Figure 14.1 in the next chapter and will be discussed in conjunction with the corresponding photon statistics.

13.3 Rate equation limit

In the following we show how the frequently used atomic rate equation model [168, 170] can be obtained from the above developed semiconductor theory as a limiting case. First the semiconductor specific source term of spontaneous emission $f_\nu^e f_\nu^h$ in Eqs. (13.10), (13.16) and (13.17) is replaced by the electron population f_ν^e . This happens because successive destruction of more than one carrier always yields zero in the case of a two-level system, where only one electron is present per independent emitter, in which case we use $c_\nu c_\nu = v_\nu v_\nu = c_\nu v_\nu = 0$. Then the source of spontaneous emission $\langle c_\alpha^\dagger v_\alpha v_\nu^\dagger c_\nu \rangle$ arising in Eq. (13.9) can be found to reduce to $\langle c_\alpha^\dagger c_\alpha \rangle = f_\alpha^e$. Moreover, full inversion of the laser transition is assumed, $1 - f_s^h = \langle v_s^\dagger v_s \rangle = 0$, which is usually well justified for atomic four-level laser systems. However, we have to point out, that this approximation is poorly justified for QDs and just serves to show the possibility of retaining the rate equations. Finally, the adiabatic solution of Eq. (13.10) is inserted into Eq. (13.7). Introducing the number of excited emitters $\bar{N} = f_s^e N$, where N is the total number of emitters that arises from the sum over all states in Eq. (13.7), we find

$$\frac{d}{dt} \langle b^\dagger b \rangle = -2\kappa \langle b^\dagger b \rangle + \frac{\beta}{\tau_{sp}} (1 + \langle b^\dagger b \rangle) \bar{N}. \quad (13.18)$$

The photon population is determined by the interplay of the cavity losses 2κ and the photon generation due to spontaneous processes $\propto \bar{N}$ and stimulated processes

$\propto \langle b^\dagger b \rangle \bar{N}$. For the number of excited emitters we obtain

$$\frac{d}{dt} \bar{N} = -\frac{\beta}{\tau_{sp}} \langle b^\dagger b \rangle \bar{N} - \frac{1}{\tau_{sp}} \bar{N} + P , \quad (13.19)$$

where, for atomic laser systems quite common, a constant pumping $NR_{p \rightarrow s}^{e,h} = P$ has been used, which describes the carrier-generation rate in the laser-transition level. The carrier recombination is determined by the stimulated emission into the laser mode $\propto \beta/\tau_{sp} = 1/\tau_l$, and by the spontaneous emission $\propto 1/\tau_{sp}$ into all available modes.

For a direct comparison with the semiconductor model, results of the rate equations (13.18) and (13.19) for the input/output curves and various values of the β -factor are shown in Fig. 13.2. We use a typical set of parameters: $\tau_{sp} = 50$ ps (spontaneous emission of QDs enhanced by the Purcell effect), $N = \tilde{N}/\beta$ with $\tilde{N} = 20$ (the number of emitters is increased with decreasing β in order to have the thresholds occur at the same pump rate), $\kappa = 20 \mu\text{eV}$. The corresponding cavity lifetime is about 17 ps, yielding a Q -factor of roughly 30,000. The curves show the typical intensity jump $\propto \beta^{-1}$ from below to above threshold. In the limit $\beta = 1$ the kink in the input/output curve disappears. It should be noted, that the fact, that the “jump” in the input/output curve is given by $\frac{1}{\beta}$ in the rate equations is often used to determine the β -factor directly from experimentally measured curves. However, it should be noted, that such a determination is not possible in general. As we will see in the Chapter 14, the lack of full inversion as well as semiconductor effects lead to strong modifications in the input/output curves.

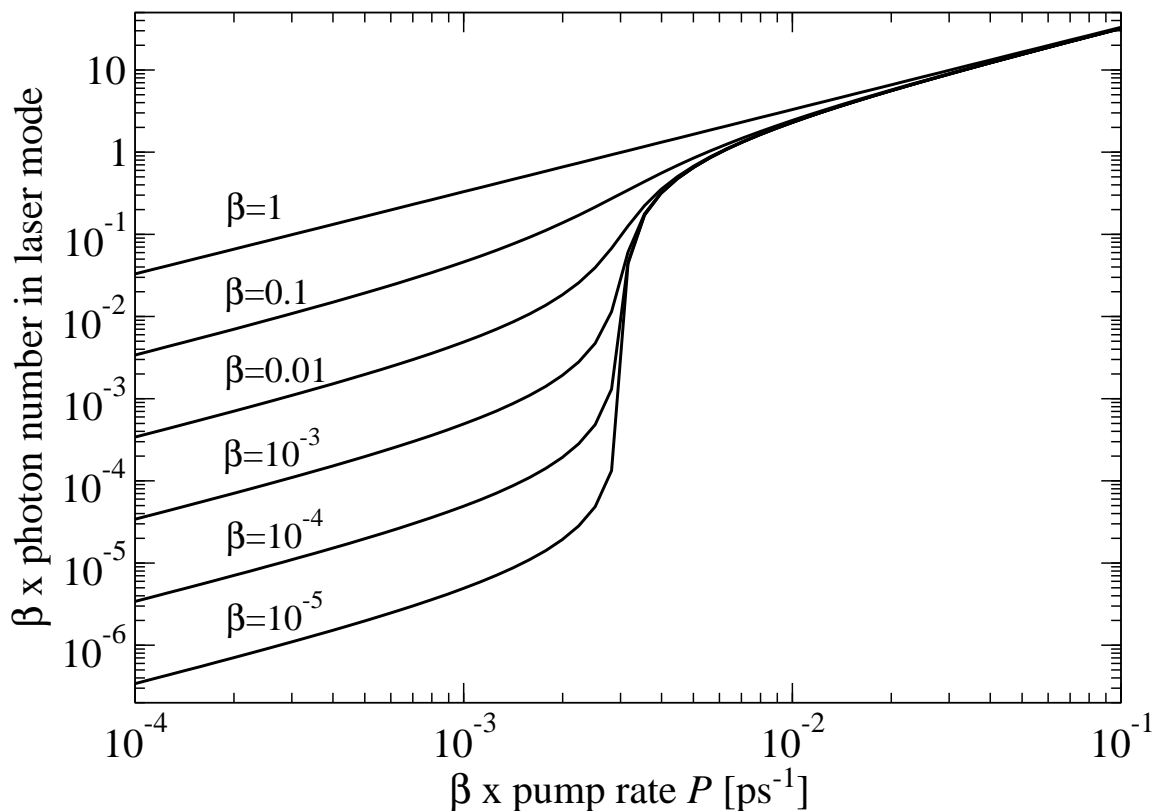


Figure 13.2: Calculated input/output curves for the atomic limit and for $\beta = 1$ to 10^{-5} from top to bottom. The picture is taken from Ref. [32]

14 From thermal to Poissonian photon statistics: the laser threshold

In the limiting case of $\beta = 1$ it is not possible to determine the laser threshold from the input/output curve. To determine whether the light emission is of thermal or coherent character, or in other words whether spontaneous or stimulated emission dominates, we have to calculate the photon statistics.

To calculate the photon statistics two approaches are possible. One can solve the quantum-mechanical von-Neumann equation for the statistical operator and compute the full probability distribution p_n . This distribution contains all relevant statistical information for a characterization of the emission process. However, such a method typically is limited to systems of few QDs and few electrons per QD. Alternatively we can follow the approach discussed in the introduction to this part and study the second order correlation function

$$g^{(2)}(\tau = 0) = \frac{\langle n^2 \rangle - \langle n \rangle}{\langle n \rangle^2}, \quad (14.1)$$

whose value at $\tau = 0$ contains information about the emission statistics. For details see Ref. [183]. In this chapter we will follow the latter approach, that has the additional advantage, that the intensity correlation function can directly be measured in a Hanbury-Brown and Twiss type coincidence measurement [171]. In the next section we will therefore discuss the necessary extensions to the laser model to include information about the intensity correlation function.

14.1 Extended laser equations

Now we turn to the extended set of laser equations including carrier-photon and photon-photon correlation functions. The statistical properties of the light emission can be described in terms of the autocorrelation function at zero delay time, as given in Eq. (14.1). In our semiconductor approach the photon number operator for

the laser mode is $n = b^\dagger b$. By means of Eq. (5.2d), we can introduce $\delta\langle b^\dagger b^\dagger bb \rangle = \langle b^\dagger b^\dagger bb \rangle - 2\langle b^\dagger b \rangle^2$. Since $\langle b \rangle = \langle b^\dagger \rangle = 0$ for a system without coherent excitation, only a factorization into doublets is possible. The factor of two arises from the two realizations for this factorization. Then the autocorrelation function can be written in terms of a quadruplet correlation function:

$$g^{(2)}(\tau = 0) = 2 + \frac{\delta\langle b^\dagger b^\dagger bb \rangle}{\langle b^\dagger b \rangle^2}. \quad (14.2)$$

To access the intensity correlations, we must calculate the correlation function in Eq. (14.2), which is a quadruplet contribution. This implies that the treatment within the cluster expansion has to be extended to the quadruplet level. Only photons from the laser mode are assumed to build up correlations, and because we consider only QDs in resonance with the cavity, the free evolution energy terms drop out and are therefore not explicitly given in the following.

The time evolution of the intensity correlation function is given by

$$\left(\hbar \frac{d}{dt} + 4\kappa \right) \delta\langle b^\dagger b^\dagger bb \rangle = 4|g|^2 \sum_{\nu'} \delta\langle b^\dagger b^\dagger b v_\nu^\dagger c_{\nu'} \rangle, \quad (14.3)$$

where the sum involves all resonant laser transitions from various QDs and, as in the preceding chapter, κ indicates the loss rate for the cavity mode. In this equation another quadruplet function enters, which represents a correlation between the photon-assisted polarization and the photon number. For the corresponding equation of motion we obtain

$$\begin{aligned} \left(\hbar \frac{d}{dt} + 3\kappa + \Gamma \right) \delta\langle b^\dagger b^\dagger b v_\nu^\dagger c_{\nu'} \rangle &= -2|g|^2 \langle b^\dagger v_\nu^\dagger c_\nu \rangle^2 \\ &\quad - (1 - f_\nu^e - f_\nu^h) \delta\langle b^\dagger b^\dagger bb \rangle \\ &\quad + 2f_\nu^h \delta\langle b^\dagger b c_\nu^\dagger c_\nu \rangle - 2f_\nu^e \delta\langle b^\dagger b v_\nu^\dagger v_\nu \rangle \\ &\quad - 2\delta\langle b^\dagger b c_\nu^\dagger v_\nu^\dagger c_\nu v_{\nu'} \rangle + \sum_{\nu'} \delta\langle b^\dagger b^\dagger v_\nu^\dagger v_{\nu'}^\dagger c_\nu c_{\nu'} \rangle. \end{aligned} \quad (14.4)$$

Here we have again scaled $\delta\langle b^\dagger b^\dagger b v_\nu^\dagger c_{\nu'} \rangle \rightarrow g \delta\langle b^\dagger b^\dagger b v_\nu^\dagger c_\nu \rangle$ with the light-matter coupling g for the laser mode. The triplet photon-carrier correlations in the third line

are the same as in Eq. (13.10), and their evolution is given by

$$\begin{aligned} \left(\hbar \frac{d}{dt} + 2\kappa \right) \delta \langle b^\dagger b c_\nu^\dagger c_\nu \rangle &= -2 |g|^2 \operatorname{Re} \left[\delta \langle b^\dagger b^\dagger b v_\nu^\dagger c_\nu \rangle \right. \\ &\quad \left. + \sum_{\nu'} \delta \langle b^\dagger v_{\nu'}^\dagger c_\nu^\dagger c_{\nu'} c_\nu \rangle + (\langle b^\dagger b \rangle + f_\nu^e) \langle b^\dagger v_\nu^\dagger c_\nu \rangle \right], \end{aligned} \quad (14.5)$$

$$\begin{aligned} \left(\hbar \frac{d}{dt} + 2\kappa \right) \delta \langle b^\dagger b v_\nu^\dagger v_\nu \rangle &= 2 |g|^2 \operatorname{Re} \left[\delta \langle b^\dagger b^\dagger b v_\nu^\dagger c_\nu \rangle \right. \\ &\quad \left. - \sum_{\nu'} \delta \langle b c_{\nu'}^\dagger v_\nu^\dagger v_{\nu'} v_\nu \rangle + (\langle b^\dagger b \rangle + f_\nu^h) \langle b^\dagger v_\nu^\dagger c_\nu \rangle \right]. \end{aligned} \quad (14.6)$$

The correlation functions in the sum, which have been scaled as $\delta \langle b^\dagger v_{\nu'}^\dagger c_\nu^\dagger c_{\nu'} c_\nu \rangle \rightarrow g \delta \langle b^\dagger v_{\nu'}^\dagger c_\nu^\dagger c_{\nu'} c_\nu \rangle$, $\delta \langle b c_{\nu'}^\dagger v_\nu^\dagger v_{\nu'} v_\nu \rangle \rightarrow g \delta \langle b c_{\nu'}^\dagger v_\nu^\dagger v_{\nu'} v_\nu \rangle$, obey equations of motion

$$\begin{aligned} \left(\hbar \frac{d}{dt} + \kappa + \Gamma \right) \delta \langle b c_{\nu'}^\dagger v_\nu^\dagger v_{\nu'} v_\nu \rangle &= (1 - \delta_{\nu\nu'}) \\ &\quad \left[(1 - f_{\nu'}^e - f_{\nu'}^h) \delta \langle b^\dagger b v_\nu^\dagger v_\nu \rangle - |g|^2 \langle b^\dagger v_\nu^\dagger c_\nu \rangle^* \langle b^\dagger v_{\nu'}^\dagger c_{\nu'} \rangle^* \right], \end{aligned} \quad (14.7)$$

$$\begin{aligned} \left(\hbar \frac{d}{dt} + \kappa + \Gamma \right) \delta \langle b^\dagger v_{\nu'}^\dagger c_\nu^\dagger c_{\nu'} c_\nu \rangle &= (1 - \delta_{\nu\nu'}) \\ &\quad \left[(1 - f_{\nu'}^e - f_{\nu'}^h) \delta \langle b^\dagger b c_\nu^\dagger c_\nu \rangle + |g|^2 \langle b^\dagger v_\nu^\dagger c_\nu \rangle \langle b^\dagger v_{\nu'}^\dagger c_{\nu'} \rangle \right]. \end{aligned} \quad (14.8)$$

In the following, we give arguments why the correlation functions, which are determined by Eqs. (14.7) and (14.8), and the last term of Eq. (14.4) only contribute if correlations between *different* QDs exist, i.e. superradiant coupling plays a role in the system. The effect of superradiance is known to rely on weak dephasing, which is difficult to realize under the considered high-excitation conditions (cf. Part III). We refer to the dipole selection rules discussed in Chapter 7, where optical transitions with a given circular light polarization are coupled to a particular electron spin and the corresponding hole total angular momentum. Specifically, the *s*-shell states for electrons are spin degenerate and the two spin states are coupled to different light polarizations. If we consider correlations between photons with the *same circular polarization*, we find that they are linked to states for which only one electron or hole per *s*-shell and QD are available. In other words, annihilating two valence-band electrons in the case of $\langle b c_{\nu'}^\dagger v_\nu^\dagger v_{\nu'} v_\nu \rangle$ and two conduction-band electrons in the case of $\langle b^\dagger v_{\nu'}^\dagger c_\nu^\dagger c_{\nu'} c_\nu \rangle$ is only possible if these carriers belong to different QDs. Hence, for $\nu = \nu'$ these expectation values, and according to their definition

$$\begin{aligned} \langle b c_{\nu'}^\dagger v_\nu^\dagger v_{\nu'} v_\nu \rangle &= -\langle b c_\nu^\dagger v_\nu \rangle f_\nu^v (1 - \delta_{\nu\nu'}) \\ &\quad + \delta \langle b c_{\nu'}^\dagger v_\nu^\dagger v_{\nu'} v_\nu \rangle, \end{aligned} \quad (14.9)$$

$$\begin{aligned} \langle b^\dagger v_{\nu'}^\dagger c_\nu^\dagger c_{\nu'} c_\nu \rangle &= -\langle b^\dagger v_{\nu'}^\dagger c_{\nu'} \rangle f_\nu^c (1 - \delta_{\nu\nu'}) \\ &\quad + \delta \langle b^\dagger v_{\nu'}^\dagger c_\nu^\dagger c_{\nu'} c_\nu \rangle , \end{aligned} \quad (14.10)$$

also the corresponding correlation functions $\delta \langle b c_\nu^\dagger v_\nu^\dagger v_{\nu'} v_\nu \rangle$ and $\delta \langle b^\dagger v_{\nu'}^\dagger c_\nu^\dagger c_{\nu'} c_\nu \rangle$ vanish exactly. The correlation functions referring to different QDs $\nu \neq \nu'$ are related to superradiant coupling. The same applies to the expectation value

$$\begin{aligned} \langle b^\dagger b^\dagger v_{\nu'}^\dagger v_\nu^\dagger c_\nu c_{\nu'} \rangle &= 2 \langle b^\dagger v_\nu^\dagger c_\nu \rangle \langle b^\dagger v_{\nu'}^\dagger c_{\nu'} \rangle (1 - \delta_{\nu\nu'}) \\ &\quad + \delta \langle b^\dagger b^\dagger v_{\nu'}^\dagger v_\nu^\dagger c_\nu c_{\nu'} \rangle , \end{aligned} \quad (14.11)$$

which also vanishes together with the corresponding correlation function for $\nu = \nu'$. Under the assumption that superradiance is weak in the system, the discussed correlation functions are neglected. If, however, the phenomenon of superradiant coupling itself is to be studied, the correlation functions must be included via their own equations of motion. Finally, the term $\delta \langle b^\dagger b c_\nu^\dagger v_\nu^\dagger c_\nu v_{\nu'} \rangle$ in Eq. (14.4) is a generalization of the correlations to the source term of spontaneous emission $C_{\alpha\nu\nu\alpha}^x = \delta \langle c_\alpha^\dagger v_\nu^\dagger c_\nu v_\alpha \rangle$. For consistency reasons, this contribution is neglected in accordance with the above discussed omission of C^x .

Effects due to the Coulomb interaction of carriers can be included along the same lines as discussed in Sections 13 and 13.2. The contributions to Eq. (14.4), that remain on the quadruplet level, are given by

$$\begin{aligned} i\hbar \frac{d}{dt} \delta \langle b^\dagger b^\dagger b v_\nu^\dagger c_\nu \rangle \Big|_{\text{Coul}} &= -2 \sum_\alpha (1 - f_\nu^e - f_\nu^h) V_{\nu\alpha\nu\alpha} \delta \langle b^\dagger b^\dagger b v_\nu^\dagger c_\nu \rangle \\ &\quad - 2(f_\alpha^e + f_\alpha^h) V_{\nu\alpha\nu\alpha} \delta \langle b^\dagger b^\dagger b v_\nu^\dagger c_\nu \rangle . \end{aligned} \quad (14.12)$$

The result shows an analogous structure like the Hartree-Fock Coulomb terms for $\langle b^\dagger v_\nu^\dagger c_\nu \rangle$ in Eq. (13.9) and can be interpreted accordingly as a renormalization of the single-particle energies and as interband exchange interaction causing additional renormalizations of the transition energies as well as a redistribution of oscillator strength between different QD transitions.

Coulomb interaction contributions to $\delta \langle b^\dagger b c_\nu^\dagger c_\nu \rangle$ and $\delta \langle b^\dagger b v_\nu^\dagger v_\nu \rangle$ are analogous to those contributing to the carrier dynamics of f_ν^e and f_ν^h discussed in detail in Ref. [88]. Their inclusion is, however, beyond the scope of this thesis and will be the subject of future investigations.

14.2 Results

We now present numerical solutions of the extended semiconductor laser theory including carrier-photon correlations based on Eqs. (13.7), (13.10), (13.16), (13.17),

and (14.3)–(14.6). Again, we use the same parameters as in Sections 13.3 and 14.3, but different relaxation times for electrons and holes are taken: $\tau_r^e = 1 \text{ ps}$, $\tau_r^h = 500 \text{ fs}$.

In Figure 14.1 the autocorrelation function is shown atop the input/output curve for various values of β . There are several striking features:

1. The jump of the intensity curve from below to above threshold is no longer determined by $1/\beta$, as in Figs. 13.2 and 14.2, obtained from a laser theory for two-level systems. This is of particular importance since measurements of the input/output characteristics are often used to experimentally deduce the β -factor according to the predictions of the two-level models. If the atomic $1/\beta$ -behavior would be used to extract the β -factors from the curves in Figure 14.1, one would obtain 0.017 instead of 0.1, 0.0017 instead of 0.01, and 0.00017 instead of 0.001.
2. For small β values, the s-shaped intensity jump is accompanied by a decrease of the second-order coherence from the Poisson value $g^{(2)}(0) = 2$ for thermal light to $g^{(2)}(0) = 1$ for coherent laser light. Using larger β values, the abrupt drop of the autocorrelation function becomes softer, and below threshold $g^{(2)}$ remains smaller than two. This decrease in the autocorrelation function is already a result of the relatively high cavity quality (long cavity lifetime). For a shorter cavity lifetime and a large number of emitters, also at $\beta = 1$ a value of $g^{(2)}(0) = 2$ is obtained in the sub-threshold regime, see below.
3. At high pump intensities saturation effects due to Pauli blocking become visible in the input/output curve, effectively limiting the maximum output that can be achieved. Additionally, effects of quenching were observed in master equation treatments [174].

14.3 Verification of the treatment of correlations: Comparison with a master equation model

In Section 13.3 we have shown that the developed laser model can be reduced to rate-equations, if the semiconductor is replaced by effective two-level systems. In the extended laser model derived in Section 14.1, the calculation of photon correlations is based on the cluster expansion that provides a truncation of the hierarchy of correlation functions. The aim of this section is to verify that such a truncation on the quadruplet level provides correct results for the photon-intensity correlations, described by the autocorrelation function $g^{(2)}$.

In quantum optics, access to photon-intensity fluctuations can either be obtained by

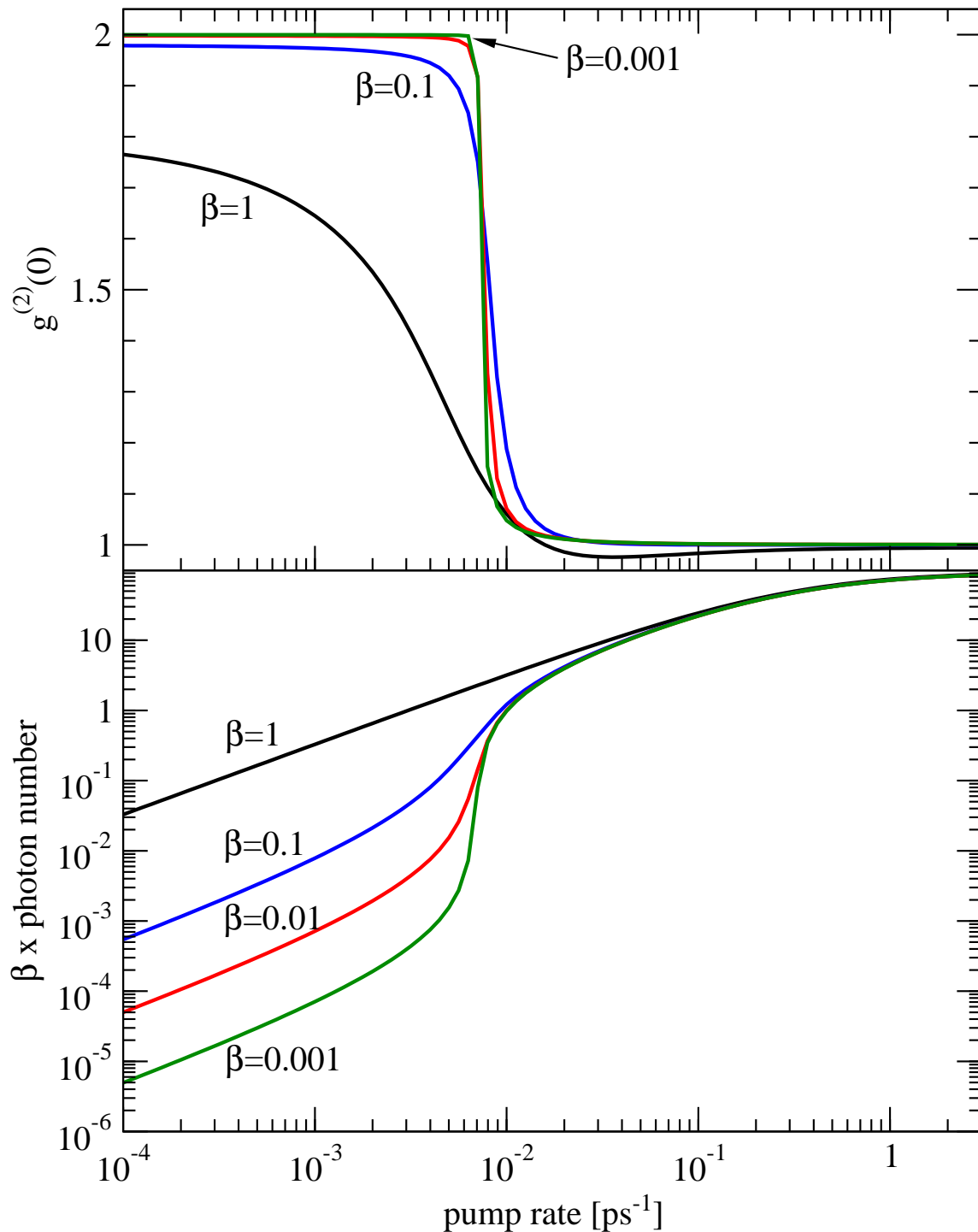


Figure 14.1: Calculated output curve (lower panel) and autocorrelation function $g^{(2)}(\tau = 0)$ (upper panel) for $\beta = 1, 0.1, 0.01$, and 0.001 . The main parameters correspond to those in Figure 13.2. The picture is taken from Ref. [32]

invoking the quantum regression theorem [148], or by using a master equation to calculate the diagonal density matrix for the coupled atom-photon system [170, 174, 175]. Both methods are not directly applicable in semiconductors due to the presence of many-body effects and the modified source term of spontaneous emission. However, our semiconductor model can be reduced to a description of two-level systems. This provides a verification method for our approach and the possibility to study how well the truncation of correlations within the cluster expansion scheme works, as carrier-photon correlations are treated on an exact level in the master equation within the two-level approach.

We have shown in Section 13.3 that the source term of spontaneous emission reduces to f_ν^e under the assumption that only one electron is present in each two-level atomic system. Additionally, the equation of motion (14.4) changes to

$$\left(\hbar \frac{d}{dt} + 3\kappa + \Gamma \right) \delta \langle b^\dagger b^\dagger b v_\nu^\dagger c_\nu \rangle = -2g^2 \langle b^\dagger v_\nu^\dagger c_\nu \rangle^2 - 4|g|^2 \langle b^\dagger v_\nu^\dagger c_\nu \rangle \operatorname{Re} \langle b^\dagger v_\nu^\dagger c_\nu \rangle - (1 - f_\nu^e - f_\nu^h) \delta \langle b^\dagger b^\dagger b b \rangle + 2\delta \langle b^\dagger b c_\nu^\dagger c_\nu \rangle , \quad (14.13)$$

again neglecting the quadruplet-level correlation functions appearing on the right hand side and scaling with the light-matter coupling strength. All other equations of motion for the correlations remain unmodified under the two-level assumptions. In order to quantitatively compare to the master equations given in Ref. [170], we must once more assume a fully inverted system, which is done by setting $1 - f_\nu^h = 0$ in Eqs. (13.10) and (14.13). Due to the coupling to the correlation functions in Eq. (13.10), an adiabatic solution in the spirit of the rate equations (13.18) and (13.19) is no longer possible. Nevertheless, the numerical steady-state solution can be directly compared to the results of the master equation.

To remain as close as possible to the semiconductor model, we solve the atomic two-level version of Eqs. (13.7) and (13.10) together with Eqs. (13.16) and (13.17) for the population dynamics of the laser and pump level (with $f_\nu^e f_\nu^h$ replaced by f_ν^e for the spontaneous emission). This allows us to avoid the introduction of a number of excited two-level systems. For the direct comparison with the master equations, $R_{p \rightarrow s}$ is used as a measure for the carrier generation rate at the laser transition level.

Figure 14.2 shows numerical results from our truncated cluster expansion model applied to two-level systems, in comparison to results obtained from the master equation in the formulation of Rice and Carmichael [170]. The values for the parameters κ , \tilde{N} , and τ_{sp} were taken as in Section 13.2 and are the same as for Figure 13.2. Additionally relaxation rates entering $R_{p \rightarrow s}^{e,h}$ for both electrons and holes of 1 ps, and a dephasing $\Gamma = 1.36$ meV, corresponding to a time of approximately 500 fs, were used. The upper part of the figure shows the second order correlation function atop the input/output curve for various values of the β -factor. Looking at the input/output curves, we see that the equation of motion approach agrees convincingly well with

the results from the master equation for all values of β . Regarding the autocorrelation function in the top panel, there is excellent agreement for small values of the β -factor. A deviation of roughly 5% becomes apparent as β is increased to unity, and the results are in good agreement regarding the onset and the end of the transition from thermal to coherent light emission.

We point out that the deviation between lines and symbols in Figure 14.2 is a measure for the applicability of the cluster expansion method leading to a truncation of carrier-photon and photon-photon correlations beyond the quadruplet level. Clearly we have to consider the tradeoff between deviations due to this truncation and the possibility to include semiconductor effects. The agreement between the truncated (cluster expansion) and non-truncated (master equation) description of atomic two-level systems depends on parameters like the cavity lifetime and the spontaneous emission rate. For the above comparison values of $\hbar\kappa = 20\mu eV$ and $\tau_{sp} = 50ps$, that are typical for current microcavities, have been used. As long as the semiconductor theory is used for parameters where its two-level version is in agreement with the master equation, we are reassured that the truncation of the cluster expansion can be applied with respect to the photonic correlations. The semiconductor theory contains additional carrier-carrier correlation effects, which are well described by means of the cluster expansion method. In fact, the cluster expansion was developed to treat many-body effects of carriers [89]. Successful applications include the photoluminescence of QDs [88, 87], and exciton formation in quantum wells [85].

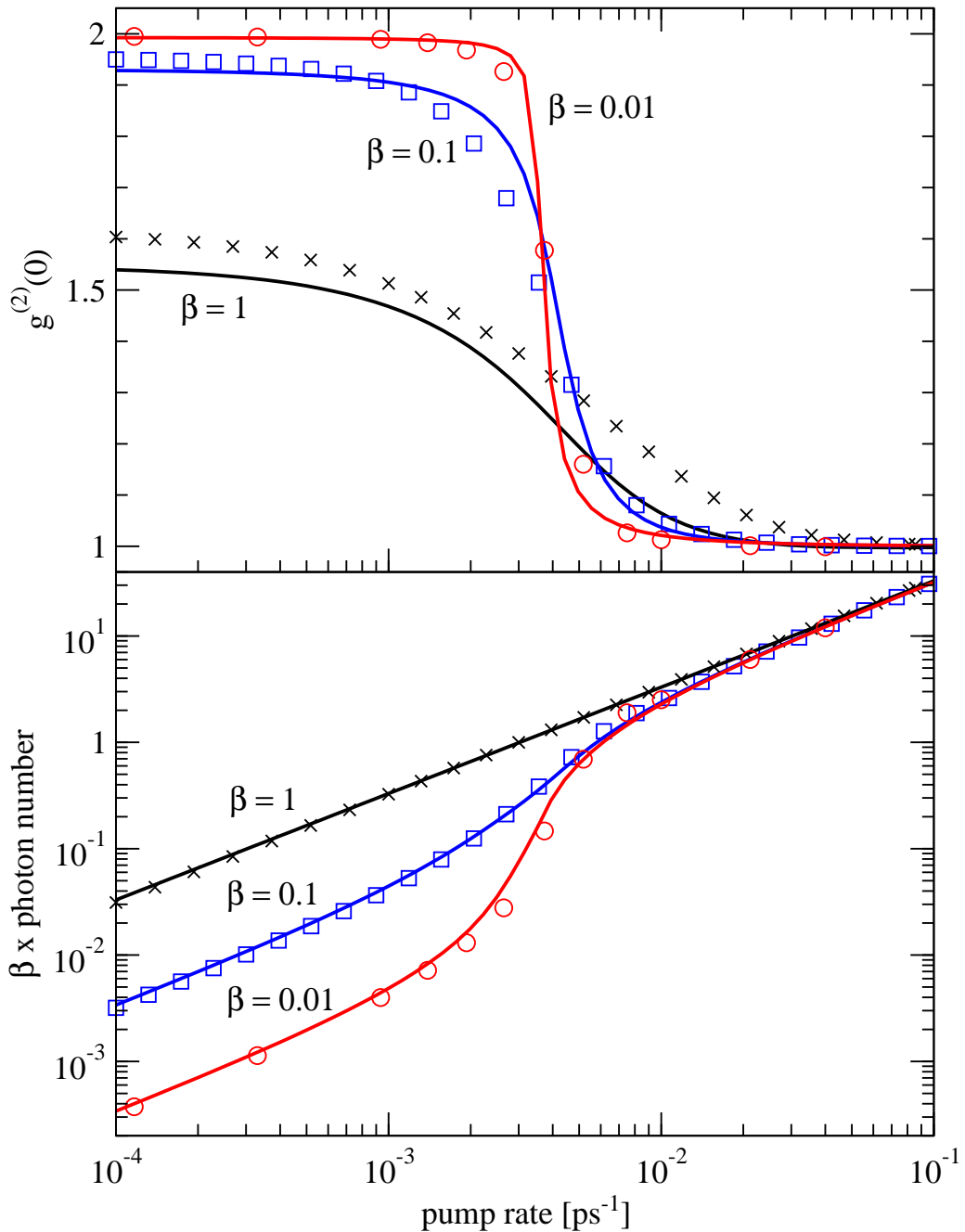


Figure 14.2: Autocorrelation function (top) and input/output curve (bottom) for a fully inverted two-level system. Comparison between the master equation (symbols) and the two-level version of the semiconductor theory (solid lines) for $\beta = 1, 0.1$, and 0.01 . On the x -axis the pump rate into the laser level is given. For the modified semiconductor theory, this corresponds to an effective carrier generation rate in the s -shell. The picture is taken from Ref. [32]

14.4 Analytical results for $g^{(2)}(0)$

In addition to the numerical results of the semiconductor model, it is instructive to study analytical solutions for $g^2(0)$ in the two limiting cases of strong and weak pumping. For this purpose we use the stationary limit of Eqs. (13.7), (13.10), and (14.3)–(14.6). Considering the resonant s -shell contributions from identical QDs, we replace $\sum_{\nu'}$ by the number of QDs N . Inserting in Eq. (13.7) the photon-assisted polarization from Eq. (13.10), ignoring spontaneous emission for the above-threshold solution, and expressing the higher-order correlations with the help of Eqs. (14.5) and (14.6), we obtain from (14.2) and (14.3)

$$g^{(2)}(0) - 1 = -\frac{\kappa(\kappa + \Gamma)}{2|g|^2 \langle b^\dagger b \rangle} \left(1 + \frac{|g|^2 N}{\kappa(\kappa + \Gamma)} (1 - f_s^e - f_s^h) \right). \quad (14.14)$$

In the limit $\langle b^\dagger b \rangle / N \gg 1$, the right hand side vanishes. Hence, we obtain $g^{(2)}(0) = 1$, i.e. well above threshold the light is coherent.

For the limiting case of weak pumping, we seek again the stationary solution of our coupled system of equations, now under the assumption that in Eq. (13.10) the stimulated emission term and the higher-order correlations $\delta\langle b^\dagger b c_\nu^\dagger c_\nu \rangle$, $\delta\langle b^\dagger b v_\nu^\dagger v_\nu \rangle$ can be neglected. A convenient way to solve for the intensity correlation function $\delta\langle b^\dagger b^\dagger b b \rangle$ is to insert Eq. (14.4) into (14.3). The higher-order correlations in Eq. (14.4) are replaced by the static solution of Eqs. (14.5) and (14.6), while in the latter $\langle b^\dagger v_\nu^\dagger c_\nu \rangle$ is replaced by Eq. (13.7), and $\delta\langle b^\dagger b^\dagger b v_\nu^\dagger c_\nu \rangle$ is traced back to $\delta\langle b^\dagger b^\dagger b b \rangle$ with the stationary solution of Eq. (14.3). As explained above, we ignore the quadruplet correlations occurring in Eq. (14.4). Together with Eqs. (14.2) and (13.7) we finally obtain

$$\begin{aligned} & \left(\frac{\kappa(3\kappa + \Gamma)}{|g|^2 N} + (1 - f_s^e - f_s^h) \right) [g^{(2)}(0) - 2] = \\ & \quad - \frac{2(f_s^e + f_s^h)}{N} [g^{(2)}(0) - 1] - \frac{2\kappa(3\kappa + 2\Gamma)}{|g|^2 N^2}. \end{aligned} \quad (14.15)$$

To evaluate this formula further, we restrict ourselves to the case

$$\frac{\kappa^2}{|g|^2 N} \gg 1, \quad (14.16)$$

or $2\kappa/\hbar \gg N/\pi_l$, i.e. the cavity loss rate is much larger than the total rate of spontaneous emission into the laser mode. In this so called “bad cavity limit” [170], in which typical semiconductor lasers operate, we obtain as an analytical result of our theory

$$g^{(2)}(0) = 2 - \frac{2}{N}. \quad (14.17)$$

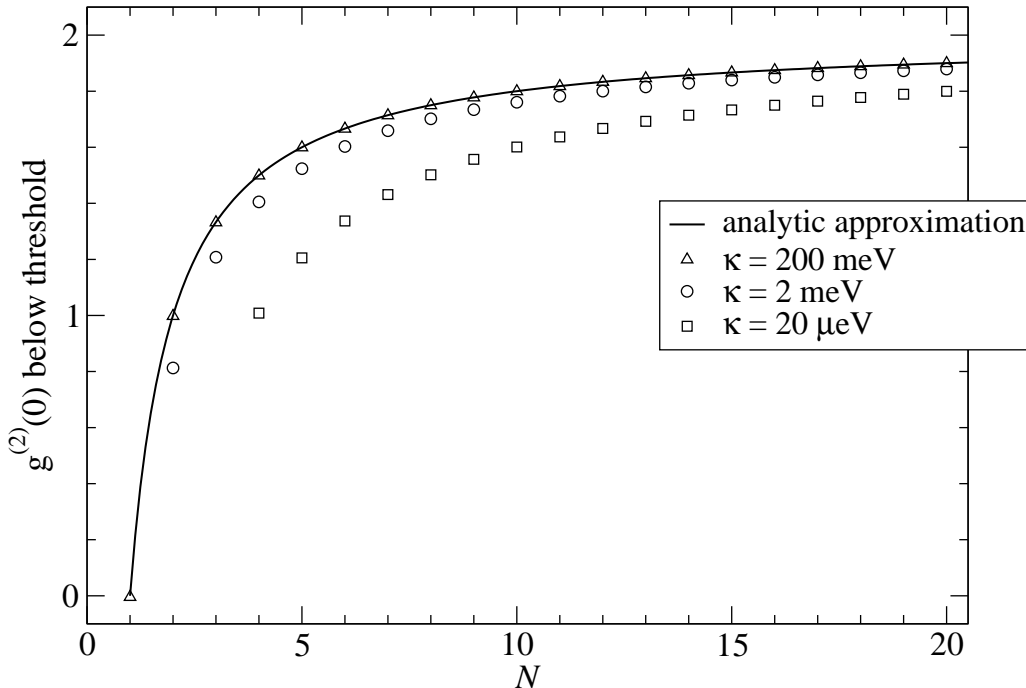


Figure 14.3: Sub-threshold values of $g^{(2)}(0)$ for $\beta = 1$ obtained from the extended semiconductor laser model. The analytical approximation in the “bad cavity” limit, Eq. (14.17), is compared to numerical results obtained with different values for the inverse cavity lifetime κ . The picture is taken from Ref. [32]

This is an important finding, because it provides the statistics of thermal light in the limit of many QDs, $g^{(2)}(0) = 2$, and in the opposite limit of a single QD it gives the statistics of a single-photon emitter, $g^{(2)}(0) = 0$.

In Figure 14.3 we show the sub-threshold value of the autocorrelation function versus the number of emitters N . The analytical solution (solid line), which was derived for the limit of large κ , is compared to numerical solutions of the extended semiconductor laser model (open symbols) for $\beta = 1$ and various values of κ . All other parameters are the same as those used in Figure 14.1. If $\kappa = 200 \text{ meV}$, the condition for the analytical solution is fulfilled and perfect agreement between analytical and numerical results is obtained. In this case, the thermal emission $g^{(2)}(0) = 2$ below the laser threshold is approached for a large number of emitters N . In the limit of one single QD, the antibunching signature $g^{(2)}(0) = 0$ is numerically obtained. On the other hand, in the theoretical limit of an infinitely good cavity $\kappa \rightarrow 0$, a constant value of $g^{(2)}(0) = 1$ is expected for atomic models [170]. The case of larger cavity lifetimes is displayed (circles and squares) and the trend of a decrease of the subthreshold value is observed. For the case of a small number of emitters in a very good cavity, photon correlations become so strong that the truncation on quadruplet

order becomes insufficient.

14.5 Conclusion

In this part of the thesis, we have developed a laser theory for semiconductor QD based devices, that includes carrier-photon correlations and allows us to determine the photon statistics of the light emission. The theory has been applied to describe microcavity lasers with QDs as active material. It has been demonstrated how the model can be reduced to obtain commonly used rate equations, and how the incorporation of two-level assumptions makes it possible to compare the photon correlations to those obtained from a master equation. By these means, we have verified that the truncation method of the arising hierarchy of equations of motion can be applied in the considered parameter regime, which is typical for current state-of-the-art microcavity lasers.

Using a numerical evaluation of the theory, we have demonstrated modifications of the characteristic emission properties due to semiconductor effects. Especially the jump in the input/output curve from below to above threshold is found not to scale with $1/\beta$, as it does in the two-level case.

Most importantly, our approach opens up the possibility to include the full spectrum of semiconductor effects in a consistent and well-defined manner. Besides a more complete inclusion of Coulomb correlations beyond the singlet level, relaxation and dephasing processes can also be treated on a microscopic level. Especially links to the gain model of Part III should be established, either by directly including the dephasing on a microscopic level, or by an effective approach using the fit formulas of Section 12.2. Furthermore, with respect to Coulomb and light-matter interaction-induced correlations between different QDs, effects of e.g. superradiant coupling can be studied. While this is beyond the scope of this thesis, it outlines a possible direction of future work.

Part V

Optical properties of nitride Quantum Dots

A very interesting and significant development in semiconductor physics in recent years has been the demonstration of lasing in III-nitride systems [23]. These components, that typically grow in the hexagonal wurtzite crystal structure, offer several technological advantages. They directly allow for emission in a wide spectral range, including the visible part, see Figure 14.4. Moreover, they also have the advantage of a significantly reduces toxicity compared to the conventional arsenide systems. For an introduction to the nitride material system and its applications, we refer the reader to the excellent books [184, 185].

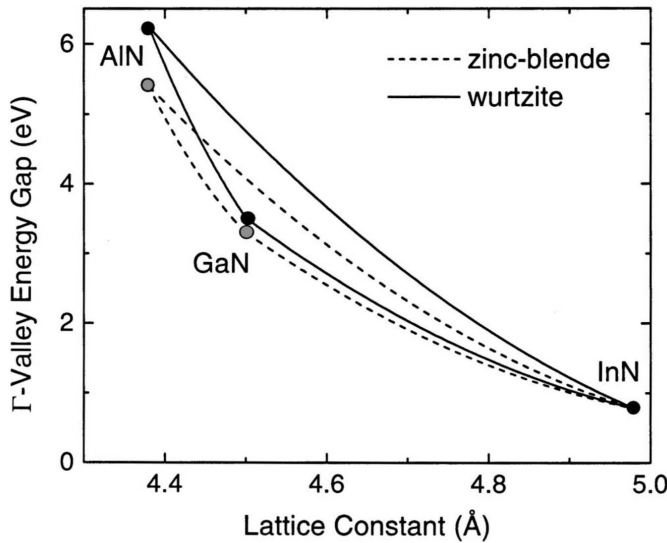


Figure 14.4: Bandgap vs. lattice constant for the nitride material system. Picture taken from Ref. [186]

However, nitride semiconductors are a challenging material system, both experimentally as well as theoretically. During growth various types of defects and dislocations can occur, making it difficult to produce nanostructures such as e.g. QDs or Bragg-reflectors of good crystalline quality. The theoretical challenges arise from the fact that nitride structures are significantly influenced by strong Coulomb and band-mixing effects. Moreover, nitride semiconductors are mostly grown on the *c*-plane. This leads to intrinsic piezoelectric fields, that strongly influence the single-particle states and therefore have to be included in the theoretical description. To incorporate these effects, extensive work has been done to study the electronic states in III-nitrides for bulk properties, see e.g. Ref. [186]. The valence band structure shows a strong non-parabolic dispersion and a pronounced mass anisotropy [187]. Corresponding calculations for the single-particle states in QD systems have been performed on the basis of $\mathbf{k} \cdot \mathbf{p}$ [188, 189, 190] or tight-binding [191, 192, 129, 193]

descriptions.

Many-body effects in nitride semiconductors, specifically carrier-carrier [135] and carrier-phonon [194] scattering, have been studied on the basis of coupled Schrödinger-Poisson equations. We will discuss the optical properties of nitride based QD systems in this part of the thesis. To describe the single-particle states on a microscopic basis, including band-mixing and piezoelectric fields, we employ a tight-binding description [129]. These single-particle states are used as a starting point for a many-body description of optical spectra, along the lines presented in Part III.

This part is organized as follows. In Chapter 15 we will discuss the properties of the wurtzite crystal structure and of our tight-binding approach for the determination of single-particle states and interaction matrix elements. Then, we will focus on optical properties of nitride QD systems in Chapter 16. As the treatment of the Coulomb interaction, that we presented in Part III is not feasible for the nitride material system, we will use a screened exchange - Coulomb hole (SX-CH) approximation to determine the lineshifts in the optical spectra. Afterwards we will discuss the carrier-phonon interaction in nitride QDs and show optical gain spectra with dephasing due to carrier-LO-phonon interaction.

We would like to point out, that the results discussed in this part of the thesis have been achieved together with Jan Seebeck, for details see Chapter 1. The tight-binding calculations of the single-particle states and the resulting optical dipole matrix elements for the QD transitions were provided by Stefan Schulz and we will refer to his excellent thesis [129] for details of the tight-binding model.

15 Tight-binding calculations for wurtzite crystals

In comparison to the InGaAs material system, that we discussed in previous parts, the nitride material systems shows additional features, that are important for the determination of their optical properties and therefore have to be considered. Depending on the growth conditions, nitride semiconductors can crystallize in zincblende or in wurtzite crystal structure. However, we will only consider nitride structures, grown in the wurtzite crystal structure in this part.

The symmetry of the zincblende structure does not allow for a preferential axis and therefore is non-polar, so that only shear strain can introduce polarization fields. The wurtzite structure in contrast shows a polar axis in *c*-direction. For GaN, InN and AlN it was shown in Ref. [195] that the conventional unit cell deviates from the ideal ratio of $\frac{c}{a} = \sqrt{\frac{8}{3}}$, leading to a spontaneous polarization in *c*-direction. Moreover, large strain-induced polarizations are known for the nitride material system. The resulting electrostatic fields lead to a separation of electron and hole wavefunction, known as the quantum-confined Stark effect (QCSE) [196, 197]. As this can drastically reduce the dipole strength of the optical transitions, an inclusion of these effects is critical for the determination of optical properties. Moreover, strong bandmixing effects are known for the nitride material system, that also influence the optical properties, via the dipole coupling and the Coulomb interaction. In this chapter we will discuss a tight-binding model for the calculation of single-particle states, that includes the piezo-electric fields and also accounts for the symmetry properties of the crystal structure.

15.1 The wurtzite crystal structure

The wurtzite crystal structure can be constructed from two interpenetrating sub-lattices, forming a hexagonally close packed lattice whose conventional unit cell is shown in Figure 15.1(a). Choosing the origin in the center of the bottom hexagon,

the basis vectors are given by

$$\mathbf{a}_1 = \left(\frac{\sqrt{3}}{2}a, -\frac{1}{2}a, 0 \right) \quad \mathbf{a}_2 = (0, a, 0) \quad \mathbf{a}_3 = (0, 0, c) \quad (15.1)$$

The unit cell of the wurtzite lattice contains four atoms located at

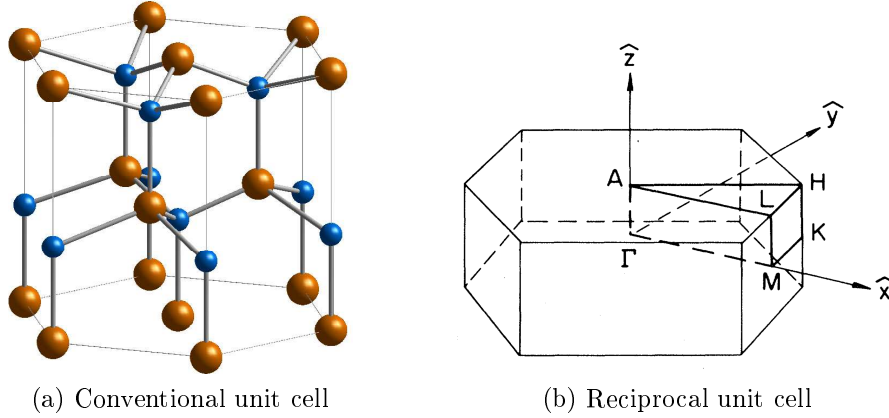


Figure 15.1: Conventional and reciprocal unit cells of the wurtzite lattice. Pictures courtesy of N. Baer.

$$\mathbf{t}_1 = (0, 0, 0) \quad \mathbf{t}_2 = \left(\frac{a}{\sqrt{3}}, 0, \frac{c}{2} \right) \quad \mathbf{t}_3 = \left(\frac{a}{\sqrt{3}}, 0, \frac{c}{8} \right) \quad \mathbf{t}_4 = \left(0, 0, \frac{5c}{8} \right) \quad (15.2)$$

where the anions are located at $\mathbf{t}_1, \mathbf{t}_2$ and the cations are located at $\mathbf{t}_3, \mathbf{t}_4$. In z-direction, the lattice has a double-layer structure as shown in Figure 15.2. The reciprocal lattice also shows a hexagonal symmetry, rotated by 30 degrees with respect to the real space lattice, and is described by the basis

$$\mathbf{b}_1 = \frac{2\pi}{a} \left(\frac{2}{\sqrt{3}}, 0, 0 \right) \quad \mathbf{b}_2 = \frac{2\pi}{a} \left(\frac{1}{\sqrt{3}}, 1, 0 \right) \quad \mathbf{b}_3 = \frac{2\pi}{c} (0, 0, 1) . \quad (15.3)$$

The corresponding Brillouin zone (BZ) is shown in Figure 15.1(b). The symmetry points in the plane of the middle hexagon of the BZ are given by

$$\mathbf{\Gamma} = (0, 0, 0) \quad \mathbf{M} = \frac{2\pi}{a} \left(\frac{1}{\sqrt{3}}, 0, 0 \right) \quad \mathbf{K} = \frac{2\pi}{a} \left(\frac{1}{\sqrt{3}}, \frac{1}{3}, 0 \right) \quad (15.4)$$

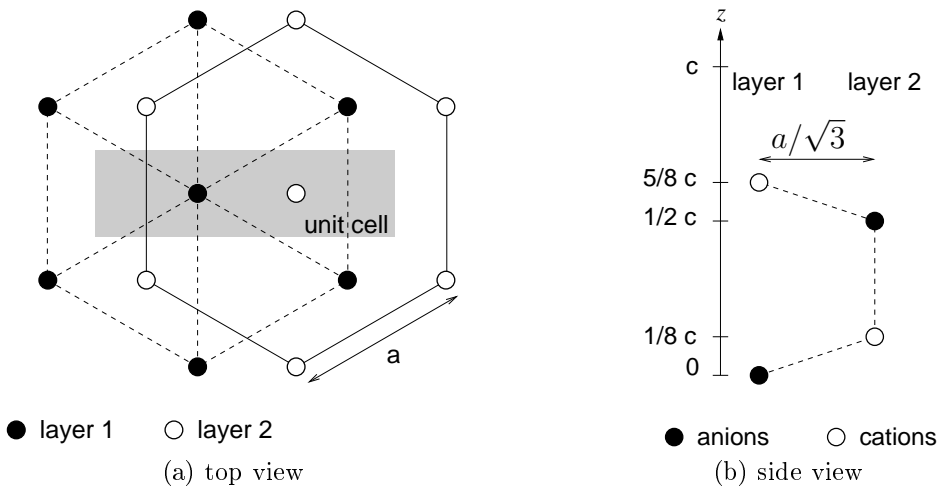


Figure 15.2: Unit cell of the wurtzite lattice in top view (a) and in side view (b).

15.2 Tight-binding wave-function model

In contrast to continuum models like the $\mathbf{k} \cdot \mathbf{p}$ approach, a TB description provides an atomistic description of the electronic properties of solids. The basic assumption is that electrons are tightly bound to their ions, similar as in atoms, and the electronic bandstructure is determined mainly by the overlap between neighboring atoms. In the following we will give only a brief introduction to the idea of TB methods. For details, we refer the reader to Refs. [132, 129]. The starting point is the Schrödinger equation for an electron in the crystal

$$[H^{\text{atom}} + \Delta V(\mathbf{R})] \psi(\mathbf{r}) = E \psi(\mathbf{r}) . \quad (15.5)$$

Here we separated the potential into its atomic part, contained in H^{atom} , and the remaining contributions $\Delta V(\mathbf{R})$. The basic assumption of the TB approach is that electrons are tightly bound to their ions and therefore one chooses the atomic orbitals as expansion basis. Using this ansatz, we can express the wavefunction of the solid as a linear combination of atomic orbitals $\phi_{\mathbf{R},\sigma}$ localized at the lattice sites \mathbf{R} ,

$$\psi(\mathbf{r}) = \sum_{\mathbf{R},\sigma} c_\sigma(\mathbf{R}) \phi_{\mathbf{R},\sigma}(\mathbf{r}) . \quad (15.6)$$

The index $\sigma \in \{\tau, \xi, s\}$ denotes the atomic orbital type τ (e.g. in a sp^3 basis), the atom type ξ and the spin s . For the case of a bulk semiconductor, we have spatial translational invariance in all three dimensions and therefore, Bloch's theorem allows to trace back the spatial dependence of the TB coefficients to a single unit-cell. This

yields for the quasi-momentum states of the bulk material

$$|\mathbf{k}\rangle \propto \sum_{\tau,\xi,s} \sum_{\mathbf{R}} e^{i\mathbf{k}\cdot\mathbf{R}} c_{\tau,\xi,s}(\mathbf{k}) |\mathbf{R},\tau,\xi,s\rangle . \quad (15.7)$$

Using this expansion we find a Schrödinger equation for the TB coefficients,

$$\sum_{\mathbf{R}',\sigma'} \langle \sigma, \mathbf{R} | \hat{H}^{\text{TB}} | \sigma', \mathbf{R}' \rangle c_{\sigma'}^{\alpha}(\mathbf{R}') = E^{\alpha} c_{\sigma}^{\alpha}(\mathbf{R}) . \quad (15.8)$$

In this work we will restrict our analysis to contributions from nearest neighbors, restricting the \mathbf{R}' summation. Orthogonalized Löwdin orbitals [129] ensure orthogonality of atomic orbitals from different lattice sites. Due to the strong localization of the atomic orbitals, the dominant contributions to the TB matrix arise from nearest-neighbor coupling. Details on the evaluation of the TB matrix elements are beyond the scope of this introductory section and can be found e.g. in Ref. [129]. For bulk semiconductors the TB matrix can be reduced to a small number of TB parameters.

15.2.1 The QD model

As discussed in the last chapter, the wavefunction is expressed as a linear combination of atomic orbitals $\phi_{\mathbf{R},\sigma}$ localized at the lattice sites \mathbf{R} ,

$$\psi(\mathbf{r}) = \sum_{\mathbf{R},\sigma} c_{\sigma}(\mathbf{R}) \phi_{\mathbf{R},\sigma}(\mathbf{r}) . \quad (15.9)$$

The index σ denotes the orbitals considered at each lattice site. In this work we consider a sp^3 basis. After having determined the tight-binding parameters for the corresponding bulk materials, we can employ an atomistic description of the QD heterostructure. To achieve this, we expand the QD wavefunction for the state α in the TB basis given above. The corresponding Schrödinger equation (15.8), represents a matrix problem, and for the matrix elements $\langle \sigma, \mathbf{R} | H^{\text{TB}} | \sigma', \mathbf{R}' \rangle$ the TB parameters of the bulk material $\langle \sigma, \mathbf{R} | H_{\text{bulk}}^{\text{TB}} | \sigma', \mathbf{R}' \rangle$ are used.

As the utilization of Bloch's theorem is not possible for a QD structure due to the lack of translational invariance, we introduce a finite supercell. Specifically, we consider a lens-shaped QD with the geometry as shown schematically in Figure 15.3. The QD consists of InN, grown in the (0001)-direction on top of a InN WL. The system is embedded in a GaN matrix. As periodic boundary conditions might lead to an artificial QD-QD coupling, we employ zero boundary conditions. This means, that the size of the supercell has to be chosen large enough, that the wavefunctions have decayed sufficiently at the boundaries.

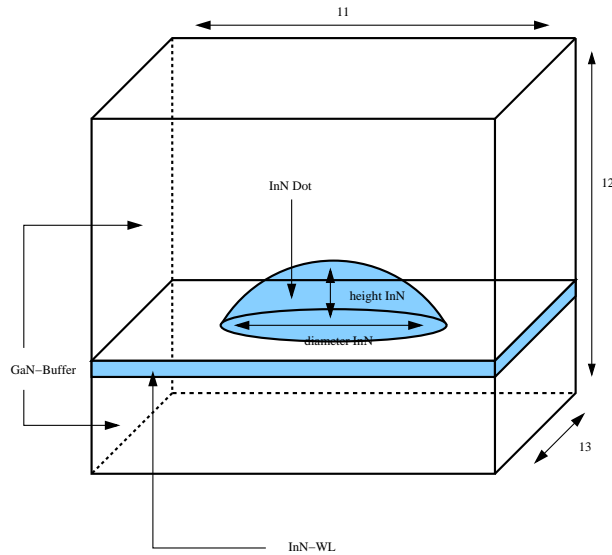


Figure 15.3: Super cell for calculation of QD states [129].

The parameter for each lattice site are chosen according to the species of the occupying atom (In, Ga, N). However, at the InN/GaN interfaces of the nanostructure the assignment of the N atoms is ambiguous and hence an averaging between InN and GaN parameters is employed [129]. The band offsets between the two materials is included as a shift in the diagonal bulk TB matrix elements [192].

A further complication of the theoretical description is given by the appearance of large electrostatic built-in fields in nitride semiconductors. In contrast to conventional III/V heterostructures consisting of the (In,Al,Ga As) material system and crystallized in the zinc-blende structure, nitride crystallized in the wurtzite structure exhibit significant electrostatic built-in fields for several reasons [198]. A small spontaneous polarization appears due to differences of the GaN and InN crystal structure to an ideal wurtzite structure [186]. This spontaneous polarization lies within the (0001)-direction, that is chosen as the growth direction for our QD model. Furthermore, we observe a strong strain-induced piezo-electric polarization. An inclusion of these electric fields is possible by treating them as site diagonal contributions $V_p(\mathbf{r}) = -e\phi_p(\mathbf{r})$ to the Hamiltonian, an approach that has been successfully applied both to QW [199] and QD [200] structures. The electrostatic potential follows from Poisson's equation $\Delta\phi_p(\mathbf{r}) = -\frac{1}{\epsilon_0\epsilon_b}\rho_p(\mathbf{r})$, where the polarization charge is given by $\nabla \cdot (\mathbf{P}_{\text{spont}} + \mathbf{P}_{\text{piezo}}) = -\rho_p(\mathbf{r})$. The strain induced contribution is approximated as in Ref. [201].

In Figure 15.4 the three energetically lowest confined states for electrons and holes are shown. The ground state both for electrons and holes shows no degeneracy (apart

from spin degeneracy). In contrast, the first excited states both for electrons and holes are double degenerate due to the C_{3v} symmetry [129].

As symmetry considerations are of paramount importance for a detailed classification of the electronic states, a lot of work has been devoted to clarify the symmetry properties of the resulting TB wavefunctions. However, as a detailed analysis of this topic would be beyond the scope of the present thesis, we will not go into the details here and refer the reader to the excellent discussions in Refs. [126, 129]. Nevertheless, we would like to summarize the main findings. Whereas a classification into s- and p-like states is directly evident for the electron states, it is much less obvious for the hole states. However, in fact such a classification is possible if we analyze the behavior of the hole states under symmetry operations of the underlying group. We find that indeed, we can classify the hole ground state as “s-like”, whereas the double degenerate excited state exhibits a “p-like” character. By “s-like” and “p-like” we here understand the invariance under the symmetry operations of the discrete group [129, 126].

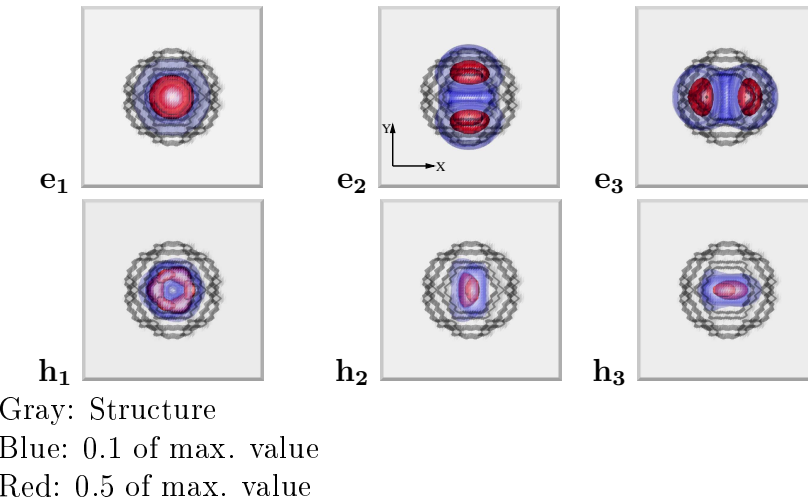


Figure 15.4: QD geometry shown from the top. The structure is visualized in gray and isosurfaces of the charge density are shown for 10% (blue) and 50% (red) of the maximum value. The picture is taken from Refs. [129, 191].

15.2.2 The WL model

As for the description of optical spectra for QDs, the inclusion of the WL plays a crucial role (cf. the discussion in Part III) we need a way to include the WL in our calculations. Due to the fact, that the QD states are given in the TB basis, we can

employ neither plane waves nor their orthogonalized versions. Rather we rely on a TB description of the WL also. This TB calculation yields Bloch states, which are the TB analogues of plane waves. Then the result is orthogonalized to the QD states like in the OPW method. This has the further advantage that the random distribution of QDs of the WL plane is taken into account, as in the usual OPW method. Were we to directly model the combined QD-WL system we would have to use periodic boundary conditions. This could lead to numerical artifacts due to artificial coupling between the QDs in different instances of the supercell. Moreover, such a procedure would imply a periodic array of QDs.

Specifically, due to translational invariance in the WL plane, the TB calculation can be restricted to a single column of unit cells along the growth direction (cf. Figure 15.5), as extension of the solution on that column to the whole system can be achieved by employing Bloch's theorem. In this sense it closely resembles the case of the bulk calculation, where one considers only one unit cell and uses the translational invariance in all three spatial dimensions. A further advantage of this approach is,

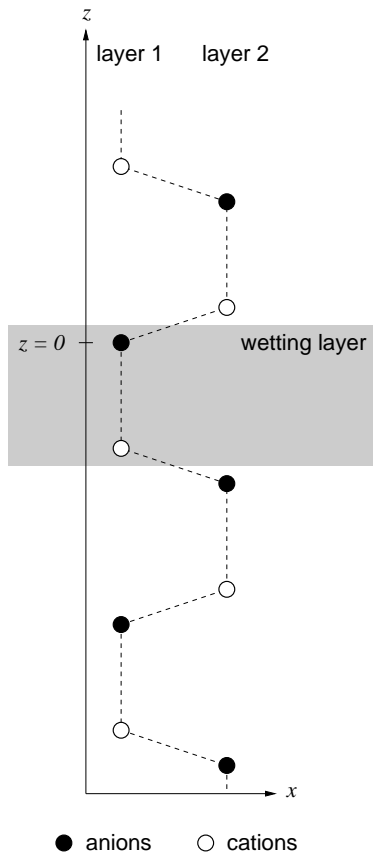


Figure 15.5: Column of unit cells for calculation of QW states.

that a direct classification of WL states using an in-plane crystal momentum $\hbar\mathbf{k}$ is

achieved. This is desirable as the translational invariance *is* present in the WL system and, at least on average, also in the QD-WL system. However, for the application of Bloch's theorem care has to be taken due to the existence of two layers within the unit cell, see Figures 15.2(b) and 15.5. For convenience let us split \mathbf{R} into an in-plane part and a z -part according to

$$\mathbf{R} = (\mathbf{R}_{||} + \mathbf{f}_l) + \mathbf{R}_z ,$$

where $\mathbf{R}_{||}$ is the in-plane position of the unit cell and \mathbf{f}_l denotes the in-plane position of layer l within the unit cell, see Figure 15.5. By this procedure we assure that $\mathbf{R}_{||}$ is always a lattice vector.

Then we can employ Bloch's theorem for the double layer structure as

$$c_{\sigma}^{\mathbf{k}}(\mathbf{R}) = c_{\sigma}^{\mathbf{k}}(\mathbf{f}_l + \mathbf{R}_z) \exp(i\mathbf{k}\mathbf{R}_{||}) . \quad (15.10)$$

Here \mathbf{f}_l point toward that layer to which the point \mathbf{R} belongs.

The results of the TB calculation for the WL are shown in Figure 15.6 for the lowest conduction band (CB) and the two highest sub-bands of the valence band (VB). For convenience we will denote these as valence bands (VBs) in the following. Around the Γ point, for the conduction band as well as for the two highest valence bands the dispersion is to a good approximation rotational invariant. For larger \mathbf{k} first the hexagonal structure of the real space lattice and than the 30% rotated hexagonal structure of the Brillouin zone is reflected in the energy dispersion.

Note that, a restriction to only one VB, as it is typically used in the arsenide material system, is not applicable, as the two highest VBs are energetically nearly degenerate at the Γ -point. Rather, we need to take both VBs into account for the calculation of optical properties. However, for further calculations, we are only interested in the bandstructure in the vicinity of the Γ -point. Therefore, in a good approximation we might use the angle-averaged band structure, which is shown in Figure 15.7.

Even though the dispersion shows a clear non-parabolic behavior, an estimate for the effective masses can be given from a fit in the vicinity of the Γ -point. For the CB we find a mass of $0.18 m_0$, whereas for the upper and lower VB $-2.84 m_0$ and $-0.19 m_0$ are found, respectively.

15.3 Coulomb matrix elements

An atomistic approach like a tight-binding calculation allows to account for symmetry properties of the wurtzite crystal structure. As discussed in the last chapter, the wavefunction is expressed as a linear combination of atomic orbitals $\phi_{\mathbf{R},\sigma}$ localized at

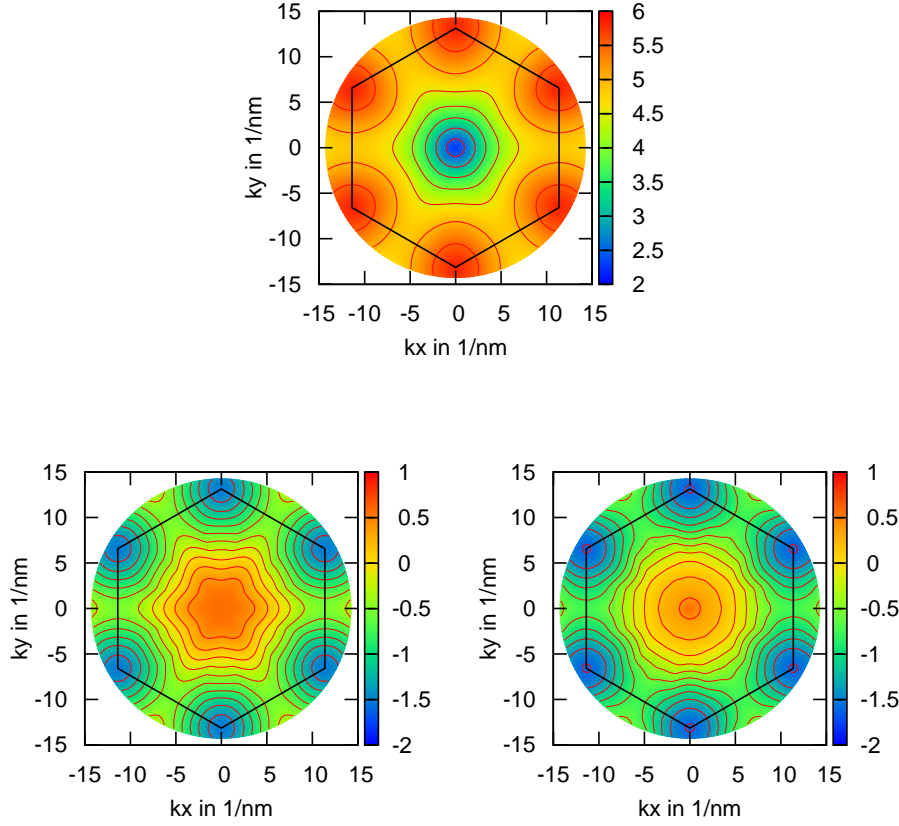


Figure 15.6: Energy dispersion as a function of the 2D in-plane wavevector \mathbf{k}_{\parallel} for conduction band (a) and the two upper valence band (b,c) electrons. The hexagonally shaped border of the Brillouin zone is marked in black.

the lattice site \mathbf{R} , as given in Eq. (15.9). In this section we perform the evaluation of the Coulomb matrix elements, that was done in Section 7.1 for the arsenide material system.

For the calculation of single-particle energies and to investigate the probability densities as in Figure 15.4, the explicit knowledge of the localized orbital functions is not needed within a TB approach. Even though, they are required in principle to calculate Coulomb matrix elements, we can avoid explicit knowledge of those orbitals in this case. The dominant contributions to the Coulomb matrix elements stem from its long-ranged part and therefore the localized orbitals in good approximation act as point charges, whereas the explicit structure of the localized orbitals only enters in the short-ranged contributions. Therefore, the real space integration of wavefunc-

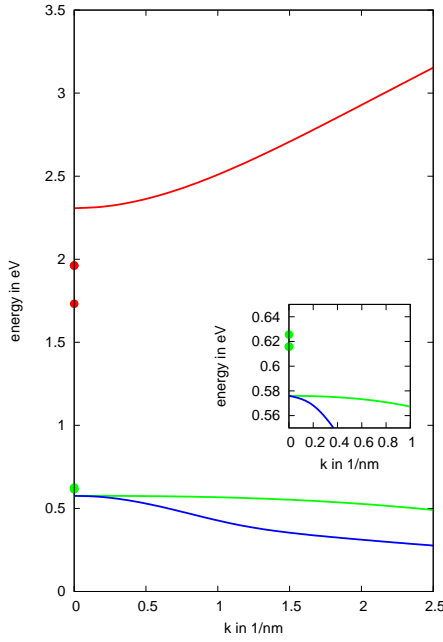


Figure 15.7: Angle-averaged band structure. The dots mark the positions of the QD energies from their respective TB calculation

tions in Eq. (7.9) can be approximated by a sum over TB coefficients at their lattice site

$$V_{\alpha\beta\gamma\delta} \approx \frac{e^2}{4\pi\varepsilon_0} \sum_{\mathbf{R}\mathbf{R}'} \sum_{\sigma\tau} c_{\sigma}^{\alpha*}(\mathbf{R}) c_{\tau}^{\beta*}(\mathbf{R}') \frac{1}{|\mathbf{R}-\mathbf{R}'|} c_{\tau}^{\gamma}(\mathbf{R}') c_{\sigma}^{\delta}(\mathbf{R}), \quad (15.11)$$

as shown in Refs. [129, 126]. This scheme can be easily used when the analysis is restricted to the localized states. It has been successfully used to determine Coulomb matrix elements for InN/GaN QDs in combination with configuration interaction calculations to describe multi-exciton spectra and the influence of symmetry properties on allowed optical transitions [202, 203].

For our purpose of calculating optical properties of nitride QDs, including both localized and delocalized states, it is more convenient to determine the Coulomb matrix elements in a Fourier basis, cf. Eq. (7.11). Using the same approximation as in Eq. (15.11), the appearing overlap integrals can be written as

$$\langle \alpha | e^{i\mathbf{q}\mathbf{r}} | \beta \rangle = \int d^3r \psi_{\alpha}^*(r) e^{+i\mathbf{q}\mathbf{r}} \psi_{\beta}(r) \approx \sum_{\mathbf{R},\sigma} c_{\sigma}^{\alpha*}(\mathbf{R}) e^{+i\mathbf{q}\mathbf{R}} c_{\sigma}^{\beta}(\mathbf{R}). \quad (15.12)$$

As the plane wave $\exp(i\mathbf{q}\mathbf{r})$ does not decay for large distances, the argument used to justify Eq. (15.11) also holds in this case.

Calculation of overlap integrals

The overlaps for two QD states can easily be calculated using Eq. (15.12). One finds

$$\langle \nu | e^{i\mathbf{q}\mathbf{r}} | \mu \rangle = \sum_{\mathbf{R}, \sigma} c_{\sigma}^{\nu*}(\mathbf{R}) e^{+i\mathbf{q}\mathbf{R}} c_{\sigma}^{\mu}(\mathbf{R}) . \quad (15.13)$$

Using Bloch's theorem we also can evaluate the QD-WL overlaps directly

$$\langle \nu | e^{i\mathbf{q}\mathbf{r}} | \mathbf{k}_0 \rangle = \sum_{\mathbf{R}, \sigma} c_{\sigma}^{\nu*}(\mathbf{R}) e^{+i\mathbf{q}\mathbf{R}} c_{\sigma}^{\mathbf{k}}(\mathbf{f} + \mathbf{R}_z) e^{i\mathbf{k}\mathbf{R}_{||}} . \quad (15.14)$$

Note, that due to the finite normalization volume for the QD states, care has to be taken, since QD and WL states must be normalized to the same normalization volume. The WL-WL overlaps require a little more attention. However, we can use Bloch's theorem and the double layer structure of the unit cell. This allows to write

$$\begin{aligned} \langle \mathbf{k}_0 | e^{i\mathbf{q}\mathbf{R}} | \mathbf{k}'_0 \rangle &= \frac{1}{N} \sum_{\sigma, \mathbf{R}} c_{\mathbf{k}, \sigma}^*(\mathbf{R}) e^{i\mathbf{q}\mathbf{R}} c_{\mathbf{k}', \sigma}(\mathbf{R}) \\ &= \frac{1}{N} \sum_{l=1}^2 \sum_{\mathbf{R}_{||}} \sum_{\sigma \mathbf{R}_z} c_{\mathbf{k}, \sigma}^*(\mathbf{R}) e^{i\mathbf{q}_z \mathbf{R}_z} e^{i\mathbf{q}_{||} \mathbf{R}_{||}} e^{i\mathbf{q}_{||} \mathbf{f}_l} c_{\mathbf{k}', \sigma}(\mathbf{R}) \\ &= \frac{1}{N} \sum_{l=1}^2 \sum_{\mathbf{R}_{||}} \left(\sum_{\sigma \mathbf{R}_z} e^{i\mathbf{q}_z \mathbf{R}_z} c_{\mathbf{k}, \sigma}^*(\mathbf{f}_l + \mathbf{R}_z) c_{\mathbf{k}', \sigma}(\mathbf{f}_l + \mathbf{R}_z) \right) e^{i(\mathbf{q}_{||} + \mathbf{k}' - \mathbf{k}) \mathbf{R}_{||}} e^{i\mathbf{q}_{||} \mathbf{f}_l} \\ &= \sum_{l=1}^2 e^{i\mathbf{q}_{||} \mathbf{f}_l} F_l(\mathbf{k}, \mathbf{k}', q_z) \frac{1}{N} \sum_{\mathbf{R}_{||}} e^{i(\mathbf{q}_{||} + \mathbf{k}' - \mathbf{k}) \mathbf{R}_{||}} \\ &= \delta_{\mathbf{q}_{||}, \mathbf{k} - \mathbf{k}'} \sum_{l=1}^2 e^{i\mathbf{q}_{||} \mathbf{f}_l} F_l(\mathbf{k}, \mathbf{k}', q_z) . \end{aligned} \quad (15.15)$$

For the two layers of the unit cell $l = (1, 2)$, separately a formfactor can be defined,

$$F_l(\mathbf{k}, \mathbf{k}', q_z) = \sum_{\sigma \mathbf{R}_z} e^{i\mathbf{q}_z \mathbf{R}_z} c_{\mathbf{k}, \sigma}^*(\mathbf{f}_l + \mathbf{R}_z) c_{\mathbf{k}', \sigma}(\mathbf{f}_l + \mathbf{R}_z) ,$$

that is analogous to previous calculations for InGaAs systems in the sense, that it splits the solution in a in-plane part, which is given by the Kronecker- δ and into the influence of the confinement in z -direction, but *for each column*.

15.4 Dipole matrix elements

The dipole matrix elements for the QD-QD transitions can be directly obtained from the TB calculation of the QD, see Ref. [203]. Numerical values are given in Tab. 15.1. In case of QD states, we find for the particular QD geometry under consideration, that direct transitions, i.e. s→s and p→p transitions, only weakly couple to the electro-magnetic field in comparison to the off-diagonal transitions s→p and p→s. For a detailed discussion of these transition rules see Refs. [129, 126]. As

d^{cv}/e	1	2	3	k
1	0.000	1.538	1.538	0.000
2	1.196	0.011	0.011	0.000
3	1.196	0.011	0.011	0.000
k	0.000	0.000	0.000	0.830

Table 15.1: Dipole matrix elements for normal incidence of the external field in nm. Piezo fields included according to Ref. [129]. The WL dipole matrix elements are calculated according to Ref. [128] with parameters taken from Ref. [186].

in later calculations our focus is on QD transitions, for simplicity values for the WL-WL dipole matrix elements are used, that are calculated according to the scheme presented in Ref. [128] from band parameters taken from Ref. [186]. However, a scheme for calculating the corresponding dipole matrix element from an TB approach is presented in Appendix E. Furthermore QD-WL matrix elements are neglected for computational reasons, though they could be included along the lines discussed in Ref. [203] and using Bloch's theorem, in close analogy to Eq. (15.14).

16 Optical properties

In this chapter we study the optical properties of nitride based QD systems, based on the TB description of single-particle states and interaction matrix elements discussed in the last chapter. Especially the off-diagonal dipole transition rules drastically complicate the implementation of the theory as discussed in Part III. Therefore we will discuss the influences of the microscopic TB calculation on the optical gain on the basis of a screened exchange - Coulomb hole approximation, that is considerably simpler than the second Born approximation employed in Chapter 9 for the InGaAs material system. The description of the carrier-phonon interaction in Chapter 10 in the polaron picture is also accessible for the nitride system and will be discussed in Section 16.4.

16.1 Kinetic equations

Our starting point for the derivation of kinetic equations are the Kadanoff-Baym equations (4.63). The equation of motion for the propagator $G^<(t,t)$ that, by means of Eq. (8.13), corresponds to the single-particle density matrix, can be written as by

$$i\hbar \frac{d}{dt} G^<(t) = [\Sigma^\delta(t), G^<(t)] + \left. \frac{d}{dt} G_{\alpha\beta}^{cv,<}(t) \right|_{\text{Coll}}. \quad (16.1)$$

In this notation, $G^<$ and Σ are to be understood in matrix notation with respect to the state and subband indices. Let us first consider only instantaneous selfenergies $\Sigma^\delta(t_1, t_2) \propto \delta(t_1 - t_2)$, like e.g. the Hartree-Fock selfenergy (cf. (9.2)). This corresponds to a consideration of the commutator in Eq. (16.1) only. The collision part will be the topic of Section 16.5. Then, Eq. (16.1) reads more explicitly

$$i\hbar \frac{d}{dt} G^{<,cc}(t) = [\Sigma^{\delta,cc} G^{<,cc} - G^{<,cc} \Sigma^{\delta,cc}] + [\Sigma^{\delta,cv} G^{<,vc} - G^{<,cv} \Sigma^{\delta,vc}] \quad (16.2)$$

$$i\hbar \frac{d}{dt} G^{<,vv}(t) = [\Sigma^{\delta,vc} G^{<,cv} - G^{<,vc} \Sigma^{\delta,cv}] + [\Sigma^{\delta,vv} G^{<,vv} - G^{<,vv} \Sigma^{\delta,vv}] \quad (16.3)$$

$$i\hbar \frac{d}{dt} G^{<,cv}(t) = [\Sigma^{\delta,cc} G^{<,cv} - G^{<,cc} \Sigma^{\delta,cv}] + [\Sigma^{\delta,vc} G^{<,vv} - G^{<,cv} \Sigma^{\delta,vv}] \quad (16.4)$$

$$i\hbar \frac{d}{dt} G^{<,vc}(t) = i\hbar \frac{d}{dt} [G^{<,cv}(t)]^\dagger \quad (16.5)$$

where only band indices are given. State and subband indices are still written in matrix notation according to

$$A^{cc} = \begin{bmatrix} \nu^c \nu^c & \nu^c \mathbf{k}^c \\ \hline \mathbf{k}^c \nu^c & \mathbf{k}^c \mathbf{k}^c \end{bmatrix} \quad A^{cv} = \begin{bmatrix} \nu^c \nu^v & \nu^c \mathbf{k}_1^v & \nu^c \mathbf{k}_2^v \\ \hline \nu^c \mathbf{k}_1^c & \mathbf{k}_1^c \mathbf{k}_1^v & \mathbf{k}_2^c \mathbf{k}_2^v \end{bmatrix} \quad (16.6)$$

$$A^{vc} = [A^{cv}]^\dagger \quad A^{vv} = \begin{bmatrix} \nu^v \nu^v & \nu^v \mathbf{k}_1^v & \nu^v \mathbf{k}_2^v \\ \hline \nu^v \mathbf{k}_1^v & \mathbf{k}_1^v \mathbf{k}_1^v & \mathbf{k}_2^v \mathbf{k}_1^v \\ \hline & & \\ \nu^v \mathbf{k}_2^v & \mathbf{k}_1^v \mathbf{k}_2^v & \mathbf{k}_2^v \mathbf{k}_2^v \end{bmatrix} \quad (16.7)$$

Here, ν indicates a QD state and \mathbf{k}_n a WL state for of the n -th subband. Please note, that even though the valence band contains two subbands, the QD states occur only once. Furthermore the matrix notation implies a “sum” over all states in the system. Depending on the sub-blocks of the matrices multiplied with each other, this “sum” is to be understood as an integration over continuous WL states or a summation over QD states and positions, as specified in Appendix A.

Considering the lesser GFs, $G^{<,cv}$ describes interband transition amplitudes diagonal and off-diagonal in the state index, i.e. direct and indirect transitions. The intraband quantities $G_{\alpha\beta}^{<,cc}$ and $G_{\alpha\beta}^{<,vv}$ describe the population for $\alpha = \beta$ and intraband transition amplitudes for $\alpha \neq \beta$.

The macroscopic polarization can be calculated from the inter-band transition amplitudes according to

$$\mathbf{P} = \sum_{\alpha\beta} \mathbf{d}_{\alpha\beta}^* i\hbar G_{\alpha\beta}^{<,cv}. \quad (16.8)$$

Note, that transitions between different QDs are neglected. Hence, for QD-QD contributions the double summation is restricted to the same QD position, which corresponds to the appearance of a $\delta_{\mathbf{R},\mathbf{R}'}$ in that case.

Whereas usually the free particle energies are incorporated into the free inverse GF G_0^{-1} (cf. Section 8.2), we choose here to incorporate them as part of the selfenergy, as this choice allows for the elegant notation of Eq. (16.1). The corresponding selfenergy can be written as

$$\Sigma_{\alpha\beta}^{\text{free},\lambda\lambda'} = \varepsilon_\alpha^\lambda \delta_{\alpha\beta} \delta_{\lambda\lambda'}, \quad (16.9)$$

where $\varepsilon_\alpha^\lambda$ contains the free particle spectrum shown in Figure 15.7. As discussed in

Section 7.1, the selfenergy describing the dipole coupling can be written as

$$\Sigma_{\alpha\beta}^{\text{pulse},\lambda\lambda'}(t) = -\mathbf{d}_{\alpha\beta}^{\lambda\lambda'} \cdot \mathbf{E}(t) . \quad (16.10)$$

Taking into account the off-diagonal dipole coupling for the QD states (cf. Section 15.4), several comments are in order. First, by the pulse only those transition amplitudes $G_{\alpha\beta}^{<,cv}$ are driven whose corresponding dipole matrix elements $d_{\alpha\beta}^{cv}$ are nonzero. In case of the selfenergy $\Sigma^\delta = \Sigma^{\text{free}} + \Sigma^{\text{pulse}}$ being diagonal in the state index, no off-diagonal elements of $G_{\alpha\beta}^<$ are driven in the SBE (16.1), even in the presence of two valence bands. Considering also off-diagonal dipole coupling for the QD states, the corresponding interband transition amplitudes $G^{<,cv}$ are driven by the pulse directly. Other inter- and intra-band transition amplitudes might be driven indirectly e.g. via the Coulomb interaction.

16.1.1 Coulomb interaction

In this section we will discuss the Coulomb interaction in Hartree-Fock (HF) approximation. As we discussed the derivation of the HF approximation in detail in Chapter 9, we will focus here on the specific features for the nitride material system. The general structure of the Hartree selfenergy reads

$$\Sigma_{\alpha\beta}^{\lambda\lambda}(t) = -i\hbar \sum_{\lambda'} \sum_{i,j} V_{\alpha\gamma\delta\beta}^{\lambda\lambda'} G_{\delta\gamma}^{<,\lambda'\lambda'}(t) . \quad (16.11)$$

As discussed in Chapter 9, the WL contributions to the Hartree selfenergy vanish and only the intra-dot contribution

$$\Sigma_{mm}^{\lambda\lambda}(t) = -i\hbar \sum_{\lambda'} \sum_{m_2} V_{mm'm'm}^{\lambda\lambda'} G_{m'm'}^{<,\lambda'\lambda'}(t) . \quad (16.12)$$

has to be considered. To facilitate the discussion of off-diagonal contributions, the diagrammatic representation of the Hartree terms (16.12) is depicted in Figure 16.1, where the overlaps of the Coulomb interaction in eigenfunction expansion (7.11) are represented by triangular vertices. As we are restricting ourselves to vertices¹ diagonal in the band index, an approximation that is supported by the results of an envelope function approach, only population functions² appear in the Hartree terms. Were we to include all possible band-index combinations in the overlaps, also Hartree contributions containing interband transition amplitudes would appear.

The Fock selfenergy reads according to Chapter 9

$$\Sigma_{\alpha\beta}^{\lambda\lambda'}(t) = i\hbar \sum_{\gamma\delta} V_{\alpha\gamma\beta\delta}^{\lambda\lambda'} G_{\delta\gamma}^{<,\lambda\lambda'}(t) . \quad (16.13)$$

¹that correspond to overlap functions in Eq. (15.12)

²In principle also intra-band transitions amplitudes

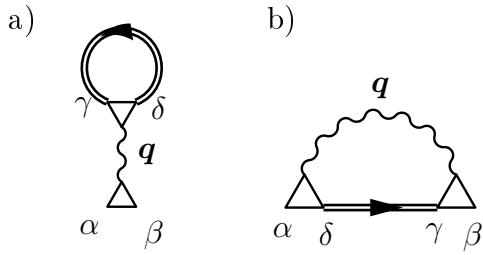


Figure 16.1: Self consistent a) direct Coulomb selfenergy (Hartree) and b) exchange Coulomb selfenergy (Fock) in eigenfunction representation.

The corresponding diagrams in eigenfunction expansion are depicted in Figure 16.1(b). Due to the off-diagonal nature of the main QD transitions, see the dipole selection rules in Section 15.4, the selfenergy for the WL states reads

$$\Sigma_{\mathbf{kk}'}^{\lambda\lambda'}(t) = i\hbar \sum_{\nu\mu} V_{\nu\mathbf{k}\mu}^{\lambda\lambda'} G_{\mu\nu}^{<,\lambda\lambda'}(t) + i\hbar \sum_{\mathbf{k}'} V_{\mathbf{k}\mathbf{k}'\mathbf{k}\mathbf{k}'}^{\lambda\lambda'} G_{\mathbf{k}'\mathbf{k}'}^{<,\lambda\lambda'}(t), \quad (16.14)$$

and as all elements of $G_{\delta\gamma}^{<,cv}$ contribute, we need all matrix elements $V_{\mathbf{k}\gamma\mathbf{k}\delta}^{\lambda\lambda'}$. As the WL-WL overlaps (15.15) contain momentum conservation, i.e. $\propto \delta_{\mathbf{kk}'}$, we can restrict our analysis to diagonal WL GFs $G_{\mathbf{kk}}^{\gtrless}$. Note that in $V_{\mathbf{kk}'\mathbf{k}\mathbf{k}'}^{\lambda\lambda'}$ we have to deal with the problem of lifting the Coulomb singularity. For details see App. D.3. Likewise we find for the QD states

$$\Sigma_{\nu\mu}^{\lambda\lambda'}(t) = i\hbar \sum_{\mathbf{k}} V_{\nu\mathbf{k}\mu\mathbf{k}}^{\lambda\lambda'} G_{\mathbf{k}\mathbf{k}}^{<,\lambda\lambda'}(t) + i\hbar \sum_{\chi\xi} V_{\nu\chi\mu\xi}^{\lambda\lambda'} G_{\xi\chi}^{<,\lambda\lambda'}(t), \quad (16.15)$$

where all QD-QD couplings $V_{\nu\chi\mu\xi}^{\lambda\lambda'}$ are included.

The complicated interplay of all transition amplitudes via the Coulomb matrix elements poses the question, whether transition amplitudes that are not directly driven by the optical field via the dipole interaction can be driven indirectly via the Coulomb interaction. To investigate this, let us consider for example the dynamics of an interband transition amplitude connecting QD and WL states $G_{\nu k}^{cv}$. The corresponding equation of motion for this GF is

$$\begin{aligned} i\hbar \frac{d}{dt} G_{\nu k}^{cv}(t) = & i\hbar \left(+ \Sigma_{\nu k}^{cc} G_{kk}^{cv} + \Sigma_{\nu k}^{cv} G_{kk}^{vv} \right. \\ & + \Sigma_{\nu\nu}^{cc} G_{\nu k}^{cv} + \Sigma_{\nu\nu}^{cv} G_{\nu k}^{vv} \\ & - G_{\nu k}^{cc} \Sigma_{kk}^{cv} - G_{\nu k}^{cv} \Sigma_{kk}^{vv} \\ & \left. - G_{\nu\nu}^{cc} \Sigma_{\nu k}^{cv} - G_{\nu\nu}^{cv} \Sigma_{\nu k}^{vv} \right) \end{aligned} \quad (16.16)$$

where k, ν are to be understood symbolically for the respective state belonging to either WL or QD. All contributions that drive this polarization are proportional to

a polarization times a population. Therefore in the linear regime these terms are not driven in the limit of vanishing background carrier density. Considering finite background carrier densities, e.g. for gain calculations, these terms in principle have to be taken into account. However, all transition amplitudes not directly driven by the optical pulse, i.e. $d_{\alpha\beta} = 0$, do not directly contribute to the macroscopic polarization (16.8) either. Their influence is restricted to the back-action on directly driven polarizations. To simplify the numerical evaluation, we therefore neglect these transition amplitudes in later calculations. Similar to the discussion for the Hartree terms, the inclusion of band off-diagonal vertices would imply additional terms.

16.1.2 Screened-exchange and Coulomb-hole approximation

The simplest selfenergy beyond the Hartree-Fock approximation is to consider terms linear in the screened interaction $W^{R/A}$, i.e. $W^{\geqslant} = 0$. For details on the screened interaction see Appendix B. Furthermore, we assume, that the screened Coulomb interaction retains its instantaneous character from the bare one, implying a instantaneous selfenergy. This is in contrast to the SBA, where even though an instantaneous screening is used, the selfenergy itself is not instantaneous, as we will discuss in more detail in Section 16.3. Such contributions are contained in the retarded selfenergy, which in general is given by

$$\Sigma^R(1, 2) = \Sigma^\delta(1, 2) + \Theta(t_1 - t_2) [\Sigma^>(1, 2) - \Sigma^<(1, 2)] = \Sigma(1, 2) - \Sigma^<(1, 2) . \quad (16.17)$$

Using the RPA selfenergy,

$$\Sigma(\underline{1}, \underline{2}) = i\hbar G(\underline{1}, \underline{2}) W(\underline{2}, \underline{1}) , \quad (16.18)$$

that corresponds to the first line of (9.14), and considering the assumptions discussed above, we find

$$\begin{aligned} \frac{1}{i\hbar} \Sigma^R(1, 2) &= G(1, 2) W(2, 1) - G^<(1, 2) W^>(2, 1) \\ &= [G^R(1, 2) + G^<(1, 2)] [W^A(2, 1) + W^>(2, 1)] - G^<(1, 2) W^>(2, 1) \\ &= [G^R(1, 2) + G^<(1, 2)] W^A(2, 1) \\ &= \frac{1}{2} [G^>(1, 2) + G^<(1, 2)] W^A(2, 1) , \end{aligned} \quad (16.19)$$

In the last step we defined $\Theta(0) = \frac{1}{2}$. This definition is meaningful, as it assures $\Theta(-x) + \Theta(+x) = 1$. In an eigenfunction expansion Eq. (16.19) can be written as

$$\begin{aligned} \Sigma_{\nu_1\nu_2}^R(t_1, t_2) &= \frac{i\hbar}{2} \sum_{\nu_3,\nu_4} [G_{\nu_3\nu_4}^>(t_1, t_2) + G_{\nu_3\nu_4}^<(t_1, t_2)] W_{\nu_1\nu_4\nu_2\nu_3} \delta(t_1 - t_2) \\ &= \begin{cases} \frac{1}{2} \sum_{\nu_3} [1 - 2 f_{\nu_3}(t_1)] W_{\nu_1\nu_3\nu_2\nu_3}(t_1) - \frac{1}{2} V_{\nu_1\nu_3\nu_2\nu_3} & \lambda_1 = \lambda_2 \\ - \sum_{\nu_3,\nu_4} \psi_{\nu_3\nu_4}(t_1) W_{\nu_1\nu_4\nu_2\nu_3}(t_1) & \lambda_1 = c, \lambda_2 = v \end{cases} \end{aligned} \quad (16.20)$$

In the last line, we neglected intraband transition amplitudes and restricted our analysis to interband transitions and population functions. For the unexcited system the screened interaction reduces to the bare one (see Appendix B) and hence to recover the Fock selfenergy (16.13), a correction, $-\frac{1}{2} V_{\nu_1\nu_3\nu_2\nu_3}$, is introduced. This procedure is similar to that employed in Section 9.1 to assure, that the renormalizations of the unexcited system vanish. Usually the contributions are separated into the *screened exchange* and the *Coulomb-hole* part

$$\Sigma_{\nu_1\nu_2}^{SX}(t) = \begin{cases} - \sum_{\nu_3} W_{\nu_1\nu_3\nu_2\nu_3}(t) f_{\nu_3}(t) & \lambda_1 = \lambda_2 \\ - \sum_{\nu_3,\nu_4} W_{\nu_1\nu_4\nu_2\nu_3}(t) \psi_{\nu_3\nu_4}(t) & \lambda_1 = c, \lambda_2 = v \end{cases} \quad (16.21)$$

$$\Sigma_{\nu_1\nu_2}^{CH}(t) = \begin{cases} \frac{1}{2} \sum_{\nu_3} [W_{\nu_1\nu_3\nu_2\nu_3}(t) - V_{\nu_1\nu_3\nu_2\nu_3}] & \lambda_1 = \lambda_2 \\ 0 & \lambda_1 = c, \lambda_2 = v \end{cases} \quad (16.22)$$

It should be noted, that the SX-CH selfenergy replaces the Fock part of the HF selfenergy. This is in contrast to the SBA selfenergy, that has to be added to the HF part.

16.2 Optical spectra

From the macroscopic polarization (16.8), the linear absorption spectrum is obtained via the optical susceptibility $\chi(\omega) = \frac{P(\omega)}{E(\omega)} \propto \alpha(\omega)$. For details, see Chapter 8. As the SX-CH and the Hartree selfenergies do not provide microscopic dephasing, we use a phenomenological value of $\gamma = 10$ meV. Calculations that additionally include microscopic dephasing due to carrier-LO-phonon interaction are presented in Section 16.5.

The InN QD under consideration exhibit deeply confined shells, especially for electrons (cf. Figure 15.7). The confinement energy for the lowest QD states with respect

to the band edge are -575.4 meV and -345.3 meV for electrons, and -49.6 meV and -39.8 meV for holes. In conjunction with the “skew” dipole selection rules discussed in Section 15.4, this corresponds to free-carrier transition energies of -615.2 meV and -394.9 meV, relative to the WL bandgap of 1731 meV. As initial carrier distribution, we assume a quasi-equilibrium situation for the CB as well as a common one for the two VBs.

The corresponding absorption spectra for a temperature of 300 K and various carrier densities are shown in Figure 16.2. With increasing carrier density, the transition energies exhibit a strong blue shift accompanied by bleaching of the absorption and transition to gain. For carrier densities exceeding $5 \times 10^{10} \text{ cm}^{-2}$ the blue shift is reduced again. This complicated behavior is due to the interplay of Hartree, screened-

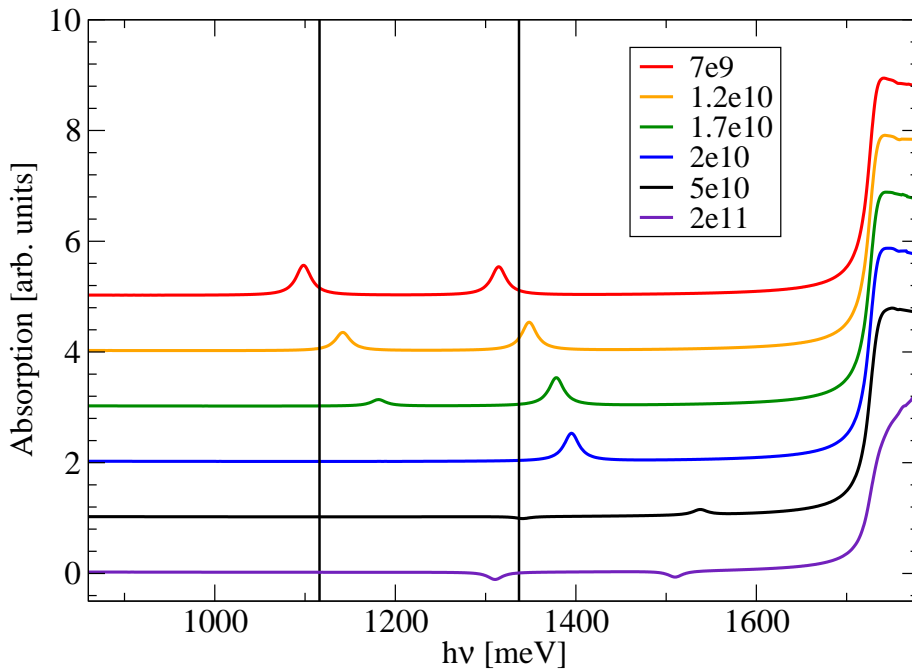


Figure 16.2: Linear optical absorption spectra for InN QDs at 300 K and for various carrier densities in $1/\text{cm}^2$. The spectra are shifted vertically for better visibility.

exchange (SX) and Coulomb hole (CH) contributions. The corresponding numbers for three exemplary carrier densities are given in Tab. 16.1. As we can infer, the CH energy shifts are practically the same for CB and VB carriers and therefore only slightly influence the interband transition energies. In contrast, Hartree as well as SX terms give rise to a relative shift of CB and VB energies. Since for each band the Hartree term contains contributions from all bands, as we can infer from Eq. (16.12) and Figure 16.1(a), the influence of the QD population on the Hartree shift is similar both for the CB and the VB. The large difference between CB and

	$2 \times 10^{10} \text{ cm}^{-2}$	$5 \times 10^{10} \text{ cm}^{-2}$	$2 \times 10^{11} \text{ cm}^{-2}$
CB			
SX 1	-73.7	-88.9	-64.5
SX 2	-17.5	-58.3	-46.3
CH 1	-14.1	-20.1	-36.5
CH 2	-13.3	-18.6	-31.9
H 1	149.0	285.5	189.4
H 2	124.8	245.7	156.2
VB			
SX 1	2.9	6.4	15.4
SX 2	2.4	5.4	14.4
CH 1	-13.9	-19.7	-35.6
CH 2	-14.0	-19.9	-36.3
H 1	-13.3	-29.1	-70.1
H 2	-14.4	-31.7	-79.1

Table 16.1: Energy shift contributions from screened-exchange (SX), Coulomb hole (CH), and Hartree (H) selfenergies in meV.

VB shifts arises from the screened interaction matrix elements. The blue shift for small to intermediate carrier densities stems from the steep increase of the Hartree contributions. For larger carrier densities, the Hartree terms saturate due to filling of the QD states. Simultaneously the screening of the Coulomb interaction increases due to filling of WL states which leads to a strong reduction of the Hartree contributions. In contrast, saturation effects are smaller for the SX terms because of increasing contributions from WL carriers. This leads in total to a reduced blue shift for high carrier densities.

16.3 Comparison between different approaches for the Coulomb interaction

In Part III absorption and gain spectra are presented for InGaAs QDs. To determine excitation-induced dephasing due to Coulomb interaction the second Born approximation (SBA) is employed, cf. Chapter 9. In contrast, for the nitride material system we use the SX-CH approximation and in the following important differences between the two approaches are discussed.

Schematically, the contributing diagrams in the KBE are depicted in Figure 16.3.

In contrast to the usual notation, the interaction line (wiggly) denotes the retarded or advanced plasmon GF $W^{R/A}$ and the carrier propagators G^{\geqslant} are represented by straight lines. Therefore, these diagrams should not be confused with Feynman diagrams as no systematic perturbation expansion is implied.

For the following discussion note, that $W^{R/A}$ is a real quantity under the assumptions discussed in Appendix B. Considering the homogeneous part of the EOM, $i\hbar \frac{d\psi}{dt} = \Delta\psi$, dephasing is described by an imaginary part of Δ . In the SX-CH selfenergy diagram (cf. Figure 16.3(a)) no retardation effects are included due to the instantaneous interaction and hence all internal times are fixed to the external ones. This implies the structure $\Delta = Wf$, which is real and provides no dephasing. In contrast, in the SBA diagrams an internal time t_2 is involved (cf. Figure 16.3

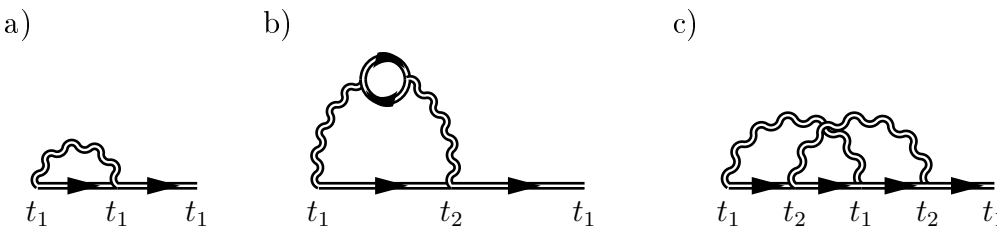


Figure 16.3: Contributions of the SX-CH (a) and of the SBA (b+c) approximations. Note that these are not Feynman diagrams as no systematic perturbation expansion is implied.

(b),(c)). Hence, retardation effects, that are included in the two-time propagators $G^{\geqslant}(t_1, t_2)$, contribute. This can be easily seen when representing the two-time propagator by means of the GKBA, which maps the two-time propagators onto the time-diagonal with the help of retarded/advanced GFs. This implies the structure $\Delta = WW^* f f f G^R G^R G^R G^R$, which is complex in general, and hence can provide dephasing.

16.4 Carrier-phonon interaction

Similar to the InGaAs material system, the polaron retarded GF obeys the Kadanoff-Baym equation (10.15), where we employ the RPA selfenergy (10.13), again neglecting the second (population dependent) term. As for the nitride material system two valence bands are considered for the WL, several comments are in order. Due to the same assumptions discussed for the Coulomb case in Section 16.1.1, the basic carrier-phonon interaction vertex does not couple different sub-bands, i.e. $M_{\alpha\beta}^{\lambda=\lambda'}(\mathbf{q})$. Therefore coupling of different bands is only obtained from off-diagonal GFs $G^{\lambda\lambda'}$, cf. Figure 16.4. Since these off-diagonal GFs are only driven by an optical field and

only weakly influence the results [147], we can restrict our analysis to band-diagonal retarded GFs. Note, that even though only band-diagonal GFs are considered, the two VBs are coupled via the QD states.

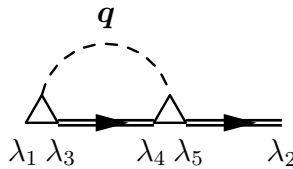


Figure 16.4: Schematic diagram for the ΣG term of the Dyson equation with RPA selfenergy.

The phonon material parameters that are used in the following are $\hbar\omega_{\text{LO}} = 90\text{meV}$ and $\alpha = 0.5$. In Figure 16.5 the retarded GF in the time domain is depicted, following from a numerical solution of the corresponding Dyson equation. The absolute value of the GF is presented as a function of time and energy, both for QD and WL states. As one can easily see from a single-pole model, the modulus of the ret. GF reflects the quasi-particle lifetime, whereas its phase describes the quasi-particle energy. This is discussed in detail in Ref. [31].

Remarkably, despite the large level splitting for the CB QD states, we find a considerable decay that corresponds to a short quasi-particle lifetime. The oscillatory character points towards a sideband structure in the spectral function, which is discussed below. For the CB WL states a phonon threshold is observed around $1 \hbar\omega_{\text{LO}}$. Below the threshold the decay is significantly slower due to reduced phonon emission processes. For the VB2 WL states a similar behavior is observed. In contrast, for the VB1 WL states no phonon threshold is present, as the energy dispersion is rather flat. To observe a phonon threshold for a flat dispersion large momentum transfer is necessary, but the corresponding matrix elements are negligible.

The corresponding spectral functions are presented in Figure 16.6. For the CB QD states a broad structure, containing multiple phonon satellites as well as hybridization effects (cf. Chapter 10), is observed. Even though the level spacing is approximately $2.55 \hbar\omega_{\text{LO}}$ for CB QD states, the QD states strongly interact via multiple-phonon processes, whereas the interaction between QD and WL states (spacing exceeds $3.8 \hbar\omega_{\text{LO}}$) is considerably smaller. In the CB WL spectral function we observe a main peak exhibiting a polaron shift and a broad satellite $1 \hbar\omega_{\text{LO}}$ energetically above.

For the VB states the picture is more involved due to the presence of several subbands. Whereas the VB2 WL spectral function resembles the effects discussed for the CB, the VB1 WL spectral function as well as the VB QD states show a qualitatively different behavior. In contrast to the CB we observe mainly satellites spaced $1 \hbar\omega_{\text{LO}}$

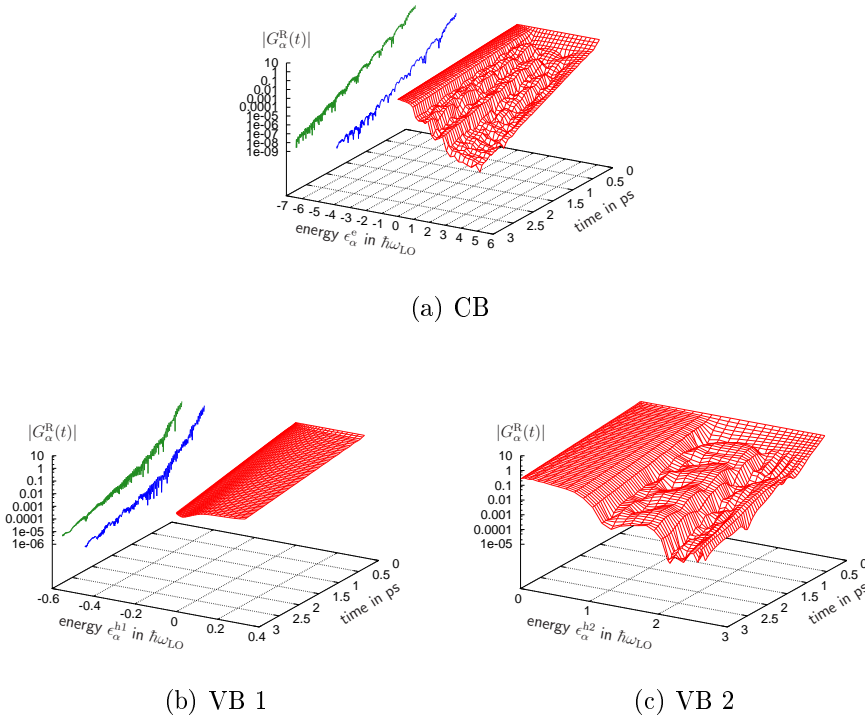
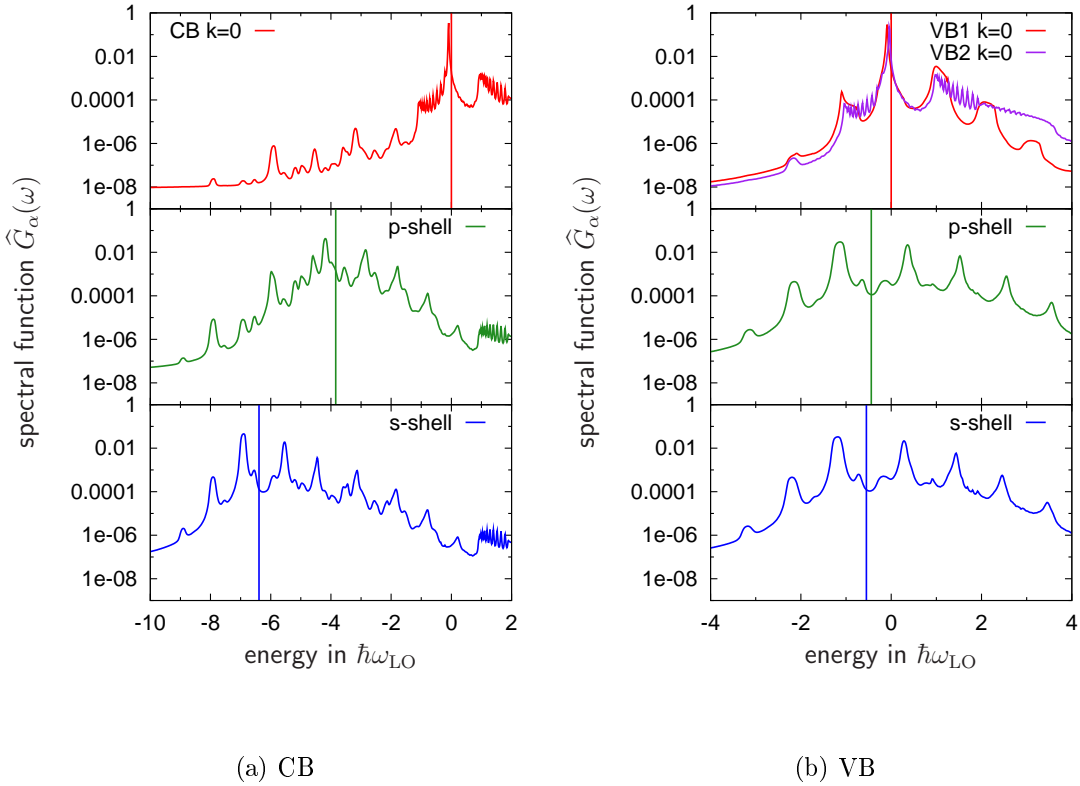


Figure 16.5: Modulus of the polaron retarded GF for the CB (a) as well as for the upper and lower VB (b),(c).

apart. Since the same physics as in the CB case, i.e. diagonal and off-diagonal coupling of QD states, is involved, one would expect hybridization effects.

To analyze the situation, we consider a two-level model that can be diagonalized numerically, cf. Ref. [31], where a phenomenological broadening was chosen to resemble the broadening in Figure 16.6(b). The two levels either describe the two QD states or one QD state and the $\mathbf{k} = 0$ WL state. Considering only the QD states whose level spacing is about $0.1 \hbar\omega_{LO}$ we find the spectral function shown in Figure 16.7(a), showing a series of satellites spaced $\approx 0.5 \hbar\omega_{LO}$ apart. In contrast, for the QD-WL coupling the level spacing is $0.56 \hbar\omega_{LO}$ for the s-shell and $0.44 \hbar\omega_{LO}$ for the p-shell, we find the spectral function shown in Figure 16.7(b) and Figure 16.7(c), showing dominant satellites spaced $\approx 1 \hbar\omega_{LO}$ apart. In addition to the level splitting, important differences arise from the ratio of diagonal and off-diagonal couplings. From the coupling matrix elements discussed in Section 15.3 we infer that the QD-WL coupling is approximately a factor of ten smaller, compared to the off-diagonal QD-QD coupling. In this sense the QD-WL coupling resembles the independent boson model (IBM) [102]. However, for the total spectral function the weight of the QD-

Figure 16.6: Spectral function for QD and WL $\mathbf{k} = 0$ states of CB (a) and VB (b).

WL spectral function dominates as an integration over the nearly dispersionless VB1 continuum is involved. An approximate superposition of both contributions to the spectral functions of the QD states is presented in Figure 16.7d. We find that this model reproduces the main features of the RPA calculation shown in Figure 16.6(b). For the VB1 spectral function the contributions of QD-WL coupling are negligible. Due to the flat band structure the main features of the IBM are found.

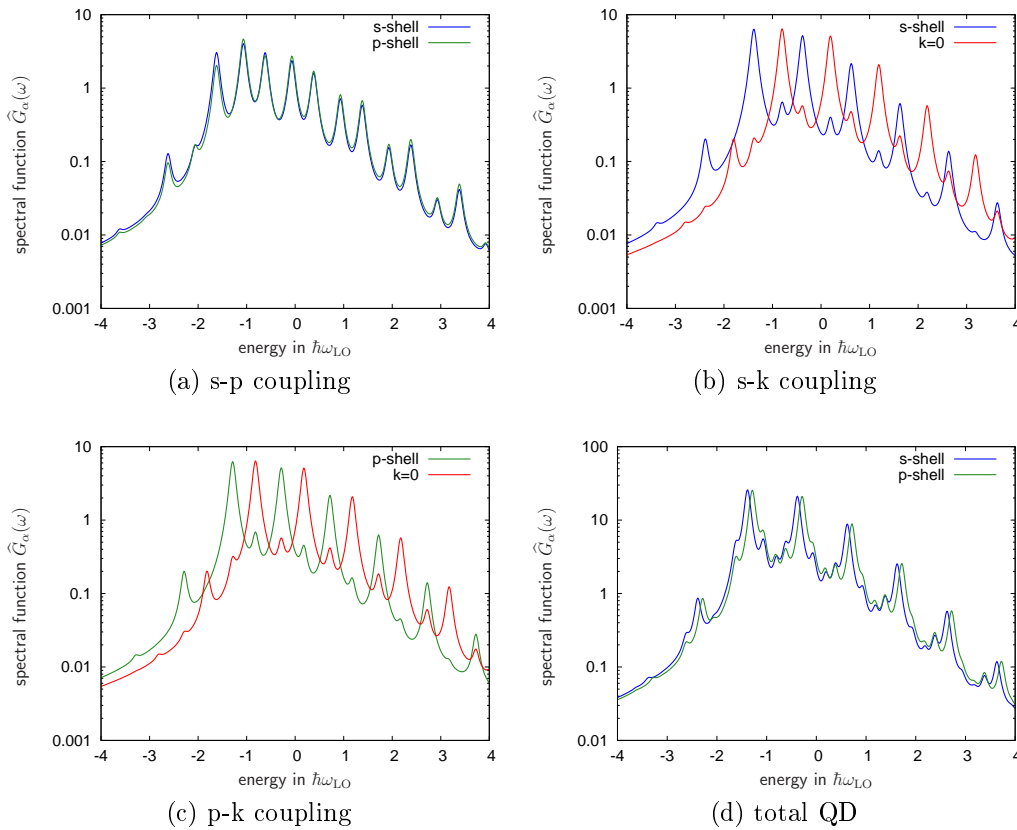


Figure 16.7: Different contributions (a-c) and total spectral functions (d) for QD states. These are calculated using exact diagonalization of an approximate model as discussed in the text.

16.5 Dephasing due to carrier-phonon interaction

From the general collision term (9.12) the Markovian limit is obtained using the GKBA in a version that provides minimum retardation [59]. Considering the RPA

polaron selfenergy, that we introduced in Chapter 10, we obtain

$$\begin{aligned}
 \frac{d}{dt} G_{\alpha\beta}^{cv,<}(t) \Big|_{\text{Coll}} = & \hbar^2 \sum_{\gamma\delta\xi} \sum_{\mathbf{q}} \int_{-\infty}^t dt_3 \left\{ \right. \\
 & + G_{\delta\xi}^{cc,>}(t) G_{\xi}^{c,R}(t, t_3) D_{\alpha\xi\gamma\delta,\mathbf{q}}^{cccc,<}(t_3, t) G_{\gamma}^{c,A}(t_3, t) G_{\gamma\beta}^{cv,<}(t) \\
 & - G_{\delta\xi}^{cc,<}(t) G_{\xi}^{c,R}(t, t_3) D_{\alpha\xi\gamma\delta,\mathbf{q}}^{cccc,>}(t_3, t) G_{\gamma}^{c,A}(t_3, t) G_{\gamma\beta}^{cv,>}(t) \\
 & + G_{\alpha\gamma}^{cc,<}(t) G_{\gamma}^{c,R}(t, t_3) G_{\delta}^{c,A}(t_3, t) G_{\delta\xi}^{cv,>}(t) D_{\gamma\xi\beta\delta,\mathbf{q}}^{cvvc,<}(t, t_3) \\
 & - G_{\alpha\gamma}^{cc,>}(t) G_{\gamma}^{c,R}(t, t_3) G_{\delta}^{c,A}(t_3, t) G_{\delta\xi}^{cv,<}(t) D_{\gamma\xi\beta\delta,\mathbf{q}}^{cvvc,>}(t, t_3) \\
 & + G_{\delta\xi}^{cv,>}(t) G_{\xi}^{v,R}(t, t_3) D_{\alpha\xi\gamma\delta,\mathbf{q}}^{cvvc,<}(t_3, t) G_{\gamma}^{v,A}(t_3, t) G_{\gamma\beta}^{vv,<}(t) \\
 & - G_{\delta\xi}^{cv,<}(t) G_{\xi}^{v,R}(t, t_3) D_{\alpha\xi\gamma\delta,\mathbf{q}}^{cvvc,>}(t_3, t) G_{\gamma}^{v,A}(t_3, t) G_{\gamma\beta}^{vv,>}(t) \\
 & + G_{\alpha\gamma}^{cv,<}(t) G_{\gamma}^{v,R}(t, t_3) G_{\delta}^{v,A}(t_3, t) G_{\delta\xi}^{vv,>}(t) D_{\gamma\xi\beta\delta,\mathbf{q}}^{vvvv,<}(t, t_3) \\
 & - G_{\alpha\gamma}^{cv,>}(t) G_{\gamma}^{v,R}(t, t_3) G_{\delta}^{v,A}(t_3, t) G_{\delta\xi}^{vv,<}(t) D_{\gamma\xi\beta\delta,\mathbf{q}}^{vvvv,>}(t, t_3) \\
 \left. \right\}. \tag{16.23}
 \end{aligned}$$

It should be noted, that due to the complicated off-diagonal nature of the transition amplitudes $G_{\alpha\beta}^{cv,<}$, a splitting into “diagonal” and “off-diagonal” dephasing contributions, similar to Part III, is not directly possible. Nevertheless, a similar compensation between different contributions also holds. Optical spectra with dephasing and line-shifts due to carrier-phonon interaction and line-shifts due to Coulomb interaction in SX-CH approximation are presented in Figure 16.8. From comparing Figures 16.2 and 16.8 we can infer that line-shifts due to polaronic effects are small in comparison to SX-CH and Hartree contributions, that are identical in both cases. The main influence of carrier-phonon scattering is dephasing of the optical polarization that corresponds to broadening of the resonances. An asymmetric line shape as well as typical linewidths of 22 meV for the energetically lower and 18 meV for the energetically higher transition are found. The difference arises due to the fact that, as already discussed in Part III, the compensating behavior between different contributions is weaker for the energetically lower transition due to the large energetic separation from the WL.

It should be noted, that the spectra of Figure 16.8 exhibit a negative structure at the low energetic side of the main QD resonances even for carrier densities for which both resonances are of absorptive character. Even though it is a minor feature, it is unphysical in principle. It stems from the application of the GKBA, that is known to be problematic for intermediate polar coupling materials like InN with $\alpha \approx 0.5$. This shortcoming could be overcome by a two-time calculation that avoids the GKBA. Such calculations for QD systems consisting of intermediate polar coupling materials

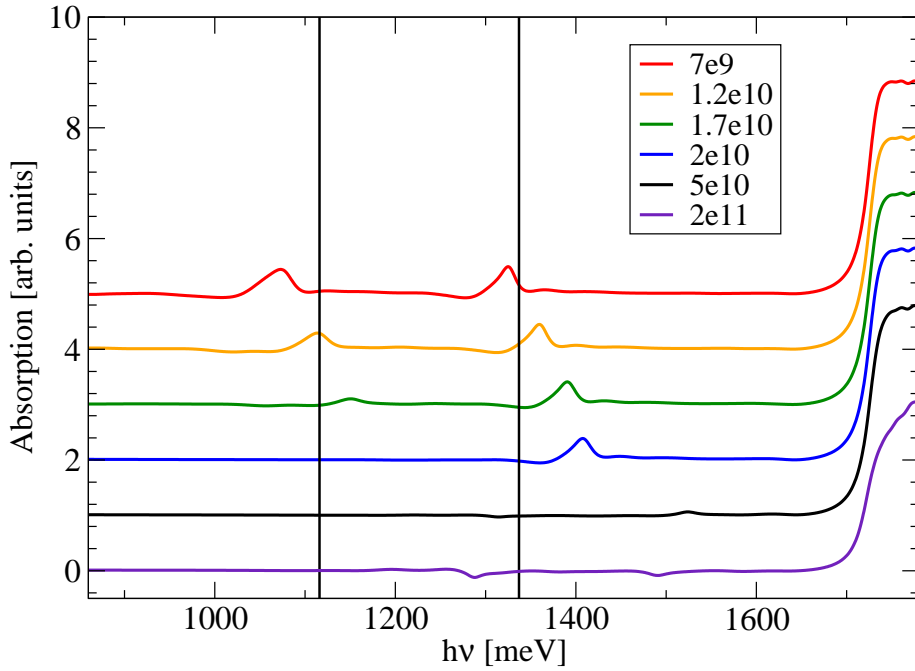


Figure 16.8: Linear optical absorption spectra for InN QDs at 300 K and for various carrier densities in $1/\text{cm}^2$. The dephasing is provided by carrier-phonon interaction. The spectra are shifted vertically for better visibility.

like CdTe were performed in Ref. [75].

16.6 Conclusion

In this part we have performed calculations of optical gain and absorption spectra for nitride QDs. It has been shown that due to symmetry properties the main dipole transitions are “off-diagonal” in character, in contrast to the arsenide systems that were studied in Part III. The QD resonances exhibit a pronounced blue shift, due to Hartree contributions that describe the charging of the QDs. The polaron for nitride QD has been investigated, and we have shown, that strong polaronic interaction effects, that lead to hybridization effects in the spectral function, exist in nitride QDs, even if the level splitting exceeds $2\hbar\omega_{\text{LO}}$. The dephasing due to carrier-phonon interaction was studied and homogeneous broadenings of the order of 20 meV were found for the specific QD geometry investigated here.

Part VI

Summary and Outlook

Conclusion

In the present thesis we have developed and applied theoretical models to describe optical properties of semiconductor quantum-dot systems. Laser characteristics as well as the underlying mechanisms of the optical gain are studied on a microscopic basis.

To investigate the dephasing and the corresponding optical gain, microscopic calculations of the influences of Coulomb interaction and carrier-LO-phonon interaction are performed in Part III. The influences of various scattering channels are studied and we show that Coulomb and LO-phonon contributions to the homogeneous linewidths are equally important even at high carrier densities. The necessity of a self-consistent treatment of single-particle energy renormalizations is emphasized, as the optical spectra can show unphysical behavior otherwise. In the resulting optical gain spectra remarkable features are found. The maximum optical gain can decrease with increasing carrier density due to the interplay of dephasing and state-filling. This behavior is unknown from other gain materials and is a direct consequence of the interplay between localized and delocalized states, quite unique to quantum-dot systems. However, the gain reduction effect is strongly masked by effects of inhomogeneous broadening. Furthermore, we evaluate the linewidth-enhancement factor in semiconductor quantum-dot systems. The values of the linewidth-enhancement factor are comparable to those found in quantum-well systems, in contrast to the predictions of atomistic models.

In Part IV laser properties of quantum-dot based microcavity devices were investigated directly. A microscopic theory including a quantum-mechanical treatment of the light field was employed. We could show that even for high β -factors, the auto-correlation function $g^{(2)}(0)$ allows for a distinction of the regimes where either spontaneous or stimulated emission dominates. Furthermore, we have demonstrated modifications of the characteristic emission properties due to a deviating behavior from the atomic case. Especially the jump in the input/output curve from below to above threshold is found not to scale with $1/\beta$. This means that for a extraction of the β -factor from experimental results theoretical modelling is needed.

Optical spectra for nitride quantum dots are studied in Part V. Nitride material systems are currently intensely investigated due to a manyfold of possible device applications. Microscopic tight-binding calculations show a change in the selection rules compared to the conventional III-V or II-VI material systems due to symmetry and band-mixing effects. Optical absorption and gain spectra are calculated from the microscopic tight-binding wave-functions. A substantial difference in the confinement potential for electrons and holes leads to charging effects of the quantum-dots. This leads to a pronounced blue shift of the quantum-dot resonances with increasing carrier density. We find strong polaronic effects in the intermediate polar coupling

nitrides. The spectral function shows pronounced hybridization effects, even though the spacing between the quantum-dot levels is much larger than the LO phonon energy. Furthermore, we observe a substantial dephasing due to carrier-phonon interaction.

Future directions

The theoretical models presented in this thesis can be extended in various ways. To further improve the dephasing model, the inclusion of exciton-phonon interaction via a T-matrix approach for the spectral functions is necessary, to avoid the problem discussed in Section 11.2. Moreover, such an approach opens the possibility to use the theory for a wider range of carrier-densities. With the newest supercomputers available, also a full time-dependent calculation of scattering and dephasing due to Coulomb interaction might be within reach. This would allow for studies of pump-probe and four-wave mixing experiments and detailed theory-experiment comparisons. Furthermore, currently underway is a direct comparison between quantum-dot and quantum-well gain for emission at a wavelength of $1.5\mu\text{m}$, being relevant for telecommunication applications.

Our semiconductor approach for the laser theory allows for an inclusion of the full range of semiconductor effects in a consistent and well-defined manner. For example relaxation and dephasing processes due to Coulomb interaction can also be treated on a microscopic level, which links to the results of Part III. Especially the effect of the gain reduction phenomenon on input/output characteristics and on the photon statistics of the emitted light should be investigated.

For the nitride quantum-dot systems a comparison of the optical gain spectra to results obtained from $\mathbf{k} \cdot \mathbf{p}$ single-particle states is currently underway. This would allow to take further effects like concentration gradients and alloys into account and allow for detailed theory-experiment comparisons. As a technical point, a two-time calculation for the carrier-phonon interaction in nitride quantum dots should be performed to overcome the problem with the generalized Kadanoff-Baym ansatz. This could also serve as a “benchmark” for possible improvements on the one-time calculation level. Furthermore, an inclusion of the dephasing due to Coulomb interaction should be concerned, even though, this will require substantially more computing power.

Part VII

Appendix

A Eigenfunctions in envelope function approximation and Coulomb matrix elements

In this chapter we will give details about the wave-function model for flat InGaAs QDs that is used in Parts III and IV. Furthermore, we will discuss the orthogonalized-plane-wave (OPW) method, that is also employed in Part V. As discussed in Chapter 7 we assume for the wavefunctions in envelope approximation a factorization of the envelope function into an two-dimensional in-plane part $\varphi(\boldsymbol{\rho})$ and an one-dimensional part $\xi(z)$ in growth direction,

$$\psi(\mathbf{r}) = \varphi(\boldsymbol{\rho}) \xi(z) u_{\mathbf{k} \approx 0}(\mathbf{r}) ,$$

with the lattice periodic Bloch function $u_{\mathbf{k} \approx 0}(\mathbf{r})$ [158, 128].

For the envelope part in growth direction we can assume one-dimensional QW wavefunctions. As the energetic separation between the subbands is large enough that transitions to the second subband are not in the energetic window we are interested in, we can restrict the analysis to the lowest subband. We will assume QW barriers of infinite height, leading to analytically known wave-functions

$$\xi(z) = \frac{1}{\sqrt{L}} \sin\left(\frac{\pi}{L} z\right) \quad (\text{A.1})$$

with the QW height L . To take barriers of finite height into account, one would have to evaluate the corresponding one-dimensional Schrödinger equation numerically. However, as the numerical results are practically unchanged by either choice, we will consider the infinite potential barrier case only.

The in-plane part of the delocalized WL states is described in the absence of QDs by two-dimensional plane-wave states,

$$\varphi_{\mathbf{k}}^0(\boldsymbol{\rho}) = \frac{1}{\sqrt{A}} e^{i\mathbf{k}\boldsymbol{\rho}} , \quad (\text{A.2})$$

where \mathbf{k} is the in-plane momentum and A is the normalization area of the QW. For flat, lens-shaped QDs in the InAs/GaAs material system the in-plane confinement

potential was shown to be harmonic in good approximation [130, 126]. The corresponding wave functions of a two-dimensional harmonic oscillator are easily computed [204] and can be classified according to their in-plane symmetry by means of angular momentum properties. Correspondingly the lowest two confined shells are referred to as s- and p-shell.

$$\varphi_{m=0}^s(\boldsymbol{\varrho} - \mathbf{R}) = \frac{\beta}{\sqrt{\pi}} e^{-\frac{\beta^2 |\boldsymbol{\varrho} - \mathbf{R}|^2}{2}}, \quad (\text{A.3a})$$

$$\varphi_{m=\pm 1}^p(\boldsymbol{\varrho} - \mathbf{R}) = \frac{\beta^2}{\sqrt{\pi}} e^{-\frac{\beta^2 |\boldsymbol{\varrho} - \mathbf{R}|^2}{2}} |\boldsymbol{\varrho} - \mathbf{R}| e^{\pm i\phi}. \quad (\text{A.3b})$$

Here \mathbf{R} denotes the position of the QD on the WL plane and the parameter $\beta = \frac{\sqrt{m\Delta E}}{\hbar}$, that determines the equidistant energy separation ΔE between the QD shells, is the inverse oscillator length that contains information about the size of the QDs. For our numerical evaluations we will always assume identical QDs. Note, that therefore sums over state indices α that appear throughout the thesis are to be read as

$$\sum_{\alpha} = \frac{1}{A} \sum_{\mathbf{k},s} + \frac{1}{A} \sum_{\nu,s} \sum_{\mathbf{R}}. \quad (\text{A.4})$$

Coulomb matrix elements

The decomposition of the wave-functions into an in-plane part and a part in growth-direction leads to the possibility of a similar splitting for the Coulomb matrix elements. Starting from the matrix elements as defined in Eq. (7.12)

$$V_{\nu_1 \nu_2 \nu_3 \nu_4} = \sum_{\mathbf{q}} V_{\mathbf{q}} \langle \xi_{\alpha_1}^{\lambda_1} \varphi_{\alpha_1}^{\lambda_1} | e^{i\mathbf{q}\mathbf{r}} | \xi_{\alpha_4}^{\lambda_1} \varphi_{\alpha_4}^{\lambda_1} \rangle \langle \xi_{\alpha_2}^{\lambda_2} \varphi_{\alpha_2}^{\lambda_2} | e^{-i\mathbf{q}\mathbf{r}} | \xi_{\alpha_3}^{\lambda_2} \varphi_{\alpha_3}^{\lambda_2} \rangle \delta_{\lambda_1, \lambda_4} \delta_{\lambda_2, \lambda_3},$$

we can use the explicit form of the eigenfunctions to cast the Coulomb matrix element into the form

$$V_{\alpha_1 \alpha_2 \alpha_3 \alpha_4}^{\lambda_1 \lambda_2 \lambda_3 \lambda_4} = \sum_{\mathbf{q}_{||}} V_{\mathbf{q}_{||}} F^{\text{QW}}(\mathbf{q}_{||}) \langle \varphi_{\alpha_1} | e^{i\mathbf{q}_{||}\boldsymbol{\varrho}} | \varphi_{\alpha_4} \rangle \langle \varphi_{\alpha_2} | e^{-i\mathbf{q}_{||}\boldsymbol{\varrho}} | \varphi_{\alpha_3} \rangle \delta_{\lambda_1, \lambda_4} \delta_{\lambda_2, \lambda_3}, \quad (\text{A.5})$$

where the q_z integration has been carried out explicitly and the dependence on the growth direction is included in the formfactor

$$F^{\text{QW}}(|\mathbf{q}_{||}|) = \int dz \int dz' \xi^*(z) \xi^*(z') e^{-q_{||}|z-z'|} \xi(z') \xi(z). \quad (\text{A.6})$$

Here

$$V_{\mathbf{q}_{||}} = \frac{1}{2\varepsilon_0 |\mathbf{q}_{||}|}$$

is the two-dimensional Fourier transform of the Coulomb potential. Naturally the screened matrix elements of Eq. (9.21) can be evaluated in a completely similar fashion as the overlap integrals entering are identical.

Orthogonalized plane waves

As for any basis that we expand our equations in, we require orthonormality between the different states involved. Specifically this means that we need to orthogonalize the WL states to the set of QD states. This is achieved by means of the OPW method, that follows from a similar idea as the Gram-Schmidt orthogonalization procedure

$$|\mathbf{k}\rangle = \frac{1}{N_{\mathbf{k}}} \left[|\mathbf{k}_0\rangle - \sum_{\nu, \mathbf{R}} |\nu, \mathbf{R}\rangle \langle \nu, \mathbf{R} | \mathbf{k}_0 \right], \quad (\text{A.7})$$

with the OPW normalization function

$$N_{\mathbf{k}}^2 = 1 - \sum_{\nu, \mathbf{R}} |\langle \nu, \mathbf{R} | \mathbf{k}_0 \rangle|^2, \quad (\text{A.8})$$

where \mathbf{R} denotes all QD positions.

Evaluating this for identical QDs and taking into account, that the QD positions only give rise to a phase factor

$$\langle \nu, \mathbf{R} | \mathbf{k}_0 \rangle = \langle \nu | \mathbf{k}_0 \rangle e^{i\mathbf{k}\mathbf{R}},$$

we find

$$|\mathbf{k}\rangle = \frac{1}{N_{\mathbf{k}}} \left[|\mathbf{k}_0\rangle - \sum_{\nu} |\nu\rangle \langle \nu | \mathbf{k}_0 \rangle \right] \quad (\text{A.9})$$

with

$$N_{\mathbf{k}}^2 = 1 - N_{\text{QD}} \sum_{\nu} |\langle \nu | \mathbf{k}_0 \rangle|^2. \quad (\text{A.10})$$

Here N_{QD} is the number of QDs on the WL plane. Furthermore, we can show, that *on average* momentum conservation is restored so that $\langle \mathbf{k} | \mathbf{k}' \rangle \propto \delta(\mathbf{k} - \mathbf{k}')$. As the plane-wave states contain the normalization area via $\frac{1}{\sqrt{A}}$, only the QD density $n_{\text{QD}} = \frac{N_{\text{QD}}}{A}$ enters the theory.

In principle the OPW scheme also leads to a modification of the energies of the WL states. However, under the assumption that the QD density and the QD sizes are sufficiently small so that only a small fraction of the WL plane is covered with QDs,

these changes can be neglected. To show this, we evaluate the expectation value of the total energy,

$$\begin{aligned} \langle \mathbf{k} | h_0 | \mathbf{k} \rangle &= \langle \mathbf{k}_0 | h_0 | \mathbf{k}_0 \rangle - N_{\text{QD}} \sum_{\nu} \langle \mathbf{k}_0 | h_0 | \nu \rangle \langle \nu | \mathbf{k}_0 \rangle - N_{\text{QD}} \sum_{\nu} \langle \mathbf{k}_0 | \nu \rangle \langle \nu | h_0 | \mathbf{k}_0 \rangle \\ &\quad + N_{\text{QD}} \sum_{\nu, \mu} \langle \mathbf{k}_0 | \nu \rangle \langle \nu | h_0 | \mu \rangle \langle \mu | \mathbf{k}_0 \rangle \\ &\approx e_{\mathbf{k}}^0 - N_{\text{QD}} \sum_{\nu} E_{\nu} |\langle \nu | \mathbf{k}_0 \rangle|^2. \end{aligned} \quad (\text{A.11})$$

In the last line we have approximated $h_0 = h_0^{\text{WL}}$, which corresponds to a neglection of the in-plane confinement potential. This approximation should be reasonable in the case of flat QDs.

Taking into account, that the overlaps $|\langle \nu | \mathbf{k}_0 \rangle|^2$ are inversely proportional to the normalization area, we find that the OPW correction terms are directly proportional to the QD density n_{QD} , hence for sufficiently low QD densities, in the sense discussed above, we can disregard the OPW corrections to the WL energies and work with the PW energies $e_{\mathbf{k}}^0$. However, as calculations of overlaps from non-orthogonal wavefunctions can lead to drastic deviations in the matrix elements, it is essential to include the OPW corrections to the wave-functions.

The advantage of this scheme is that the calculation of Coulomb matrixelements can be traced back to the calculation of overlap integrals $\langle \alpha | e^{+i\mathbf{q}\cdot\mathbf{r}} | \beta \rangle$ of known wavefunctions. Furthermore, the OPW scheme accounts for the random distribution of QDs on the WL plane, typical for selfassembled QDs.

An alternative approach would be to directly calculate the QD and WL wavefunctions for the combined QD-WL system. This would imply a periodic distribution of QD on the WL plane due to periodic boundary conditions, typically used. The advantage of the OPW scheme is to avoid this assumption. However, corrections that correspond to relative phase shifts can be present in the direct calculation, whereas these are neglected in the OPW approach.

Overlap integrals

For the calculation of Coulomb matrix elements and likewise for the matrix elements of the Fröhlich interaction of carriers and LO-phonons we need to evaluate two-dimensional overlap integrals of the form $\langle \alpha | e^{i\mathbf{q}_{\parallel} \cdot \boldsymbol{\varrho}} | \beta \rangle$ according to Eq. (A.5). Furthermore, as we express the orthogonalization procedure in terms of overlaps, this make it also accessible to the tight-bindig wavefunction model of Part V. Using the OPW scheme and assuming identical QDs, we find for the QD-WL overlaps

$$\langle \nu | e^{i\mathbf{qr}} | \mathbf{k} \rangle = \frac{1}{N_{\mathbf{k}}} \left[\langle \nu | e^{i\mathbf{qr}} | \mathbf{k}_0 \rangle - \sum_{\mu} \langle \nu | e^{i\mathbf{qr}} | \mu \rangle \langle \mu | \mathbf{k}_0 \rangle \right] \quad (\text{A.12})$$

and for the WL-WL overlaps

$$\langle \mathbf{k} | e^{i\mathbf{qr}} | \mathbf{k}' \rangle = \delta(\mathbf{q} + \mathbf{k}' - \mathbf{k}) D_{\text{OPW}}(\mathbf{k}, \mathbf{q}, \mathbf{k}') \quad (\text{A.13})$$

with

$$\begin{aligned} D_{\text{OPW}}(\mathbf{k}, \mathbf{q}, \mathbf{k}') &= \frac{1}{N_{\mathbf{k}}} \frac{1}{N_{\mathbf{k}'}} \left(1 - N_{\text{QD}} \sum_{\nu} \langle \mathbf{k}_0 | e^{i\mathbf{qr}} | \nu \rangle \langle \nu | \mathbf{k}'_0 \rangle \right. \\ &\quad - N_{\text{QD}} \sum_{\nu} \langle \mathbf{k}_0 | \nu \rangle \langle \nu | e^{i\mathbf{qr}} | \mathbf{k}'_0 \rangle \\ &\quad \left. + N_{\text{QD}} \sum_{\nu, \mu} \langle \mathbf{k}_0 | \nu \rangle \langle \nu | e^{i\mathbf{qr}} | \mu \rangle \langle \mu | \mathbf{k}'_0 \rangle \right). \end{aligned} \quad (\text{A.14})$$

More details on the OPW scheme and an explicit analytic evaluation of the overlap integrals can be found in Refs. [125, 135, 30].

B Derivation of the Lindhard formula

We consider the screening of the Coulomb interaction in the random phase approximation. The retarded component of the longitudinal polarization reads

$$P^R(1, 2) = -i\hbar [G^R(1, 2)G^<(2, 1) + G^<(1, 2)G^A(2, 1)] . \quad (\text{B.1})$$

Using the Fourier expansion

$$P^R(1, 2) = \sum_{\mathbf{q}_1, \mathbf{q}_2} e^{i(\mathbf{q}_1 \mathbf{r}_1 - \mathbf{q}_2 \mathbf{r}_2)} P_{\mathbf{q}_1, \mathbf{q}_2}^R(t_1, t_2) \quad (\text{B.2})$$

for the polarization function and a general eigenfunction expansion

$$G(1, 2) = \sum_{\alpha\beta} G_{\alpha\beta}(t_1, t_2) \varphi_\alpha(\mathbf{r}_1) \varphi_\beta^*(\mathbf{r}_2) \quad (\text{B.3})$$

for the GFs, we find

$$\begin{aligned} P_{\mathbf{q}_1, \mathbf{q}_2}^R(t_1, t_2) &= -i\hbar \sum_{\alpha\beta\gamma\delta} \langle \delta | e^{-i\mathbf{q}_1 \mathbf{r}} | \alpha \rangle \langle \beta | e^{i\mathbf{q}_2 \mathbf{r}} | \gamma \rangle \\ &\times [G_{\alpha\beta}^R(t_1, t_2) G_{\gamma\delta}^<(t_2, t_1) + G_{\alpha\beta}^<(t_1, t_2) G_{\gamma\delta}^A(t_2, t_1)] . \end{aligned} \quad (\text{B.4})$$

Using the generalized Kadanoff-Baym ansatz and restricting ourselves to retarded functions diagonal in the state and band indices, we find

$$\begin{aligned} G_{\alpha\beta}^<(t_1, t_2) &= i\hbar G_{\alpha\alpha}^R(t_1, t_2) G_{\alpha\beta}^<(t_2) \\ G_{\alpha\beta}^<(t_2, t_1) &= -i\hbar G_{\alpha\beta}^<(t_2) G_{\beta\beta}^A(t_2, t_1) , \end{aligned} \quad (\text{B.5})$$

assuming that $t_1 < t_2$. Using this in Eq. (B.4) we find

$$\begin{aligned} P_{\mathbf{q}_1, \mathbf{q}_2}^R(t_1, t_2) &= -i\hbar \left\{ \sum_{\alpha\gamma\delta} \langle \delta | e^{-i\mathbf{q}_1 \mathbf{r}} | \alpha \rangle \langle \alpha | e^{i\mathbf{q}_2 \mathbf{r}} | \gamma \rangle (-i\hbar) G_{\alpha\alpha}^R(t_1, t_2) G_{\gamma\delta}^<(t_2) G_{\delta\delta}^A(t_2, t_1) \right. \\ &\left. + \sum_{\alpha\beta\delta} \langle \delta | e^{-i\mathbf{q}_1 \mathbf{r}} | \alpha \rangle \langle \beta | e^{i\mathbf{q}_2 \mathbf{r}} | \delta \rangle (i\hbar) G_{\alpha\alpha}^R(t_1, t_2) G_{\alpha\beta}^<(t_2) G_{\delta\delta}^A(t_2, t_1) \right\} . \end{aligned} \quad (\text{B.6})$$

If we furthermore consider only overlaps from states of the same band $\langle \delta | e^{-i\mathbf{q}\mathbf{r}_1} | \alpha \rangle \propto \delta_{\lambda_\delta, \lambda_\alpha}$ and disregard intraband polarization terms $G_{\alpha\beta}^{cc, <}$, this reduces to

$$\begin{aligned} P_{\mathbf{q}_1, \mathbf{q}_2}^R(t_1, t_2) &= \hbar^2 \sum_{\alpha\beta} \langle \alpha | e^{i\mathbf{q}_2 \mathbf{r}} | \beta \rangle \langle \beta | e^{-i\mathbf{q}_1 \mathbf{r}} | \alpha \rangle \\ &\times [G_{\alpha\alpha}^R(t_1, t_2) G_{\alpha\alpha}^<(t_2) G_{\beta\beta}^A(t_2, t_1) - G_{\alpha\alpha}^R(t_1, t_2) G_{\beta\beta}^<(t_2) G_{\beta\beta}^A(t_2, t_1)] . \end{aligned} \quad (\text{B.7})$$

To get the frequency dependence of the polarization function, let us assume that it only depends on the difference of the time arguments, $P_{\mathbf{q}_1, \mathbf{q}_2}^R(t_1, t_2) = P_{\mathbf{q}_1, \mathbf{q}_2}^R(t_1 - t_2)$. This is only possible if the population function are only slowly varying. If we choose the retarded/advanced GFs to be *free* ones,

$$\begin{aligned} G_\alpha^R(t_1, t_2) &= -\frac{i}{\hbar} e^{-\frac{i}{\hbar} \varepsilon_\alpha (t_1 - t_2)} \\ G_\alpha^A(t_2, t_1) &= \frac{i}{\hbar} e^{\frac{i}{\hbar} \varepsilon_\alpha (t_1 - t_2)} \end{aligned},$$

equation (B.7) only depends on the relative time and we can perform a Fourier transform that leads to

$$\begin{aligned} P_{\mathbf{q}_1, \mathbf{q}_2}^R(\omega) &= \sum_{\alpha\beta} \langle \alpha | e^{i\mathbf{q}_2 \mathbf{r}} | \beta \rangle \langle \beta | e^{-i\mathbf{q}_1 \mathbf{r}} | \alpha \rangle (G_{\alpha\alpha}^< - G_{\beta\beta}^<) \int_0^\infty d\tau e^{\frac{i}{\hbar} (\hbar\omega - \varepsilon_\alpha + \varepsilon_\beta) \tau} \\ &= i\hbar \sum_{\alpha\beta} \langle \alpha | e^{i\mathbf{q}_2 \mathbf{r}} | \beta \rangle \langle \beta | e^{-i\mathbf{q}_1 \mathbf{r}} | \alpha \rangle \frac{G_{\alpha\alpha}^< - G_{\beta\beta}^<}{\hbar\omega - \varepsilon_\alpha + \varepsilon_\beta + i\delta} \\ P_{\mathbf{q}_1, \mathbf{q}_2}^R &= \sum_{\alpha\beta} \langle \alpha | e^{i\mathbf{q}_2 \mathbf{r}} | \beta \rangle \langle \beta | e^{-i\mathbf{q}_1 \mathbf{r}} | \alpha \rangle \frac{f_\alpha - f_\beta}{\varepsilon_\alpha - \varepsilon_\beta} . \end{aligned} \quad (\text{B.8})$$

In the last line we applied the static limit $\omega \rightarrow 0$. The screened interaction follows from

$$W_{\mathbf{q}_1, \mathbf{q}_2} = V_{\mathbf{q}_1} + \sum_{\mathbf{q}_3} V_{\mathbf{q}_1} P_{\mathbf{q}_1, \mathbf{q}_3} W_{\mathbf{q}_3, \mathbf{q}_2} \quad (\text{B.9})$$

whose solution involves a matrix inversion. In analogy to the bare Coulomb matrix elements (7.12), the screened ones are given by

$$W_{\alpha\beta\gamma\delta}^R = \sum_{\mathbf{q}_1 \mathbf{q}_2} W_{\mathbf{q}_1 \mathbf{q}_2}^R \langle \alpha | e^{-i\mathbf{q}_1 \mathbf{r}} | \delta \rangle \langle \beta | e^{+i\mathbf{q}_2 \mathbf{r}} | \gamma \rangle . \quad (\text{B.10})$$

For practical calculations we can assume that screening only comes from carriers in the WL, which is reasonable for higher carrier densities and low to intermediate

densities of QDs on the WL. As for the WL momentum conservation ($\mathbf{q}_1 = \mathbf{q}_2$) is fulfilled, in the presence of QDs at least on average, equation (B.8) reduces to

$$P_{\mathbf{q}}^R = \sum_{\alpha\beta} |\langle \alpha | e^{i\mathbf{qr}} | \beta \rangle|^2 \frac{f_\alpha - f_\beta}{\varepsilon_\alpha - \varepsilon_\beta}. \quad (\text{B.11})$$

Correspondingly the screened interaction and the matrix elements follow from

$$W_{\mathbf{q}} = \frac{V_{\mathbf{q}}}{1 - P_{\mathbf{q}}^R V_{\mathbf{q}}} \quad (\text{B.12})$$

and

$$W_{\alpha\beta\gamma\delta}^R = \sum_{\mathbf{q}} W_{\mathbf{q}}^R \langle \alpha | e^{-i\mathbf{qr}} | \delta \rangle \langle \beta | e^{+i\mathbf{qr}} | \gamma \rangle. \quad (\text{B.13})$$

C Interplay of time constants for the laser model

For the evaluation of our theory, we treat the rate of spontaneous emission into the non-lasing modes $1/\tau_{\text{nl}}$ as an extrinsic parameter, which is determined by the properties of the laser resonator. Depending on the particular cavity design, other high- Q resonator modes as well as a quasi-continuum of low- Q leaky modes can contribute.

The spontaneous emission into the laser mode can be calculated from the light-matter coupling strength $|g|^2 = |g_{qis}|^2$ for this mode, κ , and Γ . Restricting the adiabatic solution of Eq. (13.10) to the spontaneous emission into the laser mode and using Eq. (13.8) to define the corresponding rate $1/\tau_l$ according to

$$\frac{d}{dt} f_s^{e,h} \Big|_{l,\text{spont}} = -\frac{f_s^e f_s^h}{\tau_l}, \quad (\text{C.1})$$

we find

$$\frac{1}{\tau_l} = \frac{2}{\hbar} \frac{|g|^2}{\kappa + \Gamma}. \quad (\text{C.2})$$

With τ_l and τ_{nl} the β -factor follows from Eq. (13.13).

In this work we present the figures in the common style where the β -factor is varied, as it is the most important parameter characterizing the cavity efficiency, while the total rate of spontaneous emission $1/\tau_{\text{sp}} = 1/\tau_l + 1/\tau_{\text{nl}}$ is held constant. To achieve such a situation, for various β -values both τ_{nl} and τ_l need to be changed. Note that the latter requires a change of the light-matter coupling strength according to Eq. (C.2), which is possible for a given dipole coupling by a modification of the mode functions, and/or by a change of the lifetime of the cavity mode.

In Ref. [9] the presented theory is applied to pillar microcavities with various resonator diameters. In such a situation, the spontaneous emission into non-lasing modes is practically constant due to the unchanging contributions of leaky modes, while the spontaneous emission into the laser mode is modified by the Purcell effect.

The Purcell factor F_P is defined as the ratio of the rate of spontaneous emission into the cavity mode, $1/\tau_l$, to the rate of spontaneous emission into free space, $1/\tau_{\text{free}}$.

We can express the β -factor in terms of F_P as

$$\beta = \frac{F_P}{dF_P + \frac{\tau_{\text{free}}}{\tau_{\text{nl}}}} = \frac{\frac{1}{\tau_i}}{\frac{d}{\tau_i} + \frac{1}{\tau_{\text{nl}}}} , \quad (\text{C.3})$$

where additionally a possible degeneracy d of the fundamental mode has been included, see the article by J.-M. Gérard in Ref. [6].

D Material parameters and numerical methods

D.1 Material parameters

	n_{QD}	m/m_0	E_s	E_p
$1 \times 10^{10} \text{ cm}^{-2}$				
electrons		0.067	-80meV	-40meV
holes		0.150	-30meV	-15meV

Table D.1: Parameters for the InGaAs/GaAs material system used in Chapter 9-11. The QD energies are given relatively to the WL bandedge.

	n_{QD}	m/m_0	E_s	E_p
$2 \times 10^{10} \text{ cm}^{-2}$				
electrons		0.054	-142meV	-66meV
holes		0.070	-115meV	-55meV

Table D.2: Parameters for the “deep dot” system used in Part III. The QD energies are given relatively to the WL bandedge.

	n_{QD}	m/m_0	E_s
	$5 \times 10^{10} \text{ cm}^{-2}$		
electrons		0.061	-37meV
holes		0.101	-31meV

Table D.3: Parameters for the “shallow dot” system used in Part III. The QD energies are given relatively to the WL bandedge.

D.2 Numerical methods

To solve differential equations in Parts IV and V we use a 4th-order Runge-Kutta scheme that reads for a differential equation of the type

$$\frac{d}{dt}f = g[f(t), t].$$

as follows

$$\begin{aligned} f_n &= f_{n-1} + \frac{h}{6} (k_1 + 2k_2 + 2k_3 + k_4) + O(h^5) \\ \text{mit } & k_1 = g[f_{n-1}, t_{n-1}] \\ & k_2 = g\left[f_{n-1} + \frac{h}{2}k_1, t_{n-1} + \frac{h}{2}\right] \\ & k_3 = g\left[f_{n-1} + \frac{h}{2}k_2, t_{n-1} + \frac{h}{2}\right] \\ & k_4 = g[f_{n-1} + hk_3, t_{n-1} + h], \end{aligned} \quad (\text{D.1})$$

if h is the time-step size and $f_n = f(t_n)$. For differential equations that involve memory effects, like the Dyson equation for the polaronic spectra function, we use a Adams-Bashfourth-Moulton predictor-corrector method [205]. The quasi-momentum integrations are usually discretized using a modified Gauss-Chebyshev method [206].

D.3 Lifting of the Coulomb singularity

In the calculations of the Coulomb matrix elements for the nitride material system, the matrix elements $V_{\mathbf{k}\mathbf{k}'\mathbf{k}\mathbf{k}'}^{\lambda\lambda'}$ contain the Coulomb singularity at $q = 0$. To lift this singularity, we use a procedure that has been successfully implemented for the same

problem in bulk materials and QWs for a long time [158]. Let us start by writing the integral that appears in the selfenergy as

$$\Sigma_k(t) = i\hbar \int dk' d\varphi_k d\varphi_{k'} V_{\mathbf{k},\mathbf{k}'} G_{k'}^<(t) \quad (\text{D.2})$$

with the definition

$$V_{\mathbf{k},\mathbf{k}'} = \sum_{\mathbf{q}} \frac{k'}{|\mathbf{q}_{||}|^2 + q_z^2} D_{\text{OPW}}(\mathbf{k}, \mathbf{q}, \mathbf{k}') \delta(\mathbf{q}_{||} + \mathbf{k}' - \mathbf{k}) \sum_{l=1}^2 e^{i\mathbf{q}_{||}\mathbf{f}_l} F_l(\mathbf{k}, \mathbf{k}', q_z) . \quad (\text{D.3})$$

Now we add and subtract $G_k^<(t) \int dk' d\varphi_k d\varphi_{k'} V_{\mathbf{k},\mathbf{k}'} \alpha(k, k')$, with a convergence enforcing function $\alpha(k, k')$. The result can be written as

$$\begin{aligned} \Sigma_k(t) = & i\hbar \left[\int dk' d\varphi_k d\varphi_{k'} V_{\mathbf{k},\mathbf{k}'} (G_{k'}^<(t) - \alpha(k, k') G_k^<(t)) \right. \\ & \left. + G_k^<(t) \right] \int dk' d\varphi_k d\varphi_{k'} V_{\mathbf{k},\mathbf{k}'} \alpha(k, k') \end{aligned} \quad (\text{D.4})$$

and upon discretization of the k' integral

$$\Sigma_k(t) = i\hbar \left[\sum_{j \neq i} \tilde{V}_{i,j} G_j^<(t) - G_i \sum_{j \neq i} \alpha_{i,j} \tilde{V}_{i,j} - \sum_m \alpha_{i,m} \tilde{V}_{i,m} \right], \quad (\text{D.5})$$

where we introduced

$$\tilde{V}_{k,k'} = \int d\varphi_k d\varphi_{k'} V_{\mathbf{k},\mathbf{k}'}$$

and likewise for the discretized version.

E Dipole matrix elements using tight-binding coefficients

To obtain the dipole matrix elements for the QD-WL transition, a similar approach as for the QD-WL overlaps can be used, by means of Bloch's theorem.

For the WL-WL transitions we have

$$\begin{aligned} \mathbf{d}_{\mathbf{k}\mathbf{k}'}^{cv} &= e_0 \int d^3r \psi^*(\mathbf{r}) \mathbf{r} \psi(\mathbf{r}) \\ &= \frac{1}{N} e_0 \sum_{R, R', \sigma, \tau} c_{\mathbf{k}, \sigma}^{c*}(\mathbf{R}) \left(\int d^3r \phi_{\sigma, \mathbf{R}}^*(\mathbf{r}) \mathbf{r} \phi_{\tau, \mathbf{R}'}(\mathbf{r}) \right) c_{\mathbf{k}', \tau}^v(\mathbf{R}') . \end{aligned} \quad (\text{E.1})$$

As the simplest approximation we keep only the $\mathbf{R} = \mathbf{R}'$ contributions, this is possible because the atomic orbitals are localized at the atomic positions and orbitals at different atomic positions don't overlap.

$$\mathbf{d}_{\mathbf{k}\mathbf{k}'}^{cv} = \frac{1}{N} e_0 \sum_{\mathbf{R}, \sigma, \tau} c_{\mathbf{k}, \sigma}^{c*}(\mathbf{R}) \left(\int d^3r \phi_{\sigma}^*(\mathbf{r} - \mathbf{R}) \mathbf{r} \phi_{\tau}(\mathbf{r} - \mathbf{R}) \right) c_{\mathbf{k}', \tau}^v(\mathbf{R}) ,$$

because the atomic orbitals are the same at every atom position. We can introduce $\mathbf{r}' = \mathbf{r} - \mathbf{R}$ and split the integral into two contributions

$$\begin{aligned} \mathbf{d}_{\mathbf{k}\mathbf{k}'}^{cv} &= \frac{1}{N} e_0 \sum_{\mathbf{R}, \sigma, \tau} c_{\mathbf{k}, \sigma}^{c*}(\mathbf{R}) c_{\mathbf{k}', \tau}^v(\mathbf{R}) \left(\underbrace{\int d^3r' \phi_{\sigma}^*(\mathbf{r}') \mathbf{r}' \phi_{\tau}(\mathbf{r}')}_{\mathbf{d}_{\sigma, \tau}} + \phi_{\sigma}^*(\mathbf{r}') \mathbf{R} \phi_{\tau}(\mathbf{r}') \right) \\ &= \frac{1}{N} e_0 \sum_{\mathbf{R}, \sigma, \tau} c_{\mathbf{k}, \sigma}^{c*}(\mathbf{R}) c_{\mathbf{k}', \tau}^v(\mathbf{R}) \left(\mathbf{d}_{\sigma, \tau} + \mathbf{R} \int d^3r' \phi_{\sigma}^*(\mathbf{r}') \phi_{\tau}(\mathbf{r}') \right) \\ &= \frac{1}{N} e_0 \sum_{\mathbf{R}, \sigma, \tau} c_{\mathbf{k}, \sigma}^{c*}(\mathbf{R}) c_{\mathbf{k}', \tau}^v(\mathbf{R}) (\mathbf{d}_{\sigma, \tau} + \mathbf{R} \delta_{\sigma, \tau}) \end{aligned}$$

In the last step we used the orthonormality of the atomic orbitals. As in the calculation of the overlaps we can pull the WL coefficients back to the unit column by

means of Bloch's theorem, and we find

$$\begin{aligned}
\mathbf{d}_{\mathbf{k}\mathbf{k}'}^{cv} &= \frac{1}{N} e_0 \sum_{l=1}^2 \sum_{\mathbf{R}_{||}, \mathbf{R}_z, \sigma, \tau} c_{\mathbf{k}, \sigma}^{c*}(\mathbf{f}_l + \mathbf{R}_z) c_{\mathbf{k}', \tau}^v(\mathbf{f}_l + \mathbf{R}_z) e^{i(\mathbf{k}' - \mathbf{k})\mathbf{R}_{||}} (\mathbf{d}_{\sigma, \tau} + \mathbf{R}\delta_{\sigma, \tau}) \\
&= \frac{1}{N} e_0 \sum_{l=1}^2 \left(\sum_{\mathbf{R}_{||}, \mathbf{R}_z, \sigma, \tau} c_{\mathbf{k}, \sigma}^{c*}(\mathbf{f}_l + \mathbf{R}_z) c_{\mathbf{k}', \tau}^v(\mathbf{f}_l + \mathbf{R}_z) \mathbf{d}_{\sigma, \tau} \delta_{\mathbf{k}, \mathbf{k}'} \right. \\
&\quad \left. + \sum_{\mathbf{R}_z, \sigma} c_{\mathbf{k}, \sigma}^{c*}(\mathbf{f}_l + \mathbf{R}_z) c_{\mathbf{k}', \sigma}^v(\mathbf{f}_l + \mathbf{R}_z) \sum_{\mathbf{R}_{||}} \mathbf{R} e^{i(\mathbf{k}' - \mathbf{k})\mathbf{R}_{||}} \right) \quad (\text{E.2})
\end{aligned}$$

While the first part can readily be evaluated upon knowledge of $\mathbf{d}_{\sigma, \tau}$, the second part remains more tricky. First let us mention that the "prefactor" consisting of the coefficients of the same atomic orbital for conduction and valence band states is supposed to be rather small, as the conduction band states are mainly composed of s-like states, whereas the valence band states should consist mainly of p-like states. However, this argument is by no means sufficient to disregard the term, as the sum $\sum_{\mathbf{R}_{||}}$ seems to be divergent.

So let's have a closer look at

$$\sum_{\mathbf{R}_{||}} (\mathbf{R}_z + \mathbf{f}_l + \mathbf{R}_{||}) e^{i(\mathbf{k}' - \mathbf{k})\mathbf{R}_{||}} .$$

The first two terms just give a delta-function $\delta_{\mathbf{k}, \mathbf{k}'}$ and we can include it in the first term of Eq. (E.2). The remaining contribution

$$\sum_{\mathbf{R}_{||}} \mathbf{R}_{||} e^{i(\mathbf{k}' - \mathbf{k})\mathbf{R}_{||}}$$

can be written as a derivative of a delta-function $\nabla_{\mathbf{k}} \delta_{\mathbf{k}, \mathbf{k}'}$. Now we have to keep in mind, we always use the dipole matrix elements for the WL in an integration, e.g. in the Rabi-energy or in the calculation of the macroscopic polarization. This means we can integrate by parts and use the delta-function to do the integration. Now that we are rid of the divergence, we can come back to the fact that the prefactor (in terms of TB coefficients) of this term is small, so that we actually can disregard it.

In conclusion we find for the WL-WL dipole matrix elements

$$\mathbf{d}_{\mathbf{k}\mathbf{k}'}^{cv} = e_0 \delta_{\mathbf{k}, \mathbf{k}'} \sum_{l=1}^2 \sum_{\mathbf{R}_z, \sigma, \tau} c_{\mathbf{k}, \sigma}^{c*}(\mathbf{f}_l + \mathbf{R}_z) c_{\mathbf{k}', \tau}^v(\mathbf{f}_l + \mathbf{R}_z) (\mathbf{d}_{\sigma, \tau} + (\mathbf{f}_l + \mathbf{R}_z)\delta_{\sigma, \tau}) , \quad (\text{E.3})$$

in addition we of course have to specify the polarization vector of the exciting light. This can lead to further simplifications as we are only interested in $d_{\mathbf{kk}'}^{cv} = \mathbf{p}d_{\mathbf{kk}'}^{cv}$ for the given light field polarization (with polarization vector \mathbf{p}).

The quantity $\mathbf{d}_{\sigma\tau}$ that we need to calculate the matrix elements can be obtained as follows: Assume that the assumption given above holds, namely that the conduction band states are mainly composed of s-like states, whereas the valence band states consist mainly of p-like states. Then we expect only two matrix elements of $\mathbf{d}_{\sigma\tau}$ to be relevant: \mathbf{d}_{s,p_x} and \mathbf{d}_{s,p_y} . As they should behave like αx and αy the common factor α can be fitted such that the result is consistent with the Kane-parameter of $\mathbf{k}\mathbf{p}$ -calculations. Alternatively, the 16 numbers $d_{\sigma\tau}$ for a given polarization can be obtained directly using the orthogonalized Slater orbitals [202].

List of Publications

Publications in peer reviewed journals

1. T. R. Nielsen, P. Gartner, M. Lorke, J. Seebek, and F. Jahnke,
Coulomb scattering in nitride based self-assembled quantum-dot systems,
Phys. Rev. B **72**, 235311 (2005)
2. M. Lorke, T. R. Nielsen, J. Seebek, P. Gartner, and F. Jahnke,
Influence of carrier-carrier and electron-phonon correlations on optical absorption and gain in quantum-dot systems,
Phys. Rev. B **73**, 085324 (2006)
3. M. Lorke, W. W. Chow, T. R. Nielsen, J. Seebek, P. Gartner, and F. Jahnke,
Anomaly in the excitation dependence of optical gain in
semiconductor quantum dots,
Phys. Rev. B **74**, 035334 (2006)
4. C. Gies, J. Wiersig, M. Lorke, F. Jahnke
Semiconductor model for quantum dot-based microcavity lasers,
Phys. Rev. A **75**, 013803 (2007)
5. M. Lorke, W. W. Chow, and F. Jahnke
Excitation dependences of gain and carrier-induced refractive index change in
quantum-dot lasers
Appl. Phys. Lett. **90**, 051112 (2007)

Conference proceedings

1. M. Lorke, T. R. Nielsen, J. Seebek, P. Gartner, and F. Jahnke,
Quantum kinetic effects in the optical absorption of semiconductor quantum-dot systems,
Journal of Physics: Conf. Series **35**, 182 (2006)

2. J. Seebeck, T. R. Nielsen, M. Lorke, P. Gartner, and F. Jahnke,
Quantum kinetic theory of phonon-assisted carrier transitions in nitride based
quantum-dot systems,
PSS(c) **3**, 2038 (2006)
3. T. R. Nielsen, J. Seebeck, M. Lorke, P. Gartner, and F. Jahnke,
Microscopic theory of carrier-carrier scattering in nitride based quantum-dot
systems,
PSS(c) **3**, 2030 (2006)
4. M. Lorke, J. Seebeck, T. R. Nielsen, P. Gartner, and F. Jahnke,
Many-body effects in semiconductor quantum dots,
NIC-Symposium, March 2006
5. Excitation dependence of the homogeneous linewidths in quantum dots,
M. Lorke, J. Seebeck, T. R. Nielsen, P. Gartner, and F. Jahnke,
PSS(c) **3**, 2393 (2006)
6. M. Lorke, W. W. Chow, and F. Jahnke
Reduction of optical gain in semiconductor quantum dots
Proc. SPIE **6468**, 646818 (2007)
7. M. Lorke, J. Seebeck, P. Gartner, and F. Jahnke
A microscopic theory for the optical properties of semiconductor quantum-dot
systems
AIP Conf. Proc. **893**, 923 (2007)
8. J. Wiersig, C. Gies, M. Lorke and F. Jahnke
A Semiconductor Theory for Quantum-Dot Microcavity Lasers
AIP Conf. Proc. **893**, 1125 (2007)
9. J. Seebeck, M. Lorke, P. Gartner, and F. Jahnke
Carrier-carrier and carrier-phonon scattering in the low-density and low-temperature
regime for resonantly pumped semiconductor quantum dots,
to appear in PSS(c)

Conference Contributions

(the underlined person has given/presented the talk/poster)

1. M. Lorke, T. R. Nielsen, J. Seebeck, P. Gartner, and F. Jahnke,
Optischer Gewinn in Quantenpunkten,
DPG spring meeting 2005 (Berlin), talk

2. J. Wiersig, T. Aschenbrenner, N. Baer, M. Lorke, P. Gartner, F. Jahnke, M. Benyoucef, P. Michler, M. Schwab, H. Kurtze, M. Bayer, and A. Forchel,
Dynamics of spontaneous emission from quantum dots in microcavities,
DPG spring meeting 2005 (Berlin), talk
3. J. Wiersig, T. Aschenbrenner, N. Baer, M. Lorke, P. Gartner, F. Jahnke, M. Benyoucef, P. Michler, M. Schwab, H. Kurtze, and M. Bayer,
Microscopic theory of photoluminescence from semiconductor quantum dots in microcavities,
CLEO/QELS 2005 (Baltimore), talk
4. M. Lorke, T. R. Nielsen, J. Seebek, P. Gartner, and F. Jahnke,
Optical absorption in semiconductor quantum-dot systems,
Workshop “Progress in Nonequilibrium Green’s Functions 3” 2005 (Kiel), poster
5. T. R. Nielsen, J. Seebek, M. Lorke, P. Gartner, and F. Jahnke,
Microscopic theory of carrier-carrier scattering in nitride based quantum-dot systems,
ICNS6 2005 (Bremen), poster
6. J. Seebek, T. R. Nielsen, M. Lorke, P. Gartner, and F. Jahnke,
Quantum kinetic theory of phonon-assisted carrier transitions in nitride based quantum-dot systems,
ICNS6 2005 (Bremen), talk
7. M. Lorke, J. Seebek, T. R. Nielsen, P. Gartner, and F. Jahnke,
Many-body theory of optical gain in semiconductor quantum dot lasers,
CLEO/QELS 2006 (Long Beach), invited talk
8. M. Lorke, T. R. Nielsen, J. Seebek, P. Gartner, and F. Jahnke,
Influence of carrier-carrier and electron-phonon correlations on optical absorption and gain in quantum-dot systems,
NOEKS8 2006 (Münster), talk
9. M. Lorke, J. Seebek, T. R. Nielsen, P. Gartner, and F. Jahnke,
Optical absorption and gain of Quantum Dots - Influence of Coulomb and carrier-phonon correlations,
DPG spring meeting 2006 (Dresden), talk
10. M. Lorke, T. R. Nielsen, J. Seebek, P. Gartner, and F. Jahnke,
Influence of carrier-carrier and carrier-phonon correlations on optical absorption and gain in quantum-dot systems,
ICPS28 2006 (Wien), poster

11. M. Lorke, J. Seebbeck, T. R. Nielsen, P. Gartner, F. Jahnke, and W. W. Chow
Dephasing mechanisms in Quantum Dots,
Workshop “Quantum Optics in Semiconductors” 2006 (Würzburg), talk
12. M. Lorke, J. Seebbeck, P. Gartner, F. Jahnke, and W. W. Chow
Gain reduction in Semiconductor Quantum Dots,
DPG spring meeting 2007 (Regensburg), talk
13. M. Lorke, W. W. Chow, and F. Jahnke
A microscopic theory for optical gain in semiconductor quantum dots
SPIE Photonics West/OPTO 2007 meeting (2007), talk
14. M. Lorke, J. Seebbeck, P. Gartner, W. W. Chow, and F. Jahnke,
Gain reduction in semiconductor Quantum Dot systems,
DPG spring meeting 2008 (Berlin), talk
15. M. Lorke, J. Seebbeck, S. Schulz, P. Gartner, and F. Jahnke
Quantum kinetic description of dephasing in semiconductor
quantum dot systems,
NOEKS9 2008 (Klink/Müritz), poster
16. J. Seebbeck, M. Lorke, S. Schulz, P. Gartner, G. Czycholl, and F. Jahnke
Theory for Optical Spectra of Nitride Quantum Dot Systems,
IWN2008 (Montreux), talk

Bibliography

- [1] J. P. Gordon, H. J. Zeiger, and C. H. Townes. Molecular microwave oscillator and new hyperfine structure in the microwave spectrum of NH₃. *Phys. Rev.*, 95:282, 1954.
- [2] T.H. Maiman. Stimulated optical radiation in ruby. *Nature*, 187:493, 1960.
- [3] P. Walther and A. Zeilinger. Experimental realization of a photonic bell-state. *Phys. Rev. A*, 72:010302(R), 2005.
- [4] S. Gröblacher, T. Paterek, R. Kaltenbaek, C. Brukner, M. Zukowski, M. Aspelmeyer, and A. Zeilinger. An experimental test of non-local realism. *Nature*, 446:871, 2007.
- [5] Y. Masumoto and T. Takagahara, editors. *Semiconductor Quantum Dots*. Springer-Verlag, Berlin, 1. edition, 2002.
- [6] P. Michler. *Single Quantum Dots - Fundamentals, Applications and New Concepts*. Springer-Verlag, Berlin, 2003.
- [7] H.-G. Park Park, Se-Heon Kim, Soon-Hong Kwon, Young-Gu Ju, Jin-Kyu Yang, Jong-Hwa Baek, Sung-Bock Kim, and Yong-Hee Lee. *Science*, 305:1444, 2004.
- [8] S. Strauf, K. Hennessy, M. T. Rakher, Y.-S. Choi, A. Badolato, L. C. Andreani, E. L. Hu, P. M. Petroff, and D. Bouwmeester. Self-tuned quantum dot gain in photonic crystal lasers. *Phys. Rev. Lett.*, 96:127404, 2006.
- [9] S. M. Ulrich, C. Gies, J. Wiersig, S. Reitzenstein, C. Hofmann, A. Löffler, A. Forchel, F. Jahnke, and P. Michler. Photon statistics of semiconductor microcavity lasers. *Phys. Rev. Lett.*, 98:043906, 2007.
- [10] P. Michler, A. Kiraz, C. Becher, W. V. Schoenfeld, P. M. Petroff, L. Zhang, E. Hu, and A. Imamoğlu. A quantum dot single-photon turnstile device. *Science*, 290:2282, 2000.
- [11] M. Bayer, P. Hawrylak, K. Hinzer, S. Fafard, M. Korkusinski, Z. R. Wasilewski, O. Stern, and A. Forchel. Coupling and entangling of quantum states in quantum dot molecules. *Science*, 291:451, 2001.
- [12] E. Moreau, I. Robert, J. M. Gérard, I. Abram, L. Manin, and V. Thierry-Mieg. Single-mode solid-state single photon source based on isolated quantum dots in pillar microcavities. *Appl. Phys. Lett.*, 79:2865, 2001.

- [13] G. S. Solomon, M. Pelton, and Y. Yamamoto. Single-mode spontaneous emission from a single quantum dot in a three-dimensional microcavity. *Phys. Rev. Lett.*, 86:3903, 2001.
- [14] Matthew Pelton, Charles Santori, Jelena Vucković, Bingyang Zhang, Glenn S. Solomon, Jocelyn Plant, and Yoshihisa Yamamoto. Efficient source of single photons: A single quantum dot in a micropost microcavity. *Phys. Rev. Lett.*, 89:233602, 2002.
- [15] K. Sebald, P. Michler, T. Passow, D. Hommel, G. Bacher, and A. Forchel. Single-photon emission of cdse quantum dots at temperatures up to 200 k. *Appl. Phys. Lett.*, 81:2920, 2002.
- [16] Charles Santori, Matthew Pelton, Glenn Solomon, Yseulte Dale, and Yoshihisa Yamamoto. Triggered single photons from a quantum dot. *Phys. Rev. Lett.*, 86:1502, 2001.
- [17] Zhiliang Yuan, Beata E. Kardynal, R. Mark Stevenson, Andrew J. Shields, Charlene J. Lobo, Ken Cooper, Neil S. Beattie, David A. Ritchie, and Michael Pepper. Electrically driven single-photon source. *Science*, 295:102, 2002.
- [18] N. Akopian, N. H. Lindner, E. Poem, Y. Berlatzky, J. Avron, D. Gershoni, B. D. Gerardot, and P. M. Petroff. Entangled photon pairs from semiconductor quantum dots. *Phys. Rev. Lett.*, 96(13):130501, 2006.
- [19] Luis Quiroga and Neil F. Johnson. Entangled bell and greenberger-horne-zeilinger states of excitons in coupled quantum dots. *Phys. Rev. Lett.*, 83:2270–2273, 1999.
- [20] J. P. Reithmaier, G. Sek, A. Löffler, C. Hofmann, S. Kuhn, S. Reitzenstein, L.V. Keldysh, V. D. Kulakovskii, T. L. Reinecke, and A. Forchel. Strong coupling in a single quantum dot-semiconductor microcavity system. *Nature*, 432:197, 2004.
- [21] T. Yoshie, A. Scherer, J. Hendrickson, G. Khitrova, H. M. Gibbs, G. Rupper, C. Ell, O. B. Shchekin, and D. G. Deppe. Vacuum rabi splitting with a single quantum dot in a photonic crystal nanocavity. *Nature*, 432:200, 2004.
- [22] S. Nakamura, T. Mukai, and M. Senoh. Candela-class high-brightness InGaN/AlGaN double-heterostructure blue-light-emitting diodes. *Appl. Phys. Lett.*, 64:1687, 1994.
- [23] S. Nakamura, M. Senoh, S. Nagahama, N. Iwasa, T. Yamada, T. Matsushita, H. Kiyoku, and Y. Sugimoto. InGaN-based multi-quantum-well-structure laser diodes. *Japanese Journal of Applied Physics*, 35:L74, 1996.
- [24] H. Lohmeyer, K. Sebald, C. Kruse, R. Kröger, J. Gutowski, D. Hommel, J. Wiersig, N. Baer, and F. Jahnke. Confined optical modes in monolithic II-VI pillar microcavities. *Appl. Phys. Lett.*, 88:051101, 2006.

- [25] X. Fan, P. Palinginis, S. Lacey, H. Wang, and M. C. Lonergan. Coupling semiconductor nanocrystals to a fused-silica microsphere: a quantum-dot microcavity with extremely high q factors. *Opt. Lett.*, 25:1600, 2000.
- [26] P.T. Snee, Y. Chan, D.G. Nocera, and M.G. Bawendi. Whispering-gallery-mode lasing from a semiconductor nanocrystal/microsphere resonator composite. *Advanced Materials*, 17:1131, 2005.
- [27] http://en.wikipedia.org/wiki/Image:St_Pauls_aerial.jpg.
- [28] H. Lohmeyer, C. Kruse, K. Sebald, J. Gutowski, and D. Hommel. Enhanced spontaneous emission of cdse quantum dots in monolithic II-VI pillar microcavities. *Appl. Phys. Lett.*, 89:091107, 2006.
- [29] J. Wiersig and M. Hentschel. Unidirectional light emission from high-q modes in optical microcavities. *Phys. Rev. A*, 73:031802, 2006.
- [30] T.R. Nielsen. *Carrier-carrier and carrier-phonon scattering in self-assembled quantum dots*. PhD thesis, Universitt Bremen, 2005.
- [31] J. Seebeck. *Carrier-Phonon Interaction in Semiconductor Quantum Dots*. PhD thesis, Universitat Bremen, 2009.
- [32] C. Gies, J. Wiersig, M. Lorke, and F. Jahnke. Semiconductor model for quantum dot-based microcavity lasers. *Phys. Rev. A*, 75:013803, 2007.
- [33] V.I. Klimov. Nanocrystal quantum dots - from fundamental photophysics to multi-color lasing. *Los Alamos Science*, 28:214, 2003.
- [34] L. P. Kouwenhoven, D. G. Austing, and S. Tarucha. Few-electron quantum dots. *Report on Progress in Physics*, 64:701, 2001.
- [35] S. Anders, C.S. Kim, B. Klein, M.W. Keller, R.P. Mirin, and A.G. Norman. Bimodal size distribution of self-assembled $In_xGa_{1-x}As$ quantum dots. *Phys. Rev. B*, 66:125309, 2002.
- [36] W. Seifert, N. Carlsson, M. Miller, M. Pistol, L. Samuelson, and L. Reine Wallenberg. In-situ growth of quantum dot structures by the Stranski-Krastanow growth mode. *Prog. Crystal Growth and Charact.*, 33:423, 1996.
- [37] K. Jacobi. Atomic structure of InAs quantum dots on GaAs. *Progress in Surface Science*, 71:185, 2003.
- [38] R.P. Feynman. The theory of positrons. *Phys. Rev.*, 76:749, 1949.
- [39] R.P. Feynman. Space-time approach to quantum electrodynamics. *Phys. Rev.*, 76:769, 1949.

- [40] R.P. Feynman. Mathematical formulation of the quantum theory of electromagnetic interaction. *Phys. Rev.*, **80**:440, 1950.
- [41] E. Fick. *Einführung in die Grundlagen der Quantentheorie*. Aula-Verlag, Wiesbaden, 6. edition, 1988.
- [42] C. Cohen-Tannoudji, J. Dupont-Roc, and G. Grynberg. *Photons & Atoms*. Wiley, New York, 3. edition, 1989.
- [43] R. van Leeuwen. First-principles approach to the electron-phonon interaction. *Phys. Rev. B*, **69**:115110, 2004.
- [44] P.C. Martin and J. Schwinger. Theory of many-particle systems. *Phys. Rev.*, **115**:1342, 1959.
- [45] Leo P. Kadanoff and Paul C. Martin. Theory of many-particle systems. ii. superconductivity. *Phys. Rev.*, **124**:670, 1961.
- [46] G. Baym and L.P. Kadanoff. Conservation laws and correlation functions. *Phys. Rev.*, **124**:287, 1961.
- [47] A. A. Abrikosov, L. P. Gorkov, and I. E. Dzyaloshinski. *Methods of Quantum Field Theory in Statistical Physics*. Dover, New York, 1963.
- [48] L.V. Keldysh. Diagram technique for nonequilibrium processes. *Sov.Phys. JETP*, **20**:1018, 1965.
- [49] L. P. Kadanoff and G. Baym. *Quantum Statistical Mechanics*. W. A. Benjamin, New York, 1962. Reissued by Addison-Wesley, Reading, Mass., 1989.
- [50] D. F. DuBois. *Nonequilibrium quantum statistical mechanics od plasmas and radiation*. Lectures in Theoretical Physics, edited by W.E.Brittin et.al., volume 9C pages 469-620,Gordon and Breach New York, 1967.
- [51] P. Danielewicz. Quantum theory of nonequilibrium processes. *Ann. Phys.*, **152**:239, 1984.
- [52] V. Korenman. Nonequilibrium quantum statistics; application to the laser. *Annals of Physics*, **39**:72–126, 1966.
- [53] R. Binder and S.W. Koch. Nonequilibrium semiconductor dynamics. *Progress in Quant. Electron.*, **19**:307–462, 1995.
- [54] K. Henneberger and V. May. Nonequilibrium green's functions and kinetic equations for highly excited semiconductors: I. general considerations. *Physica A*, **138**:537, 1986.
- [55] K. Henneberger, G. Manzke, V. May, and R. Zimmermann. Nonequilibrium green's functions and kinetic equations for highly excited semiconductors: II. application to the study of nonlinear optical and transport properties of the many-exciton system. *Physica A*, **138**:557, 1986.

- [56] K. Henneberger. Resonant laser excitation and electron-hole kinetics of a semiconductor: I. nonequilibrium green's function treatment and fundamental equations. *Physica A*, **150**:419, 1988.
- [57] K. Henneberger and K.H. Kühn. Resonant laser excitation and electron-hole kinetics of a semiconductor: II. nonlinear particle transport and field propagation. *Physica A*, **150**:439, 1988.
- [58] J. Rammer and H. Smith. Quantum field-theoretical methods in transport theory of metals. *Rev. Mod. Phys.*, **58**:323, 1986.
- [59] W. Schäfer and M. Wegener. *Semiconductor Optics and Transport Phenomena*. Springer-Verlag, Berlin, 1. edition, 2002.
- [60] H. Haug and A.-P. Jauho. *Quantum Kinetics in Transport & Optics of Semiconductors*. Springer-Verlag, Berlin, 1. edition, 1996.
- [61] L. D. Landau and E. M. Lifschitz. *Lehrbuch der Theoretischen Physik - Band X: Physikalische Kinetik*. Akademie-Verlag, Berlin, 1. edition, 1986.
- [62] D. Kremp, M. Schlanges, and W.-D. Kraeft. *Quantum Statistics of Nonideal Plasmas*. Springer-Verlag, Berlin, 2004.
- [63] W. Nolting. *Grundkurs: Theoretische Physik - 6 Statistische Physik*. Verlag Zimmermann-Neufang, Ulmen, 1. edition, 1994.
- [64] L. E. Ballentine. *Quantum Mechanics - A Modern Development*. World Scientific, London, 1. edition, 1998.
- [65] M. Gell-Mann and F. Low. Bound States in Quantum Field Theory. *Phys. Rev.*, **84**(2):350–354, 1951.
- [66] A. L. Fetter and J. D. Walecka. *Quantum Theory of Many-Particle Systems*. Dover Publications, Mineola, New York, 2. edition, 2003.
- [67] G. D. Mahan. *Many-Particle Physics*. Plenum Press, London, 1. edition, 1981.
- [68] J. Schwinger. Brownian motion of a quantum oscillator. *J. Math. Phys.*, **2**:407, 1961.
- [69] L.V. Keldysh. Real-time nonequilibrium green's functions. In M. Bonitz and D. Semkat, editors, *Progress in Nonequilibrium Green's Function II*, page 4. World Scientific, 2003.
- [70] J. D. Jackson. *Classical Electrodynamics*. John Wiley & Sons, New York, 3. edition, 1998.
- [71] H. Haug and A.-P. Jauho. *Quantum Kinetics in Transport & Optics of Semiconductors*. Springer-Verlag, Berlin, 1. edition, 1996.

- [72] W. D. Kraeft, D. Kremp, W. Ebeling, and G. Röpke. *Quantum Statistics of Charged Particle Systems*. Akademie-Verlag, Berlin, 1986.
- [73] P. Gartner, L. Bányai, and H. Haug. Coulomb screening in the two-time Keldysh-Green-function formalism. *Phys. Rev. B*, **62**:7116, 2000.
- [74] T. Schmielau. *Optische und Ein-Teilchen-Eigenschaften von Halbleitern*. PhD thesis, Universität Rostock, 2001.
- [75] P. Gartner, J. Sebeck, and F. Jahnke. Relaxation properties of the quantum kinetics of carrier-LO-phonon interaction in quantum wells and quantum dots. *Phys. Rev. B*, **73**:115307, 2006.
- [76] H.S. Köhler and R. Binder. The interplay of electron-phonon and electron-electron scattering within the two-time green's function description. *Contrib. Plasma Phys.*, **37**:167, 1997.
- [77] P. Lipavský, V. Špička, and B. Velický. Generalized Kadanoff-Baym ansatz for deriving quantum transport equations. *Phys. Rev. B*, **34**:6933, 1986.
- [78] H.C. Tso and N.J. Morgenstern Horing. Exact functional differential variant of the generalized Kadanoff-Baym ansatz. *Phys. Rev. B*, **44**:1451, 1991.
- [79] V. Špička, B. Velický, and A. Kalvová. Long and short time quantum dynamics: I. between green's functions and transport equations. *Physica E*, **29**:154, 2005.
- [80] V. Špička, B. Velický, and A. Kalvová. Long and short time quantum dynamics: II. kinetic regime. *Physica E*, **29**:175, 2005.
- [81] V. Špička, B. Velický, and A. Kalvová. Long and short time quantum dynamics: III. transients. *Physica E*, **29**:196, 2005.
- [82] B. Velický, A. Kalvová, and V. Špička. Real-time nonequilibrium green's functions. In M. Bonitz and A. Filitov, editors, *Progress in Nonequilibrium Green's Function III*, volume 35, page 1. Journal of Physics: Conference Series, 2006.
- [83] M. Kira, F. Jahnke, W. Hoyer, and S. W. Koch. Quantum theory of spontaneous emission and coherent effects in semiconductor microstructures. *Prog. Quant. Electr.*, **23**:189, 1999.
- [84] F. Jahnke, M. Kira, W. Hoyer, and S. W. Koch. Influence of correlation effects on the excitonic semiconductor photoluminescence. *phys. stat. sol (b)*, **221**(1):189, 2000.
- [85] W. Hoyer, M. Kira, and S. W. Koch. Influence of Coulomb and phonon interaction on the exciton formation dynamics in semiconductor heterostructures. *Phys. Rev. B*, **67**:155113, 2003.

- [86] S. Chatterjee, C. Ell, S. Mosor, G. Khitrova, H. M. Gibbs, W. Hoyer, M. Kira, S. W. Koch, J. P. Prineas, and H. Stoltz. Excitonic photoluminescence in semiconductor quantum wells: Plasma versus excitons. *Phys. Rev. Lett.*, 92(6):067402, 2004.
- [87] T. Feldtmann, L. Schneebeli, M. Kira, and S. W. Koch. Quantum theory of light emission from a semiconductor quantum dot. *Phys. Rev. B*, 73:155319, 2006.
- [88] N. Baer, C. Gies, J. Wiersig, and F. Jahnke. Luminescence of a semiconductor quantum dot system. *Eur. Phys. J. B*, 50:411, 2006.
- [89] J. Fricke. Transport equations including many-particle correlations for an arbitrary quantum system: a general formalism. *Ann. Phys.*, 252:479, 1996.
- [90] J. Fricke. Improved transport equations including correlations for electron-phonon systems: comparison with exact solutions in one dimension. *Ann. Phys.*, 253:177, 1997.
- [91] W. Hoyer, M. Kira, and S. W. Koch. “Cluster expansion in semiconductor quantum optics” in Morawetz, Klaus (Ed.), *Nonequilibrium Physics at Short Time Scales*. Springer, Berlin, 2004.
- [92] G.C. Wick. The evaluation of the collision matrix. *Phys. Rev.*, 80:268, 1950.
- [93] G. Khitrova, H. M. Gibbs, F. Jahnke, M. Kira, and S. W. Koch. Nonlinear optics of normal-mode-coupling semiconductor microcavities. *Rev. Mod. Phys.*, 71:1591, 1999.
- [94] C. Gies. *Theory for Light-Matter Interaction in Semiconductor Quantum Dots*. PhD thesis, Universität Bremen, 2008.
- [95] M. Schwab, H. Kurtze, T. Auer, T. Berstermann, M. Bayer, J. Wiersig, N. Baer, C. Gies, F. Jahnke, J. P. Reithmaier, A. Forchel, M. Benyoucef, and P. Michler. Radiative emission dynamics of quantum dots in a single cavity micropillar. *Phys. Rev. B*, 74:045323, 2006.
- [96] V.M. Axt and A. Stahl. A dynamics-controlled truncation scheme for the hierarchy of density matrices in semiconductor optics. *Z. Phys. B*, 93:195, 1994.
- [97] V.M. Axt and A. Stahl. The role of the biexciton in a dynamic density matrix theory of the semiconductor band edge. *Z. Phys. B*, 93:205, 1994.
- [98] M. Buck, L. Wischmeier, S. Schumacher, G. Czycholl, F. Jahnke, T. Voss, I. Rückmann, and J. Gutowski. Light-polarization and intensity dependence of higher-order nonlinearities in excitonic FWM signals. *Eur. Phys. J. B*, 42:175, 2004.
- [99] S. Schumacher, G. Czycholl, F. Jahnke, I. Kudyk, H.I. Rückmann, J. Gutowski, A. Gust, G. Alexe, and D. Hommel. Polariton propagation in shallow-confinement heterostructures: Microscopic theory and experiment showing the breakdown of the dead-layer concept. *Phys. Rev. B*, 70:235340, 2004.

- [100] M. Buck. *Theoretische Beschreibung kohärenter optischer Nichtlinearitäten in Halbleiter-Quantenfilmen*. PhD thesis, Universität Bremen, 2004.
- [101] N.H. Kwong and R. Binder. Green's function approach to the dynamics-controlled truncation formalism: derivation of the $\chi^{(3)}$ equations of motion. *Phys. Rev. B*, **61**:8341, 2000.
- [102] G.D. Mahan. *Many-Particle Physics*. Plenum Press, New York, 1990.
- [103] B. Krummheuer, V. M. Axt, and T. Kuhn. Theory of pure dephasing and the resulting absorption lineshape in semiconductor quantum dots. *Phys. Rev. B*, **65**:195313, 2002.
- [104] R. Zimmermann and E. Runge. Dephasing in quantum dots via electron-phonon interaction. *Proc. 26th ICPS Edinburgh, IOP Conf. Series*, **171**:paper M 3.1, 2002.
- [105] A. Vagov, V.M. Axt, and T. Kuhn. Electro-phonon dynamics in optically excited quantum dots: Exact solution for multiple ultrashort laser pulses. *Phys. Rev. B*, **66**:165312, 2002.
- [106] E.A. Muljarov and R. Zimmermann. Dephasing in quantum dots: Quadratic coupling to acoustic phonons. *Phys. Rev. Lett.*, **93**:237401, 2004.
- [107] B. Krummheuer, V.M. Axt, T. Kuhn, I. D'Amico, and F. Rossi. Pure dephasing and phonon dynamics in gaas- and gan-based quantum dot structures: Interplay between material parameters and geometry. *Phys. Rev. B*, **71**:235329, 2005.
- [108] P. Borri, W. Langbein, S. Schneider, U. Woggon, R.L. Sellin, D. Ouyang, and D. Bimberg. Relaxation and dephasing of multiexcitons in semiconductor quantum dots. *Phys. Rev. Lett.*, **89**:187401, 2002.
- [109] J. Förstner, C. Weber, J. Danckwerts, and A. Knorr. Phonon-induced damping of rabi oscillations in semiconductor quantum dots. *phys. stat. sol. (b)*, **238**:419, 2003.
- [110] J. Förstner, C. Weber, J. Danckwerts, and A. Knorr. Phonon-assisted damping of rabi oscillations in semiconductor quantum dots. *Phys. Rev. Lett.*, **91**:127401, 2003.
- [111] E.A. Muljarov, T. Takagahara, and R. Zimmermann. Phonon-induced exciton dephasing in quantum dot molecules. *Phys. Rev. Lett.*, **95**:177405, 2005.
- [112] C. Hermannstädtter, G.J. Beirne, L. Wang, A. Rastelli, O.G. Schmidt, and P. Michler. Time-resolved optical spectroscopy of tunnel coupled lateral quantum dot molecules. In *Physics of Semiconductors, 28th International Conferencenal*, page 875, 2007.
- [113] P. Borri, W. Langbein, S. Schneider, U. Woggon, R. L. Sellin, D. Ouyang, and D. Bimberg. Ultralong dephasing times in ingaas quatum dots. *Phys. Rev. Lett.*, **87**:157401, 2001.

- [114] P. Borri, W. Langbein, S. Schneider, U. Woggon, R.L. Sellin, D. Ouyang, and D. Bimberg. Relaxation and dephasing of multiexcitons in semiconductor quantum dots. *IEEE Journ. Sel. Top. Quant. Elec.*, **8**:984, 2002.
- [115] H. Htoon, D. Kulik, O. Baklenov, A. L. Holmes Jr., T. Takagahara, and C. K. Shih. Carrier relaxation and quantum decoherence of excited states in self-assembled quantum dots. *Phys. Rev. B*, **63**:241303(R), 2001.
- [116] R. Oulton, J. J. Finley, A. I. Tartakovskii, D. J. Mowbray, M. S. Skolnick, M. Hopkinson, A. Vasanelli, R. Ferreira, and G. Bastard. Carrier relaxation and quantum decoherence of excited states in self-assembled quantum dots. *Phys. Rev. B*, **68**:235301, 2003.
- [117] T. Inoshita and H. Sakaki. Density of states and phonon-induced relaxation of electrons in semiconductor quantum dots. *Phys. Rev. B*, **56**:R4355, 1997.
- [118] J. Seebeck, T.R. Nielsen, P. Gartner, and F. Jahnke. Polarons in semiconductor quantum dots and their role in the quantum kinetics of carrier relaxation. *Phys. Rev. B*, **71**:125327, 2005.
- [119] Y. Z. Hu, H. Gießen, N. Peyghambarian, and S. W. Koch. Microscopic theory of optical gain in small semiconductor quantum dots. *Phys. Rev. B*, **53**:4814, 1996.
- [120] A. V. Uskov, I. Magnusdottir, B. Tromborg, J. Mørk, and R. Lang. Line broadening caused by coulomb carrier-carrier correlations and dynamics of carrier capture and emission in quantum dots. *Appl. Phys. Lett.*, **79**:1679, 2001.
- [121] H.C. Schneider, W.W. Chow, and S.W. Koch. Many-body effects in the gain spectra of highly excited quantum dot lasers. *Phys. Rev. B*, **64**:115315, 2001.
- [122] H.C. Schneider, W.W. Chow, and S.W. Koch. Excitation-induced dephasing in semiconductor quantum dots. *Phys. Rev. B*, **70**:235308, 2004.
- [123] Q.T. Vu, H. Haug, and S.W. Koch. Relaxation and dephasing quantum kinetics for a quantum dot in an optically excited quantum well. *Phys. Rev. B*, **73**:205317, 2006.
- [124] G. Manzke and K. Henneberger. Quantum-kinetic effects in the linear optical response of GaAs quantum wells. *phys. stat. sol. (b)*, **234**:233, 2002.
- [125] T.R. Nielsen, P. Gartner, and F. Jahnke. Many-body theory of carrier capture and relaxation in semiconductor quantum-dot lasers. *Phys. Rev. B*, **69**:235314, 2004.
- [126] N. Baer. *Optical and electronic properties of InGaAs and nitride quantum dots*. PhD thesis, Universität Bremen, 2006.
- [127] A. Schliwa, M. Winkelkemper, and D. Bimberg. Impact of size, shape, and composition on piezoelectric effects and electronic properties of In(Ga)As/GaAs quantum dots. *Phys. Rev. B*, **76**:205324, 2007.

- [128] W.W. Chow and S.W. Koch. *Semiconductor-Laser Fundamentals*. Springer-Verlag, Berlin, 1. edition, 1999.
- [129] S. Schulz. *Electronic and Optical Properties of Quantum Dots: A Tight-Binding Approach*. PhD thesis, Universität Bremen, 2007.
- [130] A. Wojs, P. Hawrylak, S. Fafard, and L. Jacak. Electronic structure and magneto-optics of self-assembled quantum dots. *Phys. Rev. B*, **54**:5604, 1996.
- [131] N. Baer. Optische Eigenschaften von Halbleiter-Quantenpunkten. Master's thesis, Universität Bremen, 2003.
- [132] G. Czycholl. *Theoretische Festkörperphysik*. Vieweg Verlag, Braunschweig, 2000.
- [133] N. H. Kwong, R. Takayama, I. Rumyantsev, M. Kuwata-Gonokami, and R. Binder. Evidence of nonperturbative continuum correlations in two-dimensional exciton systems in semiconductor microcavities. *Phys. Rev. Lett.*, **87**:027402, Jun 2001.
- [134] R. Hafenbrak, S.M. Ulrich, P. Michler, L. Wang, A. Rastelli, and O. G. Schmidt. Triggered polarization-entangled photon pairs from a single quantum dot up to 30 k. *New Journal of Phys.*, **9**:315, 2007.
- [135] T.R. Nielsen, P. Gartner, M. Lorke, J. Sebeck, and F. Jahnke. Coulomb scattering in nitride based self-assembled quantum-dot systems. *Phys. Rev. B*, **72**:235311, 2005.
- [136] H. Haug and A.-P. Jauho. *Quantum Kinetics in Transport & Optics of Semiconductors*. Springer-Verlag, Berlin, 2. edition, 2007.
- [137] F. Jahnke and S. W. Koch. Many-body theory for semiconductor microcavity lasers. *Phys. Rev. A*, **52**:1712, 1995.
- [138] F. Jahnke and S.W. Koch. Ultrafast intensity switching and nonthermal carrier effects in semiconductor microcavity lasers. *Appl. Phys. Lett.*, **67**:2278, 1995.
- [139] F. Jahnke, H.C. Schneider, and S.W. Koch. Combined influence of design and carrier scattering on the ultrafast emission dynamics of quantum well microcavity lasers. *Appl. Phys. Lett.*, **69**:1185, 1996.
- [140] H. Haug and S. W. Koch. *Quantum Theory of the Optical and Electronic Properties of Semiconductors*. World Scientific Publ., Singapore, 4. edition, 2004.
- [141] L. Banyai, T. Wicht, and H. Haug. *Z. Phys. B*, **77**:343, 1989.
- [142] H. Haug, L. Banyai, J. Lieber, and T. Wicht. *phys. stat. sol. (b)*, **159**:309, 1990.
- [143] F. Jahnke. A many-body theory for laser emission and excitonic effects in semiconductor microcavities, Habilitationsschrift, Universität Marburg. 1997.
- [144] H. Fröhlich. Electrons in lattice fields. *Adv. Phys.*, **3**:325, 1954.

- [145] B.A. Green. Quantitative determination of high- t_c superconductivity from the lattice polarization, structure effect and approach to 300 K t_c . *Phys. Lett. A*, **227**:372, 1997.
- [146] J. Seebeck. Quantenkinetische Beschreibung von Polaronen in Halbleiter-Quantenpunkten. Master's thesis, Universität Bremen, 2004.
- [147] P. Gartner, L. Bányai, and H. Haug. Two-time electron-LO-phonon quantum kinetics and the generalized Kadanoff-Baym approximation. *Phys. Rev. B*, **60**:14234, 1999.
- [148] P. Meystre and M. Sargent III. *Elements of Quantum Optics*. Springer, New York, 2nd edition, 1991.
- [149] M. Bayer and A. Forchel. Temperature dependence of the exciton homogeneous linewidth in $\text{In}_{0.6}\text{Ga}_{0.4}\text{As}/\text{GaAs}$ self-assembled quantum dots. *Phys. Rev. B*, **65**:041308(R), 2002.
- [150] K. Matsuda, K. Ikeda, T. Saiki, H. Saito, and K. Nishi. Carrier-carrier interaction in single $\text{In}_{0.5}\text{Ga}_{0.5}\text{As}$ quantum dots at room temperature investigated by near-field scanning optical microscope. *Appl. Phys. Lett.*, **83**:2250, 2003.
- [151] D. Bimberg, M. Grundmann, and N. N. Ledentsov. *Quantum Dot Heterostructures*. Wiley, New York, 1999.
- [152] J. Tatebayashi, N. Hatori, H. Kakuma, H. Ebe, H. Sudoand A. Kuramataand Y. Nakata, M. Sugawaraand, and Y. Arakawa. Low threshold current operation of self-assembled InAs/GaAs quantum dot lasers by metal organic chemical vapour deposition. *Electron. Lett.*, **39**:1130, 2003.
- [153] S. Deubert, R. Debusmann, J. P. Reithmaier, and A. Forchel. High-power quantum dot lasers with improved temperature stability of emission wavelength for uncooled pump sources. *Electron. Lett.*, **41**:1125, 2005.
- [154] P. M. Snowton, E. J. Pearce, H. C. Schneider, W. W. Chow, and M. Hopkinson. Filamentation and linewidth enhancement factor in InGaAs quantum dot lasers. *Appl. Phys. Lett.*, **81**:3251, 2002.
- [155] D. Bimberg. Quantum dots for lasers, amplifiers and computing. *J. Phys. D*, **38**:2055, 2005.
- [156] E. Malic, M.J.P. Bormann, P. Hovel, M. Kuntz, D. Bimberg, A. Knorr, and E. Scholl. Coulomb damped relaxation oscillations in semiconductor quantum dot lasers. *Selected Topics in Quantum Electronics, IEEE Journal of*, **13**:1242, 2007.
- [157] S. Fathpour, Z. Mi, and P. Bhattacharya. High-speed quantum dot lasers. *J. Phys. D*, **38**:2103, 2005.
- [158] H. Haug and S.W. Koch. *Quantum Theory of the Optical and Electronic Properties of Semiconductors*. World Scientific Publ., Singapore, 4. edition, 2004.

- [159] J.-Y. Bigot, M. T. Portella, R. W. Schoenlein, J. E. Cunningham, and C. V. Shank. Two-dimensional carrier-carrier screening in a quantum well. *Phys. Rev. Lett.*, 67:636, 1991.
- [160] W.A. Hügel, M.F. Heinrich, and M. Wegener. Dephasing due to carrier-carrier scattering in 2d. *phys. stat. sol. (b)*, 221:473, 2000.
- [161] H. Haug. Coulomb quantum kinetics for semiconductor femtosecond spectroscopy. *phys. stat. sol. (b)*, 221:179, 2000.
- [162] S. Osborne, P. Blood, P. Smowton, J. Lutti, Y.C. Xin, A. Stintz, D. Huffaker, and L.F. Lester. State filling in inas quantum-dot laser structures. *IEEE J. Quant. Electron.*, 40:1639, 2004.
- [163] B. Dagens, A. Markus, J. X. Chen, J. G. Provost, D. Make, O. Le Gouezigou, J. Landreau, A. Fiore, and B. Thedrez. Giant linewidth enhancement factor and purely frequency modulated emission from quantum dot lasers. *Electron. Lett.*, 41:323, 2005.
- [164] R. E. Slusher and U. Mohideen. *Optical Processes in Microcavities*, page 315. World Scientific, Singapore, 1996.
- [165] P. Michler, A. Kiraz, L. Zhang, C. Becher, E. Hu, and A. Imamoğlu. Laser emission from quantum dots in microdisk structures. *Appl. Phys. Lett.*, 77:184, 2000.
- [166] L. Zhang and E. Hu. Lasing from InGaAs quantum dots in an injection microdisk. *Appl. Phys. Lett.*, 82:319, 2002.
- [167] F. DeMartini and G. R. Jacobovitz. Anomalous spontaneous-stimulated-decay phase transition and zero-threshold laser action in a microscopic cavity. *Phys. Rev. Lett.*, 60:1711, 1988.
- [168] H. Yokoyama and S. D. Brorson. Rate equation analysis of microcavity lasers. *J. Appl. Phys.*, 66:4801, 1989.
- [169] Y. Yamamoto, S. Machida, and G. Björk. Microcavity semiconductor laser with enhanced spontaneous emission. *Phys. Rev. A*, 44:657, 1991.
- [170] P. R. Rice and H. J. Carmichael. Photon statistics of a cavity-QED laser: A comment on the laser-phase-transition analogy. *Phys. Rev. A*, 50:4318, 1994.
- [171] R. Hanbury Brown and R. Q. Twiss. Correlation between photons in two coherent beams of light. *Nature*, 177:27, 1956.
- [172] R. Jin, D. Boggavarapu, M. Sargent III, P. Meystre, H. M. Gibbs, and G. Khitrova. Photon-number correlations near the threshold of microcavity lasers in the weak-coupling regime. *Phys. Rev. A*, 49:4038, 1994.
- [173] O. Painter, R. K. Lee, A. Scherer, A. Yariv, J.D. O'Brien, P.D. Dapkus, and I. Kim. Two-dimensional photonic band-gap defect mode laser. *Science*, 284:1819, 1999.

- [174] O. Benson and Y. Yamamoto. Master-equation model of a single-quantum-dot microsphere laser. *Phys. Rev. A*, 59:4756, 1999.
- [175] C. Wiele, F. Haake, and Y. M. Golubev. Quantum-dot laser with periodic pumping. *Phys. Rev. A*, 60:4986, 1999.
- [176] J. Wiersig, C. Gies, N. Baer, and F. Jahnke. *to appear in Adv. in Solid State Phys.*, 2008.
- [177] I. E. Protsenko and M. Travagnin. Microscopic model of semiconductor laser without inversion. *Phys. Rev. A*, 65:013801, 2001.
- [178] M. Travagnin. Effects of Pauli blocking on semiconductor laser intensity and phase noise spectra. *Phys. Rev. A*, 64:013818, 2001.
- [179] Roy J. Glauber. Photon correlations. *Phys. Rev. Lett.*, 10(3):84, 1963.
- [180] D. Burak and R. Binder. Cold-cavity vectorial eigenmodes of VCSELs. *IEEE J. Quantum Electronics*, 33(7):1205–1215, 1997.
- [181] J. Wiersig. Light-matter interaction and quantum chaos in semiconductor nanostructures and optical microcavities, Habilitationsschrift, Universität Bremen. 2007.
- [182] H. Lohmeyer. *Optischer Einschluss, Lasing und Purcell-Effekt in Mikrosäulen auf Basis breitlückiger Halbleiter*. Dissertation, Universität Bremen, 2007.
- [183] R. Loudon. *The quantum theory of light*. Clarendon Press, Oxford, 2nd edition, 1983.
- [184] S. Nakamura, G. Fasol, and S. J. Pearton. *The blue laser diode*. Springer, Berlin, 2000.
- [185] S. Nakamura and F. Chichibu, editors. *Introduction to nitride semiconductor blue lasers and light emitting diodes*. CRC press, Boca Raton, 2000.
- [186] I. Vurgaftman and J.R. Meyer. Band parameters for nitrogen-containing semiconductors. *J. Appl. Phys.*, **94**:3675, 2003.
- [187] S.L. Chuang and C.S. Chang. $k \cdot p$ method for strained wurtzite semiconductors. *Phys. Rev. B*, **54**:2491, 1996.
- [188] A.D. Andreev and E.P. O'Reilly. Theory of the electronic structure of GaN/AlN hexagonal quantum dots. *Phys. Rev. B*, **62**:15851, 2000.
- [189] A. Bagga, P.K. Chattopadhyay, and S. Ghosh. Dark and bright excitonic states in nitride quantum dots. *Phys. Rev. B*, **71**:115327, 2005.
- [190] M. Winkelnkemper, R. Seguin, S. Rodt, A. Schliwa, L. Reißmann, A. Strittmatter, A. Hoffmann, and D. Bimberg. Polarized emission lines from a- and b-type excitonic complexes in single InGaN/GaN quantum dots. *J. of App. Phys.*, **101**:113708, 2007.

- [191] S. Schulz and G. Czycholl. Tight-binding model for semiconductor nanostructures. *Phys. Rev. B*, **72**:165317, 2005.
- [192] S. Schulz, S. Schumacher, and G. Czycholl. Tight-binding model for semiconductor quantum dots with a wurtzite crystal structure: From one-particle properties to coulomb correlations and optical spectra. *Phys. Rev. B*, **73**:245327, 2006.
- [193] S. Schulz, S. Schumacher, and G. Czycholl. Spin-orbit coupling and crystal-field splitting in the electronic and optical properties of nitride quantum dots with a wurtzite crystal structure. *Eur. Phys. J. B*, **64**:51, 2008.
- [194] J. Seebeck, T.R. Nielsen, P. Gartner, and F. Jahnke. Quantum kinetic theory of phonon-assisted carrier transitions in nitride-based quantum-dot systems. *Eur. Phys. J. B*, **49**:167, 2006.
- [195] P. Lawaetz. Stability of the wurtzite structure. *Phys. Rev. B*, **5**:4039, 1972.
- [196] W. W. Chow, M. Kira, and S. W. Koch. Microscopic theory of optical nonlinearities and spontaneous emission lifetime in group-III nitride quantum wells. *Phys. Rev. B*, **60**:1947, 1999.
- [197] H. C. Schneider and W. W. Chow. Theory of laser gain in InGaN quantum dots. *Appl. Phys. Lett.*, **81**:2566, 2002.
- [198] F. Bernardini, V. Fiorentini, and D. Vanderbilt. Polarization-based calculation of the dielectric tensor of polar crystals. *Phys. Rev. Lett.*, **79**:3958, 1997.
- [199] F.D. Sala, A. Di Carlo, P. Lugli, F. Bernardini, V. Fiorentini, R. Scholz, and J.-M. Jancu. Free-carrier screening of polarization fields in wurtzite GaN/InGaN laser structures. *Appl. Phys. Lett.*, **74**:2002, 1999.
- [200] T. Saito and Y. Arakawa. Electronic structure of piezoelectric $\text{In}_{0.2}\text{Ga}_{0.8}\text{N}$ quantum dots in GaN calculated using a tight-binding method. *Physica E*, **15**:169, 2002.
- [201] S. De Rinaldis, I. D'Amico, and F. Rossi. Intrinsic electric field effects on few-particle interactions in coupled GaN quantum dots. *Phys. Rev. B*, **69**:235316, 2004.
- [202] N. Baer, S. Schulz, P. Gartner, S. Schumacher, G. Czycholl, and F. Jahnke. Influence of symmetry and Coulomb correlation effects on the optical properties of nitride quantum dots. *Phys. Rev. B*, **76**:75310, 2007.
- [203] S. Schulz, S. Schumacher, and G. Czycholl. Semiconductor nanocrystals and embedded quantum dots: Electronic and optical properties. *phys. stat. sol. (b)*, **244**:2399, 2007.
- [204] C. Cohen-Tannoudji, B. Diu, and F. Laloe. *Quantum Mechanics: Volume 1*. Wiley, New York, 1991.

- [205] W.H. Press, S.A. Teukolsky, W.T. Vetterling, and B.P. Flannery. *Numerical Recipes in Fortran*. Cambridge University Press, New York, 2. edition, 1992.
- [206] I. N. Bronstein and K. A. Semendjajew. *Taschenbuch der Mathematik*. B.G. Teubner Verlagsgesellschaft, Leipzig, 25. edition, 1991.

t

Danksagung

Zuallererst geht mein Dank an Prof. Dr. Frank Jahnke für die hervorragende Betreuung und Unterstützung während der letzten Jahre. Paul Gartner danke ich für die häufigen und fruchtbaren Diskussionen, sei es über Grundlagen der theoretischen Physik oder über praktische Probleme. An Jan Wiersig geht ein herzlicher Dank für die Zusammenarbeit, besonders bezogen auf Teil IV dieser Arbeit. Bei Weng W. Chow bedanke ich mich für die enge Zusammenarbeit sowie für die Einladung nach Albuquerque.

Prof. Dr. Andreas Knorr danke ich für die bereitwillige Übernahme des Zweitgutachtens.

Ganz besonders möchte ich an dieser Stelle meinen Kollegen Jan Seebeck und Christopher Gies danken, sowohl für die angenehme Arbeitsatmophäre als auch für Unterstützung und extrem fruchtbare und enge Zusammenarbeit. Ebenso danke ich Stefan Schulz für die gute Zusammenarbeit bezüglich des Teils V, sowie für die Bereitstellung der Tight-Binding Ergebnisse. Desweiteren danke ich allen anderen Mitgliedern der Arbeitsgruppen Jahnke und Czycholl für die gute Arbeitsatmophäre und Andreas Beuthner und Klaus Bowe für die technischen Hilfestellungen während der gesamten Zeit.

Für das Korrekturlesen der Arbeit bedanke ich mich bei Jan Seebeck, Christopher Gies, Jan Wiersig, Paul Gartner und Kolja Schuh.

Schlußendlich geht mein Dank an meine Eltern und an meinen Paten Klaus Wedehase, ohne deren Unterstützung all dies nicht möglich gewesen wäre.

Schließen möchte ich mit einem Hinweis Ciceros, den ich für das Ende einer solchen, doch recht langen, Arbeit für angemessen halte.

Acti iucundi labores

Marcus Tullius Cicero